Experimental and Modelling Studies of Cold Start Processes in Proton Exchange Membrane Fuel Cells

by

Kui Jiao

A thesis
presented to the University of Waterloo
in fulfillment of the
thesis requirement for the degree of
Doctor of Philosophy
in
Mechanical Engineering

Waterloo, Ontario, Canada, 2011

Author's Declaration

I hereby declare that I am the sole author of this thesis. This is a true copy of the thesis, including any required final revisions, as accepted by my examiners.

I understand that my thesis may be made electronically available to the public.

Kui Jiao

Abstract

Proton exchange membrane fuel cell (PEMFC) has been considered as one of the most promising energy conversion devices for the future in automotive applications. One of the major technical challenges for the commercialization of PEMFC is the effective start-up from subzero temperatures, often referred to as “cold start”. The major problem of PEMFC cold start is that the product water freezes when the temperature inside the PEMFC is lower than the freezing point. If the catalyst layer (CL) is fully occupied by ice before the cell temperature rises above the freezing point, the electrochemical reaction may stop due to the blockage of the reaction sites. However, only a few of the previous PEMFC studies paid attention to cold start. Hence, understanding the ice formation mechanisms and optimizing the design and operational strategies for PEMFC cold start are critically important.

In this research, an experimental setup for the cold start testing with simultaneous measurement of current and temperature distributions is designed and built; a one-dimensional (1D) analytical model for quick estimate of purging durations before the cold start processes is formulated; and a comprehensive three-dimensional (3D) PEMFC cold start model is developed. The unique feature of the cold start experiment is the inclusion of the simultaneous measurement of current and temperature distributions. Since most of the previous numerical models are limited to either 1D or two-dimensional (2D) or 3D but only considering a section of the entire cell due to computational requirement, the measured distribution data are critically important to better understand the PEMFC cold start characteristics. With a full set of conservation equations, the 3D model comprehensively accounts for the various transport phenomena during the cold start processes. The unique feature of this model is the inclusion of: (i) the water freezing in the membrane electrolyte and its effects on the membrane conductivity; (ii) the non-equilibrium mass transfer between the water in the ionomer and the water (vapour, liquid and ice) in the pore region of the CL; and (iii) both the water freezing and melting in the CL and gas diffusion layer (GDL). This model therefore provides the fundamental framework for the future top-down multi-dimensional multiphase modelling of PEMFC. The experimental and numerical results elaborate the ice formation mechanisms and other important transport phenomena during the PEMFC cold start processes. The effects of the various cell designs, operating conditions and external heating methods on the cold start performance are studied. Independent tests are carried out to identify and optimize the important design and operational parameters.

Acknowledgements

I would like to express my deepest gratitude to my supervisor, Dr. Xianguo Li, for his invaluable guidance, steady encouragement, inspiration and support throughout my Ph.D. I would also like to thank my committee members, Dr. Nasser Ashgriz, Dr. Siva Sivoththaman, Dr. Robert A. Varin and Dr. John Z. Wen for taking the time to scrutinize my thesis. Their comments are highly appreciated.

I would like to thank all my group members, especially Ibrahim E. Alaefour, Dr. Gholamreza Karimi, Saher Al Shakhshir, Dr. Hao Wu and Dr. Nada Zamel. Without their help, encouragement and fruitful discussions throughout the course of my Ph.D., I would not have been able to put together this important publication.

The financial support by the Natural Sciences and Engineering Research Council of Canada (NSERC) through Discovery Grants and a Strategic Project Grant and by Auto21 is greatly appreciated. I would also like to thank the Chinese Government Award for Outstanding Self-financed Students Abroad and the Next Energy Inc. Graduate Scholarship in Sustainable Energy.

Table of Contents

List of Tables

List of Figures

List of Symbols

a	Water activity
A	Cell geometric area (m^2)
A_{act}	Flat active reaction area (m^2)
A_F	Interface area between flow channel and gas diffusion layer (m^2)
c	Concentration (kg m^{-3} or kmol m^{-3})
C_p	Specific heat capacity (J kg^{-1} K^{-1})
D	Mass diffusion coefficient (m^2 s^{-1})
EW	Equivalent weight of membrane (kg $kmol^{-1}$)
F	Faraday's constant (96487 C mol^{-1})
h	Latent heat (J kg^{-1}), heat transfer coefficient (W m^{-2} K^{-1})
I	Current density (A cm^{-2})
j	Reaction rate (A m^{-3})
j_0	Volumetric exchange current density (A m^{-3})
k	Thermal conductivity (W m^{-1} K^{-1})
K	Permeability (m^2)
$\dot{m}$	Mass flow rate (kg s^{-1})
M	Molecular weight (kg $kmol^{-1}$)
n_d	Electro-osmotic drag coefficient (H_2O per H^+)
N_F	Number of flow channels in parallel
p	Pressure (Pa)
$\dot{Q}$	Heat transfer rate (W)
r	Pore radius (m)
R	Universal gas constant (8.314 J mol^{-1} K^{-1})
RH	Relative humidity
s	Volume fraction
S	Source terms, entropy (J $kmol^{-1}$ K^{-1})
t	Time (s)
Δt	Time step (s)
T	Temperature (K)

T_0	Volume averaged temperature (K)
$\vec{u}$	Velocity (m s^{-1})
V	Electrical potential (V)
$\dot{V}$	Volume flow rate (m^3 s^{-1})
X	Mole fraction
Y	Mass fraction

Greek letters

α	Transfer coefficient
γ	Water phase change rate (s^{-1})
δ	Thickness (m)
ε	Porosity
ζ	Water phase change rate (s^{-1})
η	Over potential (V)
θ	Contact angle (^{o})
κ	Electrical conductivity (S m^{-1})
λ	Water content in ionomer
μ	Dynamic viscosity (kg m^{-1} s^{-1})
ξ	Stoichiometry ratio
ρ	Density (kg m^{-3})
σ	Surface tension coefficient (N m^{-1})
ϕ	Electrical potential (V)
ω	Volume fraction of ionomer in catalyst layer

Superscripts/subscripts

a	Anode
act	Activation
BP	Bipolar plate
c	Cathode
$cell$	Cell characteristic
CL	Catalyst layer
$CL-GDL$	Catalyst layer center to gas diffusion layer center

com	Compressed
conc	Concentration
cond	Condensation
desb	Desublimation
eff	Effective
ele	Electronic
EOD	Electro-osmotic drag
eq	Equilibrium
equil	Equilibrium
evap	Evaporation
f	frozen
F	Flow channel
fl	Fluid phase
FPD	Freezing point depression
fmw	Frozen membrane water
g	Gas phase
GDL	Gas diffusion layer
H_2	Hydrogen
i	Segment number
i, *j*	The i^{th} and j^{th} components
ice	Ice
in	Inlet
ion	Ionic, ionomer
lq	Liquid water
m	Mass (for source term)
mem	Membrane
MEM	Membrane
$MEM-CL$	Membrane center to catalyst layer center
N	Normal condition
nf	Non-frozen
nmw	Non-frozen membrane water
O_2	Oxygen

ohm	Ohmic
open	Open circuit
out	Outlet
ref	Reference state
rev	Reversible
sat	Saturation
sl	Solid phase including the membrane electrolyte and ice
sld	Solid phase excluding the membrane electrolyte and ice
surr	Surroundings
t	Time step
$t - \Delta t$	Previous time step of t
T	Energy (for source term)
u	Momentum (for source term)
vp	Water vapour
wall	Surrounding wall of the cell
0	Intrinsic value
l-i	Liquid water to ice (vice versa)
n-f	Non-frozen membrane water to frozen membrane water (vice versa)
n-i	Non-frozen membrane water to ice
n-v	Non-frozen membrane water to vapour (vice versa)
uncom	Uncompressed
v-i	Vapour to ice
v-l	Vapour to water liquid (vice versa)

Abbreviations

AFC	Alkaline fuel cell
AMG	Algebraic multigrid
BP	Bipolar plate
CFD	Computational fluid dynamics
CL	Catalyst layer
CV	Cyclic voltammetry
DAQ	Data acquisition
DI	Deionized

DMFC	Direct methanol fuel cell
DSC	Differential scanning calorimetry
EIS	Electrochemical impedance spectroscopy
EOD	Electro-osmotic drag
FPD	Freezing point depression
GDL	Gas diffusion layer
HOR	Hydrogen oxidation reaction
MCFC	Molten carbonate fuel cell
MEA	Membrane electrode assembly
MPL	Micro porous layer
NMR	Nuclear magnetic resonance
ORR	Oxygen reduction reaction
PAFC	Phosphoric acid fuel cell
PCB	Printed circuit board
PEM	Proton exchange membrane
PEMFC	proton exchange membrane fuel cell
PTFE	Polytetrafluoroethylene
SOFC	Solid oxide fuel cell
UDF	User defined function
VOF	Volume-of-fluid

Chapter 1

Introduction

1.1 Background

A fuel cell is an energy conversion device that converts the chemical energy stored in fuels and oxidants into electricity through electrochemical reactions. With different kinds of electrolyte being used, fuel cells can be classified into different types. The most common types of fuel cells are the proton exchange membrane fuel cell (PEMFC), direct methanol fuel cell (DMFC) (same as PEMFC but using methanol instead of hydrogen as fuel), alkaline fuel cell (AFC), phosphoric acid fuel cell (PAFC), molten carbonate fuel cell (MCFC) and solid oxide fuel cell (SOFC). Different types of fuel cells are suitable for different applications. Some types of fuel cells are most suitable for stationary power generation, such as PAFC, MCFC and SOFC; and the other types of fuel cells are widely used for vehicular or portable applications, such as PEMFC, DMFC and AFC. Low operating temperature, high power density and zero/low emission have made PEMFC the most promising fuel cell type for the future in automotive applications. PEMFC is also the most popular one under research and development compared with other types of fuel cell. It appears to offer the best prospect for further improvement until commercialization. Over the past two decades, PEMFC technology has achieved significant improvement in terms of performance and cost. However, further development is necessary before commercial application, such as cold start in the content of Canadian cold climate in winter.

In winter conditions, it is unavoidable for vehicles driving below the freezing point of water (0 ^{o}C), therefore, for successful commercialization of PEMFC in automotive applications, rapid and efficient start-up from subzero temperatures must be achieved, which is referred to as “cold start”. The major problem of PEMFC cold start is that the product water freezes when the temperature inside the PEMFC is lower than the freezing point of water. If the catalyst layer (CL) is fully covered by ice before the cell temperature rises above freezing point, the electrochemical reaction may stop due to the blockage of the reaction sites. In addition, ice formation may also result in serious damage to the structure of the membrane electrode assembly (MEA). Therefore, for PEMFC in automotive applications, successful cold start is of paramount importance. At present, rapid unassisted cold start of PEMFC is still very difficult. Most of the present PEMFC systems employ various assisted cold start methods such as: resistance heating using direct current from batteries, coolant heating, hot air blowing, catalytic hydrogen/oxygen reaction inside the PEMFC, etc. The cold start performance of PEMFC still needs significant improvement, especially for unassisted cold start, because assisted cold start increases the system volume and weight, as well as the operation complexity and installation costs. However, only a few of the previous experimental and numerical PEMFC studies paid attention to cold start, even more significant effort is needed in this area. Therefore, this research focuses on both the experimental and numerical studies of PEMFC cold start.

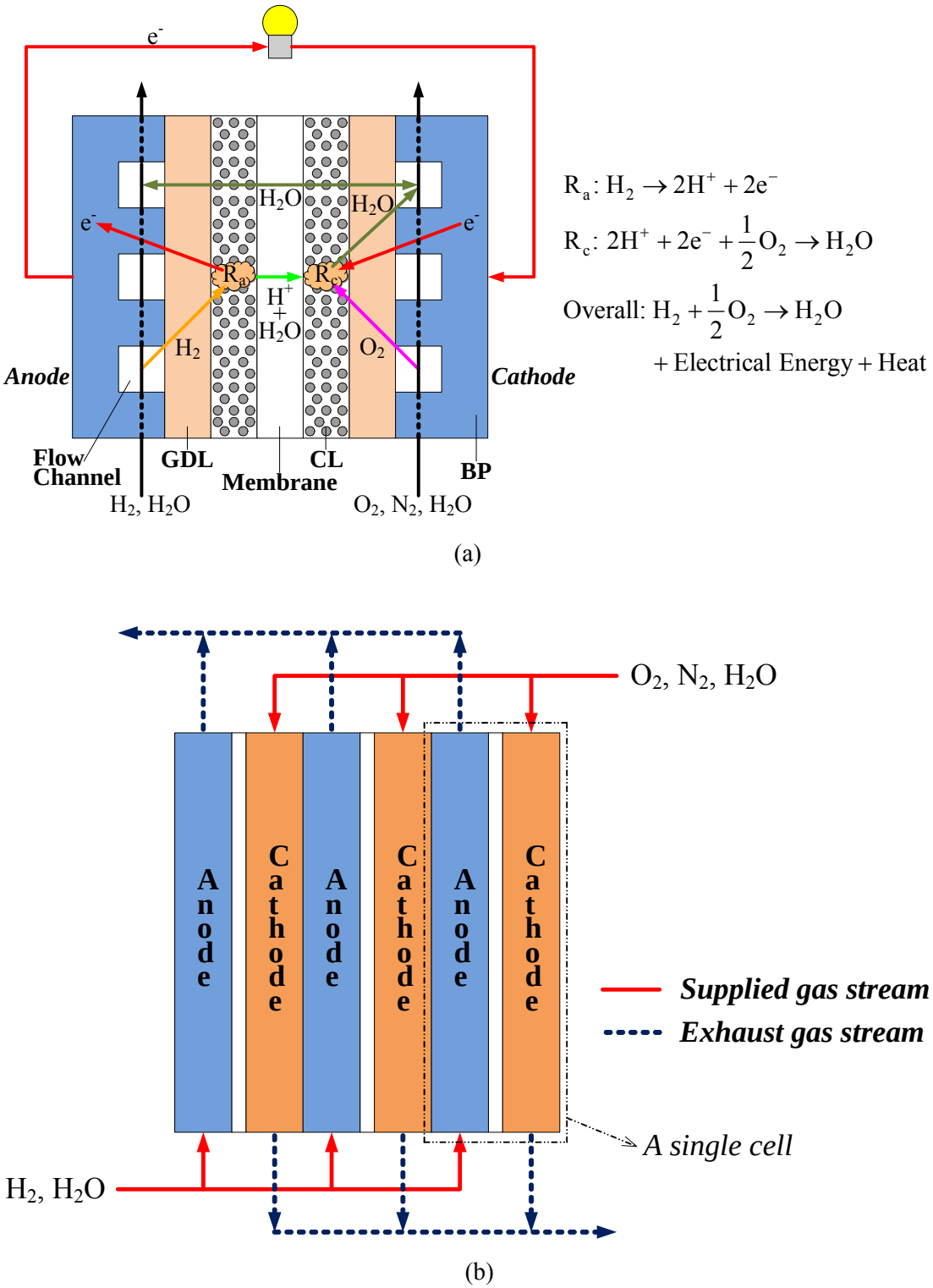

Figure 1.1: Schematics of (a) a single PEMFC and (b) a PEMFC stack with three single cells.

1.2 Fundamental Principles

PEMFC produces electrical energy by utilizing the chemical energy stored in fuels (hydrogen on the anode side) and oxidants (oxygen on the cathode side) from external supplies. Figure 1.1 shows schematics of a single PEMFC and a PEMFC stack with three single cells. Typically a single PEMFC (Figure 1.1a) consists of an anode and a cathode, and a proton exchange membrane (PEM) in between. At the anode, hydrogen flows into the flow channels through the gas diffusion layer (GDL) to the CL. In the CL of the anode, hydrogen splits into protons (hydrogen ions) and electrons. The protons pass through the membrane and travel into the cathode, however, the electrons cannot pass through the membrane, but travel through an external circuit to the cathode, thus generating electricity. At the same time, on the cathode side, air or oxygen flows into the flow channels through the GDL to the CL. In the CL of the cathode, oxygen reacts with the protons and electrons from the anode, producing water and heat. Due to the water concentration and pressure differences between the anode and cathode, and the proton transport across the membrane, water can travel through the membrane in both directions. Single cells are often connected in series to form a PEMFC stack to produce higher voltages. As shown in Figure 1.1b, with three single cells connected in series, the supplied gases have to be distributed into the single cells through the inlet manifolds, and the exhaust gases have to be removed through the outlet manifolds.

On the anode side, the reaction that hydrogen splitting into protons and electrons is called the hydrogen oxidation reaction (HOR). On the cathode side, the reaction that oxygen, protons and electrons forming water is called the oxygen reduction reaction (ORR). The reactions on the two sides are

$$\text{Anode: } H_2 \rightarrow 2H^+ + 2e^- \tag{1.1}$$

$$\text{Cathode: } \frac{1}{2}O_2 + 2H^+ + 2e^- \rightarrow H_2O \tag{1.2}$$

The HOR (Equation 1.1) is slightly endothermic, and the ORR (Equation 1.2) is strongly exothermic. Therefore, the overall reaction generates heat:

$$H_2 + \frac{1}{2}O_2 \rightarrow H_2O + \text{Electrical Energy} + \text{Heat} \tag{1.3}$$

1.3 Components

1.3.1 Proton Exchange Membrane (PEM)

The function of a PEM is to transport positively charged ions from the anode to the cathode, and to insulate the negatively charged electrons and reactant gases (hydrogen and oxygen). Therefore, a PEM must be a good conductor of protons, a good insulator of electrons and reactant gases, and mechanically and chemically strong. At present, Nafion produced by Dupont is the most widely used material for the PEM, and Nafions are made as solid membranes typically with thicknesses ranging from 0.02 to 0.2 mm. A thicker Nafion membrane provides better insulation and stability but higher proton transport resistance, and vice versa. Therefore, the thickness of the Nafion membrane must be carefully controlled for an optimal compromise. The Nafion membrane is one kind of ionomers

(synthetic polymers with ionic properties), and it contains perfluorovinyl ethers terminated by sulfonic acids with hydrophobic tetrafluoroethylene (Teflon) backbones. The proton conductivities of Nafion membrane and most other PEM materials increase with the water content inside them, because water could ionize the acid groups. Therefore, humidification of the PEM is usually necessary and this is the major reason that the reactant gases are often humidified. However, excessive humidification may cause liquid water flooding on the cathode side and blocking the reactant gases from electrochemical reactions, thus diminishing the performance. Therefore, water management is important for PEMFC operation, and the amount of water must be carefully controlled to both sufficiently hydrate the PEM and avoid water flooding.

1.3.2 Catalyst Layer (CL)

On both sides of a membrane, CLs usually form in terms of carbon supported platinum powders as the catalyst embedded in part of the membrane. PEMFC usually works at lower than 100 ^{o}C, therefore, the presence of catalyst is significant to facilitate the electrochemical reaction. Platinum is the best catalyst for both the anode and cathode, although some substitutes such as platinum alloyed compounds are currently under active research. The carbon supported platinum powders must have good contact with the ionomer of the membrane. A three-phase contact must be ensured for the CL: reactant gases, catalyst and ionomer, because the electrochemical reactions only occur at the three-phase contact interface: reactant gases are needed to participate in the reaction, and both the catalyst and ionomer are needed to transport the electrons and protons. Therefore, the CL microstructure and ionomer-catalyst interface are the important factors that affect the performance of PEMFC. Optimal balance between the three phases needs to be achieved because each of them could limit the electrochemical reaction rate. To avoid water flooding and achieve better mechanical strength, sometimes polytetrafluoroethylene (PTFE) powders are also mixed with the catalyst to make the CL hydrophobic and hold the platinum powers. The thickness of the CL is usually found to be around 0.01 mm. The platinum powders have strong affinity for CO, therefore, a common problem of PEMFC is called the “CO poisoning” if hydrogen is produced from hydrocarbons. The “CO poisoning” problem is also the major reason that ultra pure hydrogen must be used for PEMFC.

1.3.3 Gas Diffusion Layer (GDL)

As the physical support of the membrane and CL, a GDL is attached to the outside of a CL. The whole structure (a membrane, two CLs and two GDLs) is compressed to form a MEA. Carbon paper or carbon cloth with thicknesses between 0.2 and 0.3 mm is widely used as the GDL because of the high porosity that facilitates the reactant transport towards the catalyst sites. The very low electrical resistance of carbon paper or carbon cloth also makes the ohmic loss within an acceptable range. The carbon paper or carbon cloth is usually treated to be hydrophobic by coating PTFE on them to expel water.

1.3.4 Bipolar Plate (BP)

The open circuit voltage of a single PEMFC is very small with a theoretical value of around 1.23 V. It should be noticed that this is the reversible voltage that does not take into account of any loss or irreversibility. The operating voltage is even smaller, about 0.7 V when drawing a useful current.

Therefore, many cells have to be connected in series to form a fuel cell stack to produce a useful voltage. To this end, the bipolar plate (BP) is made, as it is the interconnection between the anode of one cell and the cathode of the neighbouring cell. There are channels cut on both sides of the BP so that the reactant gases can flow over the faces of the electrodes. In practice, parallel, serpentine and interdigitated are the most common flow channel designs. The ratio between channel area and land area is an important factor. A larger channel area ensures supplying enough reactant gases and reduces the cell weight; and a larger land area results in a better electrical connection between the BP and the GDL, thus lowering the contact resistance and ohmic loss. Therefore, an optimized channel to land area ratio is critical to achieve good performance. The material for BP must have high electrical and thermal conductivity, good mechanical and chemical strength as well, which is usually graphite or stainless steel. Machining flow channels on the BPs of PEMFC also contributes a significant portion of the total cost.

1.4 Performance

Figure 1.2 presents a sample current-voltage graph of a single PEMFC, which is also called the polarization curve. This figure shows the voltage outputs at different current outputs. The current has been normalized by the area of the PEMFC in terms of a standard unit of current density (A cm^{-2}), because PEMFCs with different sizes obviously produce different currents, and a normalized current unit makes the performance comparable.

Theoretically, a fuel cell would supply any amount of current under the condition of sufficient fuel supply, while maintaining a constant voltage determined by thermodynamics. In practice, however, the actual voltage output of a fuel cell is less than the ideal thermodynamically-predicted value (reversible voltage). Furthermore, the more current that is drawn from a real fuel cell, the lower the voltage output of the cell, limiting the total power that can be delivered.

It is difficult to maintain the cell voltage at a high level under current load. As shown in Figure 1.2, the voltage output of a PEMFC in operation is less than reversible voltage due to the irreversible losses. The total loss increases with the increasing current. There are four major types of losses [1-4]: activation loss, ohmic loss, mass transport or concentration loss, and loss due to fuel cross over and internal currents.

The activation loss is caused by the slowness of the reactions taking place in the CL. Part of the voltage generated is lost in driving the electrochemical reaction that transfers the electrons and protons to or from the CL. Electrons and protons do not participate in the reaction as soon as they release, and enough amounts of electrons and protons must accumulate to certain levels that the reaction can take place continuously with sufficient gas supplies. This level is equivalent to the activation loss. In Figure 1.2, it is represented by the initial sharp drop of the cell voltage.

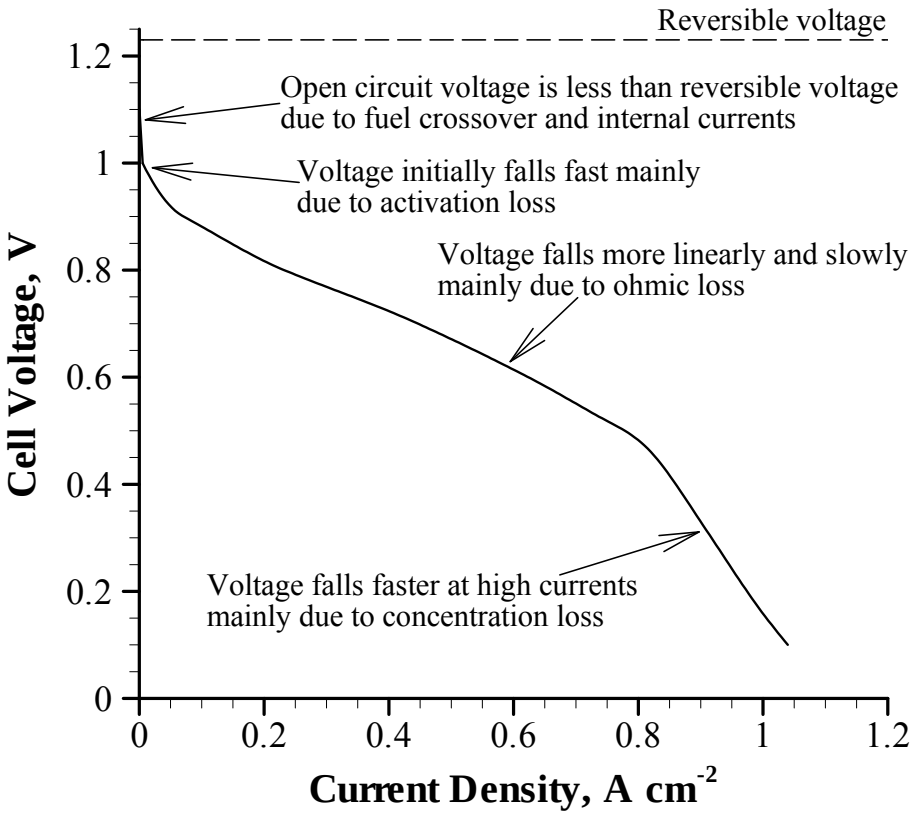

Figure 1.2: Sample polarization curve of a single PEMFC.

The ohmic loss is the resistance to the transport of electrons and protons through the materials of the electrodes, membranes and the various interconnections. This voltage drop is essentially proportional to the current density, represented by the linear fall in the middle of the performance curve in Figure 1.2.

The mass transport or concentration loss is caused by the change in concentration of the reactants in the CL as they are consumed along the flow channel from the inlet to the outlet. Concentration affects voltage via the change of partial pressure of reactant. That is why this type of irreversibility is called the concentration loss. On the other hand, since the reduction in concentration is the result of a failure to transport sufficient reactant to the CL, this type of irreversibility is also called the mass transport loss. In Figure 1.2, such loss can be observed at high current density range as a rapid drop, because a sufficient reactant supply is the controlling factor to obtain a large amount of current.

Fuel crossover and internal currents are the reactant passing and electron conduction through the membrane, respectively. The membrane should only transport ions. However, some small amounts of reactant and electron will always be possible to transport through the membrane. It does have a marked influence on the open circuit voltage of low-temperature fuel cell, which explains why the open circuit voltage is always smaller than the reversible voltage. However, this type of loss reduces considerably when a meaningful amount of current is drawn from the cell.

The operating voltage of a PEMFC at different current densities can be calculated by using the reversible voltage subtracting all the voltage losses due to the irreversibilities. Because the open

circuit voltage is equal to the reversible voltage subtracting the voltage loss due to the fuel crossover and internal currents, therefore a relationship between the operating voltage (V_{cell}, V) and the open circuit voltage (V_{open}, V) can be obtained:

$$V_{cell} = V_{open} - \eta_{act} - \eta_{ohm} - \eta_{conc} \tag{1.4}$$

where η_{act} (V), η_{ohm} (V) and η_{conc} (V) are the activation loss, ohmic loss and mass transport or concentration loss, respectively.

The reader is referred to [1-3] for more detailed discussion on PEMFC and its principles and applications.

1.5 Objectives and Scope of the Thesis

The main objectives of this thesis are to:

- identify the weakness and effectiveness of the previous experimental and modelling approaches, then develop an experimental setup and a mathematical model for PEMFC cold start based on this analysis;
- provide insight into the ice formation and heat generation processes and other important transport phenomena during PEMFC cold start processes; and
- identify and optimize the important design parameters and operational strategies that affect the performance of PEMFC cold start.

To achieve these objectives, an experimental setup for PEMFC cold start testing with simultaneous measurement of current and temperature distributions is designed and built, and a comprehensive three-dimensional (3D) model is developed to simulate the cold start processes in PEMFC. The experimental setup not only provides the functions for the normal cold start testing presented in recent literature, but can also simultaneously measure the dynamic current and temperature distributions over the entire reaction area of the tested PEMFC. The mathematical model takes into account the major water transport and phase change processes, such as the water freezing and melting in the membrane, the non-equilibrium mass transfer between the water in the ionomer and the water (vapour, liquid and ice) in the pore region of the CL, and the water freezing and melting in the CL and GDL. Based on the resulting experimental setup and mathematical model, extensive experimental measurements, numerical simulations, and data analysis are carried out to achieve the proposed objectives listed above.

This thesis is organized as follows: the relevant literatures are comprehensively reviewed in Chapter 2; the cold start experiment and experimental results are presented in details in Chapters 3 and 4, respectively; the cold start model and numerical results are comprehensively described and discussed in Chapters 5 and 6, respectively; and the summary and future work are given in Chapter 7.

Chapter 2

Literature Review

Numerous experimental and numerical studies on PEMFC were carried out in the past two decades, and significant achievements have been made. However, the studies related to PEMFC cold start are relatively scarce, even it is critically important. Previous efforts and achievements are reviewed and summarized in this chapter, and are generally categorized into experimental and numerical studies. For each category, studies focusing on normal operating conditions are reviewed first, followed by the cold start studies.

2.1 Experimental studies

2.1.1 Normal Operating Condition

The experimental studies on PEMFC can be generally categorized into in situ and ex situ studies. The in situ experiments measure the variables such as voltage, current and time to characterize the performance of operating PEMFCs. The ex situ experiments characterize the detailed structures or properties of the individual components comprising the PEMFCs when the components are removed from the cell in a non-assembled and non-functional form.

The in situ experimental study is very common as it reports the performance of operating PEMFCs. Based on the measured voltage, current, time and other variables, the cell parameters such as the activation loss, ohmic loss and exchange current density can be characterized by using different characterization techniques such as the current interruption, electrochemical impedance spectroscopy (EIS), cyclic voltammetry (CV). For example, the EIS technique was used by Springer et al. [5] to analyze the ohmic resistances of the different components of a PEMFC. Based on these characterization techniques, numerous experimental studies focusing on the effects of different designs and operating conditions on the performance of PEMFC have been carried out. Ralph et al. [6] studied the effects of different catalysts on the performance of PEMFC, and it was reported that significant cost reduction could be achieved with optimal performance. Lee et al. [7] studied the effects of GDL properties on the performance of PEMFC, and it was found that a thin GDL with small porosity results in good electrical conductivity, however, efficient mass transport requires large pores. The experimental studies carried out in [8-10] confirmed the importance of PTFE content in GDL, and the micro porous layer (MPL) was also confirmed to be an effective way for water removal. Yan et al. [11] studied the effects of the flow field design on the performance of PEMFC, and the influences of operating condition and water removal methods were tested by Mughal and Li [12]. The liquid water behaviours inside PEMFCs were also investigated experimentally. The experimental methods used include: neutron radiography/tomography [13, 14], X-ray microtomography [15] and direct imaging on transparent fuel cells [16-18]. Such experimental studies could help understand the water movement inside PEMFC and achieve better water management. Other advanced experimental techniques to measure to the distributions of current and temperature in operating PEMFCs were also developed [19-24]. These experiments could provide more detailed data to understand the transport phenomena over the reaction area.

The ex situ experimental studies mainly focused on the measurements of the properties of different PEMFC components. The parameters and correlations obtained from such experiments are very important for the modelling of PEMFC. Zawodzinski et al. [25] conducted some important measurements of the properties of Nafion membrane, including proton conductivity, water diffusivity and water uptake curve. The measurements of the contact angle between liquid water and Nafion membrane were also carried out by Zawodzinski et al. [26], and some useful information about the hydrophilicity of membrane surface was reported. The permeabilities of various fibrous materials in three perpendicular directions were measured by Gostick et al. [27]. They reported that most of the materials have higher in-plane permeability, and if a GDL is compressed to half of its original thickness, the permeability decreases by one order of magnitude. Gostick et al. [28] also measured the capillary pressure versus liquid water saturation for various commercial GDLs to provide useful correlations. Many other kinds of ex situ experiments were also carried out, such as investigation of Pt utilizations in CL [29], material degradations after operation [30], and measurements of GDL mass and heat transfer properties [31, 32].

2.1.2 Cold Start

The number of experimental studies for the cold start is much less than for the normal operating condition of PEMFC. The in situ cold start experiments mainly focused on the effects of designs and operating conditions on the cold start performance, and the performance degradations after freeze-thaw cycles; and the ex situ experiments often focused on the material degradations after freeze-thaw cycles, and measurements of the physical properties of different PEMFC components at subzero temperatures.

Tajiri et al. [33, 34] designed the experimental procedures for the in situ testing to mainly investigate the effects of MEA characteristics on the cold start performance of a PEMFC. The initial water content in Nafion membrane was controlled by different purging methods. It was found that with a higher initial membrane water content, the start-up performance was also higher, but the best cold start capability was achieved with the lowest initial water content, because more product water could be taken by the membrane from the CL, resulting in a less amount of water freezing in the CL. The results also confirmed the importance of purging for PEMFC cold start. Hou et al. [35, 36] investigated the performance degradations after freeze-thaw cycles. It was reported that no significant performance degradation was observed at any initial membrane water content and subfreezing temperature, indicating that the membrane degradation is not a major issue for PEMFC cold start. Cho et al. [37, 38] studied the freeze-thaw cycles with a subfreezing temperature of -10 ^{o}C. Three different initial conditions, without purge, with dry purge (purged with dry gas), and with solution purge (purged with antifreezes such as methanol), were tested. It was reported that the non-purged condition resulted in severe performance degradation and the degradations for the dry purge and solution purge were not significant. Guo and Qi [39] studied the freeze-thaw cycles with a subfreezing temperature of -30 ^{o}C, and severe damages to the CL and GDL were also observed if the cell was not purged before operation. Thompson et al. [40] experimentally determined the ORR kinetics for PEMFC operating at subzero temperatures, and no significant change in the ORR mechanism was found. Yan et al. [41] investigated the effects of start-up temperatures on the cold start performance of a PEMFC, and it was reported that the successful self start-up could be achieved if the start-up temperature was higher than -5 ^{o}C, and severe degradations of the MEA were observed

if the start-up temperature was lower than -5 ^{o}C. St-Pierre et al. [42] studied the effects of purging temperature, and it was found that a high temperature purge (85 ^{o}C) could result in degradation while purging at 20 ^{o}C resulted in no significant degradation. Ge and Wang [43] conducted the first visualization study of ice and liquid water formation on the cathode CL surface by cooling the cell by coolant recirculation through the cooling channels. For the in situ visualization, a transparent PEMFC with a silver mesh as the cathode GDL was used to enable the optical access to the CL. Because silver mesh was rarely used in PEMFCs, Ge and Wang [44] improved their experiment by punching small holes through a carbon paper and used it as the GDL, therefore a realistic GDL could be used for the visualization of the CL. Based on the experimental results, it was estimated that the freezing point of water in the CL was around -1 ^{o}C. Ishikawa et al. [45] also conducted an in situ visualization study, and a transparent PEMFC with a gold mesh as the GDL was used with a Peltier cooler to control the cell temperature. Both the thermograph and microscope were used to detect the temperature and visualize the liquid-ice phase transition simultaneously. It was found that during the freezing process of liquid water in the CL, the liquid water remained super cooled, and the temperature was not constant. The freezing temperature of liquid water changed between -0.1 and -2.2 ^{o}C. All these studies showed that the liquid water freezes at lower than 0 ^{o}C, and such temperature difference is called the freezing point depression (FPD). Sun et al. [46] designed a new method called the catalytic hydrogen/oxygen reaction assisted cold start, the idea was to supply mixed hydrogen and air (or oxygen) into the operating PEMFC. By controlling the concentration of hydrogen in the mixture, the explosion risk could be avoided and the reaction heat could be utilized to heat up the cell. However, even the cell successfully started, the heating process took up to 10 minutes from -20 ^{o}C, which is not acceptable for automotive applications. The performance degradation should also be investigated for this method. The literature review shows that the advanced experimental techniques used under the normal operating condition such as the current and temperature distribution measurements [19-24] were rarely applied to the cold start testing for more comprehensive results.

The ex situ experimental studies on PEMFC cold start were also carried out. McDonald et al. [47] conducted an ex situ freeze-thaw study on different MEAs, and it was reported that no degradation was observed for a dry MEA, and no water phase change was observed in the membrane. Cappadonia et al. [48, 49] conducted the experimental measurements of Nafion membrane conductance at subzero temperatures, and sharp decrements of the conductance at certain temperatures with different water contents were observed. For the modelling studies, the correlation for the Nafion membrane conductivity is needed rather than the conductance. In the experimental study in Thompson et al. [50], the conductance of Nafion membrane at subzero temperatures was measured and the conductivity was also calculated based on the membrane sample sizes. Similar changes of the membrane conductance/conductivity to Cappadonia et al. [49] were observed, and it was also found that the sharp decrements of the membrane conductivity occurred at the temperatures when the water phase transitions were observed. The amount of non-frozen membrane water content at different subzero temperatures were also estimated.

2.2 Numerical Studies

2.2.1 Normal Operating Condition

Pioneering numerical studies of PEMFC can be found in Springer et al. [51, 52] and Bernardi and Verbrugge [53, 54]. In these one-dimensional (1D) models, the fundamental framework and formulation for PEMFC modelling were established and have been widely used in most of the later numerical studies. Following [51-54], numerous studies on PEMFC modelling were carried out. A two-dimensional (2D) computational fluid dynamics (CFD) model which simultaneously considers the electrochemical kinetics, current distributions, hydrodynamics, and multi-component transport was developed by Um et al. [55]. 3D simulations of a straight flow channel in a PEMFC were performed by Dutta et al. [56] using a commercial CFD software package FLUENT. Hontanon et al. [57] also employed FLUENT to implement their 3D gas flow model. A study exploring the gas transport phenomena in parallel flow channels was conducted by Cha et al. [58], in which the oxygen concentration along a single flow channel and the other flow patterns that may affect the performance were discussed. Similarly, the gas concentrations along fuel cell flow channels were obtained numerically by Kulikovsky [59].

All the models in [51-59] assumed that the water in the flow channel and pores of GDL and CL of PEMFC only exists in gaseous state, so called the single-phase models. However, it was widely noticed that the condensation of water is almost inevitable in an operating PEMFC. Therefore, two-phase models are needed to further consider the liquid water effect. Wang et al. [60] developed a two-phase model for PEMFC cathode to predict the liquid water concentration. You and Liu [61] also considered the liquid water concentration in a straight channel on the cathode side in their model. The results in [60, 61] all showed the importance of considering liquid water in the modelling of PEMFC. In recent years, more two-phase models have been published [62-70] with more complicated formulations for liquid water transport. Different from the two-phase models that can only predict the liquid water concentration [62-70], Jiao et al. [71-77] conducted a series of 3D two-phase simulations by employing the volume-of-fluid (VOF) method, for which the detailed air-liquid flow behaviours were able to be investigated in PEMFC cathode flow channels and GDLs.

Large-scale simulations for complex flow fields were also performed [78-81]. These simulations provided more realistic results than the simulations only considering single straight flow channels. On the other hand, pore-scale models have been developed to mainly investigate the liquid water behaviours [82-85] and estimate the effective transport properties [86-88].

2.2.2 Cold Start

The number of studies on the cold start modelling is much less than on the normal operation condition for PEMFC. Sundaresan and Moore [89] developed an analytical model for the cold start of PEMFC stacks. This 1D model could predict the temperature for each single cell of a stack by performing energy balance and heat transfer analysis, and it could also reveal the effects of the endplate thermal mass and the heating methods. Khandelwal et al. [90] also conducted a 1D thermal model, and similar to Sundaresan and Moore [89], the cold start capability of PEMFC stacks can be evaluated. It was reported that adjusting the start-up current density, coolant heating, isolation of stack endplates are all the effective ways to optimize the cold start performance. Mao and Wang [91] developed an

analytical model, not only for the temperature, this 1D model could also predict the amount of ice formation in CL, water transport, changes of cell voltage and current density etc. Wang et al. [92, 93] also performed analytical studies and defined some important parameters that affect the performance of PEMFC cold start.

The analytical models in [89-93] can only roughly predict the PEMFC cold start performance. In order to investigate the fundamental physics during the cold start processes, multi-dimensional and multiphase models are needed. However, only a small amount of literatures are related to this field [94-99]. Ahluwalia and Wang [94] formulated a simple 2D cold start model for single PEMFCs. It was reported that a high start-up current density is favourable for a rapid cold start process, and the effects of feed gas temperatures, operating pressure and electrical heating on the cold start performance of PEMFC were also investigated. Mao et al. [95] developed a 3D multiphase model, and a similar but 2D model was presented by Meng [96, 97]. Based on the work in Mao et al. [95], Jiang el al. [98, 99] further conducted non-isothermal cold start simulations for PEMFCs. Some design and operational optimization methods were reported through these numerical simulations. The numerical models in [94-99] assumed instantaneous desublimation of vapour to ice, neglected the liquid water formation during the ice melting processes, and also assumed that the water in the membrane electrolyte does not freeze. Therefore, developing more comprehensive multi-dimensional multiphase cold start models that consider more detailed water phase change processes is necessary to better understand the transport phenomena and predict the performance of PEMFC cold start.

2.3 Summary

Overall, the number of studies focusing on the cold start of PEMFC is much less than the normal operating condition. Significant efforts are needed in this area before the successful commercialization of PEMFC in automotive applications. There is a significant potential to apply the advanced experimental techniques such as the current and temperature distribution measurement to the cold start in situ testing. Developing 3D multiphase cold start models that account for the detailed water phase transitions is also highly desirable. These experimental and numerical studies can provide the insight into the ice formation and heat generation processes and other important transport phenomena during the cold start processes, and also better identify and optimize the design and operating parameters that affect the performance of PEMFC cold start. These are the main objectives of this thesis. An experimental setup with the capability to simultaneously measure the current and temperature distributions [100, 101], and a 3D multiphase model considering the detailed water phase transitions [102-104] for PEMFC cold start were developed recently by Jiao et al. to achieve these objectives. These experimental and numerical studies [100-104] contribute to the main part of this thesis.

Chapter 3

Experiment Development

The dynamic distributions of current and temperature in a PEMFC during the various cold start processes determine the cold start characteristics, and are required for the optimization of design and operational strategy. Even though the distribution measurement techniques have been applied to PEMFCs under the normal operating conditions, the distributions during the cold start processes were rarely measured. Moreover, the computational domains of the present cold start models are often limited to single flow channels due to the computational limitation. Therefore, applying the distribution measurement techniques to the cold start experiment of PEMFC is needed.

In this chapter, the cold start experiment with the simultaneous measurement of the current and temperature distributions in a PEMFC are described. The current distribution mapping approach is used for the current distribution measurement, with segmented flow field plate and current collector on the anode side (sixteen segments). Sixteen thermocouples are used for the temperature distribution measurement by inserting them into the cathode flow field plate. A purging model is also developed to estimate the duration of purging before each start-up process. In the following, the experimental setup and procedures are described first, followed by the formulation of the purging model and the estimate of the purging duration. Finally, a short summary is given.

3.1 Experimental Setup

3.1.1 Control and Measurement

Figure 3.1 shows the schematic of the experimental setup. The PEMFC being tested is placed inside an environmental chamber, which is used to set the start-up temperatures. The controllable environmental temperature ranges from -70 to 170 ^{o}C. The tested PEMFC is connected to a fuel cell automated test station (FCAT S-800) and a computer controlled data acquisition (DAQ) system through a window on the environmental chamber. The fuel cell test station is a commercial product from Hyrogenics Corp., and the DAQ system is designed and built in our lab with another group member. For the tested PEMFC, the MEAs are donated by SolviCore GmbH & Co. KG, and the other components are designed in our lab with another two group members. The fuel cell test station is equipped with hydrogen, nitrogen, air and deionized (DI) water supplies. It is used to control and supply reactant gases to the tested PEMFC at different flow rates, temperatures and relative humidities. The pressures at the outlets of the tested PEMFC flow channels are controlled by the fuel cell test station corresponding to the desired operating pressures. The overall cell voltage and current are measured by the fuel cell test station, and the load bank equipped with the fuel cell test station is used to control the load condition (current or voltage) of the tested PEMFC. The DAQ system connected to the tested PEMFC is used to measure the current and temperature distributions over the active reaction area. Sixteen segments are connected to the DAQ system for each of the measured parameters (current in anode and temperature in cathode). Each segment for current measurement is connected to a small and high-precision resistor with an ohmic resistance of 0.1 Ω where the voltage drop across the resistor is measured. The current of each segment is calculated by using the measured

voltage drop across the resistor with known ohmic resistance. Sixteen type T thermocouples are used for the temperature distribution measurement. The output voltage of each thermocouple is calibrated at various reference temperatures with linear interpolation, and the measurable range is from -50 ^{o}C to 125 ^{o}C. The tolerances of the measurement devices are listed in Table 3.1. A frequency of 1 Hz for data recording is used for all the measurements. All the measurements are controlled through Labview codes.

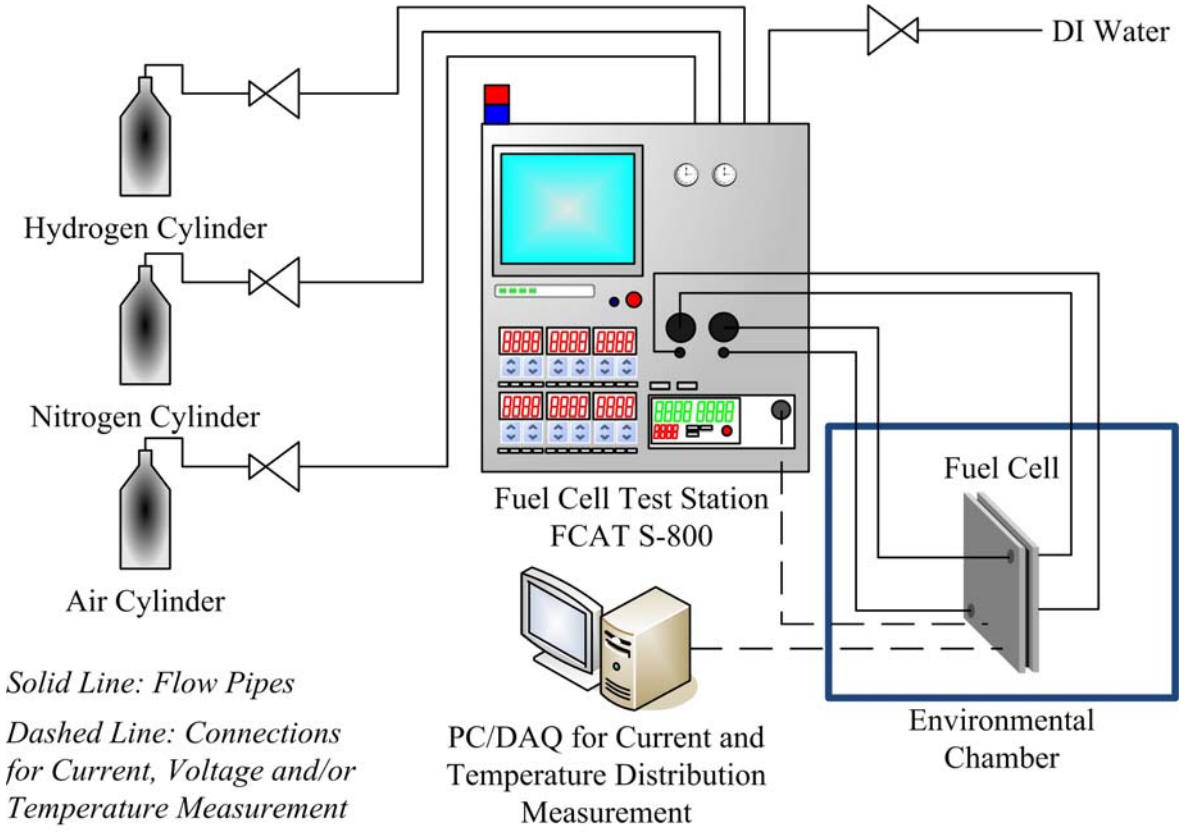

Figure 3.1: Schematic of the experimental setup.

Table 3.1: Measurement tolerances.

Measurement	Tolerance
Temperature (supplied gases and deionized water)	±1 ^{o}C
Temperature (thermocouples for temperature distribution measurement)	±0.1 ^{o}C
Volume flow rate (supplied gases)	±0.4 mL min^{-1}
Gauge pressure (at inlet and outlet of flow channel layout)	±1 kPa
Voltage (current is calculated by voltage drop and ohmic resistance)	±2.5 mV

3.1.2 Cell Design

Figures 3.2 and 3.3 show the schematics of the tested PEMFC segmentations according to the flow channel layout and for the anode current collector, and Figure 3.4 presents the schematic side view of the cell assembly. The current distribution is measured on the anode side. Since the cathode temperature has the most significant impacts on the ice formation, the temperature distribution is measured inside the cathode flow field plate. The detailed cell properties are given in Table 3.2. A parallel serpentine flow channel layout with three channels in parallel is used for both the anode and cathode with co-flow and counter-flow arrangements. There are sixteen segments over the active reaction area forming a 4 × 4 array. The MEA is not segmented to minimize the modification of the PEMFC.

On the anode side, both the flow field plate and current collector are segmented. The fabrication processes of the anode segmented flow field plate start with machining connected grooves of 1 mm wide and 4 mm deep into a graphite block of 105 × 105 × 6.5 mm to divide it into a 4 × 4 array with sixteen segments. Then the grooves are filled with an electrically insulating epoxy material that also has sufficiently strong mechanical strength to withstand the compression force for the PEMFC assembly. After curing the epoxy material at room temperature for 24 hours, the surface is polished to become clean and smooth. The back side of the graphite block is milled to a thickness of 3 mm, leaving sixteen electrically insulated segments. A three-channel parallel serpentine flow channel layout is then milled onto the front of the block with a cross section of 1 × 1 mm. Electrical resistance measurements are made before and after the cold start testing to ensure that the segments on the flow-field plate are still insulated from each other. The anode segmented current collector is made of a 105 × 105 × 1.6 mm electrically insulating circuit board with copper pads printed on both sides, so-called the printed circuit board (PCB). As shown in Figure 3.3, sixteen segments of 40 μm thick copper pads with the dimensions of 15.5 × 15.5 mm are printed as a 4 × 4 array on the front side of the circuit board. Twenty five small thru-vias connect each pad to a printed lead on the back side of the circuit board. These leads electrically join each segment to a connector array (header) for connection to the DAQ system. The copper pads and leads are electroplated with nickel diffusion barrier and 1 μm gold layer to minimize the electrical contact resistances. The front side (with sixteen 15.5 × 15.5 mm copper pads) of the PCB faces the segmented flow field plate, and the back side (with leads) faces the end plate. A silicon rubber gasket separates the leads on the PCB from the end plate (aluminum alloy) to prevent both gas leakage and electrical short circuit.

On the cathode side, sixteen type T thermocouples are inserted through the end plate (aluminum alloy) and current collector (copper plate) into the flow field plate. Each of the sixteen thermocouples is placed at the center of each of the sixteen segments shown in Figure 3.2. As shown in Figure 3.4, the temperature distribution is measured by the thermocouples on the plane about 0.25 mm from the top of the flow channels. The thermocouple holes have a diameter of 0.6 mm, and the sizes of the thermocouples with and without the plastic cover are about 0.4 mm and 0.2 mm. The thermocouples are fixed in the thermocouple holes of the cathode flow field plate by using a zircon based high temperature ceramic cement. The cement is initially a mixture of powder filler and liquid binder, filled in the holes with the thermocouples. After curing for 24 hours at room temperature, it becomes solid and holds the thermocouples in place. The cement is also excellent heat conductor and electrical insulator with good mechanical strength. The other ends of the sixteen thermocouples are connected to the DAQ system for the temperature distribution measurement. A silicon rubber gasket with

thermocouple holes is used to separate the cathode current collector from the end plate to prevent both gas leakage and electrical short circuit.

Segmentation according to the flow channel layout (anode and cathode with co-flow arrangement):

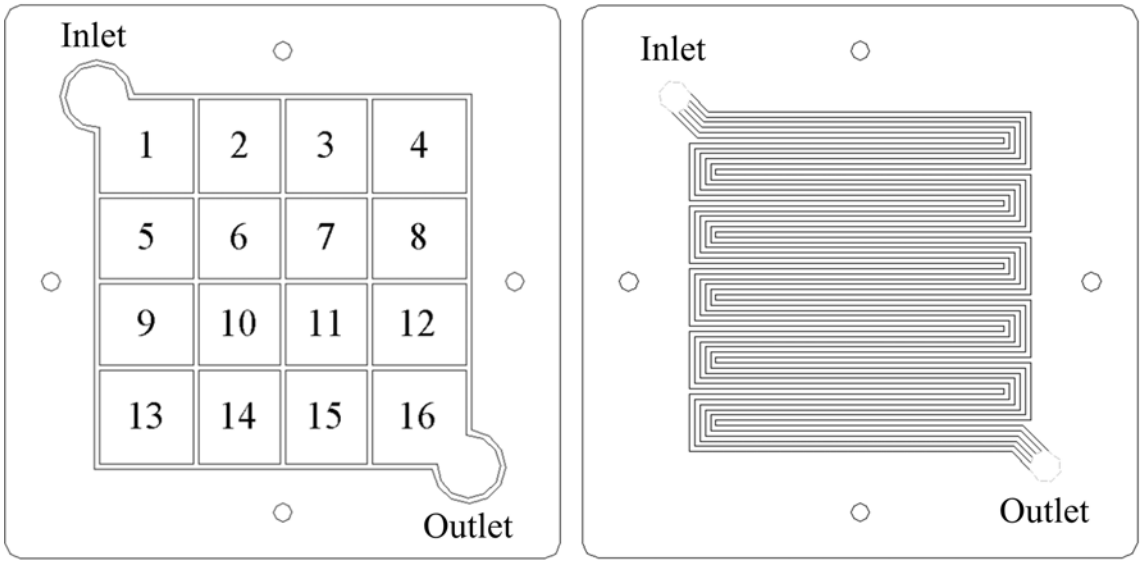

Segmentation according to the flow channel layout (anode with counter-flow arrangement):

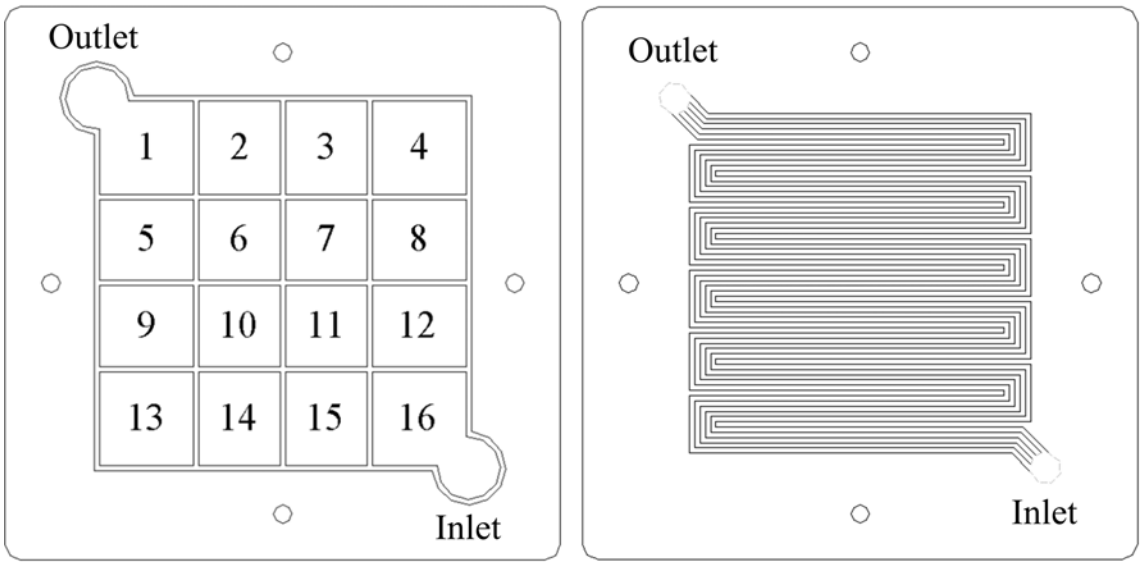

Figure 3.2: Segmentations of the cell assembly according to the flow channel layout for both the co-flow and counter-flow arrangements.

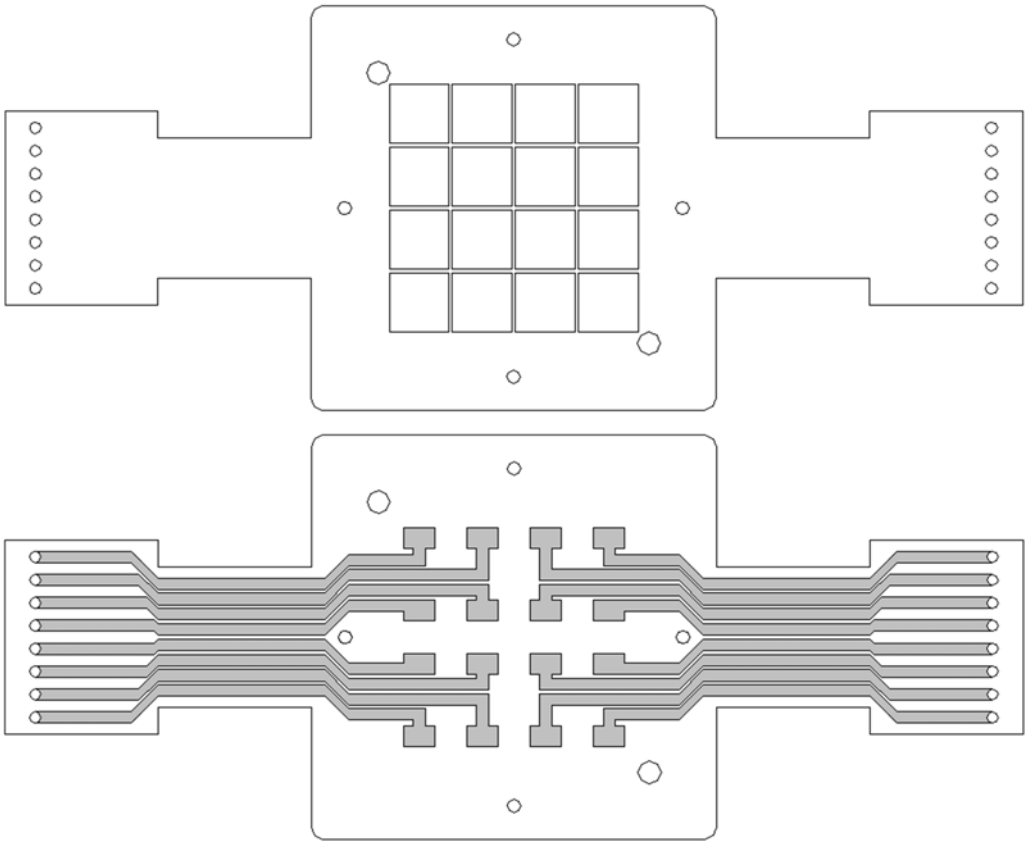

Figure 3.3: Segmentation of the current collector.

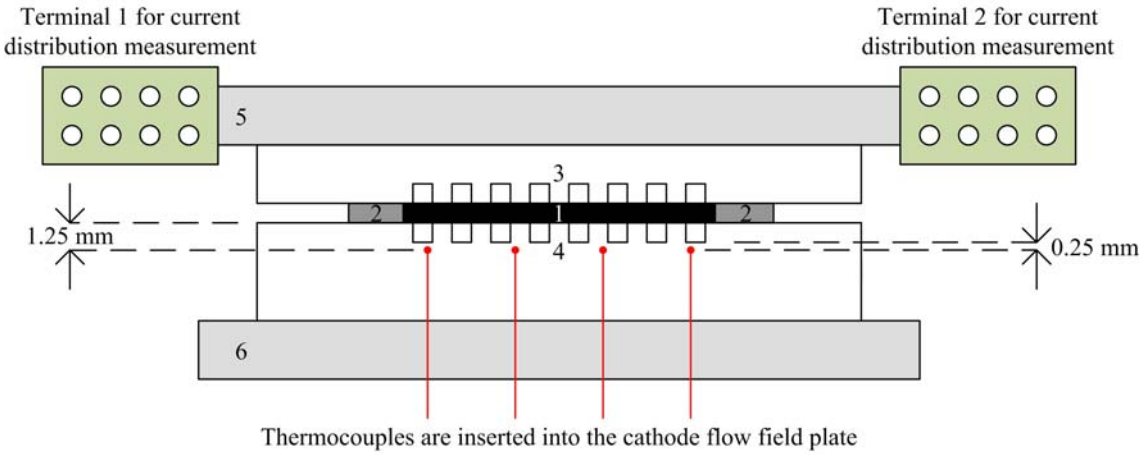

1 and 2: membrane electrode assembly with gaskets; 3: anode segmented flow field plate;
4: cathode flow field plate with thermocouples; 5: anode segmented current collector;
6. cathode current collector with thermocouples through it.

Figure 3.4: Schematic side view of the cell assembly.

Table 3.2: Cell properties.

Parameter	Values
Membrane (Nafion 112)	
Thickness	50 μm
Density	1980 kg m^{-3}
Equivalent weight	1100 kg $kmol^{-1}$
Catalyst layer (same for anode and cathode)	
Platinum loading	0.5 mg cm^{-2}
Flat active reaction area (square)	40 cm^2
Gas diffusion layer (same for anode and cathode, carbon paper, uncompressed)	
Thickness	230 μm
Porosity	0.75
Polytetrafluoroethylene (PTFE) loading by weight	30%
Gasket (silicon rubber, uncompressed)	
Thickness	254 μm
Flow channel layout (same for anode and cathode, parallel serpentine, co-flow and counter-flow arrangements)	
Number of flow channels in parallel	3
Channel width	1mm
Channel depth	1 mm
Land width	1 mm
Anode segmented flow field plate (graphite)	
Number of segments	16
Thickness	3 mm
In-plane area (surface parallel to membrane surface, square)	110.25 cm^2
Cathode flow field plate (graphite)	
Thickness	6.5 mm
In-plane area (surface parallel to membrane surface, square)	110.25 cm^2
Diameter of holes to insert thermocouples	0.6 mm
Distance between bottom of thermocouple holes and top of flow channels	0.25 mm

Number of thermocouple holes or thermocouples	16
Size of thermocouples (type T, with plastic cover / without plastic cover)	0.4 mm / 0.2 mm
Anode segmented current collector (copper pads printed on both sides of circuit board)	
Number of segments	16
Thickness/in-plane area of circuit board (electrically insulating, square)	1.6 mm/110.25 cm^2
Thickness of copper pad (16 segments, with extensions to external electrical circuit)	40 μm
Thickness of gold coating layer on copper pad	1 μm
Cathode current collector (copper, with thermocouple holes corresponding to flow field plate)	
Thickness	3.2 mm
In-plane area (surface parallel to membrane surface, square, with extension to external electrical circuit)	110.25 cm^2
Anode and cathode end plates (aluminum alloy, cathode plate with thermocouple holes corresponding to flow field plate)	
Thickness	13 mm
In-plane area (surface parallel to membrane surface, square)	210.25 cm^2
Machining of cell components	
Tolerance	±25.4 μm

3.2 Experimental Conditions and Procedures

The experimental procedures for all the cold start testing consist of four major steps: conditioning, purging, cooling down, and start-up. The operating conditions are given in Table 3.3.

The conditioning step involves operating the tested PEMFC at 70 ^oC, 1 atm and 0.3 V for 30 minutes. Fully humidified hydrogen and air are supplied at 70 ^oC with stoichiometry ratios of 1.2 and 2 corresponding to the operating current density, respectively. With continuous cold start testing, this conditonning step follows the start-up step from the previous cold start testing cycle.

After the conditioning step, the tested PEMFC is cooled down to room temperature. Then non-humidified nitrogen is supplied to both the anode and cathode flow channels at 25 ^oC for purging. The volume flow rates of nitrogen to the anode and cathode flow channels are 37.5 mL s^{-1} and 50 mL s^{-1}. For the tested PEMFC at 25 ^oC, the volume flow rate of supplied air at a stoichiometry ratio of 2 corresponding to 1 A cm^{-2} is about 22 mL s^{-1}. This indicates that the purging flow rates for both the

anode and cathode are fairly high. The duration of purging is 2 hours for all the experiments. A purging model is developed in this study, and the calculation based on this model shows that purging the cell for 2 hours is sufficient for a consistent and dry condition before the start-up processes. The formulation and estimate of purging duration are detailed in section 3.3.

Table 3.3: Operating conditions.

Parameter	Value
Start-up voltage	0.3 V
Start-up temperatures	-20 ^{o}C, -10 ^{o}C, -7 ^{o}C and -5 ^{o}C
Temperature of supplied gases	25 ^{o}C
Stoichiometry ratio of supplied hydrogen	1.2
Stoichiometry ratio of supplied air	2
Reference current density for stoichiometry ratios of supplied gases	Maximum of operating current density and 0.5 A cm^{-2}
Relative humidities of supplied gases	0
Absolute pressure at outlets	1 atm
Anode nitrogen flow rate for purging	37.5 mL s^{-1}
Cathode nitrogen flow rate for purging	50 mL s^{-1}
Temperature of nitrogen for purging	25 ^{o}C
Absolute pressure at outlets during purging	1 atm
Duration of purging	2 h
Duration of cooling down	4 h
Duration of cell conditioning	30 min
Cell voltage during cell conditioning	0.3 V
Operating temperature during cell conditioning	70 ^{o}C
Temperature of supplied gases during cell conditioning	70 ^{o}C
Absolute pressure at outlets during cell conditioning	1 atm
Relative humidity of supplied gases during cell conditioning	100%

Once the purging step is completed, the temperature inside the environmental chamber is set to the desired start-up temperatures. In this study, four start-up temperatures are tested: -20 ^{o}C, -10 ^{o}C, -7 ^{o}C and -5 ^{o}C. The duration of the cooling down process is 4 hours for all the experiments. Figure 3.5 shows the evolution of the average temperature in the cathode flow field plate (average of the sixteen thermocouple measurements) during the cooling down process to -20 ^{o}C. It can be observed that the average temperature in the cathode flow field plate remains almost constant after 1 hour and 30 minutes, indicating that a 4 hour cooling down process is more than sufficient. However, it can also

be observed that the temperature at the end of the cooling down process is still slightly higher than -20 ^{o}C. Because the pipelines, electrical wires and other connections to the tested PEMFC are connected to either the fuel cell test station or the DAQ system, which are all outside of the environmental chamber. All these connections can cause heat transfer between the tested PEMFC and the outside environment, slightly increasing the temperature of the tested PEMFC.

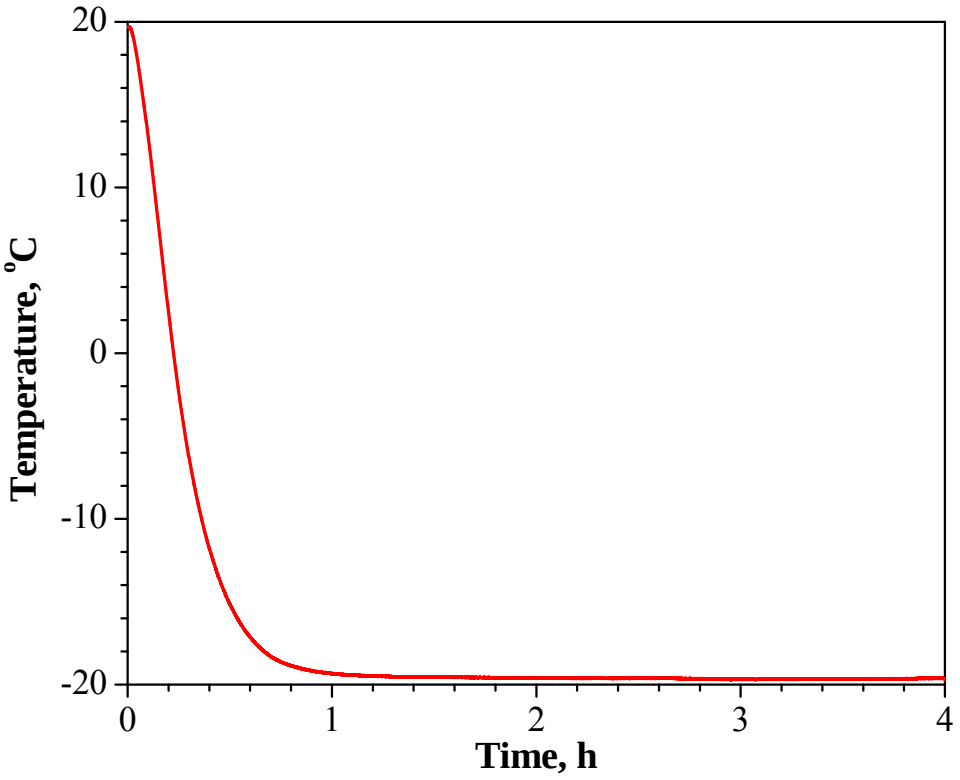

Figure 3.5: Evolution of the average temperature in cathode flow field plate (average of the sixteen thermocouple measurements) during the cooling down process to -20 ^{o}C.

Upon completing the cooling down process of the tested PEMFC, the last step is start-up. Non-humidified hydrogen and air are supplied at 25 ^{o}C, and the stoichiometry ratios are 1.2 and 2, respectively, corresponding to the operating current density. If the operating current density is lower than 0.5 A cm^{-2}, the reference current density is taken as 0.5 A cm^{-2}. This ensures sufficient reactant flow at every time instance during the cold start processes. The absolute pressure at the outlets of the anode and cathode flow channels is kept at 1 atm. All the measurements are taken and recorded at a frequency of 1 Hz during the cold start processes. More details of the operating conditions are given in Table 3.3.

By following the same experimental procedures, repeating tests are performed. Figure 3.6 shows the evolutions of current density and average temperature in the cathode flow field plate (average of the sixteen thermocouple measurements) during the repeated failed (from -10 ^{o}C) and successful

(from -5 °C) cold start processes for the cell voltage set at 0.3 V. Even though the performance of PEMFC is often expected to degrade after cold start cycles, the repeating tests by following the same experimental procedures do not show noticeable difference, perhaps because the purging duration for all the experiments is sufficiently long to remove the residual water before the cooling down and start-up processes, and the number of cold start cycles is still very low in this study.

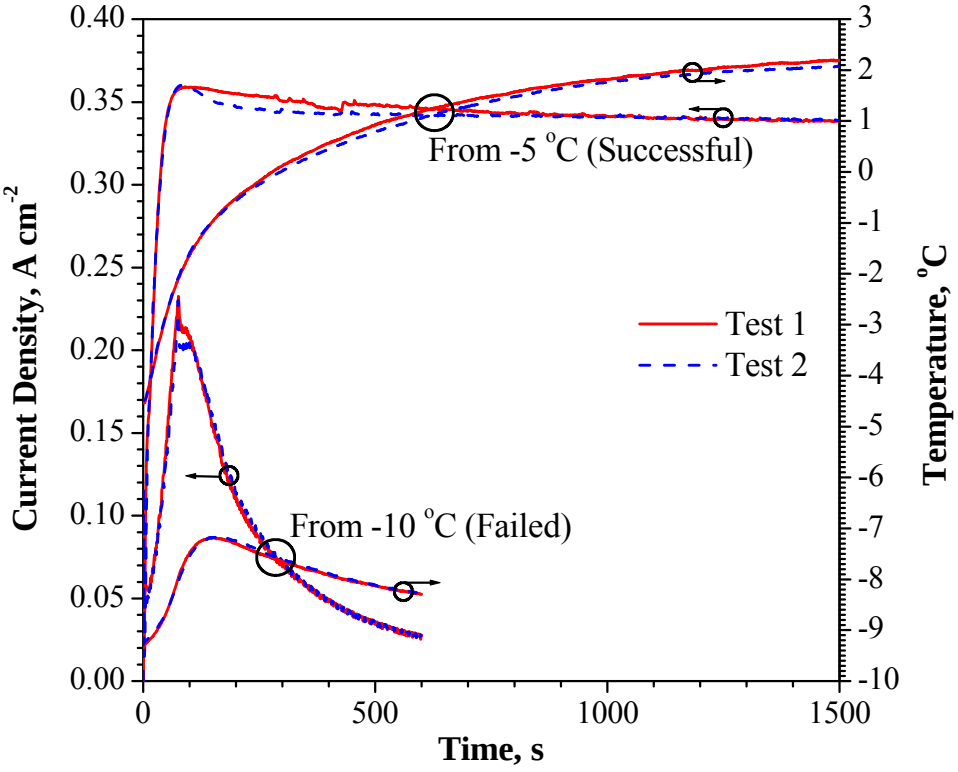

Figure 3.6: Evolutions of current density and average temperature in cathode flow field plate (average of the sixteen thermocouple measurements) during the repeated failed (from -10 °C) and successful (from -5 °C) cold start processes at 0.3 V.

3.3 Purging Duration

A 1D analytical model is developed for rapid estimate of purging duration. A sample code of this model by using the programming language C++ is given in Appendix A. Figure 3.7 shows the schematic of the purging model. This model consists of nine major parameters, and they are the volume averaged

- water content in membrane (λ_{MEM}),
- water content in ionomer of anode CL (λ_{CL}^{a}),

- water content in ionomer of cathode CL (λ_{CL}^{c}),
- vapour concentration in pores of anode CL (c_{CL}^{a} , kmol m^{-3}),
- vapour concentration in pores of cathode CL (c_{CL}^{c} , kmol m^{-3}),
- vapour concentration in pores of anode GDL (c_{GDL}^{a} , kmol m^{-3}),
- vapour concentration in pores of cathode GDL (c_{GDL}^{c} , kmol m^{-3}),
- vapour concentration in anode flow channel (c_{F}^{a} , kmol m^{-3}), and
- vapour concentration in cathode flow channel (c_{F}^{c} , kmol m^{-3}).

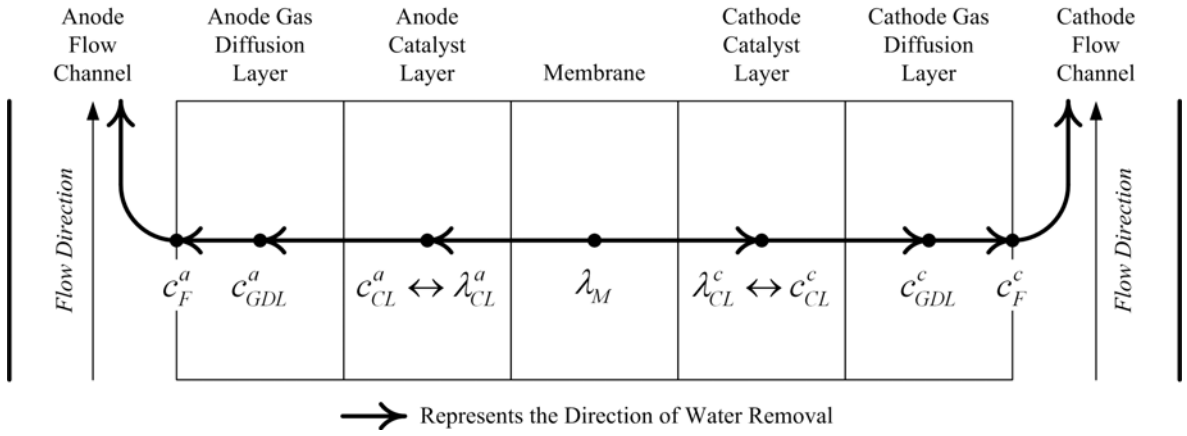

Figure 3.7: Schematic of the purging model.

Only the water transport on the through-plane direction (normal to the membrane surface) is considered since this is the only direction of water removal out of the MEA. The convective mass transport in MEA is also neglected, because it is only significant with strong cross flow on the in-plane directions (parallel to the membrane surface). The volume averaged water contents and vapour concentrations are assumed to be at the center of each layer of MEA. This assumption is reasonable because the concentration gradient is the primary driving force for mass transfer in MEA. The vapour concentration is assumed to be constant along the through-plane direction (normal to the membrane surface) in flow channels because of the quick mass transfer there. The presence of liquid water is neglected because the vapour in pores of CL and GDL are removed rapidly, resulting in rapid evaporation of liquid water; in fact, the controlling factor of purging duration is the water removal from membrane, as evidenced by the analysis of the time constants for various transport phenomena shown in Table 5 of [4]. The nine major parameters of this model are calculated based on the mass transfer in and out of the corresponding layers at each time instance based on the concentration gradients at the previous time instance.

The volume averaged vapour concentration in flow channel at the time instance t, c_F^t (kmol m^{-3}), is calculated as

$$c_F^t = c_F^{t-\Delta t} + \frac{\left(c_{GDL}^{t-\Delta t} - c_F^{t-\Delta t}\right) D_{GDL}^{eff} A_{act}}{\left(\delta_{GDL} / 2\right)} \frac{\Delta t}{A_F \delta_F} - \frac{\dot{V}_F^{in}}{N_F} c_F^{t-\Delta t} \frac{\Delta t}{A_F \delta_F} \tag{3.1}$$

where c (kmol m^{-3}) is the volume averaged vapour concentration; δ (m) is the thickness along the through-plane direction; the subscripts F and GDL represent flow channel and GDL; Δt is the time step size, therefore $t - \Delta t$ represents the previous time step of t; A_{act} (m^2) is the flat active reaction area; A_F (m^2) is the surface area at the interface between flow channel and GDL; $\dot{V}_F^{in}$ (m^3 s^{-1}) is the volume flow rate of purging gas (e.g. nitrogen) at flow channel inlet; N_F is the number of flow channels in parallel; and D_{GDL}^{eff} (m^2 s^{-1}) is the effective diffusion coefficient of vapour in GDL. The second and third terms on the right hand side of Equation 3.1 represent the vapour transport from GDL to flow channel and vapour removal by purging gas in flow channel, respectively.

The volume averaged vapour concentration in pores of GDL at the time instance t, c_{GDL}^t (kmol m^{-3}), is calculated as

$$c_{GDL}^t = c_{GDL}^{t-\Delta t} + \frac{\left(c_{CL}^{t-\Delta t} - c_{GDL}^{t-\Delta t}\right) D_{CL-GDL}^{eff} A_{act}}{\left(\delta_{CL} / 2\right) + \left(\delta_{GDL} / 2\right)} \frac{\Delta t}{A_{act} \delta_{GDL} \varepsilon_{GDL}} - \frac{\left(c_{GDL}^{t-\Delta t} - c_F^{t-\Delta t}\right) D_{GDL}^{eff} A_{act}}{\left(\delta_{GDL} / 2\right)} \frac{\Delta t}{A_{act} \delta_{GDL} \varepsilon_{GDL}} \tag{3.2}$$

where the subscript CL represents CL, and D_{CL-GDL}^{eff} (m^2 s^{-1}) is the effective diffusion coefficient of vapour from CL center to GDL center, defined as

$$D_{CL-GDL}^{eff} = \frac{\left(\delta_{CL} / 2\right) + \left(\delta_{GDL} / 2\right)}{\left(\delta_{CL} / 2\right) / \left(D_{H_2O} \varepsilon_{CL}^{1.5}\right) + \left(\delta_{GDL} / 2\right) / \left(D_{H_2O} \varepsilon_{GDL}^{1.5}\right)} \tag{3.3}$$

The second and third terms on the right hand side of Equation 3.2 represent the vapour transport from CL to GDL and from GDL to flow channel, respectively.

The volume averaged vapour concentration in pores of CL at the time instance t, c_{CL}^t (kmol m^{-3}), is calculated as

$$c_{CL}^t = c_{CL}^{t-\Delta t} + \left(\lambda_{CL} - \lambda_{CL}^{eq}\right) \xi \frac{\rho_{MEM}}{EW} A_{act} \delta_{CL} \varepsilon_{CL} \frac{\Delta t}{A_{act} \delta_{CL} \varepsilon_{CL}} - \frac{\left(c_{CL}^{t-\Delta t} - c_{GDL}^{t-\Delta t}\right) D_{CL-GDL}^{eff} A_{act}}{\left(\delta_{CL} / 2\right) + \left(\delta_{GDL} / 2\right)} \frac{\Delta t}{A_{act} \delta_{CL} \varepsilon_{CL}} \tag{3.4}$$

where ξ (s^{-1}) is the water transfer coefficient, λ the volume averaged water content in ionomer, ρ_{MEM} (kg m^{-3}) the density of dry membrane, EW (kg kmol^{-1}) the equivalent weight of membrane, and λ_{CL}^{eq} the volume averaged equilibrium water content in CL corresponding to the volume averaged vapour concentration in CL pores. The second and third terms on the right hand side of Equation 3.4 represent the water transport from ionomer to pores in CL and from CL to GDL, respectively.

The volume averaged water content in ionomer of CL at the time instance t, λ_{CL}^t, is calculated as

$$\lambda_{CL}^t = \lambda_{CL}^{t-\Delta t} + \frac{\left(\lambda_{MEM}^{t-\Delta t} - \lambda_{CL}^{t-\Delta t}\right) D_{MEM-CL}^{eff} A_{act}}{\left(\delta_{MEM} / 2\right) + \left(\delta_{CL} / 2\right)} \frac{\Delta t}{A_{act} \delta_{CL} \omega} - \left(\lambda_{CL} - \lambda_{CL}^{eq}\right) \xi A_{act} \delta_{CL} \varepsilon_{CL} \frac{\Delta t}{A_{act} \delta_{CL} \omega} \tag{3.5}$$

where the subscript MEM represents membrane; ω is the ionomer volume fraction in CL; and D^{eff}_{MEM-CL} ($m^2\ s^{-1}$) is the effective diffusion coefficient of water in ionomer from membrane center to CL center, defined as

$$D^{eff}_{MEM-CL} = \frac{\left(\delta_{MEM}/2\right)+\left(\delta_{CL}/2\right)}{\left(\delta_{MEM}/2\right)/D_{ION}+\left(\delta_{CL}/2\right)/\left(D_{ION}\omega^{1.5}\right)} \tag{3.6}$$

where D_{ION} ($m^2\ s^{-1}$) is the diffusion coefficient of water in ionomer. The second and third terms on the right hand side of Equation 3.5 represent the water transport from membrane to CL and from ionomer to pores in CL, respectively. Equations 3.1, 3.2, 3.4 and 3.5 are applicable to both the anode and cathode.

The volume averaged water content in membrane at the time instance t, λ^{t}_{MEM}, is calculated as

$$\lambda^{t}_{MEM} = \lambda^{t-\Delta t}_{MEM} - \frac{\left(\lambda^{t-\Delta t}_{MEM}-\lambda^{t-\Delta t}_{CL,a}\right)D^{eff}_{MEM-CL,a}A_{act}}{\left(\delta_{MEM}/2\right)+\left(\delta_{CL,a}/2\right)}\frac{\Delta t}{A_{act}\delta_{CL,a}\omega_a} - \frac{\left(\lambda^{t-\Delta t}_{MEM}-\lambda^{t-\Delta t}_{CL,c}\right)D^{eff}_{MEM-CL,c}A_{act}}{\left(\delta_{MEM}/2\right)+\left(\delta_{CL,c}/2\right)}\frac{\Delta t}{A_{act}\delta_{CL,c}\omega_c} \tag{3.7}$$

where the subscripts a and c represents anode and cathode, respectively. The second and third terms on the right hand side of Equation 3.7 represent the water transport from membrane to anode CL and from membrane to cathode CL, respectively.

Table 3.4: Parameters of purging duration estimate (parameters listed in Tables 3.2 and 3.3 are not repeated, the CL, GDL and flow channel layout are the same for anode and cathode).

Parameter	Value
Time step size	10^{-5} s
Thickness of gas diffusion layer after compression	200 μm
Porosity of gas diffusion layer after compression	0.71
Thickness of catalyst layer	10 μm
Porosity of catalyst layer	0.3
Ionomer volume fraction of catalyst layer	0.2
Area of the interface between flow channel and gas diffusion layer	20 cm^2
Initial water content in catalyst layer and membrane	14
Initial vapour concentration in pores of catalyst layer and gas diffusion layer	1.304 mol m^{-3} (equivalent to a water content of 14 at 25 ^oC)
Initial vapour concentration in flow channel	0

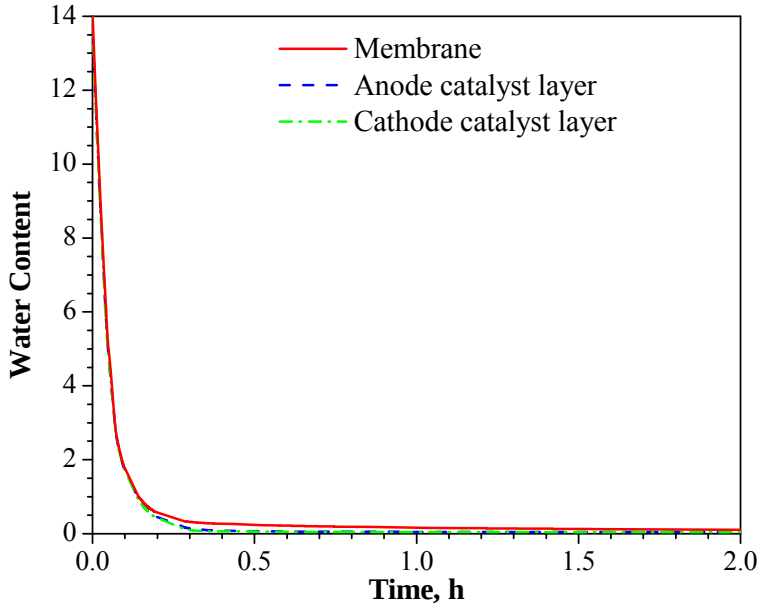

(a)

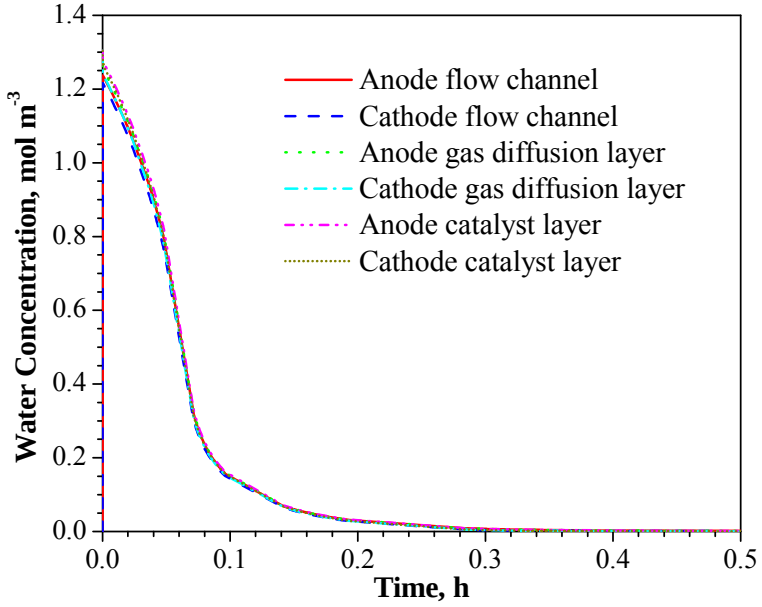

(b)

Figure 3.8: Evolutions of the (a) water content and (b) water vapour concentration in different layers during the purging process.

According to the properties of the tested PEMFC, the parameters used for the estimate of purging duration are listed in Table 3.4. Those parameters already listed in Tables 3.2 and 3.3 are not repeated in Table 3.4. A time step size of 10^{-5} s is used. Using smaller time step sizes results in almost the same results. The GDL thickness and porosity after compression are used in the calculation. By assuming that the GDL is compressed from 230 to 200 μm, and the volume of the solid material remains unchanged, the porosity after compression, ε_{com}, is

$$\varepsilon_{com} = 1 - (1 - \varepsilon_{uncom}) \frac{\delta_{uncom}}{\delta_{com}} \tag{3.8}$$

where ε_{uncom} is the uncompressed GDL porosity; and δ_{uncom} (m) and δ_{com} (m) are the uncompressed and compressed GDL thicknesses, respectively. It is assumed that the cell is initially fully humidified at 25 ^{o}C, therefore the water content in ionomer is 14 and the vapour concentration is 1.304 mol m^{-3} in pores of CL and GDL. The initial amount of water in flow channel is set to be 0 because the water in flow channel is removed immediately by purging gas.

Figure 3.8 shows the evolutions of the water content and vapour concentration in different layers during the purging process obtained by using the purging model. It can be noticed that both the water content and vapour concentration decrease rapidly at the beginning, and then the decrements become slower. As shown in Figure 3.8a, the difference in water content among the different layers is small during the whole purging process. It takes about 30 min for the water content to reach a "steady state" value (or the asymptote). The vapour is removed more quickly than the water in membrane. As presented in Figure 3.8b, it takes about 18 min to reach the "steady state". The results shown in Figure 3.8 indicate that a 2-hour purging used in all the experiments in this study is sufficient to ensure a consistent and dry cell condition before the start-up processes.

3.4 Summary

The cold start experiment is described in details in this chapter. Unique in the present cold start experiment is the inclusion of the simultaneous measurement of current and temperature distributions. An analytical model for quick estimate of purging duration is also presented in this chapter. Since most of the present numerical models are limited to either 1D or 2D or 3D but only considering a section of the entire cell due to computational requirement, the measured distribution data are critically important to better understand the PEMFC cold start characteristics.

Chapter 4

Experimental Results

With the cold start experiment presented in Chapter 3, extensive experimental measurements are conducted to study the cold start characteristics of PEMFC. The detailed experimental conditions are given in Chapter 3. In this chapter, the cold start experimental results are presented. The various cold start processes are investigated one by one with the measured current and temperature distributions. The effects of load condition, flow arrangement and start-up temperature on the cold start performance are also discussed.

4.1 Investigation of Cold Start Processes

4.1.1 Failed Cold Start Process

Figure 4.1 shows the evolutions of current density/voltage and average temperature in the cathode flow field plate (average of the sixteen thermocouple measurements) during the cold start process from -10 ^{o}C set at 0.3 V, with a co-flow arrangement as demonstrated in Figure 3.2. As shown in Figure 4.1a, even though the cell voltage is set to 0.3 V, it fluctuates in the first 40 s with a magnitude of 0.05 V. Because initially the internal resistance of the tested PEMFC is very high due to the dry membrane (2 hour of purging) and low temperature, it is perhaps difficult to accurately apply the load condition. With water being produced and hydrating the ionomer, the cell voltage becomes stable after 40 s. Upon the start-up, the current density suddenly increases quickly, and then the increment is slower and it reaches 0.23 A cm^{-2} in 76 s. The increment of current density is due to the ionomer hydration and temperature increment. After that, the current density starts decreasing and the cold start process is failed. Because the ice blockage effect that hinders the reactant delivery to the reaction sites starts overcoming the effects of ionomer hydration and temperature increment. The temperature evolution shown in Figure 4.1b also follows an increasing-decreasing trend. It can be noticed that the initial start-up temperature is slightly higher (0.68 ^{o}C higher) than -10 ^{o}C. As mentioned previously in Chapter 3, the average temperature at the end of the cooling down process is still slightly higher than the environmental temperature. Because the pipelines, electrical wires and other connections to the tested PEMFC are connected to either the fuel cell test station or the DAQ system, which are all outside of the environmental chamber. All these connections can cause heat transfer between the tested PEMFC and the outside environment, slightly increasing the temperature of the tested PEMFC. The highest average temperature for the cathode flow field plate is -7.18 ^{o}C at 152 s. After that, the average temperature starts decreasing, indicating that the heat loss to the surrounding overcomes the heat generation inside the cell. Figure 4.1 shows that the peak temperature is reached after the peak current density, because the current density is still sufficiently high, even after its peak value, to produce heat that is in excess of heat loss at the periphery of the cell. Since the tested PEMFC is a single cell with thick flow field plates, current collectors and end plates, the total thermal mass per cell is much higher than those in a PEMFC stack. Therefore, the temperature increment of PEMFC stack is expected to be quicker and higher.

The contours of current density during the cold start process from -10 ^{o}C at 0.3 V are shown in Figure 4.2. The current density is initially the highest in the region near the flow channel inlet (30 s), and the current density over the entire cell increases until the overall current peaks (70 s). Since the current density near the flow inlet region is the highest in the first 70 s, the ice formation rate is also the highest there due to the highest water production rate. Therefore, after 70 s, the high current density region starts moving downstream and the cell current output decreases (80 s, 100 s and 220 s). The overall current density peaks at 76 s (Figure 4.1a), which is in agreement with the time taken for the current density in the inlet region to reach its peak value (Figure 4.2). In fact, in the first 76 s, 40-50% of the total cell current is produced in segments 1-4 in the inlet region (refer to Figure 3.2 for segment numbers). After 76 s, the cell current density drops when the current density in the inlet region decreases, due to ice blockage of the pore regions of the cell. Since the amount of heat generation is determined by the amount of current being produced, the inlet region producing most of the cell current is most critical in determining the characteristics of cold start. Therefore, the cold start capability can be improved by avoiding or reducing ice formation in the cathode CL near the inlet region, which can be accomplished, for example, through external heating, around the inlet region of the cell.

Figure 4.3 shows the contours of temperature in the cathode flow field plate during the cold start process from -10 ^{o}C at 0.3 V. It can be noticed that the initial temperature distribution in not uniform (0 s). The temperature is slightly higher near both the flow inlets and outlets. The maximum temperature difference is about 0.5 ^{o}C. As mentioned earlier, this is due to the various connections from the tested PEMFC to the outside environment, and the flow of cooling air inside the environmental chamber may also cause temperature variations. During this cold start process, the temperature is initially the highest near the flow inlet region (50 s and 80 s), and the high temperature region becomes in both the flow inlet and middle regions of the cell (100 s and 140 s). Because the high current density region moves downstream (Figure 4.2) and the heat loss rate to the surrounding is the lowest in the middle. Then the temperature in the whole cathode flow field plate drops (200 s).

Since the initial temperature is not uniformly distributed, plotting the temperature increment rather than the magnitude helps discover the variation of heat generation and loss rates over the active reaction area. In Figure 4.4, the contours of normalized temperature are presented. By assuming an initial temperature of -10 ^{o}C everywhere in the tested PEMFC (since the environmental chamber is set to -10 ^{o}C for this test), the normalized temperature is defined as

$$T_N^i = T^i - T_{initial}^i + T_{set} \tag{4.1}$$

where T_N^i (^{o}C) is the normalized temperature of segment i, T^i (^{o}C) the real temperature measured for segment i, $T_{initial}^i$ (^{o}C) the real initial temperature measured for segment i, and T_{set} (^{o}C) the set start-up temperature (-10 ^{o}C in this case). Figure 4.4 shows that the initial normalized temperature is the highest near the flow inlet region due to the highest current density there (50 s). Then the high temperature region stays in the middle but gradually moves downstream (80 s, 100 s and 140 s) because the heat loss rate is the lowest there. Finally the temperature drops in the whole cathode flow field plate (200 s).

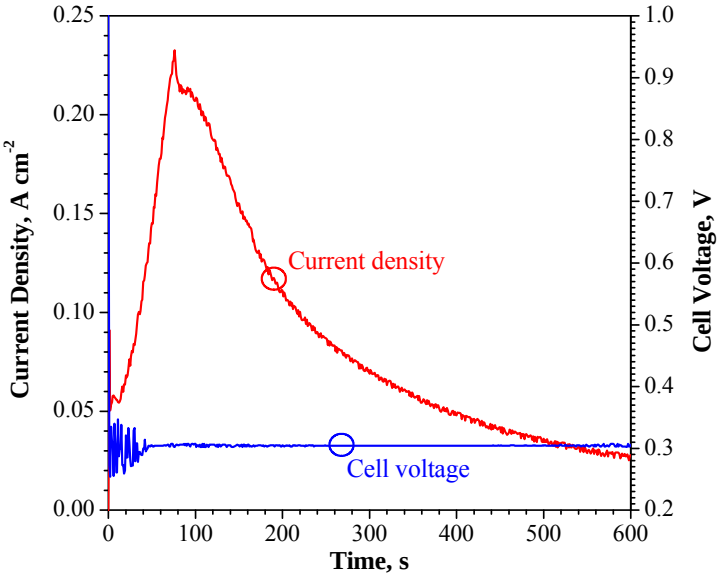

(a)

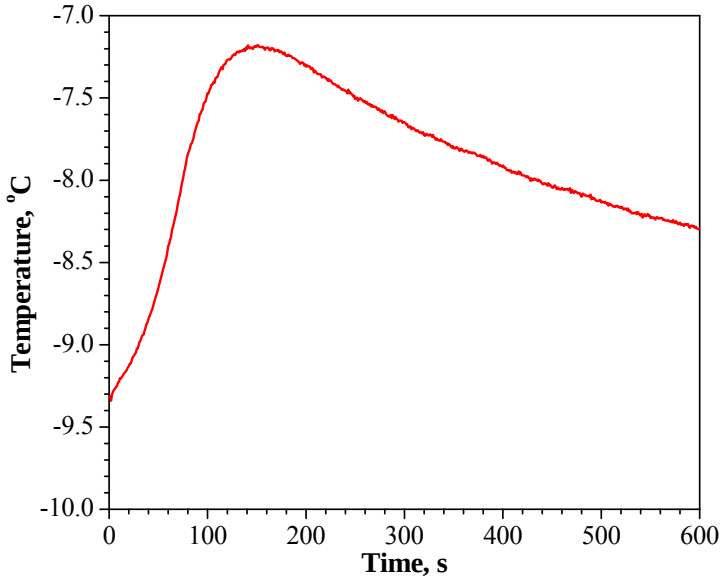

(b)

Figure 4.1: Evolutions of (a) current density/voltage and (b) average temperature in cathode flow field plate (average of the sixteen thermocouple measurements) during the cold start process from -10 ^{o}C at 0.3 V.

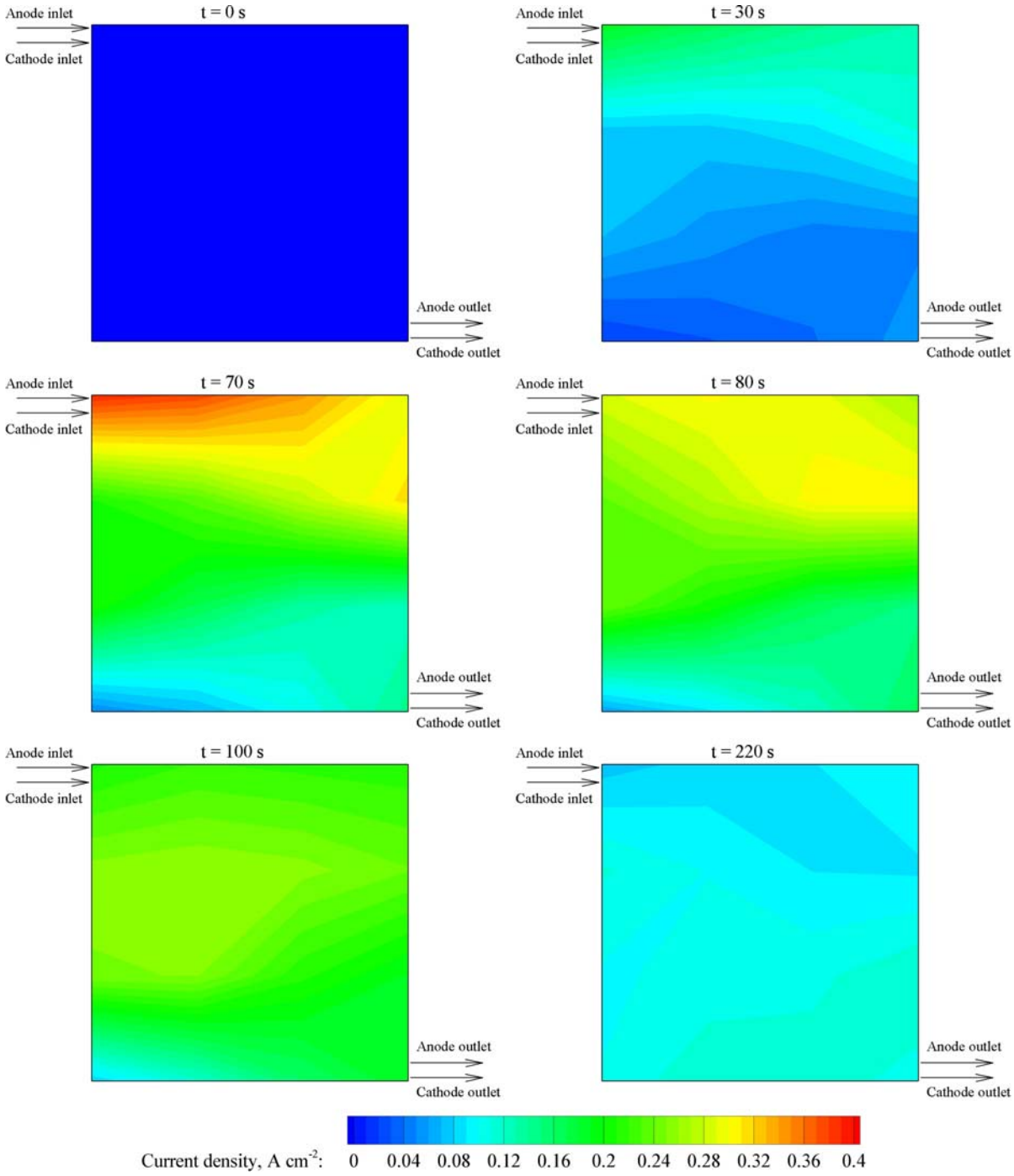

Figure 4.2: Contours of current density during the cold start process from -10 ^{o}C at 0.3 V.

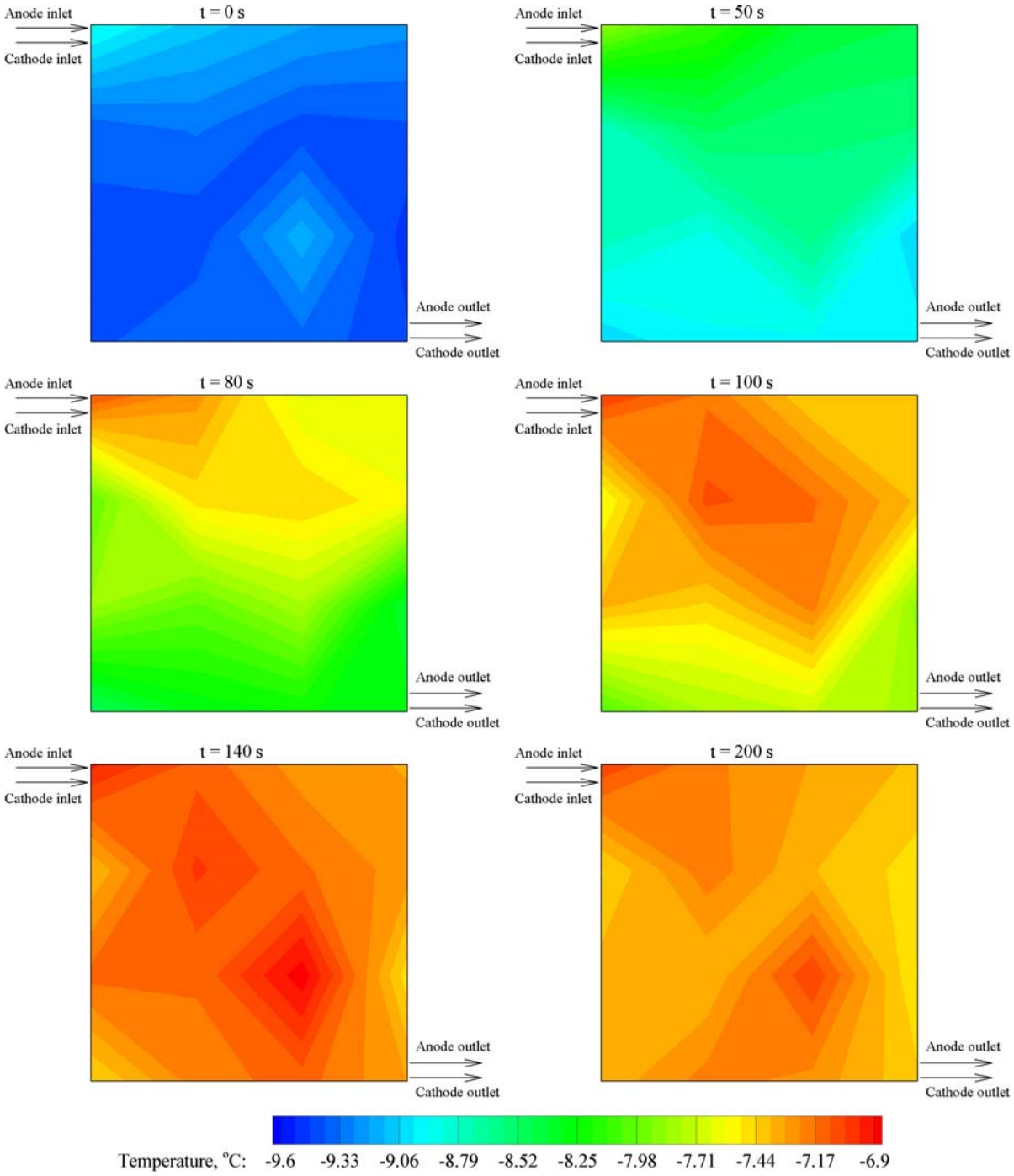

Figure 4.3: Contours of temperature in cathode flow field plate during the cold start process from -10 ^{o}C at 0.3 V.

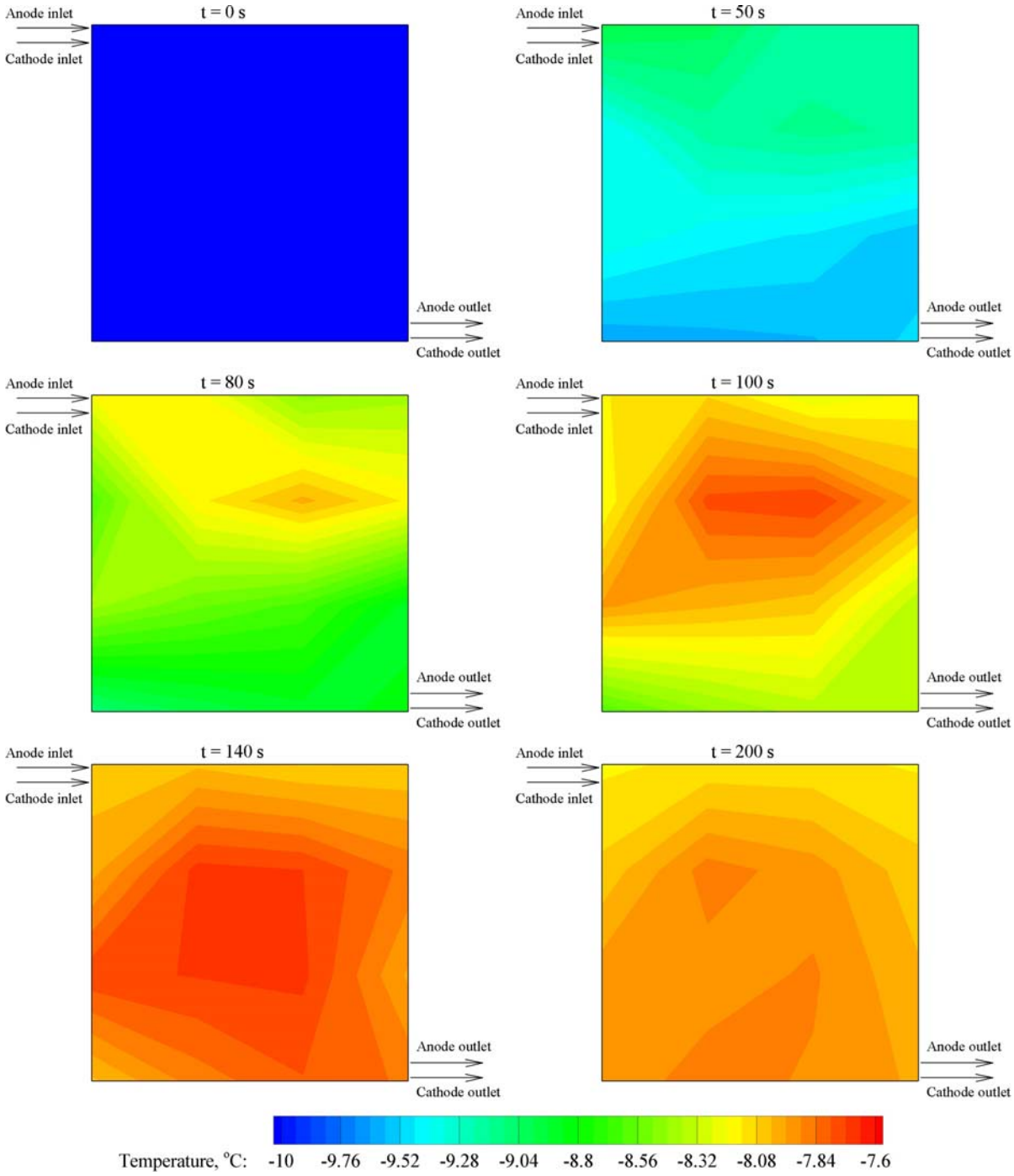

Figure 4.4: Contours of normalized temperature in cathode flow field plate during the cold start process from -10 ^{o}C at 0.3 V.

Figures 4.2-4.4 show that the temperature is the highest near the inlet region of the cell before the overall current density peaks, because almost half of the total cell current is produced there. These figures also indicate that the temperature in the middle region is also fairly high before the overall

peak current density is reached and the highest after due to the low heat loss rate there. The highest current density is located in the middle region as well after the overall current density peaks. Therefore, it can be concluded that the inlet region of the cell produces most of the heat and results in the quickest temperature increment before the cell current peaks, but also suffers significant heat loss to the surrounding and quick ice formation; and the middle region is favoured by the lowest heat loss rate there to have the longest duration of survivability. As mentioned previously, applying more external heating in these regions are more favourable than in the other regions.

4.1.2 Successful Cold Start Process

Figure 4.5 shows the evolutions of current density/voltage and average temperature in the cathode flow field plate (average of the sixteen thermocouple measurements) during the cold start process from -5 ^{o}C at 0.3 V with co-flow arrangement. The only difference between Figures 4.1 and 4.5 is the start-up temperature. The overall current density evolution shown in Figure 4.5a indicates that the total current produced in the cell increases at the beginning until reaching 0.36 A cm^{-2} at 100 s, and then remains almost steadily. During the time period from 300 s to 500 s, the overall current density fluctuates more significantly than the other time periods. Figure 4.5b shows that the cathode flow field temperature reaches above 0 ^{o}C from 300 s to 500 s. This suggests that the current density fluctuation is due to the ice melting and liquid water transport. Since the temperature reaches above 0 ^{o}C, this cold start process is successful. The increment of temperature becomes slower during the operation, indicating that the heat generation and loss rates are being balanced. Figure 4.5b also shows that the initial temperature is slightly higher (0.47 ^{o}C higher) than -5 ^{o}C, which is similar to Figure 4.1b.

The contours of current density during the cold start process from -5 ^{o}C at 0.3 V are shown in Figure 4.6. The overall distribution of current density remains similar during this successful cold start process. The current density is the highest near the flow inlet due to the high reactant concentration there. The current density generally decreases along the flow direction towards the flow channel outlet.

The temperature and normalized temperature contours in the cathode flow field plate during the cold start process from -5 ^{o}C at 0.3 V are shown in Figures 4.7 and 4.8, respectively. Both figures show that the temperature is initially the highest near the flow inlets (30 s), and then the high temperature can be observed in both the inlet and middle of the cell (70 s, 250 s, 400 s and 1000 s), because the heat loss rate is the lowest in the middle. Figure 4.7 also shows that the temperature at some areas started approaching 0 ^{o}C since 70 s, indicating that liquid water starts being formed. This is about 200 s before the average temperature in the cathode flow field plate reaches 0 ^{o}C (Figure 4.5b). The formation of liquid water seems to have no significant impact on the overall current and temperature distributions.

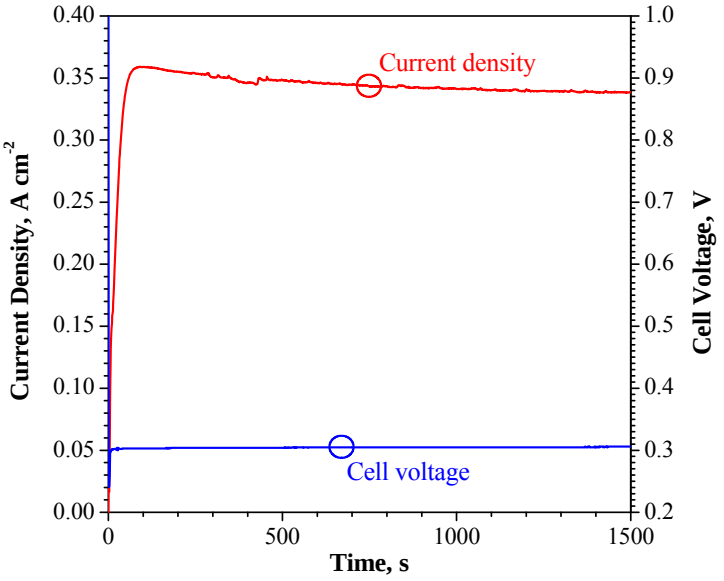

(a)

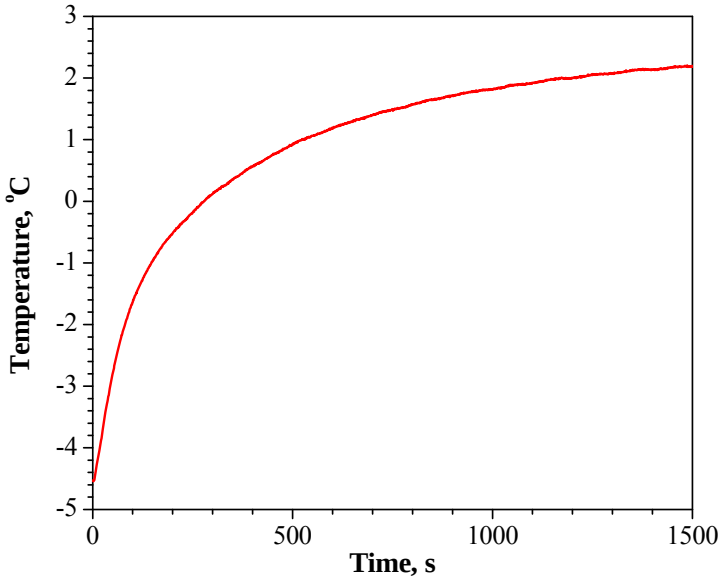

(b)

Figure 4.5: Evolutions of (a) current density/voltage and (b) average temperature in cathode flow field plate (average of the sixteen thermocouple measurements) during the cold start process from -5 °C at 0.3 V (the same to Figure 4.1 except the start-up temperature).

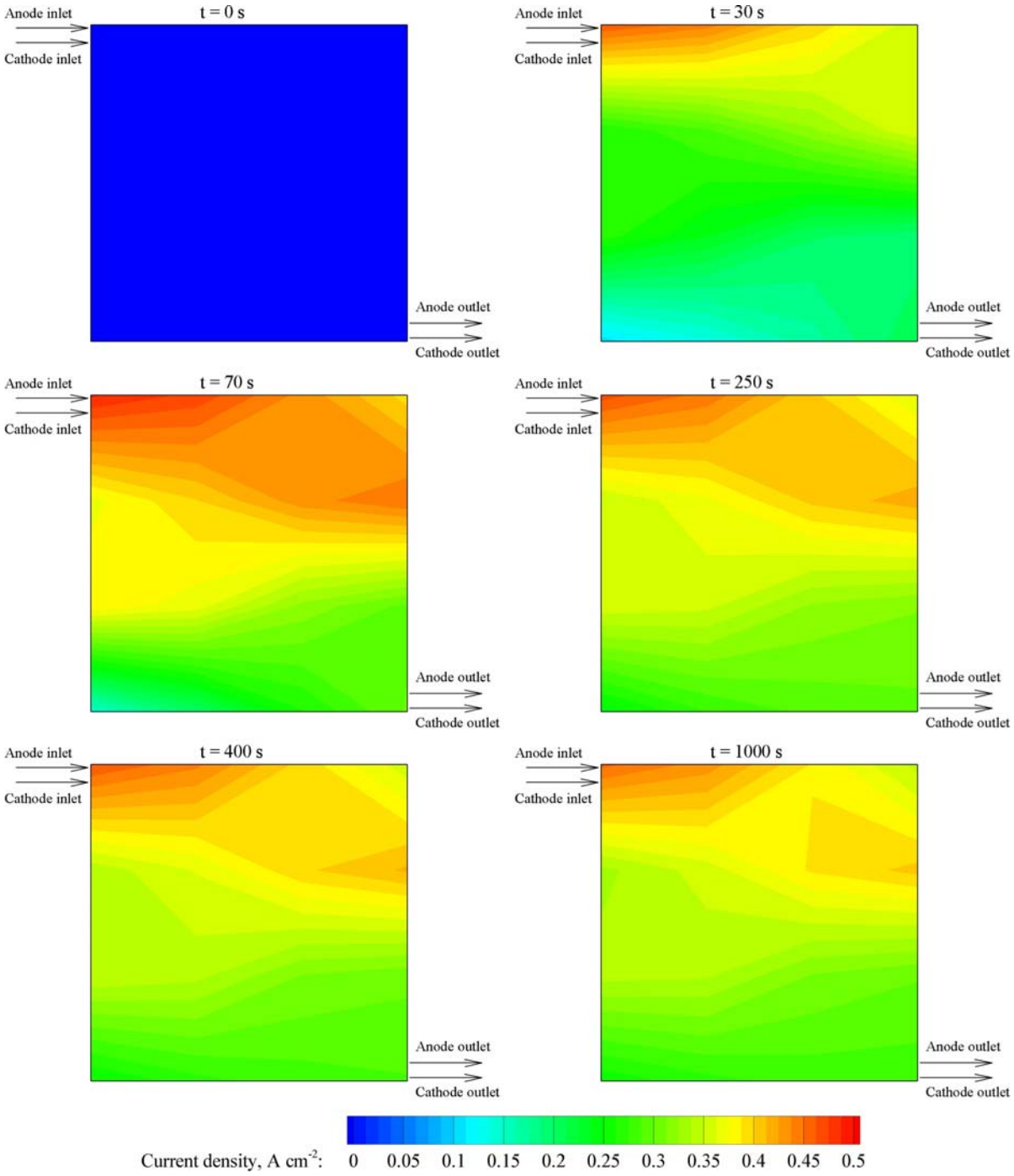

Figure 4.6: Contours of current density during the cold start process from -5 ^{o}C at 0.3 V (the same to Figure 4.2 except the start-up temperature).

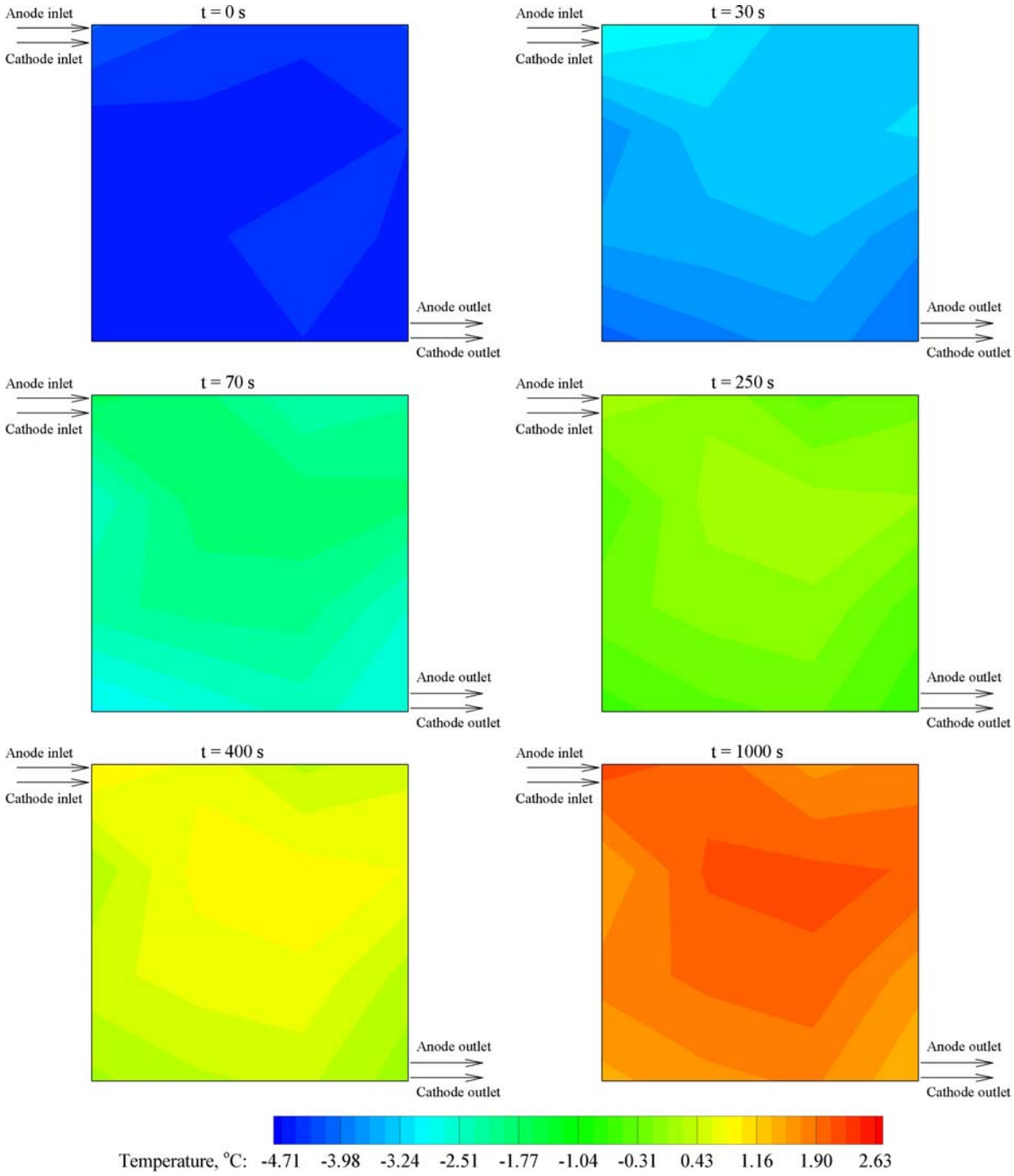

Figure 4.7: Contours of temperature in cathode flow field plate during the cold start process from -5 ^{o}C at 0.3 V (the same to Figure 4.3 except the start-up temperature).

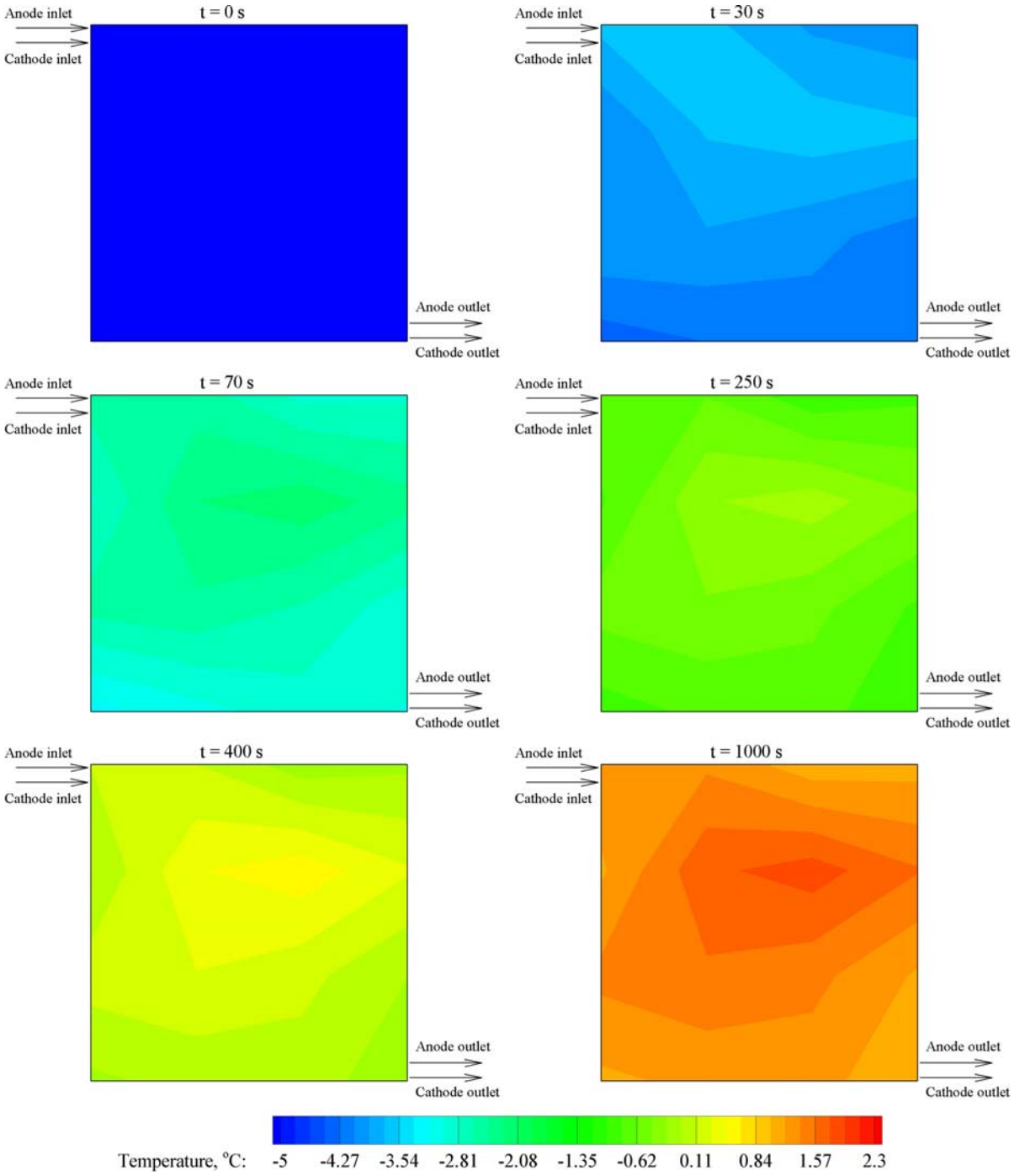

Figure 4.8: Contours of normalized temperature in cathode flow field plate during the cold start process from -5 ^{o}C at 0.3 V (the same to Figure 4.4 except the start-up temperature).

4.2 Effect of Load Condition

Figure 4.9 shows the evolutions of the cell voltages and current densities during the cold start processes from -10 ^{o}C set at 0.07 A cm^{-2} and 0.1 A cm^{-2} with co-flow arrangement, and the corresponding evolutions of the average temperatures in the cathode flow field plate (average of the sixteen thermocouple measurements) are shown in Figure 4.10. The only different between the cold start processes shown in Figures 4.9 and 4.10 and in Figure 4.1 are the load condition. Dissimilar to the constant voltage cold start processes shown in Figure 4.1, no noticeable fluctuation of the current densities and cell voltages can be observed in Figure 4.9, perhaps because the current control is easier than the voltage control. For the cold start process set at 0.07 A cm^{-2} (Figure 4.9a), the cell voltage suddenly decreases at the beginning, remains steadily after that, and then drops due to the ice blockage of the reaction sites. For the cold start process from 0.1 A cm^{-2} (Figure 4.9b), the cell voltage suddenly decreases at the beginning, followed by an increasing-decreasing trend. It can be noticed that initially the cell voltage is dropped to less than 0.02 V, indicating that the start-up current density of 0.1 A cm^{-2} is perhaps the highest possible value for a constant current start-up process. The cell voltages start decreasing at about 190 s and 100 s for the 0.07 A cm^{-2} and 0.1 A cm^{-2} cold start processes, respectively, indicating that a higher start-up current results in a quicker failed process. Figure 4.10 shows that the temperature increments are about 0.86 ^{o}C and 1.01 ^{o}C for the 0.07 A cm^{-2} and 0.1 A cm^{-2} cold start processes, respectively, indicating that increasing the start-up current density is favourable. Figures 4.1, 4.9 and 4.10 also show that cold start with constant voltage is superior to with constant current, because a low voltage ensures the highest possible current density at every time instance during a cold start process.

The contours of the current density during the cold start process from -10 ^{o}C set at 0.1 A cm^{-2} are shown in Figure 4.11 (the same to Figure 4.2 except that the load condition is different). Since the overall current density is fixed, the average current density over the active reaction area must also remain unchanged during the cold start process. The current density is initially the highest in the region near the flow channel inlet (10 s), and after that the high current density region moves downstream (50 s, 100 s, 150 s, 190 s). Figure 4.12 shows the contours of the normalized temperature in the cathode flow field plate during the cold start process from -10 ^{o}C set at 0.1 A cm^{-2} (the same to Figure 4.4 except that the load condition is different). The initial normalized temperature is the highest near the flow inlet region due to the highest current density there (10 s and 20 s). Then the high temperature region stays in the middle but gradually moves downstream (100 s and 160 s) because the heat loss rate is the lowest there. Finally the temperature becomes more evenly distributed. Dissimilar to the constant voltage start-up processes that the heat generation rates decrease with the decreased current densities, the heat generation rates during constant current start-up processes increase with the decreased cell voltages. Such characteristic results in more even temperature distribution at the end of the constant current cold start process. Other than this, the general distributions of current density and temperature during the constant current cold start process are similar to the constant voltage process.

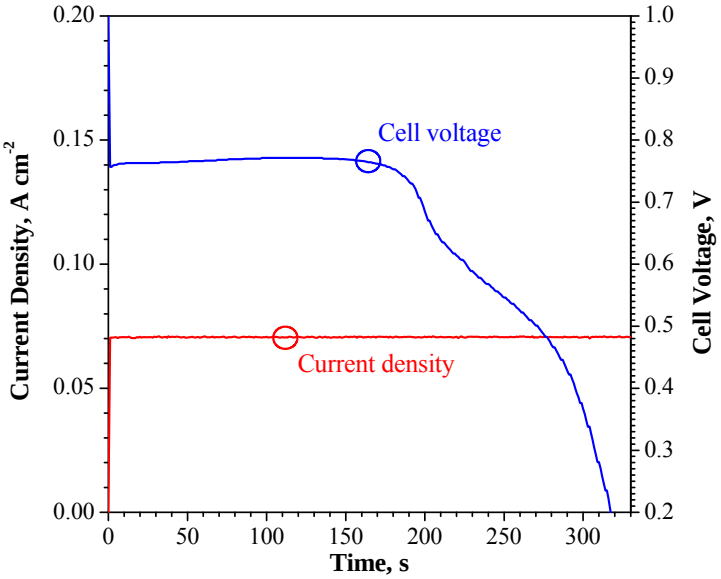

(a)

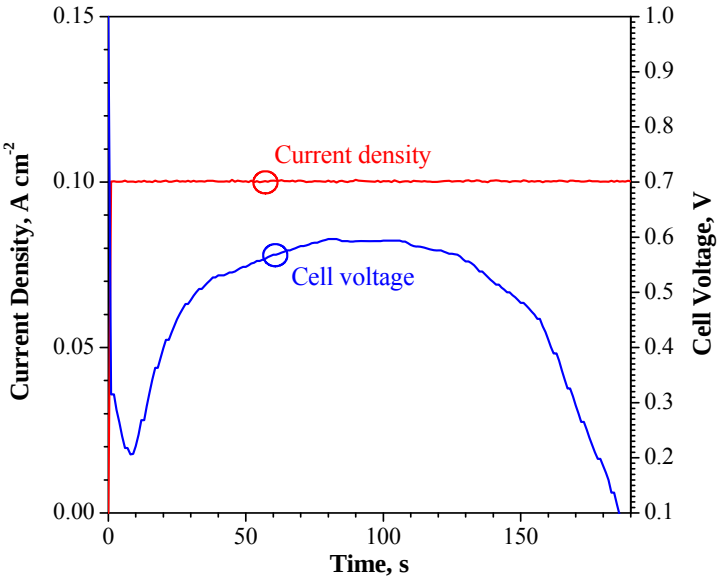

(b)

Figure 4.9: Evolutions of cell voltages/current densities during the cold start processes from -10 ^{o}C set at (a) 0.07 A cm^{-2} and (b) 0.1 A cm^{-2} (the same to Figure 4.1 except that the load conditions are different).

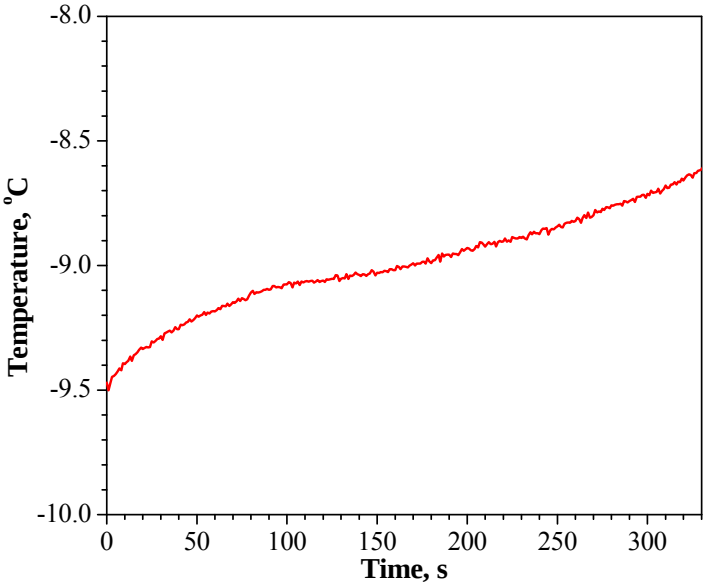

(a)

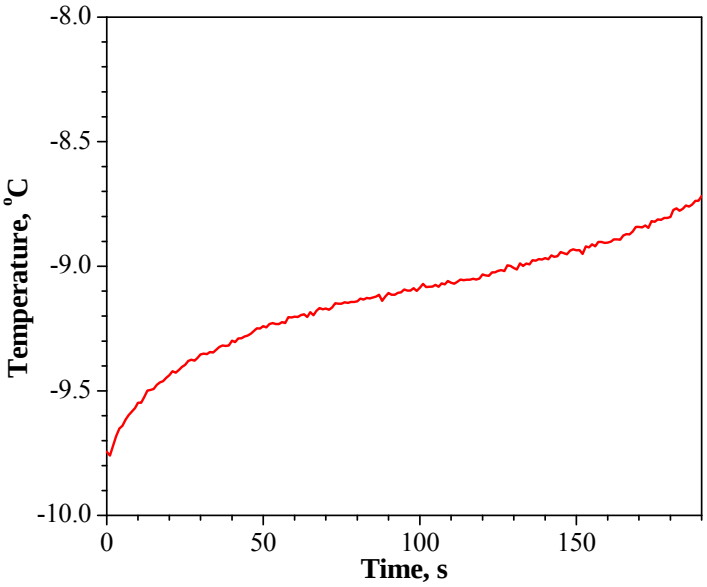

(b)

Figure 4.10: Evolutions of average temperatures in cathode flow field plate (average of the sixteen thermocouple measurements) during the cold start processes from -10 °C set at (a) 0.07 A cm^{-2} and (b) 0.1 A cm^{-2} (the same to Figure 4.1 except that the load conditions are different).

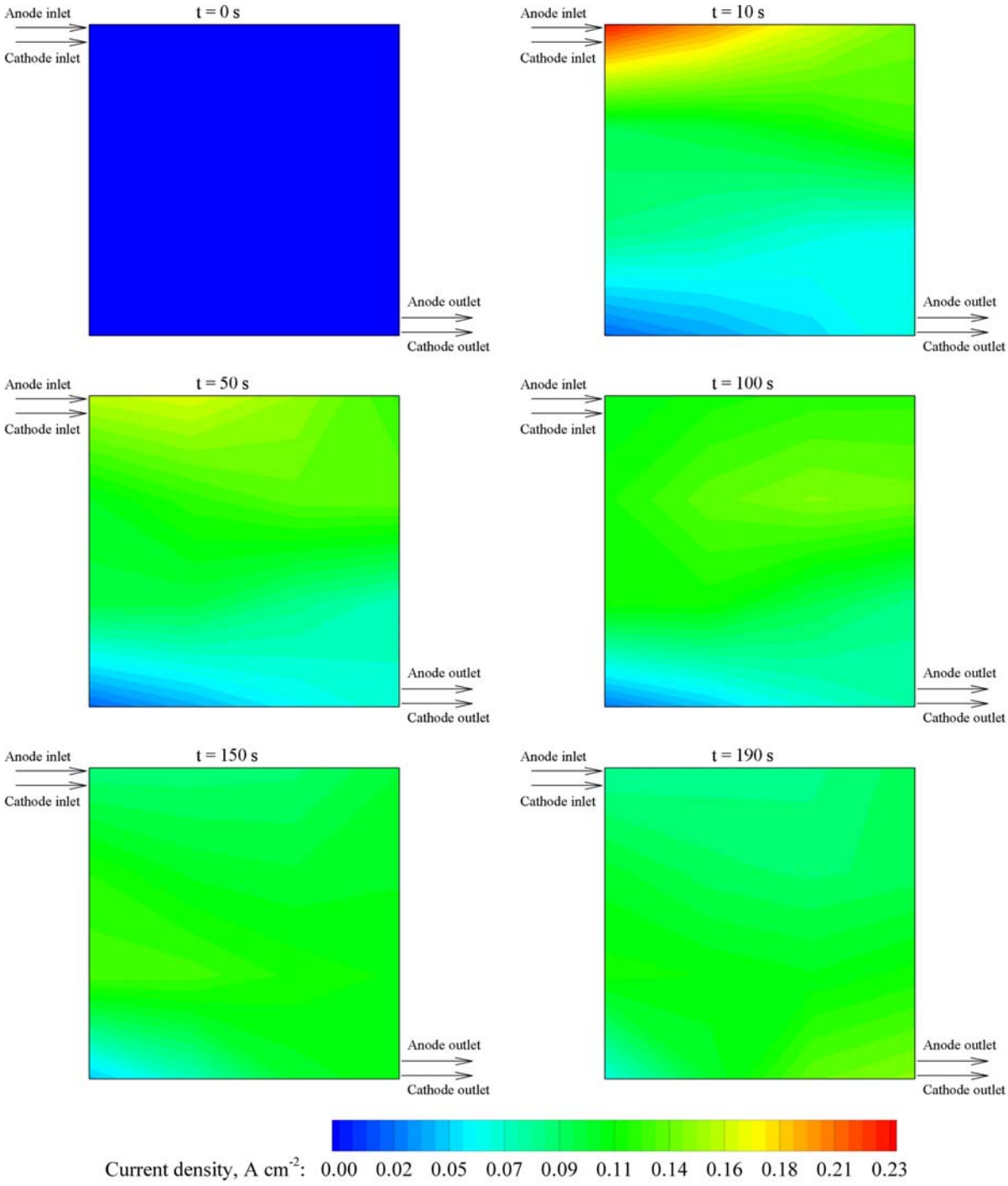

Figure 4.11: Contours of current density during the cold start process from -10 ^{o}C set at 0.1 A cm^{-2} (the same to Figure 4.2 except that the load condition is different).

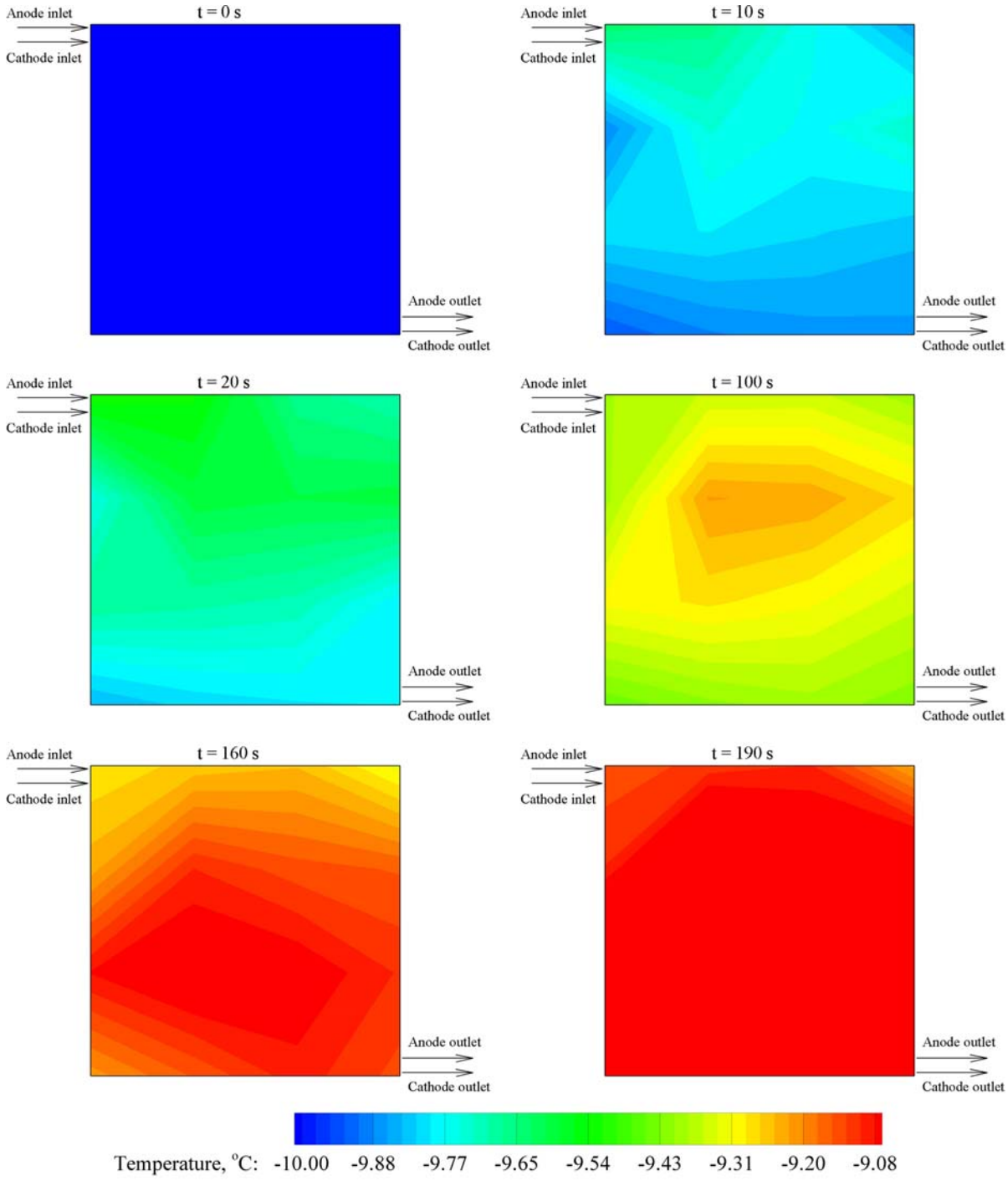

Figure 4.12: Contours of normalized temperature in cathode flow field plate during the cold start process from -10 °C set at 0.1 A cm^{-2} (the same to Figure 4.4 except that the load condition is different).

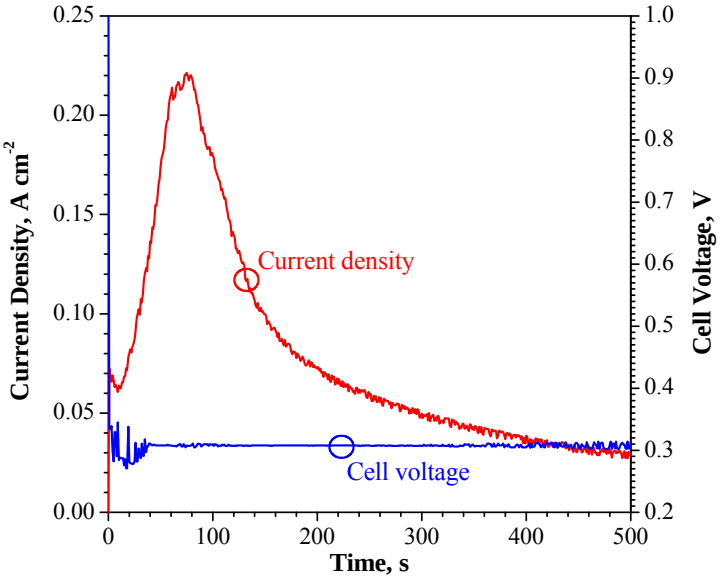

(a)

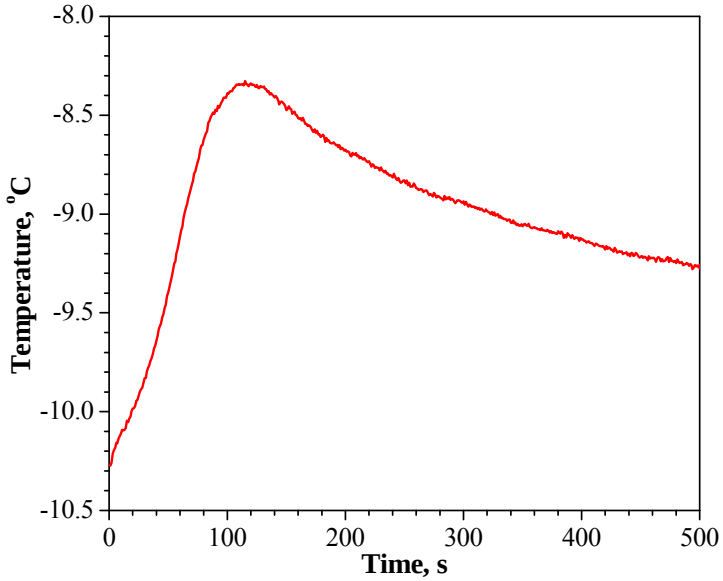

(b)

Figure 4.13: Evolutions of (a) current density/voltage and (b) average temperature in cathode flow field plate (average of the sixteen thermocouple measurements) during the cold start process from -10 ^{o}C at 0.3 V (the same to Figure 4.1 except that the flow arrangement in this figure is counter-flow).

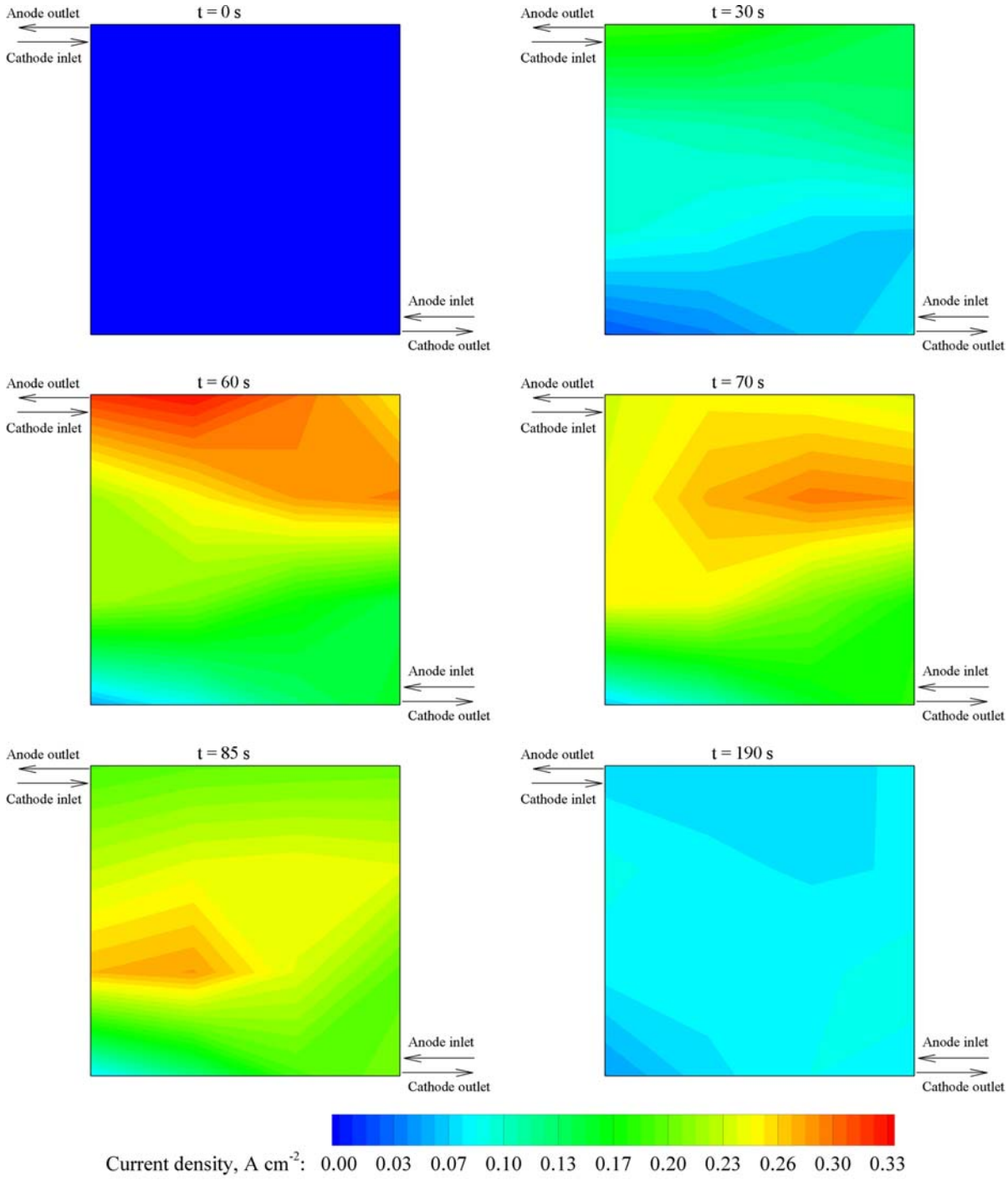

Figure 4.14: Contours of current density during the cold start process from -10 ^{o}C at 0.3 V (the same to Figure 4.2 except that the flow arrangement in this figure is counter-flow).

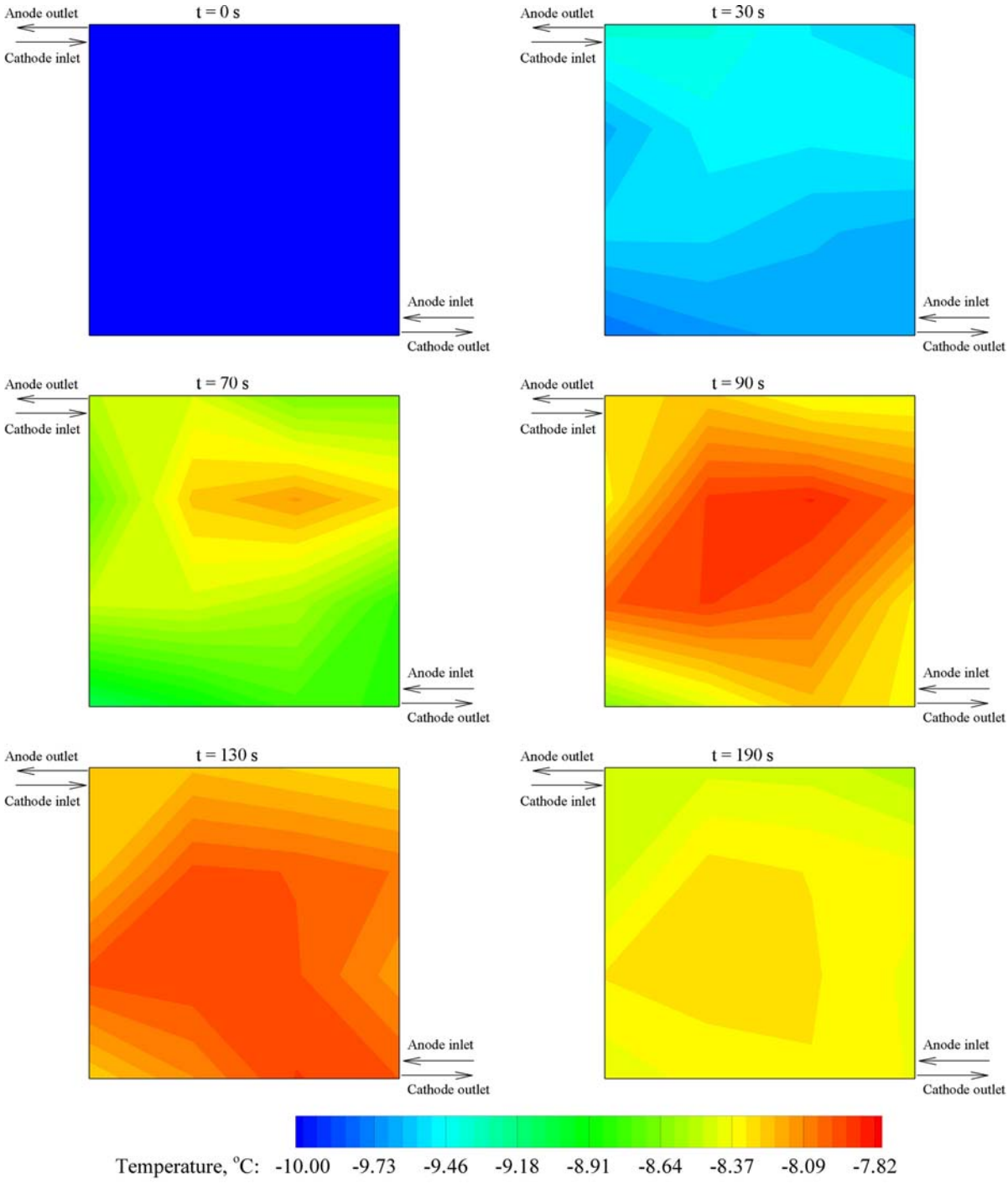

Figure 4.15: Contours of normalized temperature in cathode flow field plate during the cold start process from -10 ^{o}C at 0.3 V (the same to Figure 4.4 except that the flow arrangement in this figure is counter-flow).

4.3 Effect of Flow Arrangement

Figure 4.13 shows the evolutions of the current density and the average temperature in the cathode flow field plate (average of the sixteen thermocouple measurements) during the cold start process from -10 ^{o}C set at 0.3 V with counter-flow arrangement. The only difference between Figures 4.1 and 4.9 is the flow arrangement. Comparing Figures 4.1 and 4.13 shows that changing the flow arrangement results in negligible difference in the evolutions of the current densities and temperatures. The corresponding contours of the current density and normalized temperature are shown in Figures 4.14 and 4.15, respectively. The current density is initially the highest in the region near the cathode flow channel inlet (30 s and 60 s), and then the high current density region starts moving downstream according to the cathode flow and the cell current output decreases (70 s, 85 s and 190 s). The initial normalized temperature is the highest near the cathode flow inlet region due to the highest current density there (30 s), and then the high temperature region stays in the middle but gradually moves downstream according to the cathode flow (70 s, 90 s, 130 s and 190 s) because the heat loss rate is the lowest there. According to the cathode flow channel layout, the contours shown in Figures 4.14 and 4.15 for the counter-flow arrangement generally agrees with the contours shown in Figures 4.2 and 4.4 for the corresponding co-flow arrangement. This indicates that the cold start characteristics are mainly dominated by the cathode flow, and changing the flow arrangement has insignificant impact on the cold start performance.

4.4 Effect of Start-up Temperature

4.4.1 From -20 ^{o}C

Figure 4.16 shows the evolutions of the current density/cell voltage and the average temperature in the cathode flow field plate (average of the sixteen thermocouple measurements) during the cold start process from -20 ^{o}C set at 0.3 V with co-flow arrangement. The only difference between Figures 4.1 and 4.16 is the start-up temperature. Even though the cell voltage is set to 0.3 V, the actually cell voltage fluctuates significantly, with the fluctuation magnitudes up to 0.08 V in the first 200 s and about 0.02 V after that. The voltage fluctuation also results in unstable current density during the cold start process. For the cold start process from -10 ^{o}C (Figure 4.1), the cell voltage fluctuates in the first 40 s with a magnitude of about 0.04 V, and the fluctuation becomes negligible after that. The fluctuations occur due to the high internal resistance of the tested PEMFC at low temperatures and with dry membrane, because it is difficult to apply the load condition with high ohmic resistances. Therefore, the fluctuations occur most significantly at the low start-up temperature (-20 ^{o}C) and at the beginning of the cold start processes (dry membrane after purging). Similar to Figure 4.1, the current/temperature evolutions in Figure 4.16 also follow an increasing-decreasing trend. The peak temperatures reached are about -18.53 ^{o}C and -7.18 ^{o}C in about 340 s and 150 s for the cold start processes from -20 ^{o}C and -10 ^{o}C, respectively. The temperature increment is higher and quicker when starting from a higher temperature, due to the higher start-up current that generates more heat.

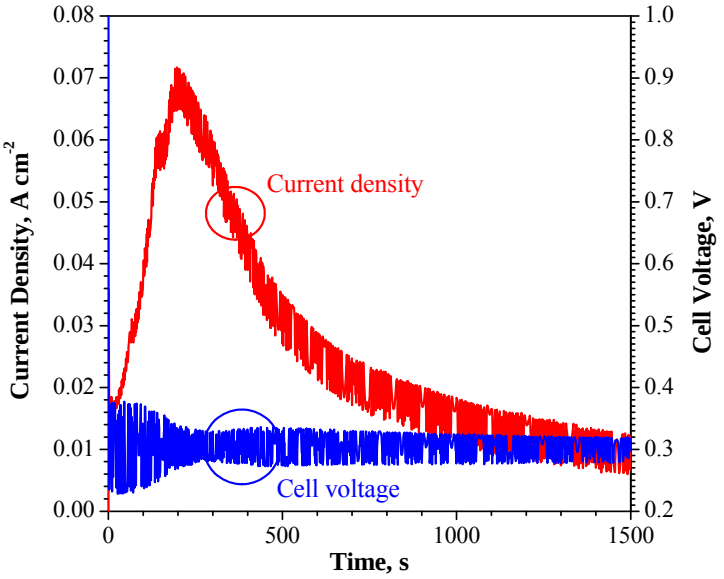

(a)

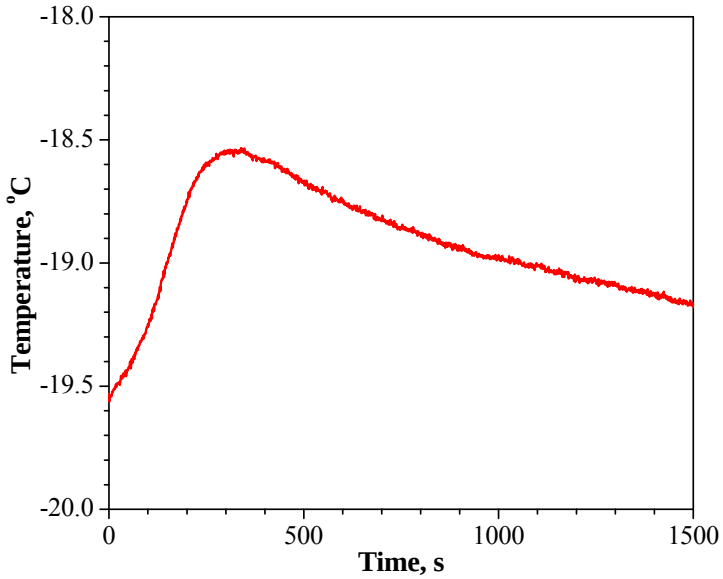

(b)

Figure 4.16: Evolutions of (a) current density/voltage and (b) average temperature in cathode flow field plate (average of the sixteen thermocouple measurements) during the cold start process from -20 °C at 0.3 V (the same to Figure 4.1 except the start-up temperature).

Figure 4.17 shows the evolutions of the current densities of segments 1 (close to inlet), 7 (close to middle) and 16 (close to outlet) during the cold start process from -20 ^{o}C set at 0.3 V with co-flow arrangement (refer to Figure 3.2 for the segment numbers). It can be noticed that the upstream peak current density is higher and the current density increment is quicker. The fluctuations of the current density can be observed at the inlet, middle and outlet, suggesting that the cell voltage and current density fluctuations shown in Figure 4.16 are over the whole active reaction area.

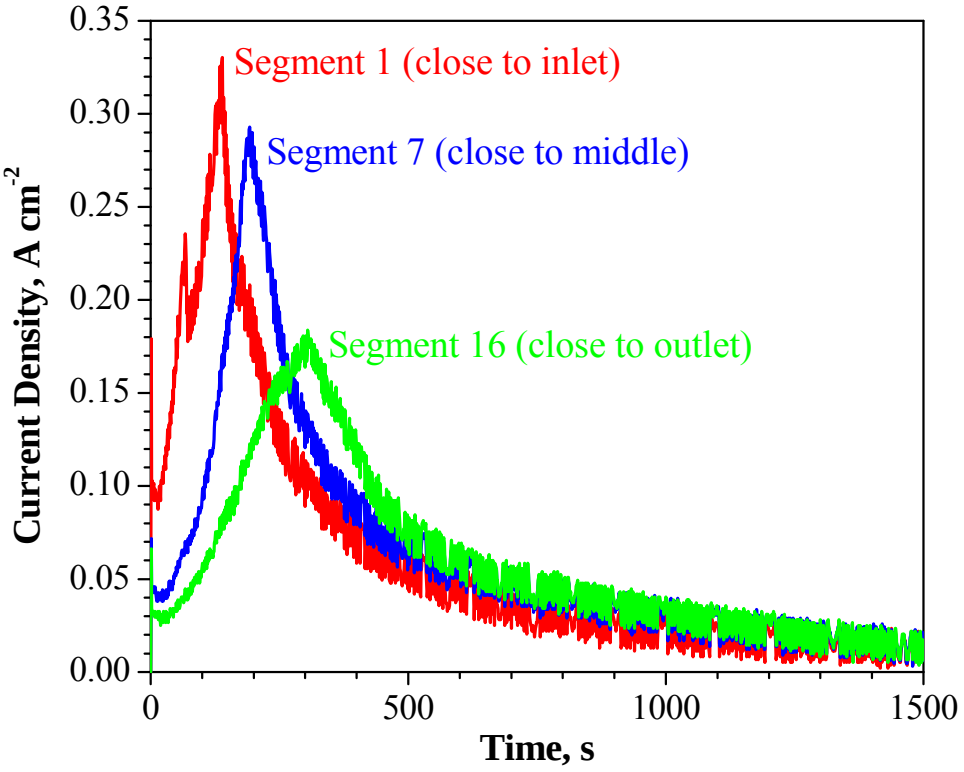

Figure 4.17: Evolutions of the current densities of segments 1 (close to inlet), 7 (close to middle) and 16 (close to outlet) during the cold start process from -20 ^{o}C set at 0.3 V.

4.4.2 From -7 ^{o}C

Figure 4.18 shows the evolutions of current density/voltage and average temperature in the cathode flow field plate (average of the sixteen thermocouple measurements) during the cold start process from -7 ^{o}C at 0.3 V with co-flow arrangement. The only difference between Figures 4.1 and 4.18 is the start-up temperature. In Figure 4.18, the current density reaches to about 0.35 A cm^{-2} at the beginning, after that it remains steadily for about 1700 s, then it suddenly decreases and the cell stops working. This can be explained with Figure 4.19, which shows the evolutions of the pressure drops through the cathode flow field during the cold start processes from -10 ^{o}C, -7 ^{o}C and -5 ^{o}C set at 0.3 V. The pressure drop remains almost constant during the cold start process from -10 ^{o}C,

suggesting that the ice formation is only significant in the cathode CL rather than in the GDL and flow channel. For the cold start processes from -7 ^{o}C and -5 ^{o}C, the pressure drops fluctuate, perhaps due to the formation of liquid water, and the pressure drop during the cold start process from -7 ^{o}C finally increases quickly. The tested PEMFC stops working because the pressure drop exceeds the safety limit of the fuel cell test station during the cold start process from -7 ^{o}C. The large pressure drop can only be caused by the ice blockages in the flow channel and GDL. Since the peak temperature in the cathode flow field plate reached is about 0.29 ^{o}C (Figure 4.18b), slightly higher than the normal freezing temperature of water, and the temperature commonly decreases from the cathode CL to flow channel, the temperature inside the cathode CL at this time instance should be higher than the freezing point of water. The water inside the cathode CL therefore can transport in liquid form into the GDL and flow channel. However, since the temperatures at some locations inside the flow channel and GDL are still lower than the freezing point of water, ice could be formed again and blocking the flow channel and GDL. This colds start failure mechanism has been rarely discovered before. It only occurs at certain narrow start-up temperature ranges (around -7 ^{o}C in this study), as the start-up process from -10 ^{o}C is failed due to the ice blockage in the cathode CL, and the corresponding start-up process from -5 ^{o}C is successful.

Based on these experimental results, three ice formation mechanisms are proposed, as demonstrated in Figure 4.20. The first mechanism is the commonly recognized one, the ice formation in cathode CL. It occurs when the temperature inside the cathode CL is lower than the freezing point of water, and is the most common cause of the cold start failure. The second and third mechanisms are the ice formations in the cathode GDL and flow channel, respectively. The ice formation in the cathode GDL occurs when the temperature in the cathode CL is higher than the freezing point of water, but the temperature is lower in the cathode GDL. This results in liquid water transport into the cathode GDL and freezing. When the temperatures in the cathode CL and GDL are all higher than the freezing point of water, but the temperature is lower in the cathode flow channel, liquid water can move into the cathode flow channel and freeze. It is likely that the second and third mechanisms often occur together since the GDL and flow channel are next to each other. However, the first mechanism seems to occur commonly without the second and third mechanisms, as indicated from the steady pressure drop during the start-up process from -10 ^{o}C shown in Figure 4.19.

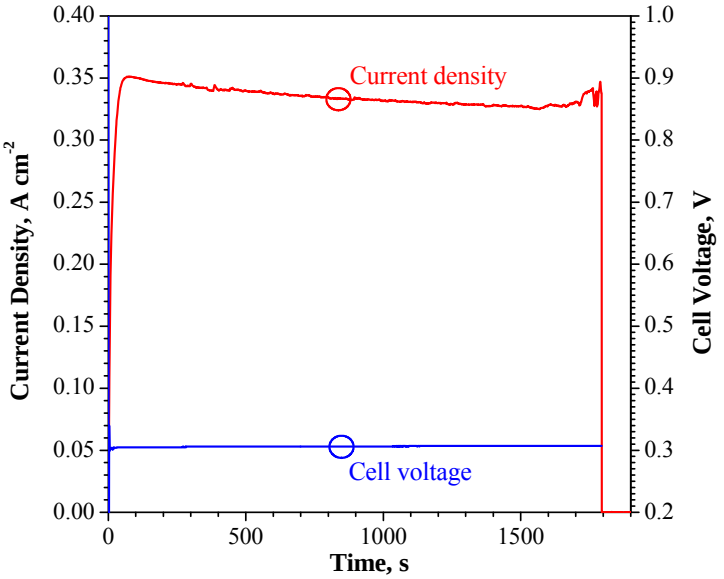

(a)

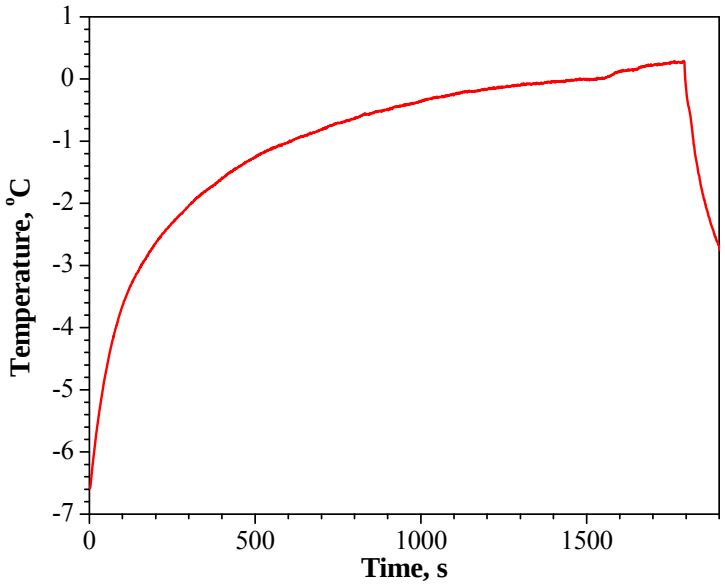

(b)

Figure 4.18: Evolutions of (a) current density/voltage and (b) average temperature in cathode flow field plate (average of the sixteen thermocouple measurements) during the cold start process from -7 ^{o}C at 0.3 V (the same to Figure 4.1 except the start-up temperature).

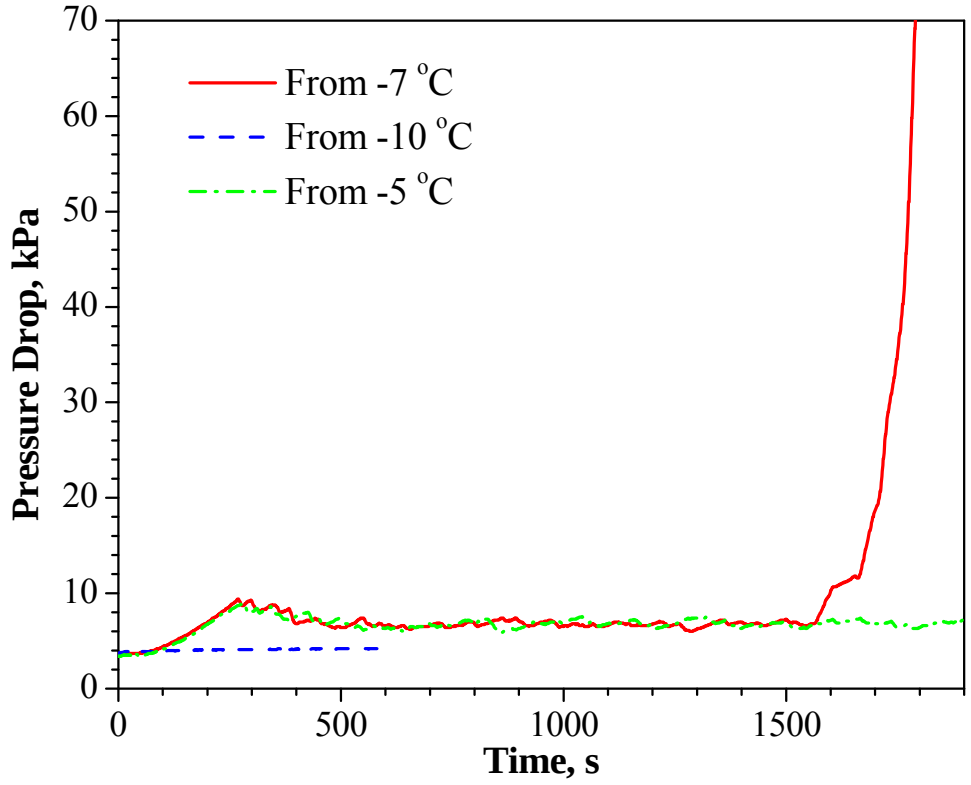

Figure 4.19: Evolutions of pressure drops through cathode flow field during the cold start processes from -10 °C, -7 °C and -5 °C set at 0.3 V.

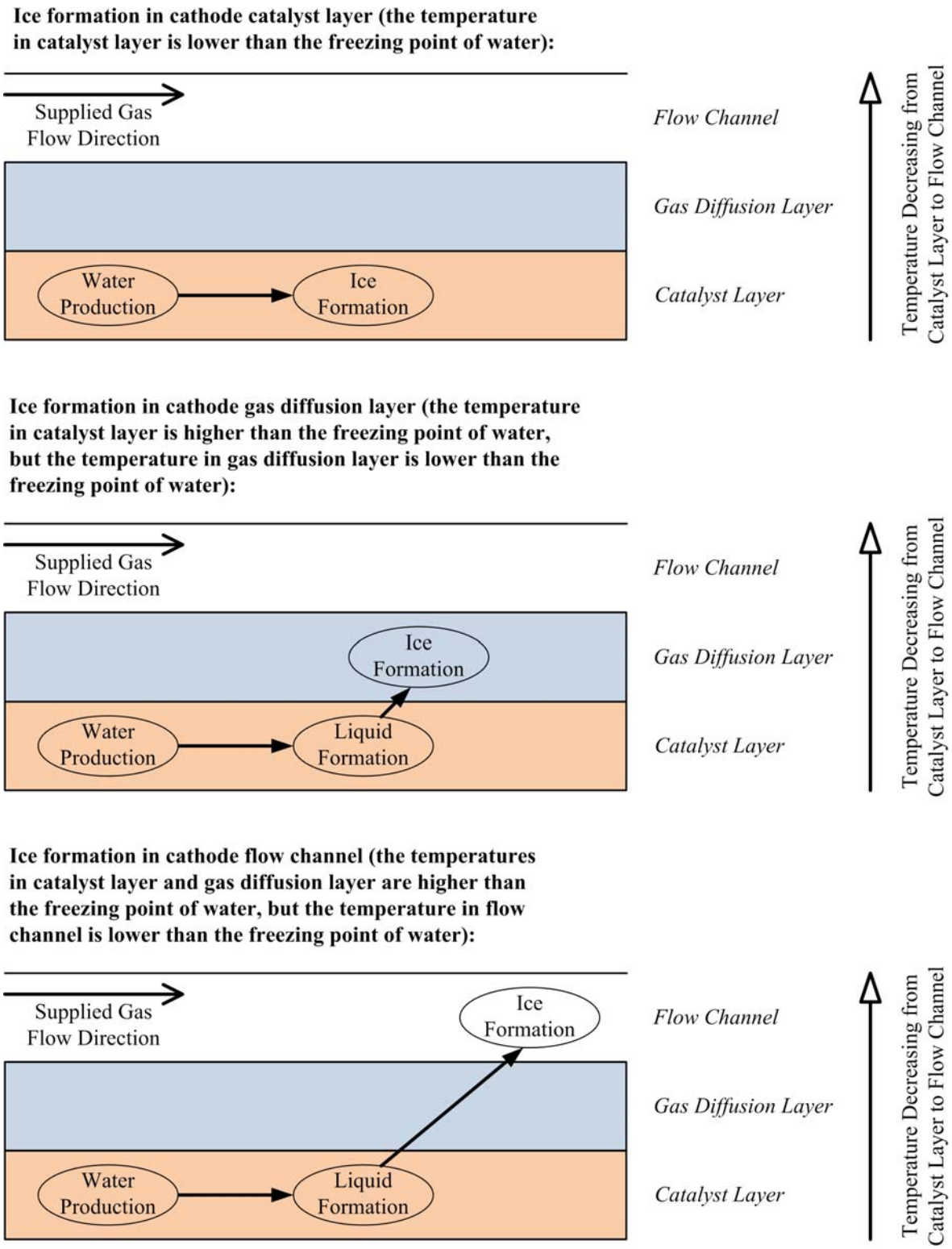

Figure 4.20: Ice formation mechanisms in different layers.

4.5 Summary

In this chapter, the results from the cold start experiment are presented. The transport phenomena and the effects of design and operating conditions on the cold start performance are investigated. During the failed cold start process, the highest current density is initially near the inlet region of the cell, and then it moves downstream, reaching the outlet region eventually. About 40-50% of the total cell current is produced in the inlet region before the overall peak current density is reached. The inlet region of the cell produces most of the heat and results in the quickest temperature increment before the cell current peaks, but also suffers significant heat loss to the surrounding and quick ice formation. The middle region of the cell is favoured by the lowest heat loss rate there to have the longest duration of survivability. Therefore, locally applying more external heating in the inlet and middle regions are more favourable than in the other regions. The evolution of the overall current density distribution over time remains similar during the successful cold start process. The current density is the highest near the flow channel inlets and generally decreases along the flow direction. For both the failed and successful cold start processes, the highest temperature is initially near the inlet region of the cell, and is also in the middle region after the overall peak current density is reached. The ice melting and liquid formation during the successful cold start process have negligible impact on the general current and temperature distributions. The experimental results also show that fluctuations of the cell voltages and current densities occur during the constant voltage start-up processes when the internal ohmic resistance of the tested PEMFC is high. The general distributions of current densities and temperatures during the constant current cold start processes are similar to the constant voltage cold start processes, except that the temperatures at the end of the constant current cold start processes are more evenly distributed due to the increased heat generation rates. The constant voltage condition is confirmed to be superior to the constant current condition, and increasing the start-up current density is also confirmed to be favourable. The cold start characteristics are mainly dominated by the cathode flow, and changing the flow arrangement has insignificant impact on the cold start performance. Rather than the cold start failure mode due to the ice blockage in cathode CL, another failure mode due to the ice blockage in flow channel and GDL leading to high pressure drop through cathode flow field is observed at a start-up temperature slightly below the lowest successful start-up temperature. Three ice formation mechanisms are proposed, corresponding to the ice formations in cathode CL, GDL and flow channel. The ice formation in cathode CL is the most common cause of the cold start failure, and the significant ice formations in cathode flow channel and GDL only occur in narrow temperature ranges when the temperature in cathode CL is higher than the freezing point of water but the temperature in the flow channel or GDL is lower. The ice formations in cathode GDL and flow channel often occur together since GDL and flow channel are next to each other. However, the ice formation in cathode CL seems to occur without noticeable ice formations in cathode GDL and flow channel.

Chapter 5

Model Development

A comprehensive PEMFC model needs to consider the transport of the multi-component gas species, transport of the multi-water phases, water phase change processes, electrochemical reaction kinetics, transport of the electron and proton, and heat generation and transfer. These transport phenomena occur in void volumes, porous media and/or solid materials. With the currently available computational power, the continuum macroscopic approach by considering the homogeneous materials of the GDL, CL and membrane with modelled effective transport properties, and simplified phase transitions and electrochemical reaction kinetics is perhaps the only way to model these transport phenomena in the major cell components simultaneously [4]. In considering the cold start processes, more complicated phase change processes involving the freezing and melting of water need to be modelled. The continuum macroscopic approach solves a set of conservation equations, with each equation describing one transport phenomenon. These conservation equations are either solved in the whole or part of the computational domain.

In this chapter, the cold start model developed in this research is presented. Firstly, the physical problem with the computational domain is described. Then, the state of water in each cell component is described, because five of the conservation equations are to describe the transport of different water phases. After that, the assumptions that are necessary for the simplification of the model are provided, followed by the conservation equations, boundary and initial conditions, numerical procedures and comparison with experimental data. Finally, a short summary is given.

5.1 Physical Problem

Figure 5.1 shows the sample computational domain and mesh for the cold start model. All the major components of a PEMFC are considered, including the BP, single straight flow channel, GDL, CL and membrane. Hydrogen and air are supplied to the anode and cathode flow channel inlets, respectively. A set of conservation equations, with each equation describing one transport phenomenon, are either solved in the whole or part of the computational domain. The detailed formulation of the present cold start model is presented in section 5.3.

5.2 State of Water

Due to the differences in the materials and the local operating conditions among the different components of PEMFC, water can present in different forms with different phase change processes. Figure 5.2 shows the schematics of a single PEMFC with the structure of each cell component illustrated for both the normal operating condition and cold start, and the schematics of water phase change is given in Figure 5.3. As shown in Figures 5.2a and 5.3 for the normal operating condition (cell temperature generally ranges from 60 to 80 ^{o}C), water exists in forms of vapour and liquid in the flow channel and pore regions of GDL and CL, the ionomer (polymer electrolyte) of the membrane and CL also absorbs certain quantities of water in liquid state or bound to H^+ (e.g. H_3O^+). As shown in Figures 5.2b and 5.3 for the cold start, the formation of liquid water can be almost neglected since it freezes to ice (note that ice and liquid water may still co-exist when the local cell temperature

increases or decreases to the freezing point of water, resulting in ice melting or liquid freezing). Therefore, water usually exists in forms vapour and ice in the pore regions of GDL and CL. Since the ice formed can easily stick on the solid materials of CL and GDL, the ice formation in flow channel might be neglected. Figures 5.2b and 5.3 also show that the water in the ionomer of the membrane and CL may also freeze at subzero temperatures. Apparently, the different water phases must be classified systematically for the modelling studies. Table 5.1 shows the classification of the state of water in each component of PEMFC, and the details are given in the following subsections.

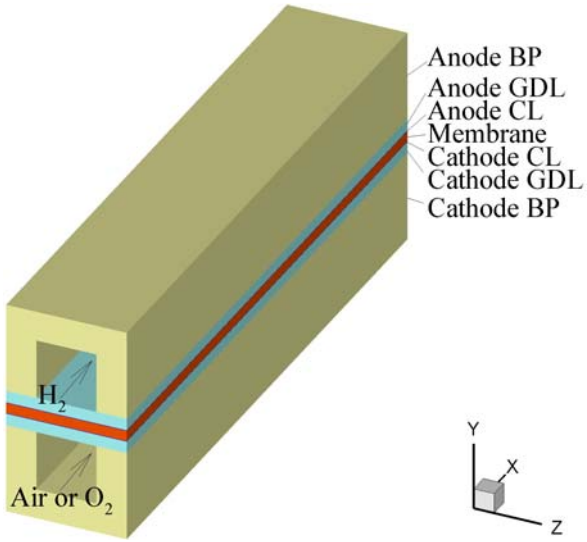

(a)

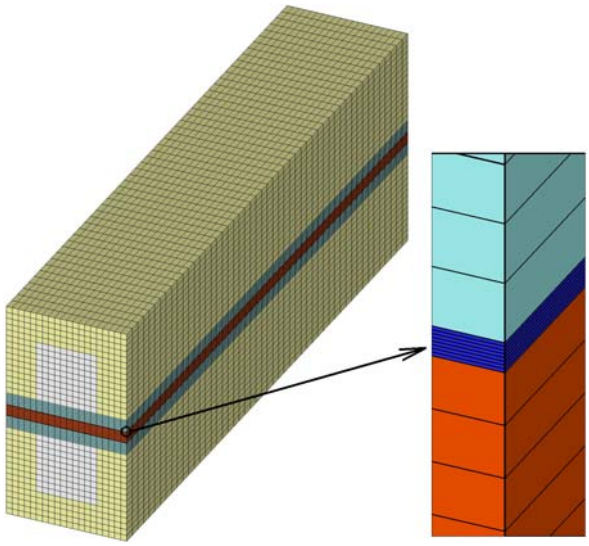

(b)

Figure 5.1: Sample (a) computational domain and (b) mesh.

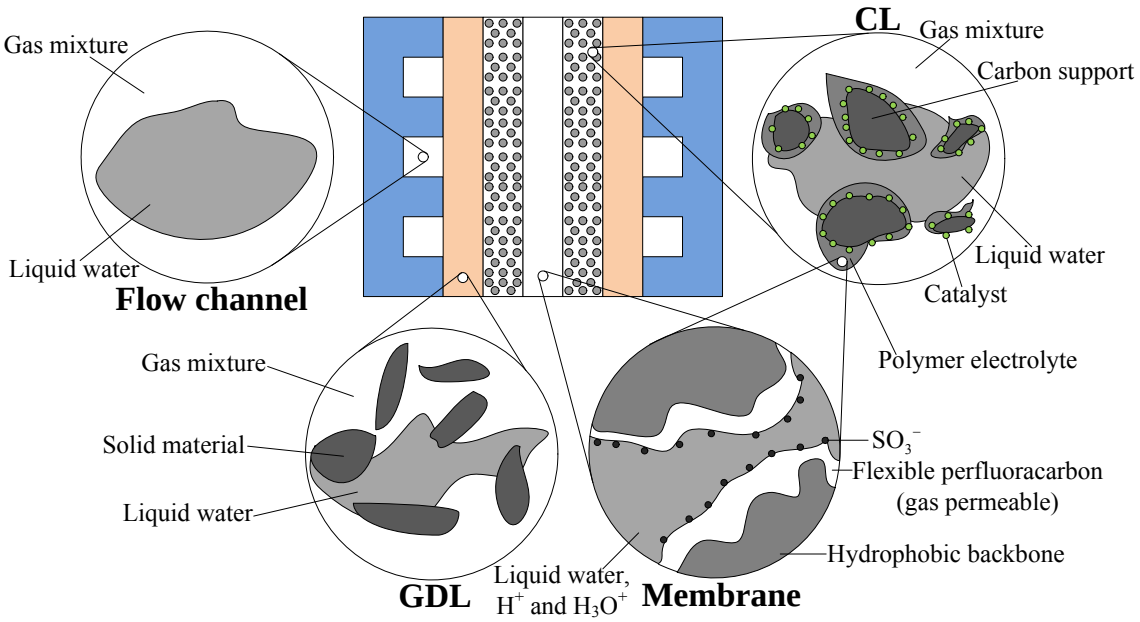

(a)

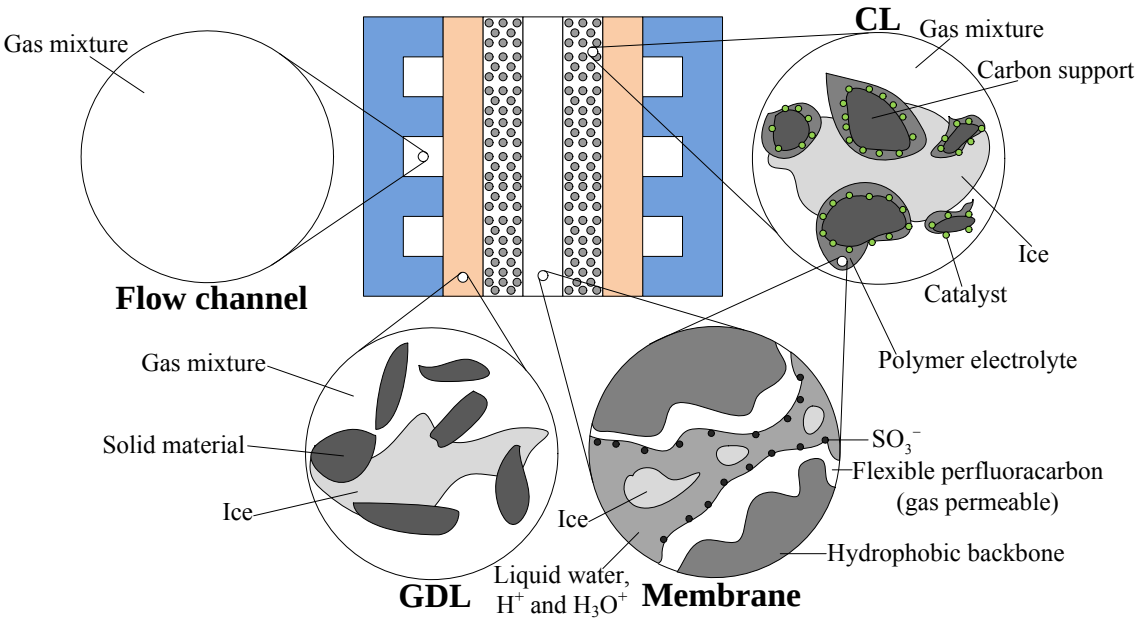

(b)

Figure 5.2: Schematics of a single PEMFC with the structure of each cell component illustrated. (a: normal operating condition; b: cold start)

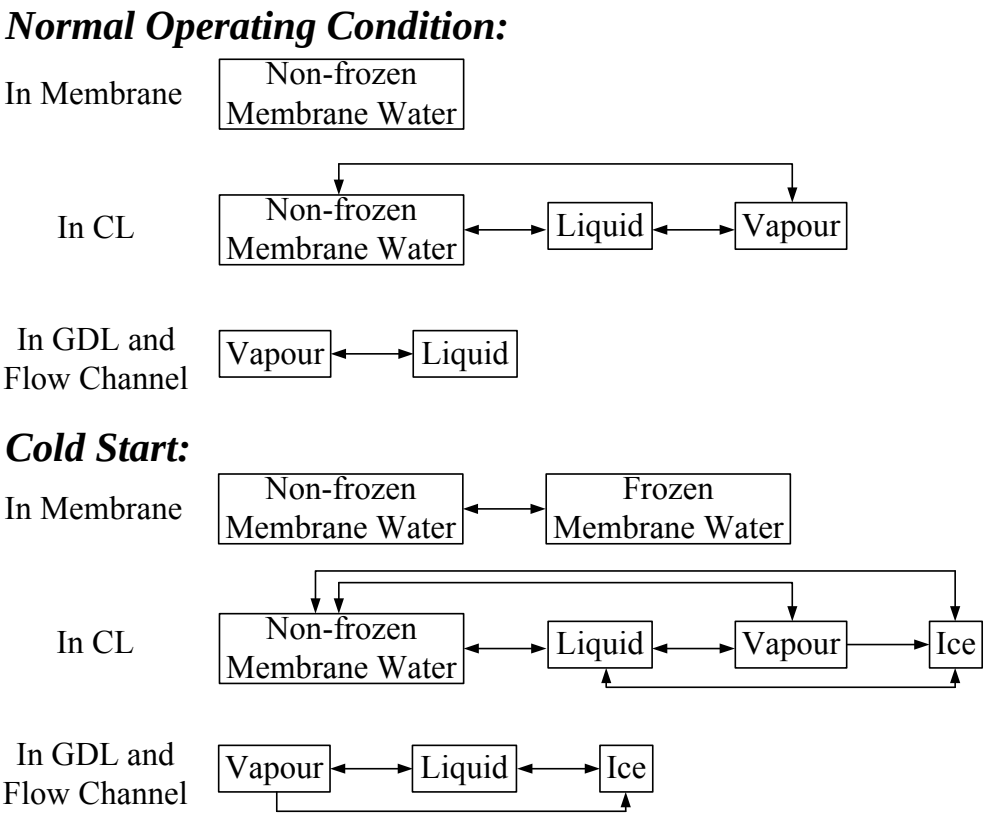

Figure 5.3: Schematics of water phase change in different components of PEMFC for both normal operating condition and cold start.

Table 5.1: State of water in each component of PEMFC. (*only presents at subzero temperatures)

Cell component	Location/material	State of water
Membrane	Ionomer	Free, Freezable, Non-freezable (the free and freezable water are all possible to freeze at subzero temperatures)
GDL	Pore region	Vapour, Liquid, Ice*
CL	Pore region	Vapour, Liquid, Ice*
	Ionomer	Free, Freezable, Non-freezable (the free and freezable water are all possible to freeze at subzero temperatures)
Flow channel	Everywhere	Vapour, Liquid, Ice* (the ice formation might be neglected)

5.2.1 In Membrane

As shown in Figure 5.2, the ionomer of the membrane and CL consists of hydrophobic backbones, flexible perfluorocarbons (gas permeable), and hydrophilic clusters with $H^+SO_3^-$ (the region in the middle of the ionomer structure demonstrated in Figure 5.2). The SO_3^- are bound to the material structures and difficult to move, and there is an attraction between the H^+ and SO_3^- for each $H^+SO_3^-$. The hydrophilic clusters with $H^+SO_3^-$ can absorb large quantities of water to form hydrated hydrophilic regions. In the hydrated hydrophilic regions, the H^+ are relatively weakly attracted to the SO_3^- and can move more easily. The hydrated hydrophilic regions can be considered as dilute acids, explaining why the membrane needs to be well hydrated for appreciable proton conductivity. The water absorption level of ionomer is often represented as the number of water molecules per SO_3^-, referred to as the water content (λ). In a well hydrated Nafion membrane, there will be about 20 water molecules for each SO_3^-, and the proton conductivity can reach higher than 10 S m^{-1}. The size of the hydrophilic region that can contain water is on the level of nanometer. The water concentration (c_{H_2O}, kmol m^{-3}) inside the ionomer of the membrane and CL can be correlated with the water content (λ):

$$\lambda = \frac{EW}{\rho_{mem}} c_{H_2O} \tag{5.1}$$

where ρ_{mem} (kg m^{-3}) is the density of dry membrane (ionomer), and EW (kg kmol^{-1}) the equivalent weight represented by the dry mass of the membrane (ionomer) over the number of moles of SO_3^-.

In considering all the operating conditions (normal and cold start), in the hydrophilic regions, the liquid water, water bound to H^+ (e.g. H_3O^+) and ice are all possible to present. The water in the ionomer can be classified into the non-frozen water and frozen water, which is based on the observations of the freezing behaviour of water by differential scanning calorimetry (DSC) and nuclear magnetic resonance (NMR) [48-50, 105, 106]. DSC was used to determine the amounts of the different types of water, and the maximum allowed amount of non-frozen water in Nafion membrane at different subzero temperatures was reported to be about 4.8 water content [50]. The non-frozen water can be further classified into the non-freezable, freezable and free water [107-109], based on how tightly they are bound to the sulphuric acids ($H^+SO_3^-$). The non-freezable water is mostly tightly bound to the $H^+SO_3^-$, and its maximum allowed amount is about 4.8 [50]. The freezable water is loosely bound to the $H^+SO_3^-$ and exhibits freezing point depressions, which has been observed in [48-50, 105, 106]. The free water may also appear if the water content is sufficiently high, confirming the observations that the water freezes in the ionomer at the temperatures close to the normal freezing temperature of water (0 ^{o}C) if the water content is high [48-50, 105, 106]. An empirical correlation to calculate the maximum allowed amount of non-frozen water content is developed based on the experimental measurement in [50]:

$$\lambda_{sat} \begin{cases} = 4.837 & \text{if } T < 223.15 \text{ K} \\ = \left[-1.304 + 0.01479T - 3.594 \times 10^{-5} T^2 \right]^{-1} & \text{if } 223.15 \text{ K} \le T < T_N \\ > \lambda_{nf} & \text{if } T \ge T_N \end{cases} \tag{5.2}$$

where λ_{sat} and λ_{nf} are the saturation (maximum allowed non-frozen water content) and non-frozen water content; and T (K) and T_N (K) are the local temperature and normal freezing temperature of water (273.15 K), respectively. It should be noticed that no further water phase change was detected when the temperature was lower than -50 ^{o}C, and the saturation water content remained at about 4.8 [50]. This amount of water content corresponds to the non-freezable water. For the temperature range from -50 to 0 ^{o}C (223.15 to 273.15 K), the maximum allowed amount of non-frozen water increases with the increment of temperature. Moreover, the water in the ionomer does not freeze if the temperature is higher than the normal freezing temperature of water ($T \geq T_N$), therefore the saturation water content is always higher than the non-frozen water content in the ionomer in this temperature range. The difference between the maximum allowed water content and the local non-frozen water content can be considered as the driving force for the water phase change in the ionomer, i.e. if λ_{nf} is larger than λ_{sat}, the water will freeze until the local equilibrium state is reached ($\lambda_{nf} = \lambda_{sat}$). It was also reported that the freezing of water in the ionomer decreases the proton conductivity, suggesting that the frozen water does not contribute to the proton transport [50].

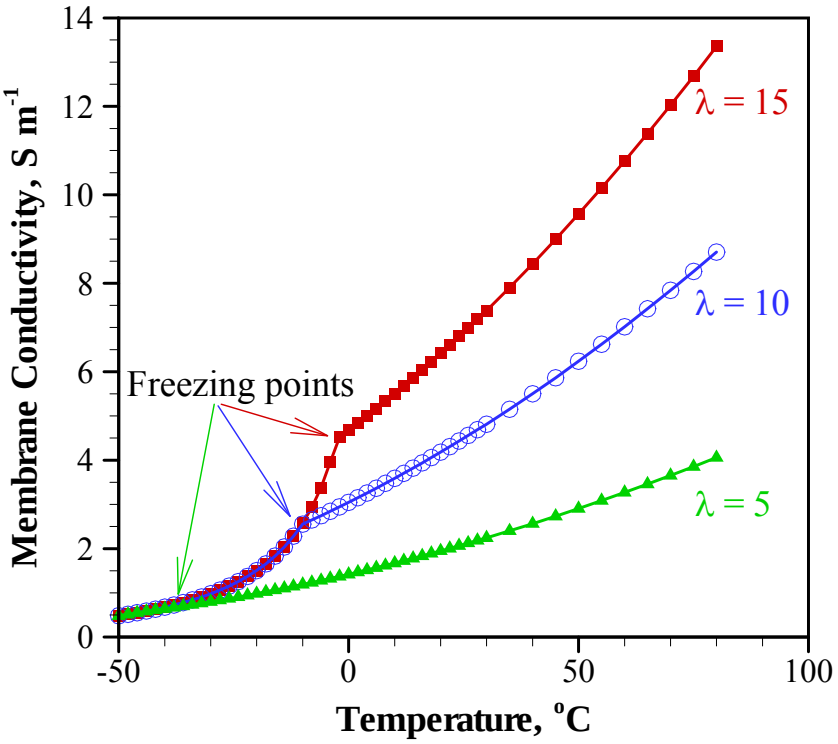

Figure 5.4: Effects of water freezing on proton conductivity of Nafion ionomer.

The proton conductivity of Nafion ionomer is usually calculated based on the correlation reported in [51], and in considering the non-frozen water content rather than the total water content, the correlation becomes

$$\kappa_{ion} = (0.5139\lambda_{nf} - 0.326)\exp\left[1268\left(\frac{1}{303.15} - \frac{1}{T}\right)\right] \tag{5.3}$$

where κ_{ion} (S m^{-1}) is the proton conductivity, and T (K) the temperature. It should be noticed that Equation 5.3 was originally correlated based on the experimental measurements between 30 and 80 ^{o}C, and the original equation overestimates the proton conductivity at subzero temperatures (sharper decrements of the proton conductivity were observed [48-50]). However, by considering the water freezing at subzero temperatures, Equation 5.3 with the non-frozen membrane water content rather than the total membrane water content provides a more reasonable agreement with the experimental measurement in [50]. Figure 5.4 shows the changes of the proton conductivity at different total membrane water contents, it can be observed that the proton conductivity starts dropping more quickly when the membrane water starts freezing.

5.2.2 In Gas Diffusion Layer (GDL)

The GDL material is usually carbon paper or carbon cloth, and the porosity is around or higher than 0.5. Water can exist in the pore regions of GDL in forms of vapour, liquid and ice. As shown in Figures 5.2a and 5.3 under the normal operating condition, the water exists in forms of vapour and liquid, and the condensation and evaporation occur depending on the local operating condition. A water phase change diagram is shown in Figure 5.5 with the melting, boiling and triple points. Under the typical opreationg pressures of PEMFC (1 to several atm), the melting point of water is around 0 ^{o}C. For the cold start as presented in Figures 5.2b and 5.3, the formation of liquid water can be almost neglected since it freezes to ice, and it should be noticed that the ice and liquid water may still co-exist when the local cell temperature increases or decreases to the freezing point of water, resulting in ice melting or liquid freezing. Therefore, the water usually exists in forms vapour and ice in the pore regions of GDL during the cold start processes. The pressure inside PEMFC is usually between 1 to several atm, and the freezing point of water in this pressure range can be treated as almost constant (0 ^{o}C). Because the operating pressure of PEMFC is always equal to or greater than the atmospheric pressure, the sublimation process (phase change from ice directly to vapour) can be safely neglected. The difference between the local temperature and the freezing temperature of water indicates the phase change direction between liquid and ice: ice will melt to liquid if the local temperature is higher than the freezing point, and vice versa. The difference between the water saturation pressure and vapour pressure indicate the phase change direction between vapour and liquid (above the freezing point), and between vapour and ice (below the freezing point). When the local temperature is above the freezing point, if the vapour pressure is higher than the saturation pressure, vapour will condense to liquid, otherwise liquid will evaporate to vapour; when the local temperature is below the freezing point, if the vapour pressure is higher than the saturation pressure, vapour will desublimate to ice, however, as mentioned earlier that ice will not sublimate to vapour under the operating conditions in PEMFC even when the vapour pressure is lower than the saturation pressure. By checking the experimental data tabulated in [110], it is found that the correlation provided by Springer et al. [51] provides acceptable agreement with the experimental data in the temperature range from -50 to 100 ^{o}C:

$$\log_{10}\left(p_{sat}/101325\right) = -2.1794 + 0.02953(T-273.15) - 9.1837\times10^{-5}(T-273.15)^{2} + 1.4454\times10^{-7}(T-273.15)^{3} \tag{5.4}$$

where p_{sat} (Pa) is the saturation pressure of water, and T (K) the temperature.

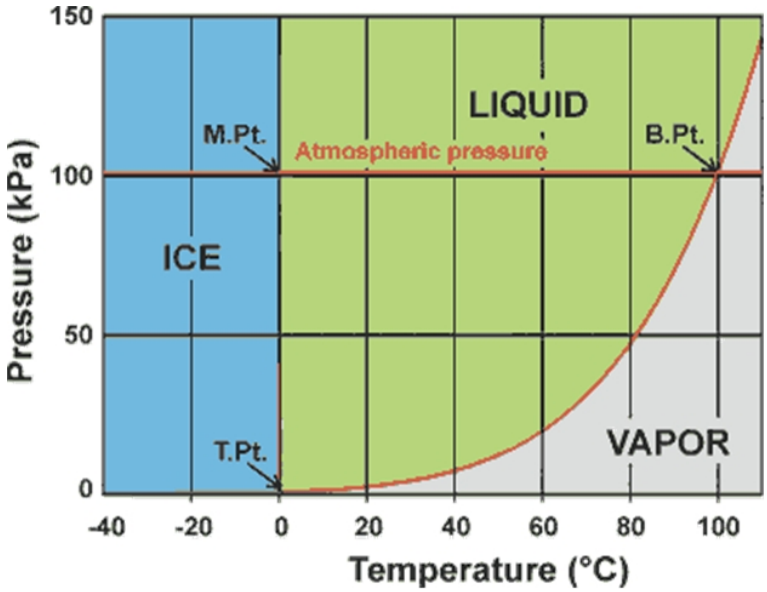

Figure 5.5: Phase diagram of water showing the melting (M.Pt.), boiling (B.Pt.) and triple (T.Pt) points [111].

5.2.3 In Catalyst Layer (CL)

The most complex scenario occurs in the CL. As shown in Figure 5.2, the carbon and platinum particles together with part of the ionomer (polymer electrolyte) have to mix together to form the reaction sites. The carbon and platinum particles have to present as the catalyst and for the electron transport, and the ionomer has to present for the proton transport. The state of water in the pore regions of CL is the same as in the pore regions of GDL. The water in the ionomer of CL is also the same as in the membrane. It should be mentioned that due to the presence of the small pores in the CL (on the level of nanometer), the surface dynamics of water is enhanced, and the freezing point of water can be depressed to about -1 ^{o}C in such small pores [46-48].

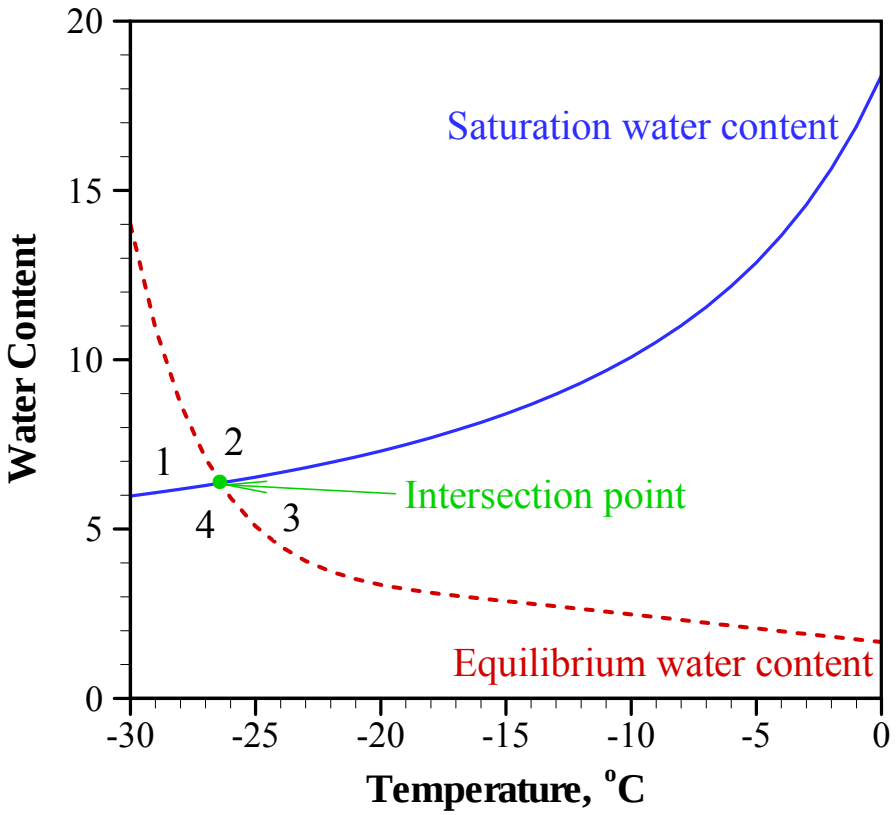

Figure 5.6: Temperature dependence of the equilibrium water content (λ_{equil}) for the phase change between the non-frozen water in the ionomer of CL and the vapour in the pores of CL, and the saturation water content (λ_{sat}) for the phase change between the non-frozen water in the ionomer and the ice in the pores of CL or the frozen water in the membrane layer for the temperature range from -30 to 0 ^{o}C. (note that in the calculation of equilibrium water content shown in this figure, the vapour amount in the pores of CL is assumed to be equivalent to a water activity of 1 at -30 ^{o}C and liquid water is not considered because it freezes to ice at subzero temperatures; also note that the two lines, equilibrium water content and saturation water content, separate this figure into four regions as marked in the figure, and for the non-frozen water content in the ionomer (λ_{nf}) falling in these different regions, the water phase change processes are different, as detailed in Table 5.2)

Table 5.2: Water phase change processes that involve the ionomer in CL for the non-frozen water content in the ionomer (λ_{nf}) in the different regions and on the different dividing lines of Figure 5.6.

For the non-frozen water content in the different regions of Figure 6	Phase change between the non-frozen water in the ionomer and the vapour in the pores	The non-frozen water in the ionomer freezing to the ice in the pores
In Region 1	Occur	Occur
In Region 2	Occur	Occur
In Region 3	Occur	Stop
In Region 4	Occur	Stop
On the line between Regions 1 and 2	Stop	Occur
On the line between Regions 2 and 3	Occur	Stop
On the line between Regions 3 and 4	Stop	Stop
On the line between Regions 4 and 1	Occur	Stop
At the intersection point	Stop	Stop

In the CL and at the interface between the CL and membrane, both the liquid water and vapour can be absorbed or desorbed by the ionomer from or to the pore regions of CL. The non-frozen membrane water, liquid or vapour can freeze or desublimate to ice, as shown in Figure 5.3. The different water phase change processes can occur simultaneously or separately. It should be noticed that the ice in CL in Figure 5.3 represents the ice in both the ionomer and pore regions. To simplify the phase change processes, one assumption made in this cold start model is that when the water in the ionomer of CL freezes, it leaves the ionomer and only forms ice in the pore regions of CL, based on the experimental observation that the frozen water does not contribute to the proton transport in ionomer [50]. Equation 5.2 can be used to determine whether the water in the ionomer freezes to ice or not (if the non-frozen water content is higher than the saturation water content, it will freeze). The equation first used in [51] can be used to indicate the mass transfer (phase change) direction between the water in the ionomer and the vapour/liquid in the pore regions:

$$\lambda_{equil} = \begin{cases} 0.043 + 17.81a - 39.85a^2 + 36.0a^3 & \text{if } 0 \le a \le 1 \\ 14.0 + 1.4(a-1) & \text{if } 1 < a \le 3 \end{cases} \tag{5.5}$$

where λ_{equil} is the equilibrium water content (the water content in the ionomer corresponding to the amount of the surrounding water), and a the water activity in the pore regions, defined as

$$a = \frac{X_{vp} p_g}{p_{sat}} + 2s_{lq} \tag{5.6}$$

where X_{vp} is the mole fraction of water vapour in the pore regions, p_g (Pa) the pressure of the gas mixture in the pore regions, p_{sat} (Pa) the water saturation pressure, and s_{lq} the liquid water volume fraction in the pore regions.

Non-humidified gases are often supplied during the cold start processes to reduce the ice formation. Therefore, even at the temperatures above the freezing point, the presence of liquid water may still be neglected. Based on this premise, a further assumption to simplify the water phase change processes between the non-frozen membrane water and vapour/liquid is made in this cold start model. It is assumed that only the phase change between the non-frozen membrane water and vapour occurs when non-humidified inlet gases are supplied; only the phase change between the non-frozen membrane water and liquid occurs in cathode CL with fully humidified inlet gases; and only the phase change between the non-frozen membrane water and vapour occurs in anode CL no matter the inlet gases are humidified or not, due to the fact that water is not produced in anode and the electro-osmotic drag (EOD) effect dries out the anode.

Based on the assumption mentioned above, Figure 5.6 shows the temperature dependence of the equilibrium water content (λ_{equil}) for the phase change between the non-frozen water in the ionomer of CL and the vapour in the pores of CL, and the saturation water content (λ_{sat}) for the phase change between the non-frozen water in the ionomer and the ice in the pores of CL or the frozen water in the membrane layer for the temperature range from -30 to 0 ^{o}C. Note that in the calculation of the equilibrium water content shown in this figure, the vapour amount in the pores of CL is assumed to be equivalent to a water activity of 1 at -30 ^{o}C and liquid water is not considered because it freezes to ice at subzero temperatures. In Figure 5.6, the equilibrium water content decreases monotonically with the temperature, because the vapour amount in the pores of CL has been assumed to be saturated at -30 ^{o}C. Correspondingly, the vapour becomes more and more unsaturated as the temperature is increased, leading to the decrease in the equilibrium water content. On the other hand, the saturation water content increases monotonically with the temperature since more non-frozen water can be maintained in the ionomer to avoid freezing. The two curves in Figure 5.6 divide the figure into four regions, and for the non-frozen water content in the different regions and on the different dividing lines, the two water phase change processes (from the non-frozen membrane water to ice, and between the non-frozen membrane water and vapour) can either occur or stop simultaneously, or one process can also occur when the other stops, as illustrated in Table 5.2. The principal driving forces for these water phase change processes in the CL are the differences between the non-frozen water content in the ionomer and the equilibrium water content, and between the non-frozen water content and the saturation water content.

5.2.4 In Flow Channel

The state of water in the flow channel is similar to as in the GDL. As shown in Figures 5.2 and 5.3, for the normal operating condition, liquid water and vapour can co-exist, and the condensation and evaporation can occur based on the difference between the vapour and saturation pressures; and for the cold start, since water usually freezes in the CL and GDL first and stick on the solid materials that is difficult to move, and non-humidified gases are often supplied for PEMFC cold start to reduce the amount of ice formation, therefore the chance of ice formation in the flow channel is much lower than in the CL and GDL.

5.3 Assumptions

Without losing the generic physical characteristics of a PEMFC, the following assumptions are made for this cold start model:

1. the gravity effect is neglected;
2. the reactant gases are ideal gases;
3. the flow is laminar in the flow channel and pores of GDL and CL;
4. only hydrogen, oxygen, water vapour and nitrogen are considered as the gas species, therefore there is no contaminating gases;
5. the membrane is impermeable to all the gas species;
6. the liquid water in the flow channel is neglected, because it can be instantaneously removed by the gas flow in the single straight flow channels considered in this model;
7. the sublimation of ice to vapour is neglected;
8. the ice in the pores of GDL and CL and the frozen water in the membrane stick on the solid materials and do not move;
9. the frozen water in the membrane does not contribute to the proton transport;
10. the presence of ice in the flow channel is neglected;
11. the phase change between the non-frozen membrane water and liquid is ignored in the anode and cathode CLs when non-humidified inlet gases are supplied, the phase change between the non-frozen membrane water and vapour is ignored in the cathode CL with fully humidified inlet gases, and the phase change between the non-frozen membrane water and liquid is ignored in the anode CL no matter the inlet gases are humidified or not.

The assumptions 1-10 can be easily justified. The assumption 11 and some of the water transport related assumptions listed above are also justified in section 5.2. With these assumptions, the schematics of water phase change presented in Figure 5.3 can be simplified in this model, as shown in Figure 5.7.

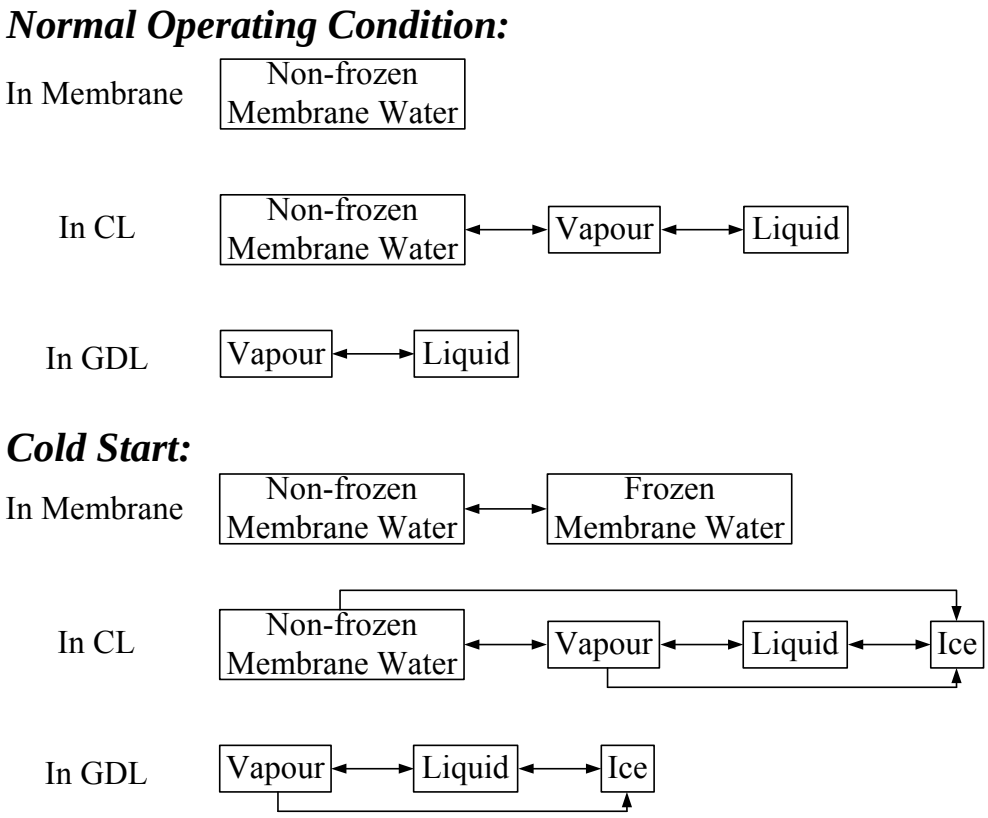

Figure 5.7: Schematics of water phase change considered in the cold start model in different components of PEMFC for both normal operating condition and cold start.

5.4 Conservation Equations

The sample computational domain and mesh for the cold start model are shown in Figure 5.1. As mentioned earlier, all the major components of a PEMFC are considered, including the BP, single straight flow channel, GDL, CL and membrane. Fourteen conservation equations are formulated and solved simultaneously in different layers of the computational domain:

Mass of gas mixture in the flow channel, GDL and CL:

$$\frac{\partial}{\partial t}\left(\varepsilon\left(1-s_{lq}-s_{ice}\right)\rho_g\right)+\nabla\cdot\left(\rho_g\vec{u}_g\right)=S_m \tag{5.7}$$

Momentum of gas mixture in the flow channel, GDL and CL:

$$\begin{aligned}&\frac{\partial}{\partial t}\left(\frac{\rho_g\vec{u}_g}{\varepsilon\left(1-s_{lq}-s_{ice}\right)}\right)+\nabla\cdot\left(\frac{\rho_g\vec{u}_g\vec{u}_g}{\varepsilon^2\left(1-s_{lq}-s_{ice}\right)^2}\right)=-\nabla p_g\\&+\mu_g\nabla\cdot\left(\nabla\left(\frac{\vec{u}_g}{\varepsilon\left(1-s_{lq}-s_{ice}\right)}\right)+\nabla\left(\frac{\vec{u}_g^{\,T}}{\varepsilon\left(1-s_{lq}-s_{ice}\right)}\right)\right)-\frac{2}{3}\mu_g\nabla\left(\nabla\cdot\left(\frac{\vec{u}_g}{\varepsilon\left(1-s_{lq}-s_{ice}\right)}\right)\right)+S_u\end{aligned} \tag{5.8}$$

Mass of gas species (i : hydrogen, oxygen or water vapour) in the flow channel, GDL and CL:

$$\frac{\partial}{\partial t}\left(\varepsilon\left(1-s_{lq}-s_{ice}\right)\rho_g Y_i\right)+\nabla\cdot\left(\rho_g\vec{u}_g Y_i\right)=\nabla\cdot\left(\rho_g D_i^{eff}\nabla Y_i\right)+S_i \tag{5.9}$$

Mass of liquid water in the GDL and CL:

$$\frac{\partial\left(\varepsilon s_{lq}\rho_{lq}\right)}{\partial t}+\nabla\cdot\left(\frac{K_{lq}\mu_g}{K_g\mu_{lq}}\rho_{lq}\vec{u}_g\right)=\nabla\cdot\left(\rho_{lq}D_{lq}\nabla s_{lq}\right)+S_{lq} \tag{5.10}$$

Mass of ice in the GDL and CL:

$$\frac{\partial\left(\varepsilon s_{ice}\rho_{ice}\right)}{\partial t}=S_{ice} \tag{5.11}$$

Non-frozen membrane water in the CL and membrane:

$$\frac{\rho_{mem}}{EW}\frac{\partial\left(\omega\lambda_{nf}\right)}{\partial t}=\frac{\rho_{mem}}{EW}\nabla\cdot\left(\omega^{1.5}D_{nmw}\nabla\lambda_{nf}\right)+S_{nmw} \tag{5.12}$$

Frozen membrane water in the membrane:

$$\frac{\rho_{mem}}{EW}\frac{\partial\left(\omega\lambda_f\right)}{\partial t}=S_{fmw} \tag{5.13}$$

Electronic potential in the BP, GDL and CL:

$$0=\nabla\cdot\left(\kappa_{ele}^{eff}\nabla\phi_{ele}\right)+S_{ele} \tag{5.14}$$

Ionic potential in the CL and membrane:

$$0=\nabla\cdot\left(\kappa_{ion}^{eff}\nabla\phi_{ion}\right)+S_{ion} \tag{5.15}$$

Energy in the whole computional domain:

$$\frac{\partial}{\partial t}\left(\left(\rho C_p\right)_{fl,sl}^{eff}T\right)+\nabla\cdot\left(\left(\rho C_p\right)_{fl}^{eff}\vec{u}_g T\right)=\nabla\cdot\left(k_{fl,sl}^{eff}\nabla T\right)+S_T \tag{5.16}$$

Table 5.3: Source terms.

Source term	Unit
$S_m = S_{H_2} + S_{O_2} + S_{vp}$	kg m^{-3} s^{-1}
$S_u = \begin{cases} -\dfrac{\mu_g}{K_g}\vec{u}_g & \text{(in CL and GDL)} \\ 0 & \text{(in other zones)} \end{cases}$	kg m^{-2} s^{-2}
$S_{H_2} = \begin{cases} -\dfrac{j_a}{2F}M_{H_2} & \text{(in anode CL)} \\ 0 & \text{(in other zones)} \end{cases}$ $\quad S_{O_2} = \begin{cases} -\dfrac{j_c}{4F}M_{O_2} & \text{(in cathode CL)} \\ 0 & \text{(in other zones)} \end{cases}$	kg m^{-3} s^{-1}
$S_{vp} = \begin{cases} -S_{v-l} - S_{v-i} + S_{n-v}\mathrm{M}_{\mathrm{H_2O}} & \text{(in CL)} \\ -S_{v-l} - S_{v-i} & \text{(in other zones)} \end{cases}$	kg m^{-3} s^{-1}
$S_{lq} = S_{v-l} - S_{l-i}$ $\quad S_{ice} = \begin{cases} S_{v-i} + S_{l-i} + S_{n-i}\mathrm{M}_{\mathrm{H_2O}} & \text{(In CL)} \\ S_{v-i} + S_{l-i} & \text{(in other zones)} \end{cases}$	kg m^{-3} s^{-1}
$S_{nmw} = \begin{cases} -S_{n-f} & \text{(in membrane)} \\ \dfrac{j_c}{2F} - S_{n-v} - S_{n-i} + S_{EOD} & \text{(in cathode CL)} \\ -S_{n-v} - S_{n-i} + S_{EOD} & \text{(in anode CL)} \end{cases}$ $\quad S_{fmw} = S_{n-f}$	kmol m^{-3} s^{-1}
$S_{ele} = \begin{cases} -j_a & \text{(in anode CL)} \\ j_c & \text{(in cathode CL)} \\ 0 & \text{(in other zones)} \end{cases}$ $\quad S_{ion} = \begin{cases} j_a & \text{(in anode CL)} \\ -j_c & \text{(in cathode CL)} \\ 0 & \text{(in other zones)} \end{cases}$	A m^{-3}
$S_T = \begin{cases} j_a\lvert\eta_{act}\rvert + \lVert\nabla\phi_{ele}\rVert^2\kappa_{ele}^{eff} + \lVert\nabla\phi_{ion}\rVert^2\kappa_{ion}^{eff} + S_{pc} & \text{(in anode CL)} \\ -\dfrac{j_c T\Delta S}{2F} + j_c\lvert\eta_{act}\rvert + \lVert\nabla\phi_{ele}\rVert^2\kappa_{ele}^{eff} + \lVert\nabla\phi_{ion}\rVert^2\kappa_{ion}^{eff} + S_{pc} & \text{(in cathode CL)} \\ \lVert\nabla\phi_{ele}\rVert^2\kappa_{ele}^{eff} + S_{pc} & \text{(in GDL)} \\ \lVert\nabla\phi_{ele}\rVert^2\kappa_{ele}^{eff} & \text{(in BP)} \\ \lVert\nabla\phi_{ion}\rVert^2\kappa_{ion}^{eff} + S_{pc} & \text{(in membrane)} \\ 0 & \text{(in other zones)} \end{cases}$	W m^{-3}

Table 5.4: Transport properties [4, 65, 110, 114].

Parameter	Correlation / Value (T in K, p in Pa)	Unit
Hydrogen dynamic viscosity	$\mu_{H_2} = 3.205\times10^{-3}(T/293.85)^{1.5}(T+72)^{-1.0}$	kg m^{-1} s^{-1}
Oxygen dynamic viscosity	$\mu_{O_2} = 8.46\times10^{-3}(T/292.25)^{1.5}(T+127)^{-1.0}$	kg m^{-1} s^{-1}
Water vapour dynamic viscosity	$\mu_{vp} = 7.512\times10^{-3}(T/291.15)^{1.5}(T+120)^{-1.0}$	kg m^{-1} s^{-1}
Hydrogen and water vapour diffusivities in anode	$D^a_{H_2} = D^a_{vp} = 1.055\times10^{-4}(T/333.15)^{1.5}(101325/p)$	m^2 s^{-1}
Oxygen diffusivity in cathode	$D^c_{O_2} = 2.652\times10^{-5}(T/333.15)^{1.5}(101325/p)$	m^2 s^{-1}
Water vapour diffusivity in cathode	$D^c_{vp} = 2.982\times10^{-5}(T/333.15)^{1.5}(101325/p)$	m^2 s^{-1}
Liquid water dynamic viscosity	$\mu_{lq} = 2.414\times10^{-5}\times10^{\frac{247.8}{T-140}}$	kg m^{-1} s^{-1}
Liquid water and ice densities	$\rho_{lq} = 990 \quad \rho_{ice} = 920$	kg m^{-3}
Evaporation, condensation, desublimation, fusion, melting rates	$\gamma_{evap,cond,desb,fusn,melt} = 1.0$	s^{-1}
Water phase change rates	$\zeta_{n-v,v-n,n-i,n-f,f-n} = 1.0$	s^{-1}
Latent heat of fusion	$h_{fusn} = 3.336\times10^5$	J kg^{-1}
Specific heat capacities of different gas species, liquid water, and ice	$(C_p)_{H_2} = 14283 \quad (C_p)_{O_2} = 919.31$ $(C_p)_{vp} = 2014 \quad (C_p)_{lq} = 4182 \quad (C_p)_{ice} = 2050$	J kg^{-1} K^{-1}
Thermal conductivities of different gas species, liquid water, and ice	$k_{H_2} = 0.1672 \quad k_{O_2} = 0.0246$ $k_{vp} = 0.0261 \quad k_{lq} = 0.6 \quad k_{ice} = 2.3$	W m^{-1} K^{-1}
Entropy change of reaction	$\Delta S = -163110$	J kmol^{-1} K^{-1}

As shown above, the conservation equations include the conservation of the mass of the gas mixture, momentum of the gas mixture, masses of the gas species, mass of the liquid water, mass of the ice, non-frozen membrane water, frozen membrane water, electronic potential, ionic potential, and energy. The gas mixture mass and momentum conservation equations (Equations 5.7 and 5.8) and the gas species conservation equations (Equation 5.9) are the standard conservation equations with porous formulation [112]. The volume fractions of the solid materials of the GDL and CL and the liquid water and ice are all accounted for to calculate the effective porosity of the gas mixture. These equations are solved in the flow channel, GDL and CL. The liquid water conservation equation (Equation 5.10) was derived based on the capillary pressure in porous media [113], and it is solved in the GDL and CL. The ice conservation equation (Equation 5.11) only consists of a transient term and

a source term. The convection and diffusion terms can be neglected because the ice sticks on the solid materials of the GDL and CL and cannot move. This equation is solved in the GDL and CL. The non-frozen water conservation equation (Equation 5.12) consists of transient, diffusion and source terms, and the convection term can be safely neglected because the convective mass transfer is negligible [1, 4]. This equation is solved in the CL and membrane. Similar to the ice conservation equation, the frozen membrane water conservation equation (Equation 5.13) also only consists of a transient term and a source term, and it is solved in the membrane. The electronic and ionic potentials conservation equations (Equations 5.14 and 5.15) only consist of a diffusion (conduction) term and a source term. The transient terms are neglected due to the fast electrochemical double layer charging and discharging [4]. The energy conservation equation (Equation 5.16) takes into account all the transport properties, including the solid, liquid and gaseous phases. The corresponding source terms of the conservation equations are given in Table 5.3. In addition, the related transport properties are listed in Table 5.4.

5.4.1 Gas Transport

In the conservation equations for the gas transport (Equations 5.7-5.9), the effects of the porous regions, liquid water and ice on the gas transport are considered by modifying the gas phase permeability in the momentum equation and effective mass diffusion coefficients in the species transport equations. The gas phase and liquid phase permeabilities (K_g and K_{lq}, respectively, m^2) depend on the intrinsic permeabilities of the porous materials (K_0, m^2) and the local volume fraction of liquid water (usually with an exponent of 4.0) [28, 65]. In this model, by considering that the effects of ice and liquid on the permeabilities are similar, the gas phase and liquid phase permeabilities can be calculated as

$$K_g = K_0 \left(1 - s_{lq} - s_{ice}\right)^{4.0} \tag{5.17}$$

$$K_{lq} = K_0 s_{lq}^{4.0} \left(1 - s_{ice}\right)^{4.0} \tag{5.18}$$

where both the liquid and ice volume fractions (s_{lq} and s_{ice}) are considered. Equation 5.17 depicts that if the local pore volume of the GDL or CL is full of liquid water and ice, the gas phase permeability will become zero, resulting in an infinite negative value for the momentum source term (Table 5.3). Similarly, Equation 5.18 represents that if the local pore volume of the GDL or CL is full of ice, the liquid phase permeability will also become zero.

The gas mixture density (ρ_g, kg m^{-3}) is calculated based on the ideal gas law

$$\rho_g = p_g \left(RT \sum\nolimits_i \frac{Y_i}{M_i} \right)^{-1} \tag{5.19}$$

where p_g is the gas phase pressure (Pa), T the temperature (K), R the universal gas constant (J K^{-1} $kmol^{-1}$), and Y_i and M_i (kg $kmol^{-1}$) the mass fraction and molecular weight of species i. The dynamic viscosity of the ideal gas mixture (μ_g, kg m^{-1} s^{-1}) is calculated based on kinetic theory [114] as

$$\mu_g = \sum_i \frac{X_i \mu_i}{\sum_j X_i \psi_{ij}} \tag{5.20}$$

$$\psi_{ij} = \frac{\left[1 + \left(\mu_i / \mu_j\right)^{0.5} \left(M_i / M_j\right)^{0.25}\right]^{0.5}}{\left[8\left(1 + M_i / M_j\right)\right]^{0.5}} \tag{5.21}$$

where X_i is the mole fraction of species i, and i and j represent different species. Since this model can simulate the PEMFC operation from subzero to normal operating temperatures, the changes of different parameters with temperature must be considered. Table 5.4 shows the correlations of the dynamic viscosity and mass diffusivity of each species with the changes of temperature and pressure based on the correlations and experimental data in [111, 114]. In the GDL and CL, the Bruggemann correlation is used to account for the effects of porosity and tortuosity on the effective mass diffusion coefficients. In some multiphase models (e.g. in [65]), the effect of liquid water on the effective diffusion coefficients is treated the same as the porosity with an exponent of 1.5. In this model, the effect of ice formation is also treated the same as the liquid water, and the diffusion coefficients are corrected by the porosity (ε) and volume fractions of liquid water and ice:

$$D_i^{eff} = D_i \varepsilon^{1.5} \left(1 - s_{lq} - s_{ice}\right)^{1.5} \tag{5.22}$$

where D_i ($m^2\ s^{-1}$) is the mass diffusion coefficient for species i. If the local pore volume of the GDL and CL is full of liquid water and ice, the diffusion coefficient will become zero, reflecting the blockage due to the liquid water and ice.

5.4.2 Water Transport

Based on the densities of liquid water and ice tabulated in [111], it is found that the changes of liquid water and ice densities with temperature are insignificant. Therefore, in this model, the liquid water and ice are considered to have constant densities, and the values are listed in Table 5.4. Since the liquid water dynamic viscosity (μ_{lq}) strongly depends on temperature, a correlation for the temperature dependence is used rather than using a constant value, as shown in Table 5.4. The capillary diffusion coefficient of liquid water (D_{lq}, $m^2\ s^{-1}$) in the GDL and CL is defined by considering the effect of capillary pressure [65, 113]:

$$D_{lq} = -\frac{K_g}{\mu_{lq}} \frac{dp_c}{ds_{lq}} \tag{5.23}$$

where the capillary pressure (p_c, Pa) is calculated as a function of the liquid water volume fraction (the Leverett function) [115, 116] as

$$p_c = \begin{cases} \sigma \cos\theta \left(\dfrac{\varepsilon}{K_0}\right)^{0.5} \left[1.42\left(1 - s_{lq}\right) - 2.12\left(1 - s_{lq}\right)^2 + 1.26\left(1 - s_{lq}\right)^3\right] & \text{if } \theta < 90^o \\ \sigma \cos\theta \left(\dfrac{\varepsilon}{K_0}\right)^{0.5} \left[1.42 s_{lq} - 2.12 s_{lq}^2 + 1.26 s_{lq}^3\right] & \text{if } \theta > 90^o \end{cases} \tag{5.24}$$

where θ is the static contact angle, which depends on the wettabilities of the GDL and CL surfaces. σ (N m^{-1}) is the surface tension coefficient between liquid water and gas mixture. Based on the experimental data tabulated in [111], the following linear correlation is developed to account for the temperature dependence between 273.15 and 373.15 K:

$$\sigma = -0.0001676T + 0.1218;\ 273.15\ \text{K} \le \text{T} \le 373.15K \tag{5.25}$$

where the units of σ and T are N m^{-1} and K, respectively. The liquid phase pressure (p_{lq}, Pa) is calculated based on the capillary pressure (p_c, Pa) and gas phase pressure (p_g, Pa) as [65, 113]

$$p_{lq} = p_g - p_c \tag{5.26}$$

and the liquid phase velocity ($\vec{u}_{lq}$, m s^{-1}) can be calculated based on the liquid phase pressure as

$$\vec{u}_{lq} = -\frac{K_{lq}}{\mu_{lq}} \nabla p_{lq} \tag{5.27}$$

Tables 5.5 and 5.6 show the water phase change functions. The related parameters are given in Table 5.4. The saturation pressure (p_{sat}) is calculated by using Equation 5.4.

The experiments in [43-45] all observed that the fusion and desublimation of water in the CL take place at the temperatures below the normal freezing point of water (273.15 K), which is mainly due to the wettability and extremely small pore size in the CL, known as the Gibbs-Thomson undercooling [117]. The difference between the freezing point in small pores and normal freezing point of water (T_N = 273.15 K) is defined as T_{FPD} (K), and is calculated as

$$T_{FPD} = \frac{T_N \sigma\big|_{273.15K} \cos\theta}{\rho_{ice} h_{fusn} r_{CL,GDL}} \tag{5.28}$$

where h_{fusn} (J kg^{-1}) is the latent heat of fusion as listed in Table 5.4, and $r_{CL,GDL}$ (m) the pore radius of CL or GDL. The units of and σ and ρ_{ice} are N m^{-1} and kg m^3, respectively. T_{FPD} is typically around -1 K in a PEMFC CL.

The diffusion coefficient of non-frozen membrane water (D_{nmw}, m^2 s^{-1}) can be calculated as [118]

$$D_{nmw} = \begin{cases} 3.1\times10^{-7}\lambda_{nf}\left[\exp\left(0.28\lambda_{nf}\right)-1\right]\exp\left(\dfrac{-2346}{T}\right) & \text{if } 0 < \lambda_{nf} < 3 \\ 4.17\times10^{-8}\lambda_{nf}\left[161\exp\left(-\lambda_{nf}\right)+1\right]\exp\left(\dfrac{-2346}{T}\right) & \text{if } 3 \le \lambda_{nf} < 17 \end{cases} \tag{5.29}$$

where the unit of T is K.

Table 5.5: Water phase change functions in pores of CL and GDL.

Phase change function	Unit
Vapour and liquid water:	kg m^{-3} s^{-1}
$S_{v-l} = \begin{cases} \begin{cases} \gamma_{cond}\varepsilon\left(1-s_{lq}-s_{ice}\right)\dfrac{\left(p_g X_{vp}-p_{sat}\right)M_{H_2O}}{RT} & \text{if } p_g X_{vp} \geq p_{sat} \\ \gamma_{evap}\varepsilon s_{lq}\dfrac{\left(p_g X_{vp}-p_{sat}\right)M_{H_2O}}{RT} & \text{if } p_g X_{vp} < p_{sat} \end{cases} & \text{if } T \geq T_N + T_{FPD} \\ 0 & \text{if } T < T_N + T_{FPD} \end{cases}$	
Vapour and ice:	kg m^{-3} s^{-1}
$S_{v-i} = \begin{cases} \begin{cases} \gamma_{desb}\varepsilon\left(1-s_{lq}-s_{ice}\right)\dfrac{\left(p_g X_{vp}-p_{sat}\right)M_{H_2O}}{RT} & \text{if } p_g X_{vp} \geq p_{sat} \\ 0 & \text{if } p_g X_{vp} < p_{sat} \end{cases} & \text{if } T < T_N + T_{FPD} \\ 0 & \text{if } T \geq T_N + T_{FPD} \end{cases}$	
Liquid water and ice:	kg m^{-3} s^{-1}
$S_{l-i} = \begin{cases} \gamma_{fusn}\varepsilon s_{lq}\rho_{lq} & \text{if } T < T_N + T_{FPD} \\ -\gamma_{melt}\varepsilon s_{ice}\rho_{ice} & \text{if } T \geq T_N + T_{FPD} \end{cases}$	

The effect on the water transport due to the EOD is considered by adding a term (S_{EOD}) into the source term of the non-frozen membrane water conservation equation, as shown in Tables 5.3 and 5.6. The EOD coefficient (n_d) is calculated as [51]

$$n_d = \frac{2.5\lambda_{nf}}{22} \tag{5.30}$$

The EOD coefficient is the number of water molecules dragged per hydrogen ion moved through the ionomer. In addition, the saturation and equilibrium water content (λ_{equil} and λ_{sat}) are calculated by using Equations 5.2 and 5.5.

Table 5.6: Membrane water related phase change functions.

Phase change / water transfer function	Unit
Non-frozen membrane water and vapour: $S_{n-v} = \zeta_{n-v} \frac{\rho_{mem}}{EW}\left(\lambda_{nf} - \lambda_{equil}\right)$	kmol m^{-3} s^{-1}
Non-frozen membrane water and ice: $S_{n-i} = \begin{cases} \zeta_{n-i} \frac{\rho_{mem}}{EW}\left(\lambda_{nf} - \lambda_{sat}\right) & \text{if } \lambda_{nf} \geq \lambda_{sat} \\ 0 & \text{if } \lambda_{nf} < \lambda_{sat} \end{cases}$	kmol m^{-3} s^{-1}
Non-frozen membrane water and frozen membrane water: $S_{n-f} = \begin{cases} \zeta_{n-f} \frac{\rho_{mem}}{EW}\left(\lambda_{nf} - \lambda_{sat}\right) & \text{if } \lambda_{nf} \geq \lambda_{sat} \\ \zeta_{n-f} \frac{\rho_{mem}}{EW}\lambda_{f} & \text{if } \lambda_{nf} < \lambda_{sat} \end{cases}$	kmol m^{-3} s^{-1}
Membrane water transfer due to EOD: $S_{EOD} = \nabla \cdot \left(\frac{n_d}{F} \kappa_{ion}^{eff} \nabla \phi_{ion} \right)$	kmol m^{-3} s^{-1}

5.4.3 Electron and Ion Transport

The ion (proton) conductivity of the membrane ionomer is calculated by using Equation 5.3. The effective electron conductivity in the CL and GDL and ion conductivity in the CL are further modified with the porosities (ε) of the CL and GDL and the ionomer volume fraction in the CL (ω). Based on the Bruggemann correlation, an exponent of 1.5 is used:

$$\kappa_{ele}^{eff} = \left(1 - \varepsilon - \omega\right)^{1.5} \kappa_{ele} \tag{5.31}$$

$$\kappa_{ion}^{eff} = \omega^{1.5} \kappa_{ion} \tag{5.32}$$

The reaction rates (j_a and j_c, A m^{-3}) in the anode and cathode CLs are calculated by using the Butler-Volmer equation:

$$j_a = \left(1 - s_{lq} - s_{ice}\right) j_{0,a}^{ref} \left(\frac{c_{H_2}}{c_{H_2}^{ref}} \right)^{0.5} \left[\exp\left(\frac{2\alpha_a F}{RT} \eta_{act} \right) - \exp\left(-\frac{2\alpha_c F}{RT} \eta_{act} \right) \right] \tag{5.33}$$

$$j_c = \left(1 - s_{lq} - s_{ice}\right) j_{0,c}^{ref} \frac{C_{O_2}}{C_{O_2}^{ref}} \left[-\exp\left(\frac{4\alpha_a F}{RT} \eta_{act} \right) + \exp\left(-\frac{4\alpha_c F}{RT} \eta_{act} \right) \right] \tag{5.34}$$

where F is the Faraday's constant (C kmol^{-1}), and c the concentration (kmol m^{-3}). A linear relationship to reflect the blockage of the reaction sites due to the ice and liquid water is assumed [95-

99]. The correlations and values of the parameters related to the electrochemical reactions are given in Table 5.7.

Table 5.7: Parameters related to electrochemical reactions [4, 65].

Parameter	Correlation / Value (T in K)	Unit
Overpotential (activation loss)	$\eta_{act} = \phi_{ele} - \phi_{ion}$	V
Transfer coefficient	$\alpha_a = \alpha_c = 0.5$	Dimensionless
Volumetric reference exchange current density in anode	$j_{0,a}^{ref} = j_{0,a}^{ref}\Big\|_{353.15K} \exp\left[-1400\left(\frac{1}{T} - \frac{1}{353.15}\right)\right]$	A m^{-3}
Volumetric reference exchange current density in cathode	$j_{0,c}^{ref} = j_{0,c}^{ref}\Big\|_{353.15K} \exp\left[-7900\left(\frac{1}{T} - \frac{1}{353.15}\right)\right]$	A m^{-3}

5.4.4 Energy Transport

The effective volumetric heat capacities (J m^{-3} K^{-1}) in the energy conservation equation (Equation 5.16) are determined as

$$\left(\rho C_p\right)_{fl,sl}^{eff} = \varepsilon\left[s_{lq}\rho_{lq}\left(C_p\right)_{lq} + s_{ice}\rho_{ice}\left(C_p\right)_{ice} + \left(1 - s_{lq} - s_{ice}\right)\rho_g\left(C_p\right)_g\right] + \left(1 - \varepsilon - \omega\right)\rho_{sld}\left(C_p\right)_{sld} + \omega\rho_{mem}\left(C_p\right)_{mem} \tag{5.35}$$

$$\left(\rho C_p\right)_{fl}^{eff} = \varepsilon\left[s_{lq}\rho_{lq}\left(C_p\right)_{lq}\frac{K_{lq}\mu_g}{K_g\mu_{lq}} + \left(1 - s_{lq} - s_{ice}\right)\rho_g\left(C_p\right)_g\right] \tag{5.36}$$

where $\left(C_p\right)_g$ (J kg^{-1} K^{-1}) is the specific heat capacity of the gas mixture, and it is determined based on the mass fraction of each species:

$$C_p = \sum_i Y_i\left(C_p\right)_i \tag{5.37}$$

$\left(C_p\right)_{sld}$ (J kg^{-1} K^{-1}) represents the specific heats of the electron conducting materials (platinum powders, carbon powders etc.) in the CL and all the solid materials in the GDL and BP. For simplicity, the effective thermal conductivity (W m^{-1} K^{-1}) in the energy conservation equation is assumed to be a volume averaged value:

$$k_{fl,sl}^{eff} = \varepsilon\left[s_{lq}k_{lq} + s_{ice}k_{ice} + \left(1 - s_{lq} - s_{ice}\right)k_g\right] + \left(1 - \varepsilon - \omega\right)k_{sld} + \omega k_{mem} \tag{5.38}$$

where the thermal conductivity of the gas mixture, k_g (W m^{-1} K^{-1}), is calculated based on kinetic theory as [114]

$$k_g = \sum_i \frac{X_i k_i}{\sum_j X_i \psi_{ij}} \tag{5.39}$$

$$\psi_{ij} = \frac{\left[1+\left(k_i / k_j\right)^{0.5}\left(M_i / M_j\right)^{0.25}\right]^{0.5}}{\left[8\left(1+M_i / M_j\right)\right]^{0.5}} \tag{5.40}$$

The specific heat capacities and thermal conductivities are all considered to be constants for all the substances in this model. Because based on the values tabulated in [111], it is found that the changes of these parameters of different substances between -50 and 100 ^{o}C are insignificant. The values of these two parameters for the gas species, liquid water and ice are given in Table 5.4.

The latent heat function, S_{pc} (W m^{-3}) in Table 5.3, is defined based on the water phase change and transfer rates:

$$S_{pc} = \begin{cases} h_{cond} S_{v-l} + \left(h_{cond} + h_{fusn}\right) S_{v-i} + h_{fusn} S_{l-i} & \text{(in GDL)} \\ h_{cond}\left(S_{v-l} - S_{n-v} M_{H_2O}\right) + \left(h_{cond} + h_{fusn}\right) S_{v-i} + h_{fusn}\left(S_{l-i} + S_{n-i} M_{H_2O}\right) & \text{(in CL)} \\ h_{cond} S_{n-f} M_{H_2O} & \text{(in membrane)} \\ 0 & \text{(in other zones)} \end{cases} \tag{5.41}$$

It should be noticed that the non-frozen membrane water is considered to be the same as liquid water in this model [50]. Therefore, the water vapour absorption into a membrane is a process similar to a vapour condensation process and involves a release of heat. Similarly, the water leaving a membrane as vapour is similar to a liquid evaporation process. By comparing these processes, Ostrovskii and Gostev [119] showed that the difference in the amounts of heat released or absorbed is very small, and the numerical simulations in [67] also confirmed that such difference can be safely neglected. Moreover, the specific or molar entropy of the non-frozen membrane water is also not available in literature. Therefore, it is reasonable to consider the non-frozen membrane water the same as liquid water. Therefore, the product water is considered as in liquid phase in ionomer. The entropy change of the overall reaction, ΔS (J kmol^{-1} K^{-1}), is defined based on liquid water product, as given in Table 5.4. A constant value of ΔS is used by neglecting the insignificant temperature effects (based on the values listed in [110]). The temperature dependence of the latent heat of condensation, h_{cond} (J kg^{-1}), is considered by fitting the values tabulated in [110]:

$$h_{cond} = -2438.5T + 3170700 \tag{5.42}$$

where the units of h_{cond} and T are J kg^{-1} and K, respectively.

5.5 Boundary and Initial Conditions

This model employs a single computational domain. Therefore, the boundary conditions only need to be specified at the outer surfaces to complete the model formulation. These boundary conditions can be varied based on the conditions of the inlet reactant flow, operating temperature, operating pressure and electric load.

At the inlets of the flow channels, the mass flow rates (kg s^{-1}) are defined as

$$\dot{m}_a = \frac{\rho_g^a \xi_a I_{ref} A}{2Fc_{H_2}} \quad \dot{m}_c = \frac{\rho_g^c \xi_c I_{ref} A}{4Fc_{O_2}} \tag{5.43}$$

$$c_{H_2} = \frac{\left(p_g^a - RH_a p_{sat}\right)}{RT_{in}^a} \quad c_{O_2} = \frac{0.21\left(p_g^c - RH_c p_{sat}\right)}{RT_{in}^c} \tag{5.44}$$

where ξ_a and ξ_c are the stoichiometry ratios for the anode and cathode, respectively, I_{ref} the reference current density (A cm^{-2}), A the flat active surface area of the CL (m^2). Constant temperatures are defined at the anode and cathode flow channel inlets (T_{in}, K).

The liquid water volume fraction is fixed at zero in the flow channels, reflecting the condition that the liquid water can be removed from the flow channel quickly.

The electronic potentials on the end surfaces of the BPs for both the anode and cathode are defined as

$$\phi_{ele}^{c,end} = 0; \quad \phi_{ele}^{a,end} = V_{rev} - V_{cell} = \eta_{total} \tag{5.45}$$

where V_{rev} and V_{cell} are the reversible and operating voltages, and η_{total} represents the total voltage loss. For liquid water product, the reversible cell voltage is calculated as:

$$V_{rev} = 1.23 - 0.9\times10^{-3}\left(T_0 - 298\right) + \frac{RT_0}{2F}\left(\ln p_{H_2}^{in} + \frac{1}{2}\ln p_{O_2}^{in}\right) \tag{5.46}$$

In this equation, the inlet partial pressures of hydrogen and oxygen (atm), and the operating temperature (volume average temperature) (T_0, K) are used for the calculation.

On the surrounding walls of the cell, a heat transfer coefficient is defined based on normal atmosphere condition. Therefore, the heat transfer rate between the cell wall and surroundings can be calculated as

$$\dot{Q} = hA_{wall}\left(T_{surr} - T_{wall}\right) \tag{5.47}$$

where $\dot{Q}$ (W) is the heat transfer rate between the cell wall and the surroundings, a positive value indicates that heat is absorbed by the cell, and vice versa; h is the heat transfer coefficient (W m^{-2} K^{-1}); A_{wall} is the surface area of the cell wall (m^2); T_{surr} is the temperature of the surroundings (K); and T_{wall} is the temperature of the cell wall (K).

The initial condition is defined according to the cell condition at the beginning of each start-up processes.

5.6 Numerical Procedures

The computational grid is created by using a built-in pre-processing software, GAMBIT. Then, the grid is imported into a finite volume based software, FLUENT 6.3, to discretize and solve the conservation equations (Equations 5.7-5.16). Since the FLUENT built-in model only provides the gas mass, momentum and species and energy conservation equations (Equations 5.7-5.9, 5.16), the other conservation equations (Equations 5.10-5.15) are coded by using the programming language C in

terms of the user defined functions (UDFs). The various source terms, model parameters, material properties, correlations, boundary conditions, and the iteration/under-relaxation stabilization schemes are also coded through the UDFs. A sample code of this model is given in Appendix B.

The individual variables of the conservation equations are solved sequentially by using the pressure-based segregated solver of FLUENT [112]. Each conservation equation is segregated from the other equations when it is solved. The constraint of the gas mass conservation on the gas velocity field is achieved by solving a pressure correction equation, and the pressure correction equation is derived from the gas mass and momentum conservation equations. The PISO algorithm is used. Even it uses more CPU time per iteration than the SIMPLE/SIMPLEC algorithms, the number of iterations for each time step can be significantly reduced for the transient cold start simulations [112]. An algebraic multigrid (AMG) method with a Gauss-Seidel type smoother is used to accelerate the convergence [112]. For each iteration, the segregated solver follows the loop [112]:

1. Define the initial condition (only for the first iteration of the first time step).
2. Update the properties (e.g. density, specific heat capacity) based on the current solution.
3. Solve the momentum equations one by one by using the updated properties.
4. Solve the pressure correction equation by using the values obtained from step 3.
5. Correct the mass fluxes, pressure and velocity field by using the values obtained from step 4.
6. Solve the rest of the conservation equations one by one.
7. Check for the convergence of the equations. If not, start again from step 2.

A second-order upwind scheme is used to discretize the convection terms, a second-order central differencing scheme is used to discretize the diffusion terms, and a first-order backward differencing scheme is used to discretize the transient terms in the conservation equations [112]. The whole conservation equations are evaluated in an implicit manner at each time step, and adaptive time stepping is employed, with a minimum of 10^{-6} s and a maximum of 0.1 s time step sizes. The adaptive time stepping algorithm automatically adjusts the time step size based on the estimation of the truncation error associated with the time integration scheme to ensure both the accuracy and optimal computational expense [112]. Strict convergence criteria with a residual of 10^{-8} are used for all variables. The residual represents the summation of imbalance scaled by a factor representative of the flow rate through the domain [112].

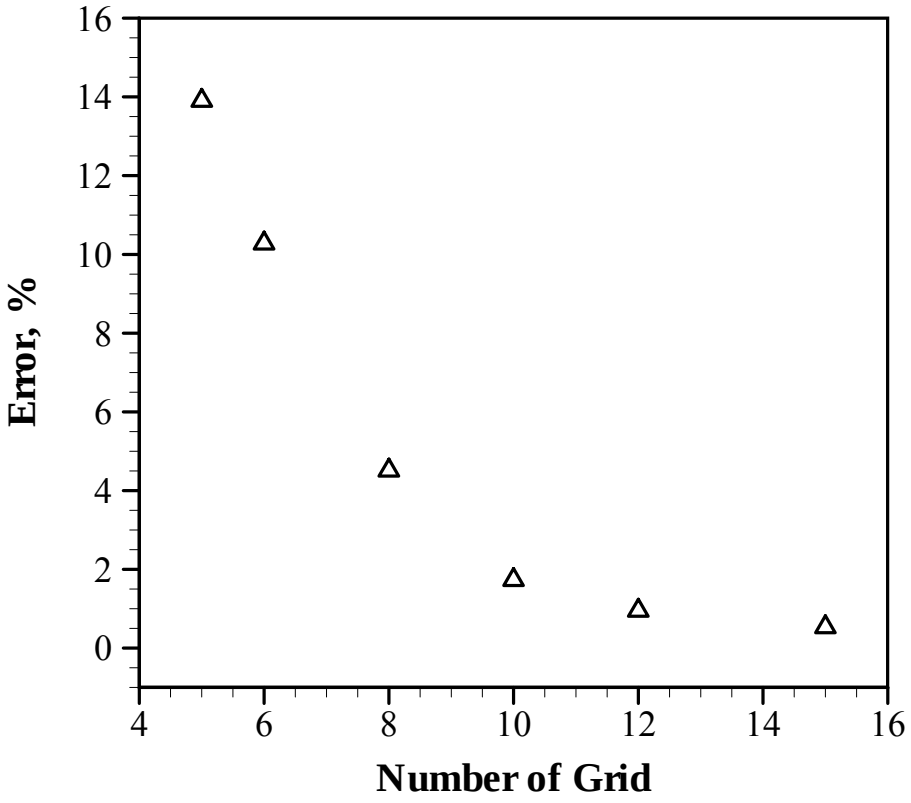

Figure 5.8: Effect of the number of grid points along the y-direction (refer to Figure 5.1) in each layer of the computational domain on the error of cold start failure duration for a cold start process from -10 ^{o}C (20 grid points in each layer is assumed to be the "exact" solution to calculate the error).

5.7 Grid Independency

Theoretically, increasing the number grid points enhances the accuracy, and an exact solution can be achieved when the grid size is infinitely small. However, the number of grid points needs to be limited to save the computational time and accelerate the convergence process. For this 3D model, the effects of the number of grid points along the three directions on the results are tested. A sample grid/mesh being used is shown in Figure 5.1. The number of grid points along the x-direction depends on the length of the flow channel. Along the y-direction, the same number of grid points is considered in the different layers. Along the z-direction, it depends on the number of parallel flow channels, and it should be the same for the single straight flow channels considered in this model. The grid is uniform in the different layers. Similar grid systems were also used extensively in the previous full cell models [4, 120].

Grid independent study is performed along all the three directions. The solution is affected most significantly by the number of grid points along the y-direction. By considering a computational domain with a channel length of 140 mm (a typical single channel length in a vehicle PEMFC), the number of grid points along the x- and z-directions are fixed at 140 and 20 [4, 120]. Figure 5.8 shows

the effect of the number of grid points along the y-direction in each layer of the computational domain on the error of cold start failure duration for a cold start process from -10 ^{o}C. 20 grid points is assumed to be the "exact" solution to calculate the error. Further increasing the number of grid points makes the solution difficult to converge, perhaps because the aspect ratio of the computational cells are too high with the high number of grid points along the y-direction. The cold start failure duration means the total time for the ice to fully block the cathode CL, which is the most important parameter for PEMFC cold start. It was also found that the cold start failure duration is more sensitive to the grid system than the other important parameters such as the temperature reached when the cold start is failed. Therefore, it is used for the grid independent study. Figure 5.8 shows that 10 grid points in each layer results in an error of about 1.73%. Since further increasing the number of grid points (12 and 15) not only increases the computational time, but also makes the solution more difficult to converge (perhaps due to the high aspect ratio of the cells). Therefore, 10 grid points is chosen along the y-direction in each layer of the computational domain. The number of grid points along the x- and z-directions are chosen to be 140 (1 grid point per mm, note that the channel length considered in this research is always higher than 50 mm) and 20, with the errors of about 0.33% and 0.01% comparing with the results with doubled number of grid points, respectively. The total number of gird points of the selected computational domain with a channel length of 140 mm is therefore 224,000. This grid system is also similar to the ones often used in the previous full cell models for PEMFC [4, 120].

5.8 Comparison with Experimental Data

In order to examine the accuracy of the present cold start model, the evolutions of the cell voltages for both the failed (from -10 ^{o}C and -20 ^{o}C) and successful (from -3 ^{o}C and -5 ^{o}C) cold start processes obtained from the experimental measurements in this research (Figures 5.9a and 5.9b) and in [34] (Figures 5.9c and 5.9d) are compared with the model predictions, as shown in Figure 5.9. The model parameters are adjusted according to the experimental conditions to obtain good agreements with the experimental data. For the failed cold start process in Figure 5.9a, the start-up temperature is -10 ^{o}C; the start-up current density is 0.07 A cm^{-2}; the stoichiometry ratios are 1.2 and 2.0 corresponding to the operating current density for the anode and cathode non-humidified inlet gases, respectively; the inlet gas temperatures are equal to the room temperature; and the membrane thickness is 50 μm. For the successful cold start process in Figure 5.9b, the start-up temperature is changed to -5 ^{o}C, and the start-up voltage is fixed at 0.3 V. For the failed cold start process in Figure 5.9c, the start-up temperature is -20 ^{o}C; the start-up current density is 0.04 A cm^{-2}; the stoichiometry ratio is 2.0 corresponding to the operating current density for both the anode and cathode non-humidified inlet gases; and the membrane thickness is 30 μm. For the successful cold start process in Figure 5.9d, the start-up temperature is changed to -3 ^{o}C.

It can be observed from Figure 5.9 that the cell voltage and current density evolutions are generally consistent between the model predictions and the experimental data. For the failed cold start processes (Figures 5.9a and 5.9c), the model predictions agree well with the experimental data at the beginning. After that, the cell voltage starts decreasing due to the ice formation, and the model predictions show sharper decrements of the cell voltage than the experimental data. Since the present model uses a linear relationship to reflect the blockage of the reaction sites due to the ice and liquid water formation [95-99] (Equations 5.33 and 5.34), further modifications of this linear relationship

may result in better agreement with the experimental data. This will require further pore-scale investigation on the ice and liquid water distributions in the CL are needed.

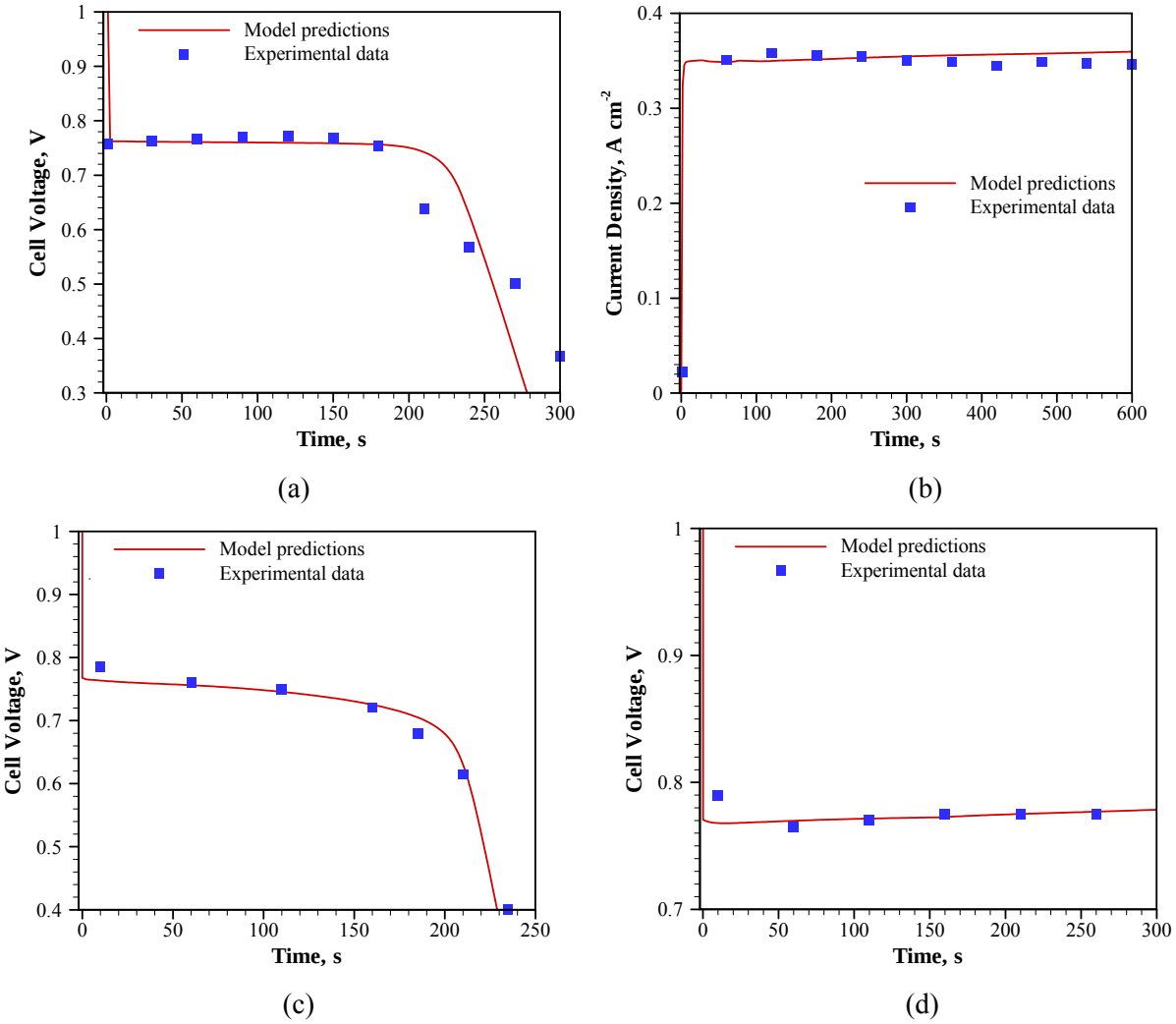

Figure 5.9: Comparison between the present model predictions and the experimental data (a: from -10 ^{o}C at 0.07 A cm^{-2}, experimental data from this research; b: from -5 ^{o}C at 0.3 V, experimental data from this research; c: from -20 ^{o}C at 0.04 A cm^{-2}, experimental data from [34]; d: from -3 ^{o}C at 0.04 A cm^{-2}, experimental data from [34])

5.9 Summary

The cold start model is described in details in this chapter. By solving a complete set of conservation equations (fourteen equations), this model accounts for all the typical transport phenomena during the PEMFC cold start processes. Unique in the present cold start model is the inclusion of the following phenomena: (i) the water freezing in the membrane electrolyte and its effects on the membrane

conductivity; (ii) the non-equilibrium mass transfer between the water in the ionomer and the water (vapour, liquid and ice) in the pore region of the CL; and (iii) both the water freezing and melting in the CL and GDL. This model therefore provides the fundamental framework for the future top-down multi-dimensional multiphase model of PEMFC. These features also make the model a powerful tool to understand the transport phenomena and evaluate the various designs and operational strategies.

Chapter 6

Modelling Results

With the cold start model presented in Chapter 5, extensive numerical simulations are conducted to study the cold start characteristics of PEMFC. In this chapter, the numerical results from the cold start model are presented. The transport phenomena during the cold start processes are investigated first. The effects of various cell designs and operating conditions on the cold start performance are then studied. The external heating methods on the cold start performance are also discussed. The cell properties and operating conditions considered in the numerical simulations are given in Table 6.1. The computational domain is shown in Figure 5.1 in the previous chapter.

6.1 Investigations of Cold Start Processes

6.1.1 Failed Cold Start Process

The evolutions of both the current density and ice volume fraction in the cathode CL for the cold start process from -10 ^{o}C are shown in Figure 6.1. For this cold start process, a constant cell voltage of 0.3 V is applied. Such a low cell voltage is applied in order to produce high start-up current densities considered to be beneficial for a successful cold start process. Based on the measurements of the water contents and distributions after purge in [121], as well as the setup of the initial conditions in [98], the initial water content is set to be 5.0 in the membrane and CLs, and the initial ice volume fraction is set to be 0.15 in the CLs and GDLs. The current density increases quickly at the beginning due to the fast electrochemical double layer charging and discharging process. Then the variation of the current density becomes the minimum for a period of time, owing to the combined effects of the membrane hydration, temperature increment and ice blockage. Finally the current density drops fast indicating that the cold start process is failed. This trend is consistent with the experimental measurements presented in Chapter 4. The fast drop of the current density is caused by the ice blockage on the active catalyst surface, and it occurs when the ice volume fraction in the cathode CL reaches unity (about higher than 0.9). The linear increment of the ice volume fraction shown in Figure 6.1 is consistent with the numerical results in [95]. Since the product water is in the ionomer in cathode CL, during the cold start process, the mass transfer between the water in the ionomer and the water vapour takes place, and the freezing of the water in the ionomer into ice occurs as well. Therefore, there are two sources of ice formation: desublimation of vapour and freezing of membrane water. Before these ice formation processes can take place, the water content in the ionomer must reach certain values: to reach 14.0 in order to have saturated water vapour to desublimate (Equation 5.5), and to reach λ_{sat} (10.1 at -10 ^{o}C) in order to have the membrane water to freeze (Equation 5.2). Since the initial water content is 5.0, the ice volume fraction in the cathode CL in Figure 6.1 remains unchanged in the first second of the cold start process. It indicates that purging the cell reduces the rate of ice formation during cold start.

Table 6.1: Cell properties and operating conditions.

Parameter	Value
Channel length; width; depth; rib width	50 and 140; 1.0; 1.0; 1.0 mm
Thicknesses of membrane (Nafion 117, 115 and 112); CL; GDL (carbon paper)	0.178, 0.127 and 0.051; 0.01; 0.2 mm
Membrane density; equivalent weight	$\rho_{mem} = 1980$ kg m^{-3}; EW $= 1100$ kg kmol^{-1}
Volume fraction of ionomer in CL, and the porosities of CL; GDL	$\omega = 0.2;\ 0.4$; $\varepsilon_{CL,GDL} = 0.3 / 0.5;\ 0.6$
Contact angles and pore radii of CL; GDL	$\theta_{CL,GDL} = 100^{o}$; $r_{CL,GDL} = 1.2\times10^{-8}; 3.89\times10^{-5}$ m
Intrinsic permeabilities of CL; GDL	$K^{0}_{CL,GDL} = 6.2\times10^{-13};\ 6.2\times10^{-12}$ m^2
Densities of CL; GDL; BP	$\rho_{CL,GDL,BP} = 1000$ kg m^{-3}
Specific heat capacities of membrane; CL; GDL; BP	$\left(C_p\right)_{mem,CL,GDL,BP} = 833;\ 3300;\ 568;\ 1580$ J kg^{-1} K^{-1}
Thermal conductivities of membrane; CL; GDL; BP	$k_{mem,CL,GDL,BP} = 0.95;\ 1.0;\ 1.0;\ 20$ W m^{-1} K^{-1}
Electrical conductivities of CL; GDL; BP	$\kappa_{CL,GDL,BP} = 300;\ 300;\ 20000$ S m^{-1}
Cell voltages (constant voltage start-up)	$V_{cell} = 0.3;\ 0.7$ V
Current densities (constant current start-up)	$I = 0.05;\ 0.15$ A cm^{-2}
Stoichiometry ratios at 1.0 A cm^{-2}	$\xi_{a,c} = 2.0$
Relative humidities of inlet gases	$RH^{in}_{a,c} = 0$
Inlet gas temperatures	$T^{in}_{a,c} = T_0$ = volume averaged cell temperature or $T^{in}_{a,c} = T_{surr}$ = surrounding temperature or $T^{in}_{a,c} = 80\ ^{o}C$
Absolute total pressure at outlets	$p^{out}_{a,c} = 1$ atm
Surrounding temperatures and heat transfer coefficients	$T_{surr} = -3, -10, -20$ ^{o}C $h = 50$ (default value); 100 W m^{-2} K^{-1}
External heating power on the end surfaces of the BPs	$\dot{Q}_{ext} = 0$ (default value); 0.126; 0.504 W
Initial ice volume fraction	0; 0.15; 0.3
Initial non-frozen water content and frozen water content	0 , 5 and 10; 0

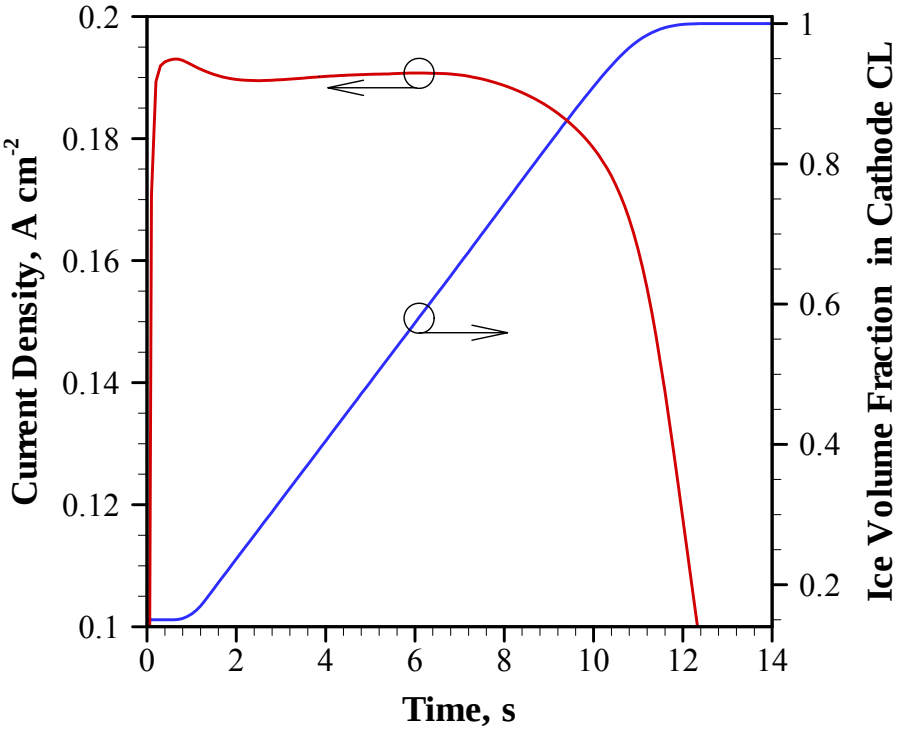

Figure 6.1: Evolutions of current density and ice volume fraction in cathode CL from -10 ^{o}C.

The contours of the ice volume fraction in the cathode CL in a y-z plane for the cold start process from -10 ^{o}C are shown in Figure 6.2. The ice first appears under the land because the temperature is low in those areas (close to the surrounding walls), which results in low λ_{sat} . In the areas close to the membrane, more water in the ionomer could diffuse into the membrane due to the large gradient of water content; and in the areas close to the flow channel, the temperature is lower. Therefore, the ice is also first generated at the locations away from both the membrane/CL and GDL/CL interfaces. As time passes, more ice is formed and the cathode CL is fully blocked (12 s), indicating that no further electrochemical reaction can take place.

The evolution of the non-frozen water content in the membrane and CLs for the cold start process from -10 ^{o}C is illustrated in Figure 6.3. The water content in the cathode CL increases fast and the changes of the water content in the membrane and anode CL are relatively slow. The reason is that the water production rate is higher than the water diffusion rate in the ionomer (low diffusivity at subzero temperatures). Figure 6.3 even shows that the water content difference across the membrane is still very significant even at 35 s (23 s after the electrochemical reaction stops). The results suggest that increasing the ionomer fraction in the cathode CL has more significant effects than increasing the thickness of the membrane layer in reducing the amount of ice formation.

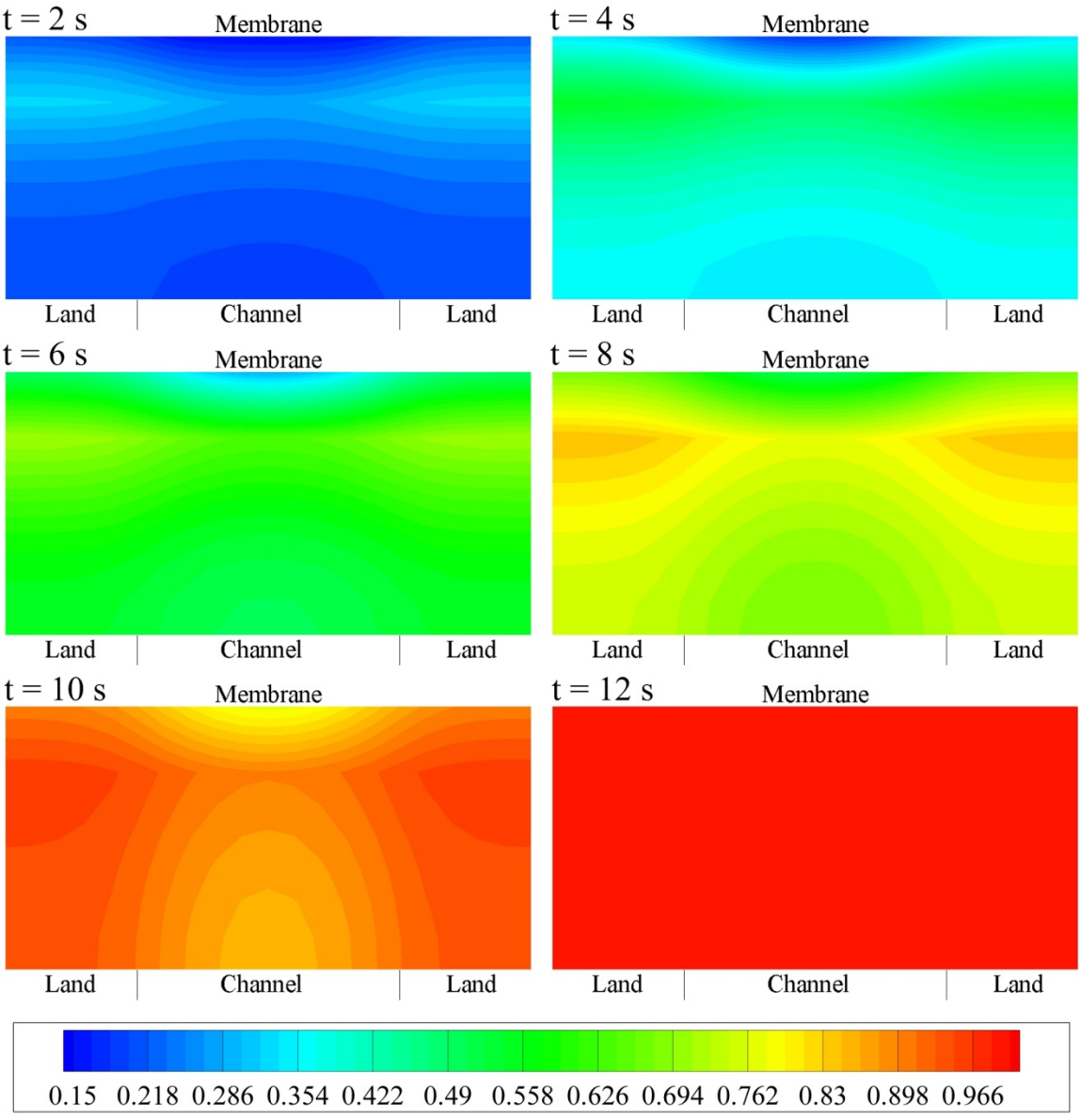

Figure 6.2: Evolution of ice volume fraction in cathode CL in a y-z plane for the cold start process from -10 ^{o}C.

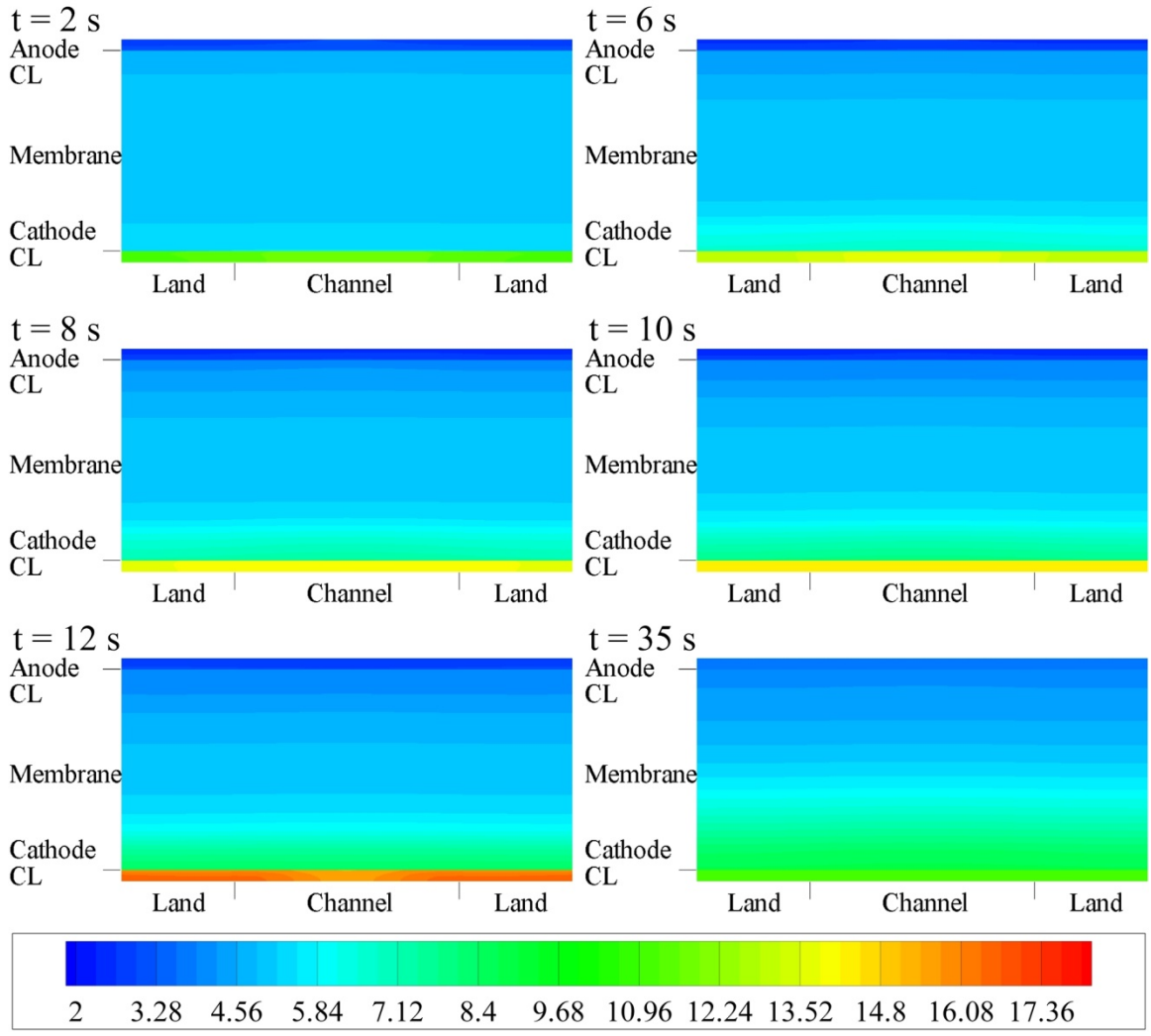

Figure 6.3: Evolution of non-frozen water content in membrane and CLs in a y-z plane for the cold start process from -10 ^{o}C.

The evolutions of the various heat generation rates, heat loss rate through the surrounding walls, and cell temperature for the cold start process from -10 ^{o}C are presented in Figure 6.4. It should be noticed that the cell temperature presented in this figure is the volume averaged temperature of the whole computational domain, and the heat generation rates and the heat loss rate are the total values for the whole computational domain. The largest heating source is found to be the ohmic heat, mainly due to the low membrane conductivity at subzero temperatures. The activational heat in this case is about half of the ohmic heat, however, the numerical simulations in [98] showed that the activational heat is higher than the ohmic heat. The reason is that the start-up current density in this study (0.19 A cm^{-2}) is higher than the current density in [98] (0.1 A cm^{-2}). The last equation in Table 5.3 shows that the ohmic heat increases with an exponent of 2 with the increment of current density, and the activational heat changes almost linearly with the current density (the major change of η_{act} occurs at very low current densities). Both the reversible heat and latent heat are much lower, and at 12 s, all

the heat generations drop down to almost zero due to the blockage of ice. The evolutions of the heat loss through the surrounding walls and the cell temperature are in the same trend (the heat loss increases linearly with the cell temperature if the heat transfer coefficient is constant), and it should be noticed that the heat exchange through the flow inlets and outlets can be safely neglected (the level of 10^{-5} W) because the inlet gases are set to be equal to the cell temperature. The cell temperature reaches to about -3.5 ^{o}C (12 s, when the electrochemical reaction is stopped) and then decreases again due to the heat loss to the surroundings.

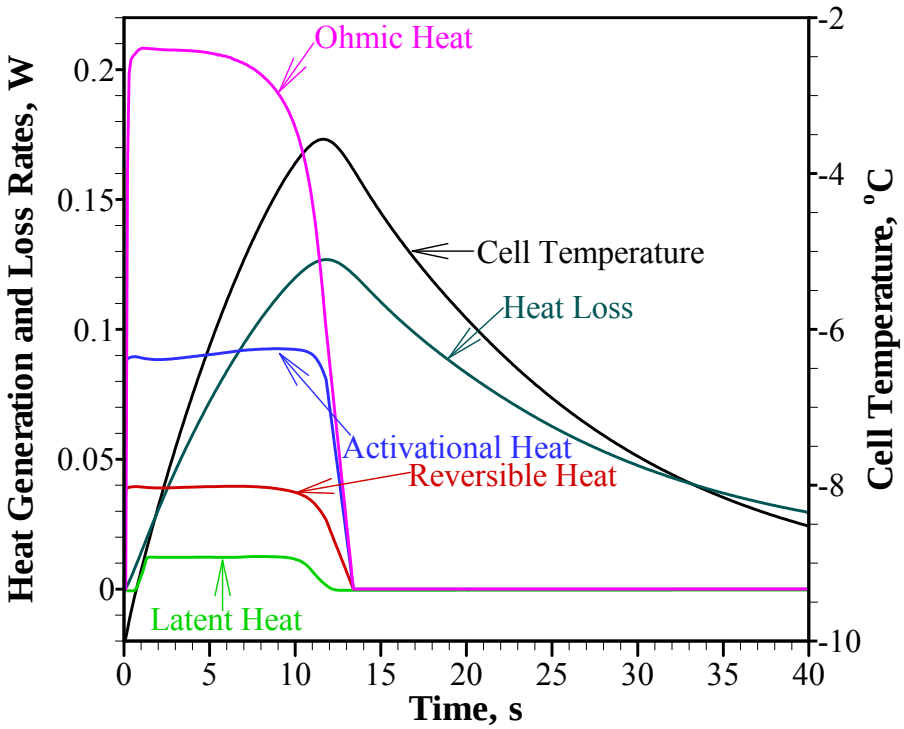

Figure 6.4: Evolutions of various heat generation rates, heat loss rate through surrounding walls, and cell temperature for the cold start process from -10 ^{o}C.

The contours of temperature in a y-z plane for the cold start from -10 ^{o}C are given in Figure 6.5. Due to the fact that the ohmic heat is mainly caused by the low membrane conductivity, the highest temperature is very close to the membrane, a slight shift to the cathode CL due to the other heating sources (activational heat, reversible heat and latent heat). The temperature is also the highest under the flow channel rather than under the land because the heat is lost at the surrounding walls. It is also observed that the temperature in the anode is slightly higher than in the cathode, and the reasons are: 1) the ohmic heat is the highest in the anode CL (a low water content results in a low membrane conductivity); 2) the heat transfer rate is higher in the anode, due to the higher thermal conductivity of hydrogen by comparing with oxygen and the blockage of ice in the cathode CL.

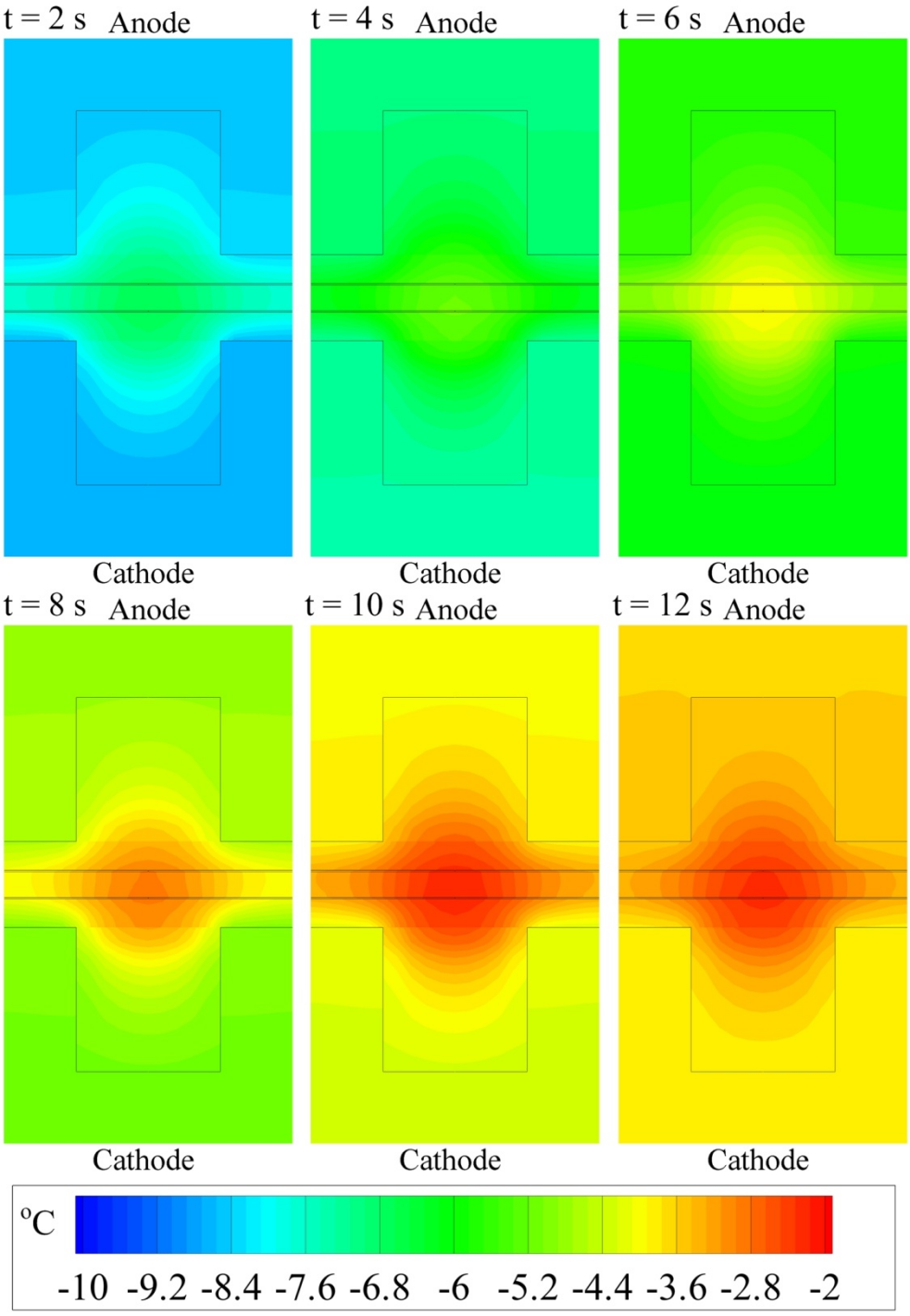

Figure 6.5: Evolution of temperature in a y-z plane for the cold start process from -10 °C.

6.1.2 Successful Cold Start Process

Figure 6.6 shows evolutions of current density and cell temperature for the cold start process from -3 ^{o}C. In this successful cold start process, the current density increases with the increment of the cell temperature, and the increment of the cell temperature becomes the lowest at around 0 ^{o}C, because heat is needed for ice melting. Even Figure 6.6 shows that the cell temperature reaches 0 ^{o}C at about 5 s, the evolutions of ice and liquid water volume fractions in Figure 6.7 shows that the ice starts melting at about 1 s in the CLs and 2.5 s in the GDLs, due to the higher temperatures in these regions as well as the FPD effect. The liquid water volume fractions change more dramatically than the ice volume fractions. In the cathode (Figure 6.7a), the liquid water volume fraction in the CL increases up to 0.2 at the beginning, due to both the ice melting and water production, followed by a fast drop due to the liquid water removal and the stoppage of the ice melting. The liquid water volume fractions in the cathode CL and GDL reach almost constants at about 10 s by balancing both the water production and removal. The liquid water volume fractions in the anode (Figure 6.7b) are less than in the cathode, and the maximum volume fractions are reached at the end of the ice melting process, and then decreases with time due to both the water evaporation and the water absorption by the ionomer.

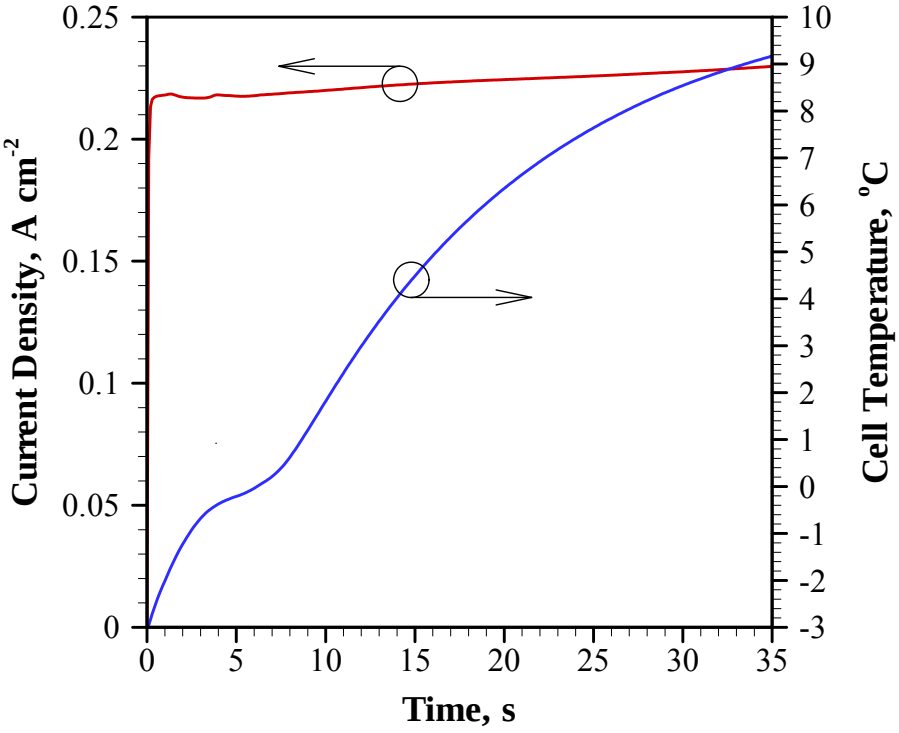

Figure 6.6: Evolutions of current density and cell temperature from -3 ^{o}C.

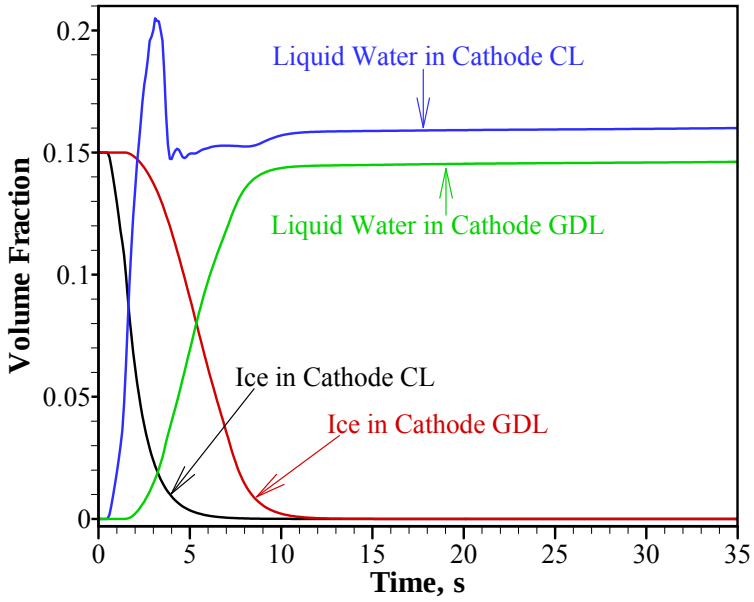

(a)

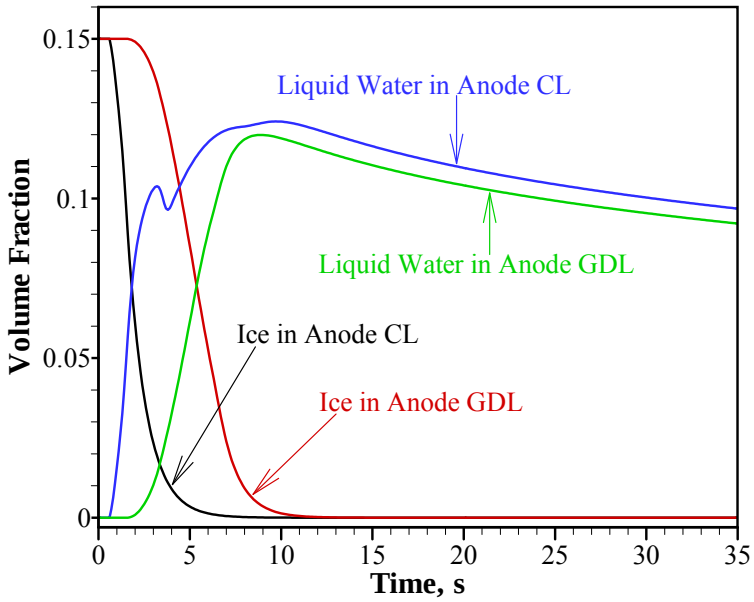

(b)

Figure 6.7: Evolutions of ice and liquid water volume fractions in CLs and GDLs for the cold start process from -3 ^{o}C (a: cathode; b: anode).

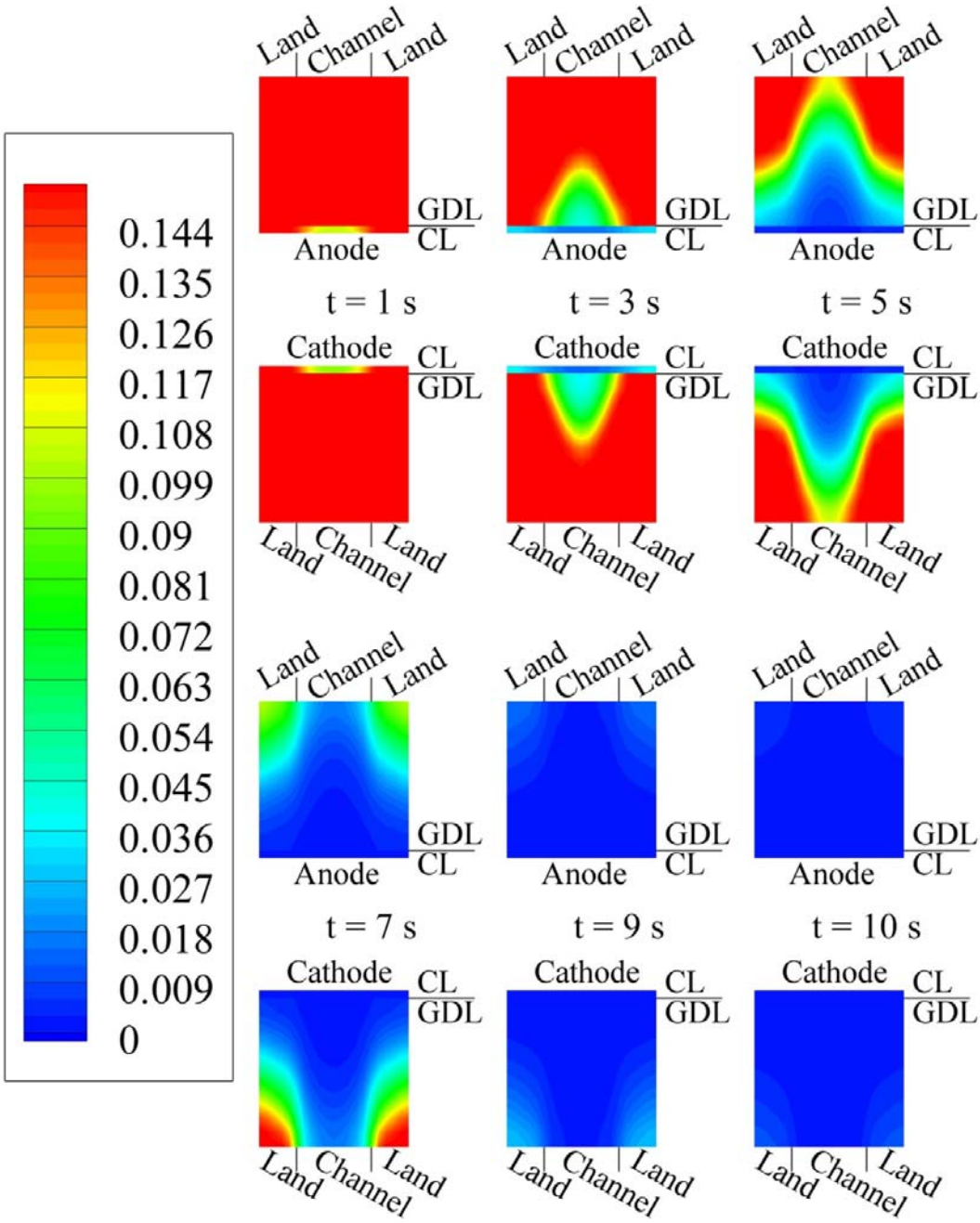

Figure 6.8: Evolution of ice volume fraction in CLs and GDLs in a y-z plane for the cold start process from -3 ^{o}C.

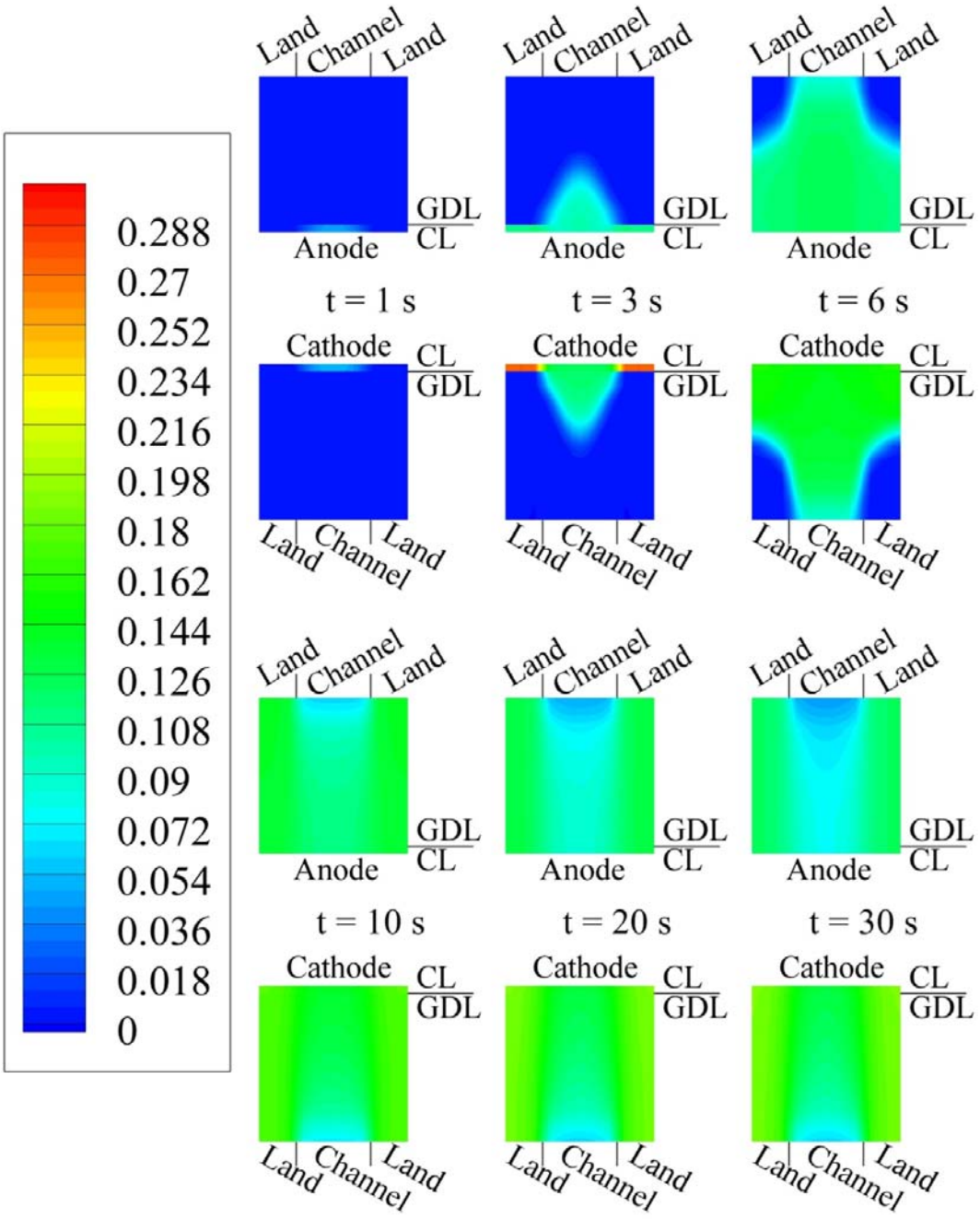

Figure 6.9: Evolution of liquid water volume fraction in CLs and GDLs in a y-z plane for the cold start process from -3 ^{o}C.

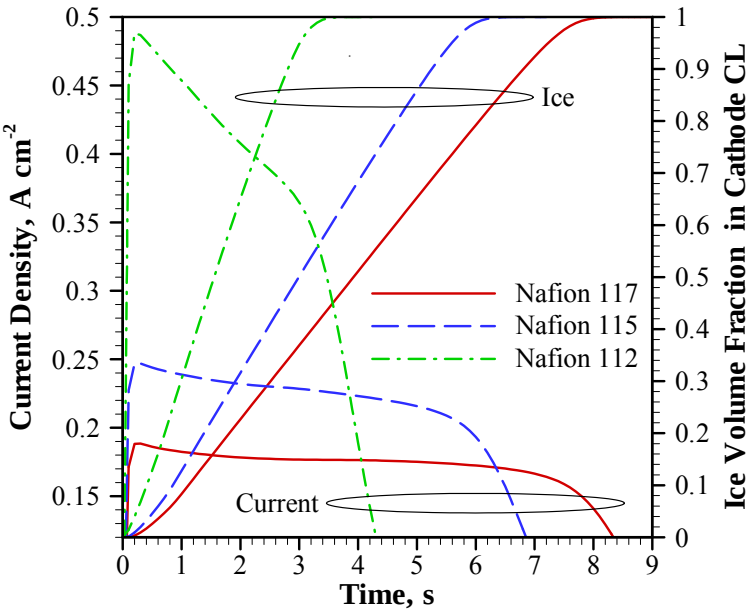

(a)

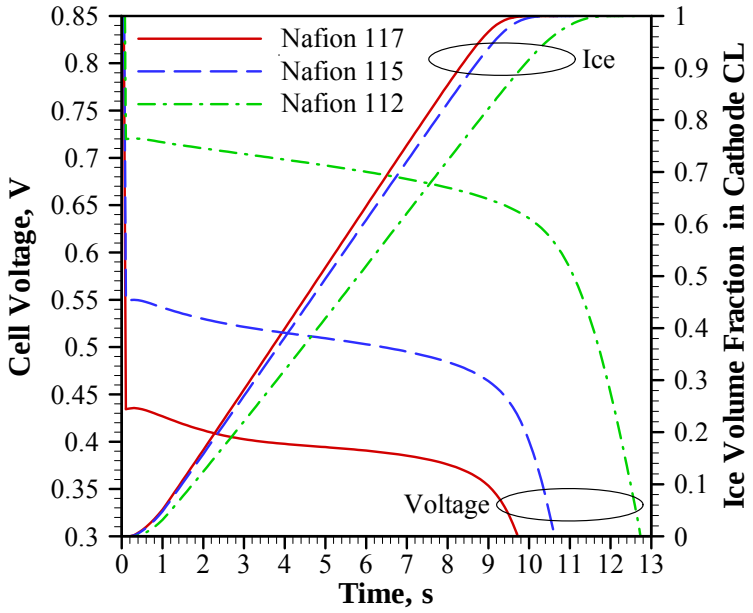

(b)

Figure 6.10: Effects of membrane thickness on cold start performance for potentiostatic (a: cell voltage is 0.3 V) and galvanostatic (b: current density is 0.15 A cm^{-2}) cold start processes from -20 ^{o}C.

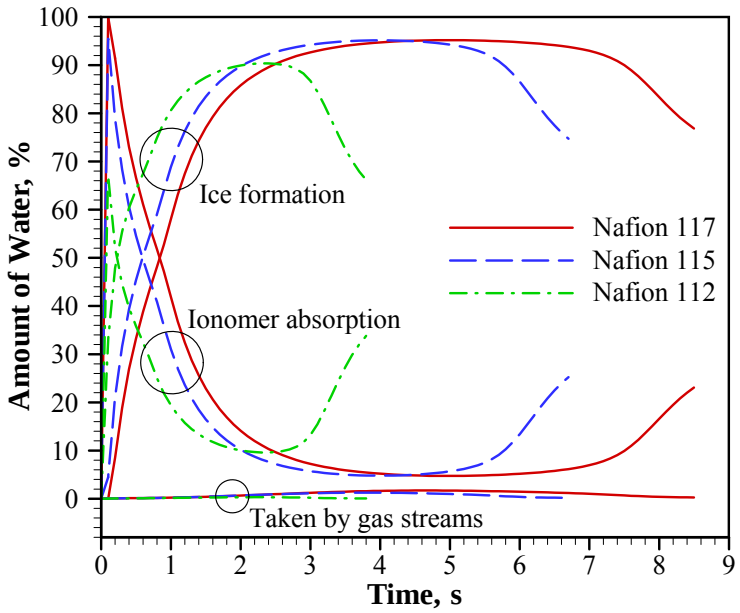

(a)

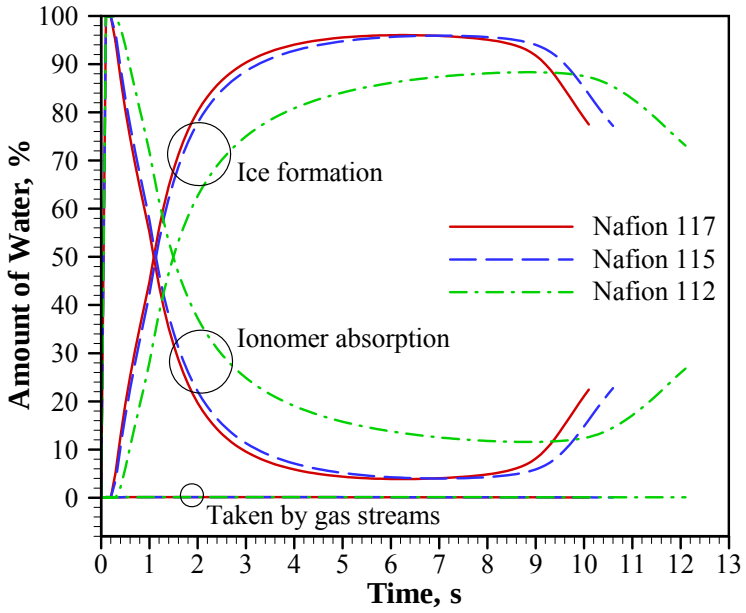

(b)

Figure 6.11: Evolutions of amounts of ice formation, amounts of water absorbed by ionomer, and amounts of water taken by gas streams for potentiostatic (a: cell voltage is 0.3 V) and galvanostatic (b: current density is 0.15 A cm^{-2}) cold start processes from -20 ^{o}C.

Figure 6.8 shows the contours of ice volume fraction in the CLs and GDLs in a y-z plane for the cold start process from -3 ^{o}C. The ice first melts in the CLs under the land (t = 1 s), then the whole CL and the GDL under the land, and finally the whole area. It is also observed that the ice melting in the anode is slightly faster than in the cathode, due to the faster heat transfer in the anode, as mentioned before. The contours of liquid water volume fraction in the CLs and GDLs in a y-z plane for the cold start process from -3 ^{o}C are presented in Figure 6.9. The locations of the liquid water formation match the locations of the ice melting in Figure 6.8. The liquid water in the cathode CL becomes the maximum at 3 s, and at 30 s, the liquid water in the anode is still decreasing and it remains almost unchanged in the cathode, this observation is consistent with the results shown in Figure 6.7.

6.2 Effect of Design

6.2.1 Membrane Thickness

The effects of membrane thickness on cold start performance for both the potentiostatic and galvanostatic cold start processes from -20 ^{o}C are shown in Figure 6.10. During a potentiostatic cold start process, the cell voltage is controlled while the current density varies and mainly depends on the cell voltage, temperature increment/decrement, ionomer hydration/dehydration and water freezing/melting. On the other hand, the current density is controlled during a galvanostatic cold start process and therefore the cell voltage changes. For the potentiostatic cold start processes in Figure 6.10a, it can be noticed that the highest current densities achieved during the cold start processes are about 0.19, 0.25 and 0.49 A cm^{-2} with Nafion 117, 115 and 112, respectively. Such significant difference among the three membranes is mainly attributed to the different ohmic losses, which are mainly caused by the difference in the membrane thickness. Since the membrane conductivities at subzero temperatures are much lower than at normal operating temperatures (e.g. the membrane conductivity with a water content of 15 at -20 ^{o}C is only about 10% of at 80 ^{o}C), the effects of membrane thickness on the cell performance are therefore more significant at subzero temperatures. Due to the fact that the water production rate is proportional to the current density, the ice formation process is the slowest with Nafion 117 and the quickest with Nafion 112, and the failure times of the cold start processes are about 8, 7, and 4 s with Nafion 117, 115 and 112, respectively. For the galvanostatic cold start processes in Figure 6.10b (the water production rates are same), different from the potentiostatic condition, the thinnest membrane results in the slowest ice formation process for the galvanostatic condition. The reason is that the Nafion 112 membrane can absorb water more quickly than the other two membranes (to be explained with Figure 6.11).

To further examine the effects of the membranes on the ice formation processes, the evolutions of amounts of ice formation, amounts of water absorbed by ionomer, and amounts of water taken by the gas streams for the potentiostatic (cell voltage is 0.3 V) and galvanostatic (current density is 0.15 A cm^{-2}) cold start processes from -20 ^{o}C are shown in Figure 6.11. All the water amounts shown in this figure are normalized by the amounts of the water production. The summation of the amount of water absorbed by the ionomer, amount of ice formation and amount of water taken by the gas streams is equal to the amount of the water production. Therefore, the normalized amounts of water in Figure 6.11 represent the percentages of the product water in different forms. In Figure 6.11a for the potentiostatic cold start process, it can be observed that the amount of water taken by the gas streams can be neglected, due to the fact that the saturation pressures of water vapour are very low at subzero

temperatures. Initially most of the product water is absorbed by the ionomer, and most of the absorbed water is in the cathode CLs. With the increments of the non-frozen water content in the ionomer of the cathode CLs, the saturation levels are reached, and then most of the product water becomes ice. Figure 6.11a shows that the Nafion 117 membrane is able to absorb the largest portions of the product water among the three membranes before the CLs are severely blocked by ice. However, for the galvanostatic cold start process in Figure 6.11b, the water production rates are the same for the different membranes (same current density), therefore it is more meaningful to compare the effects of membrane thickness on the ice formation. By using Nafion 112 the ionomer can absorb about 10% more of the product water than by using Nafion 115 and 117, and the reason is that a thinner membrane results in a larger water gradient across the membrane, hence faster water absorption. Even the thinnest membrane (Nafion 112) shows the greatest effect on reducing the ice formation, it should be mentioned that the thickness of membrane still needs to be sufficiently high to maintain enough water capacity to store the product water.

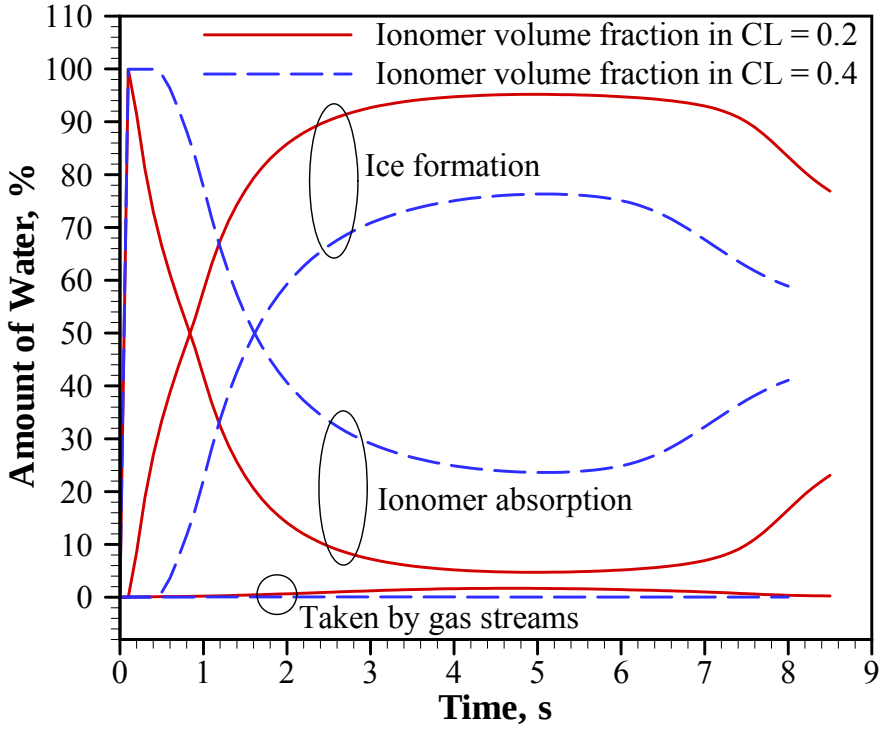

Figure 6.12: Evolutions of amounts of ice formation, amounts of water absorbed by ionomer, and amounts of water taken by gas streams when Nafion 117 is used for potentiostatic (cell voltage is 0.3 V) cold start processes from -20 ^{o}C with different ionomer volume fractions in CLs.

6.2.2 Ionomer Fraction in Cathode Catalyst Layer (CL)

With the same membrane, the effect of ionomer volume fraction on the ice formation is investigated in Figure 6.12. It can be observed that increasing the ionomer volume fraction in the CLs from 0.2 to

0.4 can absorb 20% more of the product water, which is a significant improvement in reducing the ice formation. One of the reasons is that the higher ionomer volume fraction increases the water capacity of the ionomer in the CLs; and another is that it also provides wider paths for the water transport in the CLs, therefore the membrane can absorb the product water in the cathode CLs more effectively.

6.3 Effect of Cell Conditions

6.3.1 Load Condition

The evolutions of the various heat generation rates, heat loss rates through BPs, and cell temperatures when Nafion 112 is used for both the potentiostatic and galvanostatic cold start processes from -20 ^{o}C are presented in Figure 6.13. During a cold start process, heat is generated from the electrochemical reactions (activational heat and reversible heat), electron and ion transport (ohmic heat), and water phase change (latent heat). For the potentiostatic cold start process in Figure 6.13a, the largest heating source is the ohmic heat, mainly due to the low membrane conductivity at subzero temperatures. The activational heat is the second largest heating source, followed by the reversible heat and latent heat. The heat loss is caused by the heat transfer at the outer surfaces of the BPs and by the outflow of the gas streams, and it has been found that the heat loss due to the outflow of the gas streams can be neglected by comparing with the heat loss from the BPs. For the galvanostatic cold start process in Figure 6.13b, the activational heat generation rates increase when the ice volume fractions are high, due to the fact that higher activational energy is needed to maintain the current density when the reaction area becomes smaller due to the ice blockage. The largest heating source is the activational heat, because the current density is lower than the potentiostatic condition in Figure 6.13a. The latent heat is the lowest. The heat losses to surroundings all increase with the increment of cell temperature for both the potentiostatic and galvanostatic cold start processes in Figure 6.13, and the cell temperature increments become slower during the cold start processes.

Since the highest possible current density varies during a cold start process due to the combined effects of the temperature increment/decrement, ionomer hydration/dehydration and water freezing/melting, operating at a low cell voltage can always ensure high heat generation rates during the entire cold start process (by ensuring high current densities at different time paces), while operating at a constant current density can only ensure high heat generation rates during part of the cold start process (if the upper limit of the current density becomes much higher than the operating current density, the heat generation rate is not the highest possible). With the previous discussions of Figures 6.10, 6.11 and 6.13, therefore, the potentiostatic condition is more favourable than the galvanostatic condition. In addition, since a low cell voltage results in a high current density and a high heat generation rate, it can be concluded that the potentiostatic condition with low cell voltages is the most favourable load condition for PEMFC cold start.

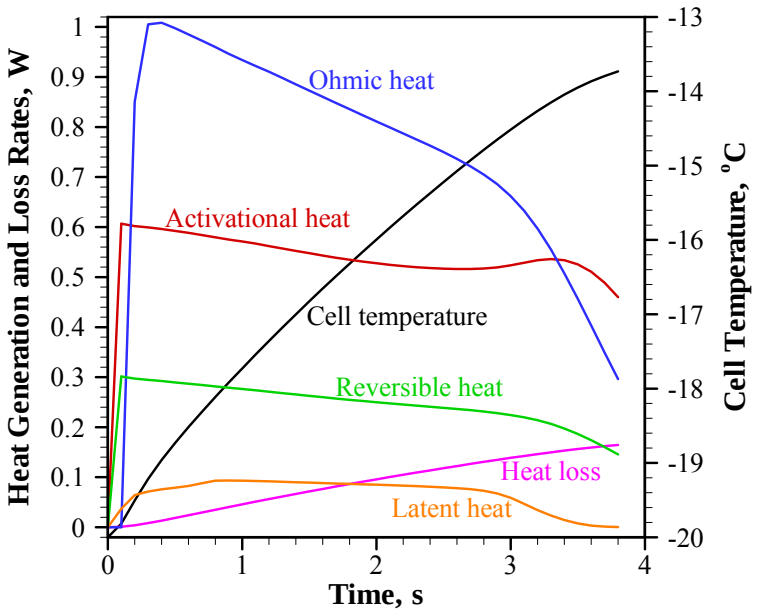

(a)

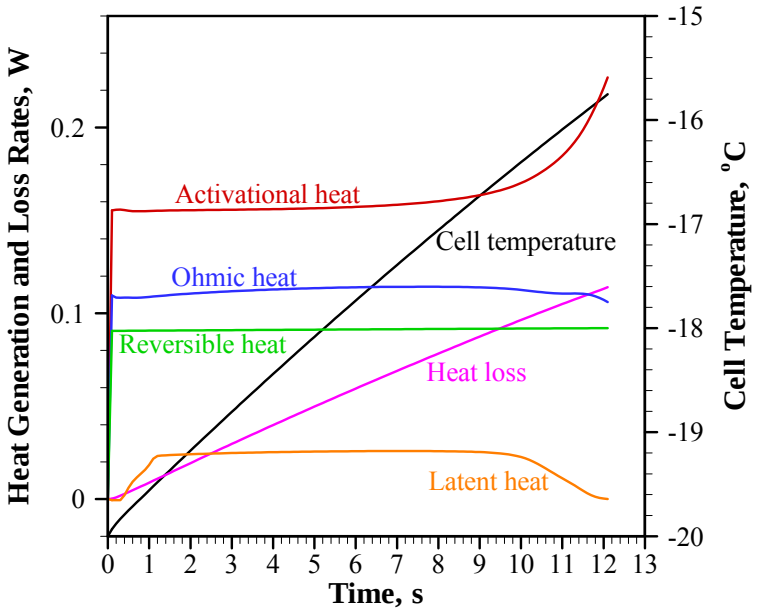

(b)

Figure 6.13: Evolutions of various heat generation rates, heat loss rates through BPs, and cell temperatures when Nafion 112 is used for potentiostatic (a: cell voltage is 0.3 V) and galvanostatic (b: current density is 0.15 A cm^{-2}) cold start processes from -20 °C.

6.3.2 Purging Duration

Figure 6.14 shows the evolutions of current density and ice volume fraction in the cathode CL from -10 ^{o}C, and the evolutions of various heat generation rates, heat loss rate through the surrounding walls, and cell temperature for the cold start process from -10 ^{o}C are presented in Figure 6.15. The cold start conditions in Figures 6.14 and 6.15 are the same to Figures 6.1 and 6.4, except that the initial water content and ice volume fractions in Figures 6.1 and 6.4 are 5 and 0.15, and they are 10 and 0.3 in Figures 6.14 and 6.16. Figures 6.14 and 6.15 correspond to a shorter purging time after operation, which leads to a higher amount of water left in the cell before cold start. Therefore, both the initial water content and ice volume fraction in Figures 6.14 and 6.15 are higher than in Figures 6.1 and 6.4.

The start-up current density is higher in Figure 6.14 than in Figure 6.1, due to the lower ohmic loss (higher water content). The ice formation takes place at the beginning of the cold start process in Figure 6.14 due to the high initial water content (the ionomer cannot absorb any more water). With high water production rates, the cold start process in Figure 6.14 only lasts about 5 s and then the cathode CL is fully covered by ice.

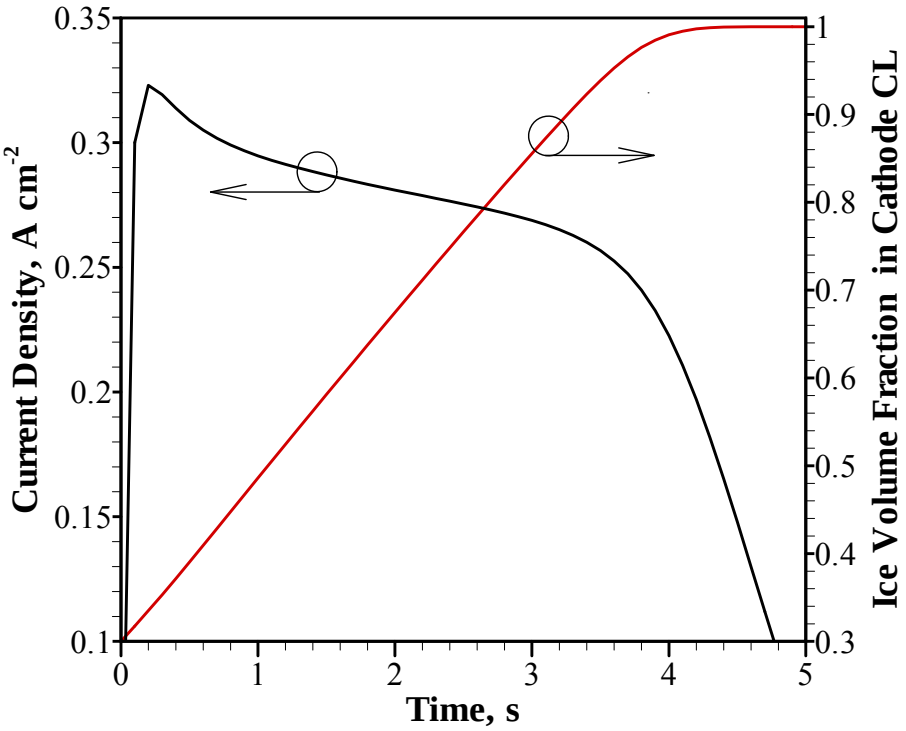

Figure 6.14: Evolutions of current density and ice volume fraction in cathode CL from -10 ^{o}C (same to Figures 6.1 and 6.4, except that the initial water content and ice volume fractions in Figures 6.1 and 6.4 are 5 and 0.15, and they are 10 and 0.3 in this figure).

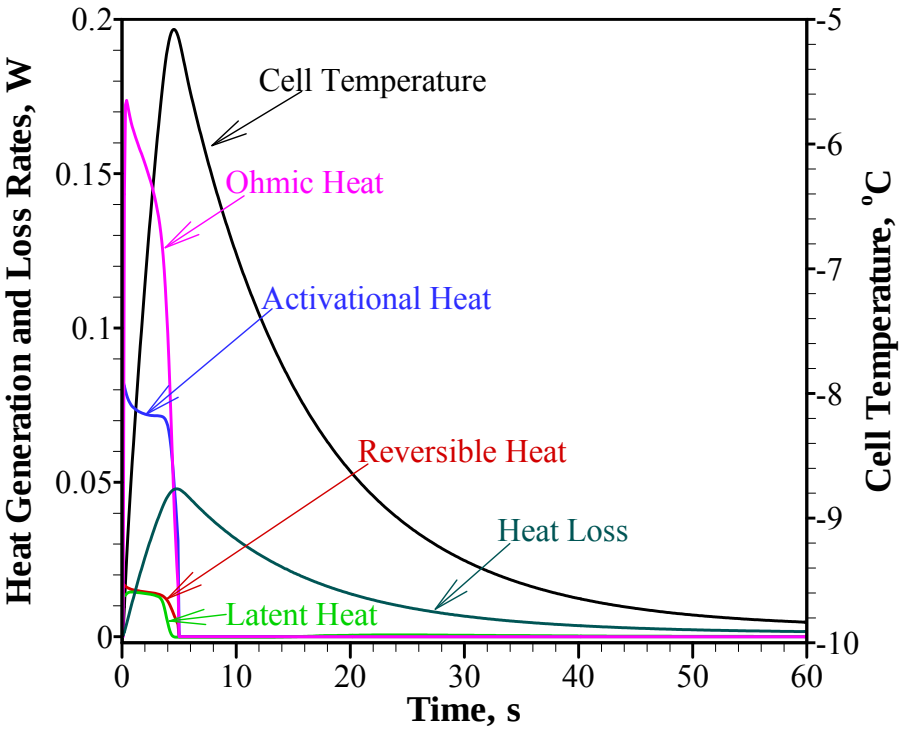

Figure 6.15: Evolutions of various heat generation rates, heat loss rate through surrounding walls, and cell temperature for the cold start process from -10 °C. (same to Figures 6.1 and 6.4, except that the initial water content and ice volume fractions in Figures 6.1 and 6.4 are 5 and 0.15, and they are 10 and 0.3 in this figure).

The heat generation rates in Figure 6.15 are much higher than in Figure 6.4. In Figure 6.15, the largest heating source is found to be the ohmic heat, and the activational heat in this case is about half of the ohmic heat. Such high ohmic heat is caused by the high current density in this case. Similar in these two figures, both the reversible heat and latent heat are still the lowest. In Figure 6.15, the cell reaches the maximum temperature (about -5 °C) when the cold start process is failed (about 5 s), this maximum temperature is lower than in Figure 6.4 (-3.5 °C), indicating that a low initial membrane water content is favourable for PEMFC cold start. The results suggest that effectively purging the cell is critically important for PEMFC cold start.

6.3.3 Humidification of Supplied Hydrogen

Since no ice formation is observed in the anode CL during the various cold start processes, and the ionomer in the anode CL dries out fast due to the EOD effect. Therefore, in Figure 6.16, the supplied hydrogen gas is humidified with an inlet relative humidity of 0.8 to hydrate the ionomer. The other conditions in Figure 6.16 are the same to Figures 6.1 and 6.4. However, the evolutions of current density and cell temperature in Figure 6.16 show almost indistinguishable results by comparing with Figures 6.1 and 6.4. The equation for water vapour saturation pressure (Equation 5.4) indicates that the saturation pressure of water vapour at -10 °C is 332.4 Pa, and it is 47311.2 Pa at 80 °C (a normal

operating temperature). This suggests that the inlet gas cannot carry enough amount of water at the subzero temperatures. Therefore, it can be concluded that humidifying the cold hydrogen at the anode inlet has negligible effects on the cold start performance.

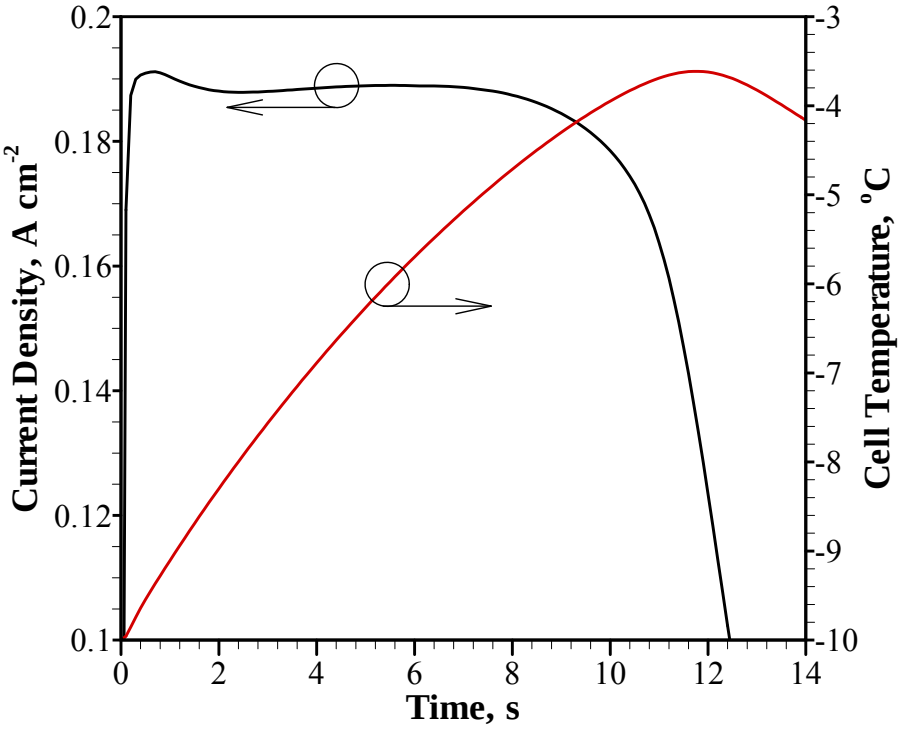

Figure 6.16: Evolutions of current density and cell temperature in cathode CL from -10 ^{o}C (same to Figures 6.1 and 6.4, except that non-humidified hydrogen is supplied in Figures 6.1 and 6.4, and the relative humidity of supplied hydrogen is 0.8 in this figure).

6.3.4 External Heating

Figure 6.17 presents the evolutions of current densities and cell temperatures for the self and assisted potentiostatic (cell voltage is 0.3 V) cold start processes from -20 ^{o}C. It can be noticed that cell insulation, heating the outer surface and inlet air can all accelerate the temperature increment. However, since all the cold start processes failed at about the same time (about 9 s), the ice formation rate is not effectively reduced. A heating power of 0.04 W cm^{-2} is needed to increase the cell temperature for 1 ^{o}C in 9 s when heating the outer surface. However, a heating power of only 0.01 W cm^{-2} is needed for the same effect when heating the inlet air. This indicates that heating the inlet air is more efficient than heating the outer surface, because heating the inlet air results in higher temperature increment in the CL, which increases the reaction rate and therefore the heat generation. However, heating on the outer surface is easier than heating the inlet air, because the inlet air must be heated to very high temperatures to carry enough amount of heat, or the inlet air flow rate needs to be significantly high.

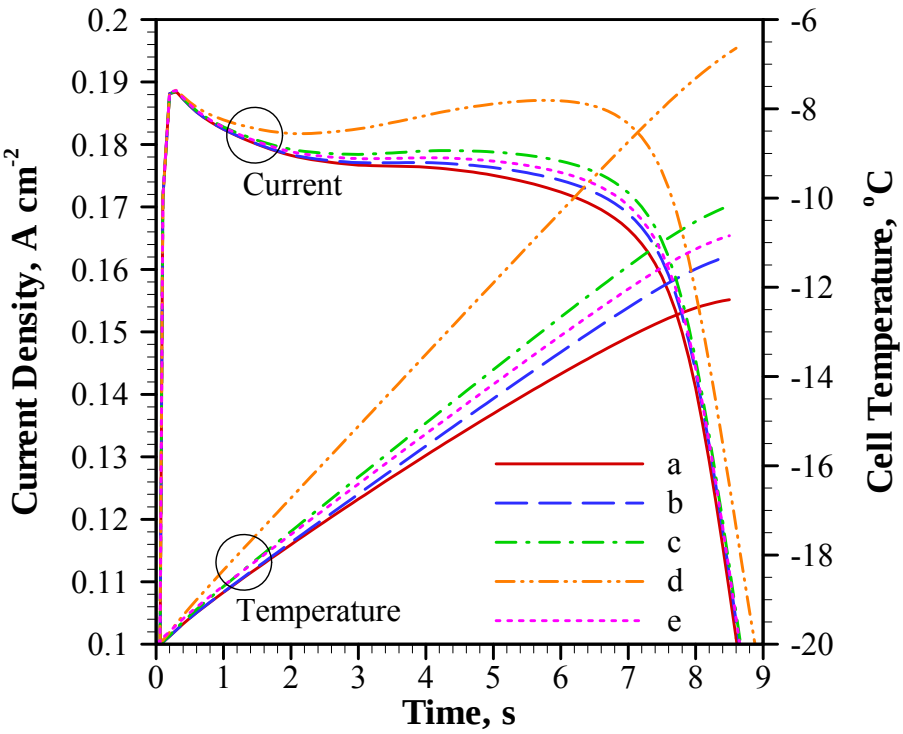

Figure 6.17: Evolutions of current densities and cell temperatures for self and assisted potentiostatic (cell voltage is 0.3 V) cold start processes from -20 ^{o}C (a: self cold start without cell insulation; b: cold start with cell insulation; c: cold start with 0.045 W cm^{-2} heating on outer surface and with cell insulation; d: cold start with 0.18 W cm^{-2} heating on outer surface and with cell insulation; e: cold start with inlet air heated to from -20 to 80 ^{o}C without cell insulation).

6.4 Comparison of Temperaure Evolution with Experimental Data

Figure 6.18 presents the comparison of temperature evolutions between the model prediction and expeiremtnal data. For the cold start process in this figure, the start-up temperature is -10 ^{o}C; the start-up current density is 0.07 A cm^{-2}; the stoichiometry ratios are 1.2 and 2.0 corresponding to the operating current density for the anode and cathode non-humidified inlet gases, respectively; the inlet gas temperatures are equal to the room temperature; and the membrane thickness is 50 μm.The solid line represents the volume averaged temperature of the cathode BP from the model prediciton, and the symbols are the average temperature of the sixteen thermocouples and the tempeatures of segments 1 (close to flow inlet) and 16 (close to flow outlet). Refer to Chapter 3 for the details of the measurmenet. It can be observed that the temperature evolutions do not agree as well as the voltage and current evolutions presented in Chatpter 5. Since the present model uses isotropic thermal conductivities of the MEA, further employing the non-isotropic properties are expected to provide

better agreement. In addition, rather than considering single straight flow channels, further multi-channel simulations according to the design of the tested PEMFC may also result in better agreement with the experimental data.

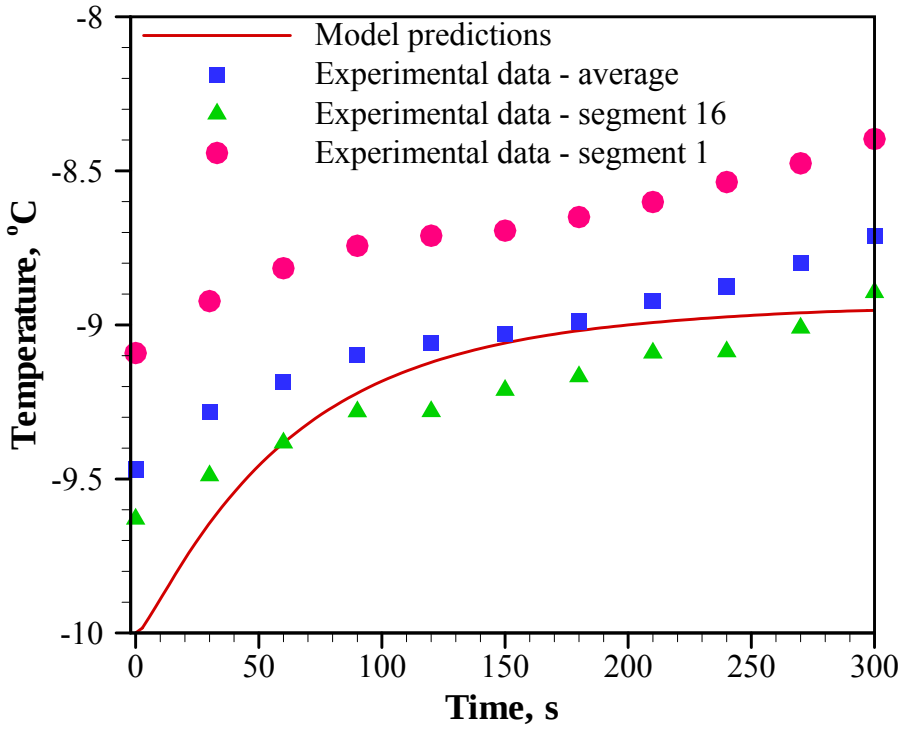

Figure 6.18: Comparison of temperature evolutions between model prediction and expeiremtnal data.

6.5 Summary

In this chapter, the results from the cold start model are presented. The transport phenomena and the effects of design and operating conditions on the cold start performance are investigated. During a failed cold start process, the ice first appears under the land and at the locations away from both the membrane/CL and GDL/CL interfaces. At low cell voltages, it is found that the ohmic heat is the largest heating source during the cold start processes, which reduces the temperature difference between the anode and cathode. During a successful cold start process, the ice melts first in the CLs and then in the GDLs, and the melting process first starts under the flow channel and then under the land. The melted water in the anode is also removed faster than in the cathode, due to both the water evaporation and the water absorption by the ionomer. A thinner membrane is more favourable in reducing the ice formation since it can result in a larger water gradient across the membrane thus accelerating the water absorption from the cathode CL into the membrane. However, the membrane thickness still needs to be kept sufficiently high to ensure a sufficient amount of water capacity to store the product water. The gas streams can only take negligible portion of the product water due to the low saturation pressures of water at subzero temperatures, and therefore has negligible

improvement in reducing the ice formation. Optimizing the ionomer volume fraction in the CLs is an effective way to decelerate the ice formation by increasing the water capacity of the ionomer in the CLs and accelerating the water diffusion into the membrane. The potentiostatic condition is more favourable than the galvanostatic condition for PEMFC cold start. Effectively purging the cell is critically important for PEMFC cold start. Humidifying the cold hydrogen at the anode inlet has negligible effects on the cold start performance. The external heating on the outer surfaces of PEMFCs results in direct improvements in raising the cell temperature, however, with negligible improvement in reducing the ice formation. Heating up the inlet air can increase the cell temperature more effectively than applying heat on the outer surfaces of PEMFCs. However, heating on the surfaces of PEMFCs may be easier to implement than heating the inlet air, because the inlet air must be heated to considerably high temperatures to carry enough amount of heat, otherwise the inlet air flow rate must be very high.

Chapter 7

Summary and Future Work

In this research, an experimental setup for proton exchange membrane fuel cell (PEMFC) cold start testing with simultaneous measurement of current and temperature distributions has been designed and built; a one-dimensional (1D) analytical model for quick estimate of purging duration has been formulated; and a comprehensive three-dimensional (3D) numerical model has been developed to simulate the cold start processes in PEMFC. Unique in the present cold start experiment is the inclusion of the simultaneous measurement of current and temperature distributions. Since most of the present numerical models are limited to either 1D or two-dimensional (2D) or 3D but only considering a section of the entire cell due to computational requirement, the measured distribution data are critically important to better understand the PEMFC cold start characteristics. By solving a complete set of conservation equations, the 3D numerical model comprehensively takes into account the various transport phenomena during PEMFC cold start processes. Unique in the present model is the inclusion of the following phenomena: (i) the water freezing in the membrane electrolyte and its effects on the membrane conductivity; (ii) the non-equilibrium mass transfer between the water in the ionomer and the water (vapour, liquid and ice) in the pore region of the catalys layer (CL); and (iii) both the water freezing and melting in the CL and gas diffsuon layer (GDL). This model therefore provides the fundamental framework for the future top-down multi-dimensional multiphase model of PEMFC.

The key conclusions from this research are

- the potentiostatic (constant voltage) condition is superior to the galvanostatic (constant current) condition, and increasing the start-up current density (decreasing the cell voltage) is favourable;
- the inlet and middle regions (according to cathode flow channel layout) are the most critical parts that generate most of the current and heat during the cold start processes, therefore, need to receive prior consideration in terms of external heating and design optimization;
- the start-up characteristics are mainly dominated by the cathode flow, and changing the flow arrangement has insignificant impact on the cold start performance;
- three ice formation mechanisms are proposed, corresponding to the ice formations in cathode CL, GDL and flow channel;
- the ice formation in cathode CL is the most common cause of the cold start failure, and the significant ice formations in cathode flow channel and GDL only occur in narrow temperature ranges when the temperature in cathode CL is higher than the freezing point of water but the temperature in the flow channel or GDL is lower;
- a thinner membrane is more favourable in reducing the ice formation since it can result in a larger water gradient across the membrane thus accelerating the water absorption from the cathode CL into the membrane, however, the membrane thickness still needs to be kept sufficiently high to ensure an enough water capacity to store the product water;

- optimizing the ionomer volume fraction in the CLs is an effective way to decelerate the ice formation by increasing the water capacity of the ionomer in the CLs and accelerating the water diffusion into the membrane;
- the gas streams can only take negligible portion of the product water due to the low saturation pressures of water at subzero temperatures, and therefore has negligible improvement in reducing the ice formation, for the same reason, humidifying the cold hydrogen at the anode inlet also has negligible effect on the cold start performance;
- effectively purging the cell is critically important to reduce the ice formation;
- the external heating on the outer surfaces of PEMFCs results in direct improvements in raising the cell temperature, however, with negligible improvement in reducing the ice formation; and
- heating up the inlet air can increase the cell temperature more efficiently than applying heat on the outer surfaces of PEMFCs, however, it is difficult for the inlet air to carry enough amount of heat.

This research also highlights some areas for future studies:

- the gas concentration distribution measurement can be implemented into the cold start experiment by inserting gas sampling ports into the tested PEMFC for more comprehensive results;
- optical windows can be made on the tested PEMFC with high speed charge-coupled device cameras for the visualization of ice formation processes during the cold start experiment;
- the cold start processes of industrial-size fuel cells and stacks can be simulated by using the numerical model developed in this research with more powerful computational power in terms of parallel processing, and can also be tested by using the experimental setup built in this research;
- in considering the industrial-size (multi-channel) simulations, the liquid water transport in the flow channels can be an important factor for successful cold start processes, therefore, the liquid water transport in flow channel needs to be formulated; and
- design of cathode CLs with unevenly distributed catalyst loading and ionomer fraction has a significant potential to improve the cold start performance, because the catalyst loading and ionomer fraction all have significant effects on the ice formation and heat generation rates, and the novel designs can be evaluated both experimentally and numerically with the cold start experiment and model developed in this research.

References

[1] Li X. Principles of fuel cells. New York: Taylor & Francis; 2006.

[2] Larminie J, Dicks A. Fuel cell systems explained. Chichester: John Wiley & Sons; 2003.

[3] O'Hayre R, Cha SW, Collela W, Prinz FB. Fuel cell fundamentals. New York: John Wiley & Sons; 2006.

[4] **Jiao K**, Li X. Water transport in polymer electrolyte membrane fuel cells. Progress in Energy and Combustion Science 2011; 37: 221-291.

[5] Springer TE, Zawodzinski TA, Wilson MS, Gottesfeld S. Characterization of polymer electrolyte fuel cells using AC impedance spectroscopy. Journal of Electrochemical Society 1996; 140: 587-599.

[6] Ralph TR, Hards GA, Keating JE, Campbell SA, Wilkinson DP, Davis M, St-Pierre J, Johnson MC. Low cost electrodes for proton exchange membrane fuel cells. Journal of Electrochemical Society 1997; 144: 3845-3857.

[7] Lee HK, Park JH, Kim DY, Lee TH. A study on the characteristics of the diffusion layer thickness and porosity of the PEMFC. Journal of Power Sources 2004; 131: 200-206.

[8] Jordan LR, Shukla AK, Behrsing T, Avery NR, Muddle BC, Forsyth M. Diffusion layer parameters influencing optimal fuel cell performance. Journal of Power Sources 2000; 86: 250-254.

[9] Park GG, Sohn YJ, Yang TH, Yoon YG, Lee WY, Kim CS. Effect of PTFE contents in the gas diffusion media on the performance of PEMFC. Journal of Power Sources 2004; 131: 182-187.

[10] Lin G, Nguyen TV. Effect of thickness and hydrophobic polymer content of the gas diffusion layer on electrode flooding level in a PEMFC. Journal of Electrochemical Society 2005; 152: A1942-A1948.

[11] Yan WM, Yang CH, Soong CY, Chen F, Mei SC. Experimental studies on optimal operating conditions for different flow field designs of PEM fuel cells. Journal of Power Sources 2006; 160: 284-292.

[12] Mughal A, Li X. Experimental diagnostics of PEM fuel cells. International Journal Environmental Studies 2006; 63: 377-389.

[13] Geiger AB, Tsukada A, Lehmann E, Vontobel P, Wokaun A, Scherer GG. In situ investigation of two-phase flow patterns in flow fields of PEFCs using neutron radiography. Fuel Cells 2002; 2: 92-98.

[14] Satija R, Jacobson DL, Arif M, Werner SA. In situ neutron imaging technique for evaluation of water management systems in operating PEM fuel cells. Journal of Power Sources 2004; 129: 238-245.

[15] Sinha PK, Halleck P, Wang CY. Quantification of liquid water saturation in a PEM fuel cell diffusion medium using X-ray microtomography. Electrochemical and Solid-State Letters 2006; 9: A344-A348.

[16] Tuber K, Pocza D, Hebling C. Visualization of water buildup in the cathode of a transparent PEM fuel cell. Journal of Power Sources 2003; 124: 403-414.

[17] Yang XG, Zhang FY, Lubawy AL, Wang CY. Visualization of liquid water transport in a PEFC. Electrochemical and Solid-State Letters 2004; 7: A408-A411.

[18] **Jiao K**, Park J, Li X. Experimental investigations on liquid water removal from the gas diffusion layer by reactant flow. Applied Energy 2010; 87: 2770-2777.

[19] Stumper J, Campell S, Wilkinson D, Johnson M, Davis M. In-situ methods for the determination of current distributions in PEM fuel cells. Electrochimica Acta 1998; 43: 3773-3783.

[20] Dong Q, Mench MM, Cleghorn S, Beuscher U. Distributed performance of polymer electrolyte fuel cells under low-humidity conditions. Journal of Electrochemical Society 2005; 152: A2114-A2122.

[21] Ghosh PC, Wuster T, Dohle H, Kimiaie N, Mergel J, Stolten D. In-situ approach for current distribution measurement in fuel cells. Journal of Power Sources 2006; 154: 184-191.

[22] Hogarth WH, Steiner J, Benziger JB, Hakenjos A. Spatially-resolved current and impedance analysis of a stirred tank reactor and serpentine fuel cell flow-field at low relative humidity. Journal of Power Sources 2007; 164: 464-471.

[23] Wilkinson M, Blanco M, Gu E, Martin J, Wilkinson D, Zhan J, Wang H. In situ experimental technique for measurement of temperature and current distribution in proton exchange membrane fuel cells. Electrochemical and Solid State Letters 2006; 9: A507-A511.

[24] Alaefour IE, Karimi G, **Jiao K**, Al Shakhshir S, Li X. Experimental study on the effect of reactant flow arrangements on the current distribution in proton exchange membrane fuel cells. Electrochimica Acta 2011; 56: 2591-2598.

[25] Zawodzinski TA, Neeman M, Sillerud LO, Gettesfeld S. Determination of water diffusion coefficients in perfluorosulfonate ionomeric membranes. Journal of Physical Chemistry 1991; 95: 6040-6044.

[26] Zawodzinski TA, Gottesfeld S, Shoichet S, McCarthy TJ. The contact angle between water and the surface of perfluorosulphonic acid membranes. Journal of Applied Electrochemistry 1993; 23: 86-88.

[27] Gostick JT, Fowler MW, Pritzker MD, Ioannidis MA, Behra LM. In-plane and through-plane gas permeability of carbon fiber electrode backing layers. Journal of Power Sources 2006; 162: 228-238.

[28] Gostick JT, Fowler MW, Ioannidis MA, Pritzker MD, Volfkovich YM, Sakars A. Capillary pressure and hydrophilic porosity in gas diffusion layers for polymer electrolyte fuel cells. Journal of Power Sources 2006; 156: 375-387.

[29] Cheng X, Yi B, Han M, Zhang J, Qiao Y, Yu J. Investigation of platinum utilization and morphology in catalyst layer of polymer electrolyte fuel cells. Journal of Power Sources 1999; 79: 75-81.

[30] Tan J, Chao YJ, Van Zee JW, Lee WK. Degradation of elastomeric gasket materials in PEM fuel cells. Materials and Science Engineering A 2007; 445-446: 669-675.

[31] Zamel N, Astrath NGC, Li X, Shen J, Zhou J, Astrath FBG, Wang H, Liu ZS. Experimental measurements of effective diffusion coefficient of oxygen-nitrogen mixture in PEM fuel cell diffusion media. Chemical Engineering Science 2010; 65: 931-937.

[32] Zamel N, Litovsky E, Al Shakhshir S, Li X, Kleiman J. Measurement of in-plane thermal conductivity of carbon paper diffusion media in the temperature range of -20 oC to +120 oC. Applied Energy 2011; Submitted.

[33] Tajiri K, Tabuchi Y, Wang CY. Isothermal cold start of polymer electrolyte fuel cells. Journal of Electrochemical Society 2007; 154: B147-B152.

[34] Tajiri K, Tabuchi Y, Kagami F, Takahashi S, Yoshizawa K, Wang CY. Effects of operating and design parameters on PEFC cold start. Journal of Power Sources 2007; 165: 279-286.

[35] Hou J, Yu H, Zhang S, Sun S, Wang H, Yi B, Ming P. Analysis of PEMFC freeze Degradation at -20 °C after gas purging. Journal of Power Sources 2006; 162: 513-520.

[36] Hou J, Yi B, Yu H, Hao L, Song W, Fu Y, Shao Z. Investigation of resided water effects on PEM fuel cell after cold start. International Journal of Hydrogen Energy 2007; 32: 4503-4509.

[37] Cho EA, Ko JJ, Ha HY, Hong SA, Lee KY, Lim TW, Oh IH. Characteristics of the PEMFC repetitively brought to temperatures below 0 °C. Journal of Electrochemical Society 2003; 150: A1667-A1670.

[38] Cho EA, Ko JJ, Ha HY, Hong SA, Lee KY, Lim TW, Oh IH. Effects of water removal on the performance degradation of PEMFCs repetitively brought to < 0°C. Journal of Electrochemical Society 2004; 151: A661-A665.

[39] Guo Q, Qi Z. Effect of freeze-thaw cycles on the properties and performance of membrane-electrode assemblies. Journal of Power Sources 2006; 160: 1269-1274.

[40] Thompson EL, Jorne J, Gasteiger HA. Oxygen reduction reaction kinetics in subfreezing PEM fuel cells. Journal of Electrochemical Society 2007; 154: B783-B792.

[41] Yan Q, Toghiani H, Lee YW, Liang K, Causey H. Effect of sub-freezing temperatures on a PEM fuel cell performance, startup and fuel cell components. Journal of Power Sources 2006; 160: 1242-1250.

[42] St-Pierre J, Roberts J, Colbow K, Campbell S, Nelson A. PEMFC operational and design strategies for sub zero environments. Journal of New Materials for Electrochemical Systems 2005; 8: 163-176.

[43] Ge S, Wang CY. In situ imaging of liquid water and ice formation in an operating PEFC during cold start. Electrochemical and Solid-State Letters 2006; 9: A499-A503.

[44] Ge S, Wang CY. Characteristics of subzero startup and water/ice formation on the catalyst layer in a polymer electrolyte fuel cell. Electrochimica Acta 2007; 52: 4825-4835.

[45] Ishikawa Y, Morita T, Nakata K, Yoshida K, Shiozawa M. Behavior of water below the freezing point in PEFCs. Journal of Power Sources 2007; 163: 708-712.

[46] Sun S, Yu H, Hou J, Shao Z, Yi B, Ming P, Hou Z. Catalytic hydrogen/oxygen reaction assisted the proton exchange membrane fuel cell (PEMFC) startup at subzero temperature. Journal of Power Sources 2008; 177: 137-141.

[47] McDonald RC, Mittelsteadt CK, Thompson EL. Effects of deep temperature cycling on Nafion 112 membranes and membrane electrode assemblies. Fuel Cells 2004; 4: 208-213.

[48] Cappadonia M, Erning JW, Stimming U. Proton conduction of Nafion 117 membrane between 140 K and room temperature. Journal of Electroanalytical Chemistry 1994; 376: 189-193.

[49] Cappadonia M, Erning JW, Saberi Niaki SM, Stimming U. Conductance of Nafion 117 membranes as a function of temperature and water content. Solid State Ionics 1995; 77: 65-69.

[50] Thompson EL, Capehart TW, Fuller TJ, Jorne J. Investigation of low-temperature proton transport in Nafion using direct current conductivity and differential scanning calorimetry. Journal of Electrochemical Society 2006; 153: A2351-A2362.

[51] Springer TE, Zawodzinski TA, Gottesfeld S. Polymer electrolyte fuel cell model. Journal of Electrochemical Society 1991; 138: 2334-2342.

[52] Springer TE, Wilson MS, Gottesfeld S. Modeling and experimental diagnostics in polymer electrolyte fuel cells. Journal of Electrochemical Society 1993; 140: 3513-3526.

[53] Bernardi DM, Verbrugge MW. A mathematical model of the solid-polymer-electrolyte fuel cell. Journal of Electrochemical Society 1992; 139: 2477-2491.

[54] Bernardi DM, Verbrugge MW. Mathematical model of a gas diffusion electrode bonded to a polymer electrolyte. AIChE Journal 1991; 37: 1151-1163.

[55] Um S, Wang CY, Chen KS. Computational fluid dynamics modeling of proton exchange membrane fuel cells. Journal of Electrochemical Society 2000; 147: 4485-4493.

[56] Dutta S, Shimpalee S, Van Zee JW. Three-dimensional numerical simulation of straight channel PEM fuel cells. Journal of Applied Electrochemistry 2000; 30: 135-146.

[57] Hontanon E, Escudero MJ, Bautista C, Garcia-Ybarra PL, Daza L. Optimisation of flow-field in polymer electrolyte membrane fuel cells using computational fluid dynamics techniques. Journal of Power Sources 2000; 86: 363-368.

[58] Cha SW, O'Hayre R, Saito Y, Prinz FB. The scaling behavior of flow patterns: a model investigation. Journal of Power Sources 2004; 134: 57-71.

[59] Kulikovsky AA. Numerical simulation of a new operational regime for a polymer electrolyte fuel cell. Electrochemistry Communications 2001; 3: 460-466.

[60] Wang ZH, Wang CY, Chen KS. Two phase flow and transport in the air cathode of proton exchange membrane fuel cells. Journal of Power Sources, 2001; 94: 40-50.

[61] You L, Liu H. A two-phase flow and transport model for the cathode of PEM fuel cells. International Journal of Heat and Mass Transfer 2002; 45: 2277-2287.

[62] Pasaogullari U, Wang CY. Two-phase modeling and flooding prediction of polymer electrolyte fuel cells. Journal of Electrochemical Society 2005; 152: A380-A390.

[63] Meng H, Wang CY. New model of two-phase flow and flooding dynamics in polymer electrolyte fuel cells. Journal of Electrochemical Society 2005; 152: A1733-1741.

[64] Wang Y, Wang CY. A non-isothermal, two-phase model for polymer electrolyte fuel cells. Journal of Electrochemical Society 2006; 153: A1193-1200.

[65] Ye Q, Nguyen TV. Three-dimensional simulation of liquid water distribution in a PEMFC with experimentally measured capillary functions. Journal of Electrochemical Society 2007; 154: B1242-1251.

[66] Wang Y, Wang CY. Two-phase transients of polymer electrolyte fuel cells. Journal of Electrochemical Society 2007; 154: B636-B643.

[67] Wu H, Li X, Berg P. On the modeling of water transport in polymer electrolyte membrane fuel cells. Electrochimica Acta 2009; 54: 6913-6927.

[68] Wu H, Berg P, Li X. Steady and unsteady 3D non-isothermal modeling of PEM fuel cells with the effect of non-equilibrium phase transfer. Applied Energy 2009; 87: 2778-2784.

[69] **Jiao K**, Li X. Effect of surface dynamic wettability in proton exchange membrane fuel cells. International Journal of Hydrogen Energy 2010; 35: 9095-9103.

[70] Wu H, Berg P, Li X. Modeling of PEMFC transients with finite-rate phase-transfer processes. Journal of Electrochemical Society 2010; 157: B1-B12.

[71] **Jiao K**, Zhou B, Quan P. Liquid water transport in parallel serpentine channels with manifolds on cathode side of a PEM fuel cell stack. Journal of Power Sources 2006; 154: 124-137.

[72] **Jiao K**, Zhou B, Quan P. Liquid water transport in straight micro-parallel-channels with manifolds for PEM fuel cell cathode. Journal of Power Sources 2007; 157: 226-243.

[73] **Jiao K**, Zhou B. Innovative gas diffusion layers and their water removal characteristics in PEM fuel cell cathode. Journal of Power Sources 2007; 169: 296-314.

[74] **Jiao K**, Zhou B. Effects of electrode wettabilities on liquid water behaviours in PEM fuel cell cathode. Journal of Power Sources 2008; 175: 106-119.

[75] **Jiao K**, Zhou B. Accelerated numerical test of liquid behaviour across gas diffusion layer in PEM fuel cell cathode. Journal of Fuel Cell Science and Technology 2009; 5: 041011-1-041001-10.

[76] Mondal B, **Jiao K**, Li X. Three-dimensional simulation of water droplet movement in PEM fuel cell flow channels with hydrophilic surfaces. International Journal of Energy Research 2010; In Press, DOI: 10.1002/er.1776.

[77] Mondal B, **Jiao K**, Li X. Three-dimensional simulation of water droplet movement in PEM fuel cell flow channels with hydrophobic surfaces. International Journal of Energy Research 2010; Submitted.

[78] Meng H, Wang CY. Large-scale simulation of polymer electrolyte fuel cells by parallel computing. Chemical Engineering Science 2004; 59: 3331-3343.

[79] Ju H, Wang CY. Experimental validation of a PEM fuel cell model by current distribution data. Journal of Electrochemical Society 2004; 151: A1954-A1960.

[80] Ju H, Wang CY, Cleghorn S, Beuscher U. Nonisothermal modeling of polymer electrolyte fuel cells. Journal of Electrochemical Society 2005; 152; A1645-A1653.

[81] Wang Y, Wang CY. Ultra large-scale simulation of polymer electrolyte fuel cells. Journal of Power Sources 2006; 153: 130-135.

[82] Sinha PK, Wang CY. Pore-network modeling of liquid water transport in gas diffusion layer of a polymer electrolyte fuel cell. Electrochimica Acta 2007; 52: 7936-7945.

[83] Sinha PK, Mukherjee PP, Wang CY. Impact of GDL structure and wettability on water management in polymer electrolyte fuel cells. Journal of Materials Chemistry 2007; 17: 3089-3103.

[84] Schulz VP, Becker J, Wiegmann A, Mukherjee PP, Wang CY. Modeling of two-phase behavior in the gas diffusion medium of PEFCs via full morphology approach. Journal of Electrochemical Society 2007; 154: B419-B426.

[85] Park J, **Jiao K**, Li X. Numerical investigations on liquid water removal from the porous gas diffusion layer by reactant flow. Applied Energy 2010; 87: 2180-2186.

[86] Zamel N, Li X, Shen J, Becker J, Wiegmann A. Estimating effective thermal conductivity in carbon paper diffusion media. Chemical Engineering Science 2010; 65: 3994-4006.

[87] Zamel N, Li X, Shen J. Correlation for the effective gas diffusion coefficient in carbon paper diffusion media. Energy Fuels 2010; 23: 6070-6078.

[88] Zamel N, Li X, Becker J, Wiegmann A. Effect of liquid water on transport properties of the gas diffusion layer of polymer electrolyte membrane fuel cells. International Journal of Hydrogen Energy 2011; In Press, doi:10.1016/j.ijhydene.2011.01.146.

[89] Sundaresan M, Moore RM. Polymer electrolyte fuel cell stack thermal model to evaluate sub-freezing startup. Journal of Power Sources 2005; 145: 534-545.

[90] Khandelwal M, Lee S, Mench MM. One-dimensional thermal model of cold-start in a polymer electrolyte fuel cell stack. Journal of Power Sources 2007; 172: 816-830.

[91] Mao L, Wang CY. Analysis of cold start in polymer electrolyte fuel cells. Journal of Electrochemical Society 2007; 154: B139-B146.

[92] Wang Y. Analysis of the key parameters in the cold start of polymer electrolyte fuel cells. Journal of Electrochemical Society 2007; 154: B1041-B1048.

[93] Wang Y, Mukherjee PP, Mishler J, Mukundan R, Borup RL. Cold start of polymer electrolyte fuel cells: three-stage startup characterization. Electrochimica Acta 2010; 55: 2636-2644.

[94] Ahluwalia RK, Wang X. Rapid self-start of polymer electrolyte fuel cell stacks from subfreezing temperatures. Journal of Power Sources 2006; 162: 502-512.

[95] Mao L, Wang CY, Tabuchi Y. A multiphase model for cold start of polymer electrolyte fuel cells. Journal of Electrochemical Society 2007; 154: B341-B351.

[96] Meng H. A PEM fuel cell model for cold-start simulations. Journal of Power Sources 2008; 178: 141-150.

[97] Meng H. Numerical studies of cold-start phenomenon in PEM fuel cells. Electrochimica Acta 2008; 53: 6521-6529.

[98] Jiang F, Fang W, Wang CY. Non-isothermal cold start of polymer electrolyte fuel cells. Electrochimica Acta 2007; 53: 610-621.

[99] Jiang F, Wang CY, Chen KS. Current ramping - a strategy for rapid startup of PEM fuel cells from subfreezing environment. Journal of Electrochemical Society 2010; 157: B342-347.

[100] **Jiao K**, Alaefour IE, Karimi G, Li X. Simultaneous measurement of current and temperature distributions in a proton exchange membrane fuel cell during cold start processes. Electrochimica Acta 2011; 56: 2967-2982.

[101] **Jiao K**, Alaefour IE, Karimi G, Li X. Cold start characteristics of proton exchange membrane fuel cells. International Journal of Hydrogen Energy 2011; Submitted.

[102] **Jiao K**, Li X. Three-dimensional multiphase modeling of cold start processes in polymer electrolyte membrane fuel cells. Electrochimica Acta 2009; 54: 6876-6891.

[103] **Jiao K**, Li X. Effects of various operating and initial conditions on cold start performance of polymer electrolyte membrane fuel cells. International Journal of Hydrogen Energy 2009; 34: 8171-8184.

[104] **Jiao K**, Li X. Cold start analysis of polymer electrolyte membrane fuel cells. International Journal of Hydrogen Energy 2010; 35: 5077-5094.

[105] Yoshida H, Miura Y. Behavior of water in perfluorinated ionomer membranes containing various monovalent cations. Journal of Membrane Science 1992; 68: 1-10.

[106] Pineri M, Volino F, Escoubes M. Evidence for sorption-desorption phenomena during thermal cycling in highly hydrated perfluorinated membranes. Journal of Polymer Science Part B: Polymer Physics 1985; 23: 2009-2020.

[107] Nakamura K, Hatekeyama T, Hatekeyama H. Relationship between hydrogen bonding and bound water in polyhydroxystyrene derivatives. Polymer 1983; 24: 871-876.

[108] Kim YS, Dong L, Hickner MA, Glass TE, Webb V, McGrath JE. State of water in disulfonated poly(arylene ether sulfone) copolymers and a perfluorosulfonic acid copolymer (Nafion) and its effect on physical and electrochemical properties. Macromolecules 2003; 36: 6281-6285.

[109] Siu A, Schmeisser J, Holdcroft S. Effect of water on the low temperature conductivity of polymer electrolytes. Journal of Physical Chemistry B 2006; 110: 6072-6080.

[110] Lide DR, editors. CRC handbook of chemistry and physics, 88th ed. Boca Raton: CRC Press/Taylor and Francis; 2007.

[111] http://www.btinternet.com/~martin.chaplin/explan.html#a

[112] FLUENT 6.3 Documentation, 2006.

[113] He W, Yi JS, Nguyen TV. Two-phase flow model of the cathode of PEM fuel cells using interdigitated flow fields. AIChE Journal 2000; 46: 2053-2064.

[114] Bird RB, Stewart WE, Lightfoot EN. Transport phenomena. New York: John Wiley & Sons; 1960.

[115] Dullien FAL. Porous media: fluid transport and pore structure. 2ed ed. San Diego: Academic Press; 1992.

[116] Udell KS. Heat transfer in porous media considering phase change and capillarity - the heat pipe effect. International Journal of Heat and Mass Transfer 1985; 28: 485-495.

[117] Kurz W, Fisher J. Fundamentals of solidification. Aedermannsdorf: Trans Tech Publications; 1989.

[118] Motupally S, Becker AJ, Weidner JW. Diffusion of water in Nafion 115 membranes. Journal of Electrochemical Society 2000; 147: 3171-3177.

[119] Ostrovskii VE, Gostev BV. Heat effects and rates and molecular mechanisms of water sorption by perfluorinated polymer materials bearing functional groups. Journal of Thermal Analysis and Calorimetry 1996; 46: 397-416.

[120] Wang CY. Fundamental models for fuel cell engineering. Chemical Reviews 2004; 104: 4727-4766.

[121] Bradean R, Haas H, Desousa A, Rahmani R, Fong K, Eggen K, Ayotte D, Huang A. 2005 ACS Annual Meeting-Fuel Processing Session I: Modeling and System Integration, Cincinnati, OH, October 30 - November 4, 2005.

Appendix A

Sample Code of Purging Model

```
//-------------------------------------------------------------------------------//
//                          PEMFC Purging Model
//-------------------------------------------------------------------------------//

#include <iostream.h>
#include <fstream.h>
#include <stdio.h>
#include <stdlib.h>
#include <math.h>
#include <iomanip.h>
#include <string>


//-------------------------------------------------------------------------------//
//                           User Input
//-------------------------------------------------------------------------------//

double dt = 0.00001; /* time step size, in second */
double tt = 9210; /* total purging time, in second */

double T = 298.15; /* purging temperature, in K */

double flow_a = 0.0000375/3.0; /* anode purging flow rate, m3/s */
double flow_c = 0.00005/3.0; /* cathode purging flow rate, m3/s */

double A_act = 0.004; /* flat active reaction area, m2 */
double A_ch = 0.002; /* area between flow channel and GDL, m2 */

double roh_mem = 1980.0; /* dry density of membrane, kg/m3 */
double EW = 1100.0; /* equivalent weight of membrane, kg/kmol */

double th_mem = 0.00005; /* membrane thickness, m */
double th_cl = 0.00001; /* catalyst layer thickness, m */
double th_gdl = 0.0002; /* GDL thickness, m */
double th_ch = 0.001; /* channel depth, m */

double por_cl = 0.3; /* catalyst layer porosity */
double por_gdl = 0.71; /* GDL porosity */

double lm = 0.2; /* ionomer volume fraction in catalyst layer */

double kv = 1.0; /* water desorption rate, s-1 */

double R_gas = 8314.0; /* universal gas constant, J/kmol-K */
```

```
//--------------------------------------------------------------------------//
//                          Member Functions
//--------------------------------------------------------------------------//

double Get_P_sat()          /* saturation pressure of vapour, Pa */
{
        double P_sat;
        double dT = T - 273.15;
        double exponent = -2.1794 + 0.02953*dT - 9.1837e-5*dT*dT + 1.4454e-7*dT*dT*dT;

        P_sat = pow(10.,exponent) * 101325.0;

        return P_sat;
}


double Get_Diff()         /* binary diffusivity between vapour and N2, m2/s */
{
        return 0.0000248*pow((T/298.15),1.5);
}


double Get_Diff_cl_gdl()          /* effective diffusivity between vapour and N2 from CL to GDL,
m2/s */
{
        double diff = 0.0000248*pow((T/298.15),1.5);
        return (th_cl/2.0 + th_gdl/2.0) / (th_cl/2.0/(diff*pow(por_cl,0.5)) +
th_gdl/2.0/(diff*pow(por_gdl,0.5)));
}


double Get_Diff_gdl()         /* effective diffusivity in GDL, m2/s */
{
        return 0.0000248*pow((T/298.15),1.5)*pow(por_gdl,0.5);
}


double Get_Diff_lm(double lam)    /* water diffusivity in ionomer, m2/s */
{
        double D_wm;

        if (lam < 0.0) lam = 0.0;
        if (lam > 17.0)  lam = 17.0;

        if (lam > 0 && lam <= 3.0) D_wm = 3.1e-7*lam*(exp(0.28*lam)-1.0)*exp(-2346.0/T);
        else D_wm = 4.17e-8*lam*(1.0+161.0*exp(-lam))*exp(-2346.0/T);
```

```
        return D_wm;
}


double Get_Diff_mem_cl(double lam_cl, double lam_mem)    /* effective water diffusivity from
membrane to CL, m2/s */
{
        return (th_mem/2.0 + th_cl/2.0) / (th_mem/2.0/Get_Diff_lm(lam_mem) +
th_cl/2.0/(Get_Diff_lm(lam_cl)*pow(lm,0.5)));
}


double Get_eqlam(double con)        /* equilibrium water content in ionomer of CL, unit of input:
kmol/m3 */
{
        double act = con*R_gas*T/Get_P_sat();

        return 0.04 + 17.81*act -39.85*act*act + 36.0*act*act*act;
}


//-------------------------------------------------------------------------------//
//                          Main Calculation
//-------------------------------------------------------------------------------//

void main()
{
   ofstream myfile;
   myfile.open ("results.txt");

   int N_time = tt/dt;
        int i;
        double t;

   /* initial values */
   double cf_a = 0.0;
        double cf_c = 0.0;
   double cgdl_a = Get_P_sat()/R_gas/T;
        double cgdl_c = Get_P_sat()/R_gas/T;
        double ccl_a = Get_P_sat()/R_gas/T;
        double ccl_c = Get_P_sat()/R_gas/T;
        double lamcl_a = Get_eqlam(ccl_a);
        double lamcl_c = Get_eqlam(ccl_c);
        double lammem = Get_eqlam((ccl_a+ccl_c)/2.0);

   for (i = 0; i <= N_time; i++)
   {
      t = i*dt;
```

```
if (cf_a < 0.0) cf_a = 0.0;
if (cf_c < 0.0) cf_c = 0.0;

double cf_a_p = cf_a;
double cf_c_p = cf_c;
double cgdl_a_p = cgdl_a;
double cgdl_c_p = cgdl_c;
double ccl_a_p = ccl_a;
double ccl_c_p = ccl_c;
double lamcl_a_p = lamcl_a;
double lamcl_c_p = lamcl_c;
double lammem_p = lammem;

if (i == 0)
{
cout << setw(1) << t << setw(16) << setprecision(10) << cf_a << setw(16) <<
setprecision(10) << cf_c << setw(16) << setprecision(10) << cgdl_a << setw(16) <<
setprecision(10) << cgdl_c << setw(16) << setprecision(10) << ccl_a << setw(16) <<
setprecision(10) << ccl_c << setw(16) << setprecision(10) << lamcl_a << setw(16)
<< setprecision(10) << lamcl_c << setw(16) << setprecision(10) << lammem <<
endl;
myfile << setw(1) << t << setw(16) << setprecision(10) << cf_a << setw(16) <<
setprecision(10) << cf_c << setw(16) << setprecision(10) << cgdl_a << setw(16) <<
setprecision(10) << cgdl_c << setw(16) << setprecision(10) << ccl_a << setw(16) <<
setprecision(10) << ccl_c << setw(16) << setprecision(10) << lamcl_a << setw(16)
<< setprecision(10) << lamcl_c << setw(16) << setprecision(10) << lammem <<
endl;
}

else
{
cf_a = cf_a_p + ((cgdl_a_p-cf_a_p)/(th_gdl/2.0)*Get_Diff_gdl()*A_act -
flow_a*cf_a_p)*dt/(A_ch*th_ch);
cf_c = cf_c_p + ((cgdl_c_p-cf_c_p)/(th_gdl/2.0)*Get_Diff_gdl()*A_act -
flow_c*cf_c_p)*dt/(A_ch*th_ch);
cgdl_a = cgdl_a_p + ((ccl_a_p-
cgdl_a_p)/(th_gdl/2.0+th_cl/2.0)*Get_Diff_cl_gdl()*A_act - (cgdl_a_p-
cf_a_p)/(th_gdl/2.0)*Get_Diff_gdl()*A_act)*dt/(A_act*th_gdl*por_gdl);
cgdl_c = cgdl_c_p + ((ccl_c_p-
cgdl_c_p)/(th_gdl/2.0+th_cl/2.0)*Get_Diff_cl_gdl()*A_act - (cgdl_c_p-
cf_c_p)/(th_gdl/2.0)*Get_Diff_gdl()*A_act)*dt/(A_act*th_gdl*por_gdl);
ccl_a = ccl_a_p + ((lamcl_a_p-
Get_eqlam(ccl_a_p))*kv*roh_mem/EW*A_act*th_cl*por_cl - (ccl_a_p-
cgdl_a_p)/(th_gdl/2.0+th_cl/2.0)*Get_Diff_cl_gdl()*A_act)*dt/(A_act*th_cl*por_cl)
;
ccl_c = ccl_c_p + ((lamcl_c_p-
Get_eqlam(ccl_c_p))*kv*roh_mem/EW*A_act*th_cl*por_cl - (ccl_c_p-
cgdl_c_p)/(th_gdl/2.0+th_cl/2.0)*Get_Diff_cl_gdl()*A_act)*dt/(A_act*th_cl*por_cl)
;
```

```
                lamcl_a = lamcl_a_p + ((lammem_p-
                lamcl_a_p)/(th_mem/2.0+th_cl/2.0)*Get_Diff_mem_cl(lamcl_a_p,
                lammem_p)*A_act - (lamcl_a_p-
                Get_eqlam(ccl_a_p))*kv*A_act*th_cl*lm)*dt/(A_act*th_cl*lm);
                lamcl_c = lamcl_c_p + ((lammem_p-
                lamcl_c_p)/(th_mem/2.0+th_cl/2.0)*Get_Diff_mem_cl(lamcl_c_p,
                lammem_p)*A_act - (lamcl_c_p-
                Get_eqlam(ccl_c_p))*kv*A_act*th_cl*lm)*dt/(A_act*th_cl*lm);
                lammem = lammem_p - ((lammem_p-
                lamcl_a_p)/(th_mem/2.0+th_cl/2.0)*Get_Diff_mem_cl(lamcl_a_p,
                lammem_p)*A_act + (lammem_p-
                lamcl_c_p)/(th_mem/2.0+th_cl/2.0)*Get_Diff_mem_cl(lamcl_c_p,
                lammem_p)*A_act)*dt/(A_act*th_mem);

                if (cf_a < 0.0) cf_a = 0.0;
                if (cf_c < 0.0) cf_c = 0.0;

    if (t/1.00 == (int)t)
    {
       cout << setw(1) << t << setw(16) << setprecision(10) << cf_a << setw(16) <<
       setprecision(10) << cf_c << setw(16) << setprecision(10) << cgdl_a << setw(16) <<
       setprecision(10) << cgdl_c << setw(16) << setprecision(10) << ccl_a << setw(16) <<
       setprecision(10) << ccl_c << setw(16) << setprecision(10) << lamcl_a << setw(16) <<
       setprecision(10) << lamcl_c << setw(16) << setprecision(10) << lammem << endl;
       myfile << setw(1) << t << setw(16) << setprecision(10) << cf_a << setw(16) <<
       setprecision(10) << cf_c << setw(16) << setprecision(10) << cgdl_a << setw(16) <<
       setprecision(10) << cgdl_c << setw(16) << setprecision(10) << ccl_a << setw(16) <<
       setprecision(10) << ccl_c << setw(16) << setprecision(10) << lamcl_a << setw(16) <<
       setprecision(10) << lamcl_c << setw(16) << setprecision(10) << lammem << endl;
    }
                }

  }

    myfile.close();
}
```

Appendix B

Sample Code of Cold Start Model

```
/*
 *=======================================================================
 *        PEMFC Cold Start Model
 *=======================================================================
*/

#include "udf.h"
#include "sg.h"
#include "stdio.h"
#include "math.h"

/*
 *=======================================================================
 *         Zone IDs, corresponding to different case file
 *=======================================================================
*/

#define Bp_a 10
#define Bp_c 9
#define Channel_a 8
#define Channel_c 7
#define GDL_a 6
#define GDL_c 5
#define CL_a 4
#define CL_c 3
#define Membrane 2

/*
 *=======================================================================
 *         Species, UDSs, UDMs
 *=======================================================================
*/

enum    /* species */
{
    i_h2,
    i_o2,
    i_h2o,
    i_n2,
    NUM_SPECIES
};

enum    /* UDSs */
{
```

```
    Vs,                         /* 0 electronic potential */
    Vm,                         /* 1 Ionic potential */
    Mw,                         /* 2 membrane water content */
    Lq,                         /* 3 liquid water */
    Ice,                        /* 4 ice */
    Fmw,                        /* 5 frozen membrane water content*/
    Pl,                         /* 6 liquid phase pressure, execute on demand */
    NUM_UDS
};

enum    /* UDMs */
{
    eta,                        /* 0 overpotential */
    Ri,                           /* 1 reaction rate */
    activity,                   /* 2 water activity */
    lambda,                             /* 3 water content, unfrozen */
    flambda,          /* 4 frozen water content */
    S_vl,                               /* 5 source of phase change (vapor - liquid) */
    S_vi,                               /* 6 source of phase change (vapor - ice) */
    S_li,                       /* 7 source of phase change (liquid - ice) */
    S_nv,                               /* 8 source of phase change (nonfrozen - vapour) */
    S_ni,                               /* 9 source of phase change (nonfrozen - ice) */
   S_nf,                        /* 10 source of phase change (nonfrozen - frozen) */
    S_reac,                       /* 11 source of water due to reaction */
    S_drag,                       /* 12 source of water due to osmotic drag in CL */
    S_rev,           /* 13 source of heat due to reversible loss */
    S_act,           /* 14 source of heat due to activation loss */
    S_ohm,             /* 15 source of heat due to ohmic loss */
    S_latent,         /* 16 source of heat due to phase change */
    Js_x,                               /* 17 solid phase current density, x-direction */
    Js_y,           /* 18 solid phase current density, y-direction */
    Js_z,           /* 19 solid phase current density, z-direction */
    Jm_x,                               /* 20 membrane phase current density, x-direction */
    Jm_y,            /* 21 membrane phase current density, y-direction */
    Jm_z,            /* 22 membrane phase current density, z-direction */
    Tfpd,           /* 23 freezing point depression */
    eqlambda,          /* 24 equilibrium water content */
   stlambda,         /* 25 saturated water content */
    S_nl,           /* 26 source of ohase change (nonfrozen - liquid) */
   Net_flux_coef,               /* 27 net water transfer coefficient, only execute on demand */
    Jl_x,                       /* 28 liquid water flux, x-direction, only execute on demand */
    Jl_y,           /* 29 liquid water flux, y-direction, only execute on demand */
    Jl_z,           /* 30 liquid water flux, z-direction, only execute on demand */
    Ul_x,                               /* 31 liquid water velocity, x-direction, only execute on
    demand */
    Ul_y,            /* 32 liquid water velocity, y-direction, only execute on demand */
    Ul_z,            /* 33 liquid water velocity, z-direction, only execute on demand */
    Lqq,             /* 34 liquid volume fraction */
    Icee,           /* 35 ice volume fraction */
```

```
    NUM_UDM
};

/*
 *=====================================================================
 *        Parameter values
 *=====================================================================
*/

#define unsteady_on 1                    /* 0: steady state modeling, 1: unsteady modeling */
#define ice_on 1                         /* 0: Ice formation not considered, 1: Ice formation
    considered */
#define flambda_on 1                     /* 0: Frozen membrane water content not considered, 1:
    Frozen membrane water content considered */
#define V_out 0.3                        /* working cell voltage, or output cell voltage */
#define ST_a 2.0                         /* stoicheomic ratio, anode */
#define ST_c 2.0                         /* stoicheomic ratio, cathode */
static double Ref_curr = 0.2;   /* reference current density, A/cm2 */
#define Act_area 2.8          /* active area of MEA, depending on the computational domain, cm2 */
#define Inlet_area 1.0e-6      /* Inlet area of anode and cathode, depending on the computational
    domain, m2 */
#define P_a 1.0                          /* inlet gas pressure, anode */
#define P_c 1.0                          /* inlet gas pressure, cathode */
#define P0 101325.0           /* reference value, do not change! */
static double T0 = 253.15;     /*operating / initial temperature*/
#define Tin 253.15
#define Farad 96487000.0       /* Faraday's constant, C/kmol */
#define alpha_a 0.5
#define alpha_c 0.5
#define gamma_a 0.5
#define gamma_c 1.0
#define n_a 2.0
#define n_c 4.0
#define R_gas 8314.0       /* universal gas constant, J/Kkmol */
#define rcl 1.2e-8                       /* pore radius of CL */
#define rgdl 3.89e-5               /* pore radius of GDL */
#define K_CL 6.2e-13       /* Intrinsic permeability of CL */
#define K_GDL 6.2e-12    /* Intrinsic permeability of GDL */
#define EW 1100.0                        /* equivalent weight kg/kmol */
#define Rho_m 1980.0             /* membrane density kg/m3*/
#define lm 0.2                           /* ionomer fraction in CL */
#define Sigma_GDL 300.0                  /* GDL electrical conductivity */
#define Sigma_CL 300.0                   /* CL electrical conductivity */
#define Sigma_Bp 20000.0       /* Bp conductivity */
#define Kvl 1.0                  /* vapour - liquid phase change rate, condendation */
#define Klv 1.0                  /* liquid - vapour phase change rate, evaporation */
#define Kvi 1.0                  /* vapour - ice phase change rate, desublimation */
#define Kiv 0.0                  /* ice - vapour phase change rate, sublimation */
#define Kli 1.0        /* liquid - ice phase change rate, fusion */
```

```
#define Kil 1.0        /* ice - liquid phase change rate, melting */
#define Knv 1.0        /* nonfrozon - vapour phase change rate */
#define Kvn 1.0        /* vapour - nonfrozen phase change rate */
#define Kni 1.0      /* nonfrozon - ice phase change rate */
#define Kin 0.0        /* ice - nonfrozen phase change rate */
#define Knl 1.0      /* nonfrozon - liquid phase change rate */
#define Kln 0.0        /* liquid - nonfrozen phase change rate */
#define Knf 1.0        /* nonfrozon - frozen phase change rate */
#define Kfn 1.0        /* frozen - nonfrozen phase change rate */
#define delta_S_L 163110.0              /* entropy change, membranew water or liquid product */
#define delta_S_V 43207.0               /* entropy change, vapor product, not using */
#define hfg80 2.308e6                   /* condensation latent heat (J/kg), @80 Celsius */
#define hfl 3.336e5                        /* fusion latent heat (J/kg), @0 Celsius */
#define hmfg 2.906e6                    /* phase change latent heat of hydronium (52300 J/mol,
    Berg, JES2004) */
#define Rho_l 990.0                        /* liquid water density, @50 Celsius averaged over 0 -
    100 Celsius */
#define Rho_i 920.0                        /* ice density, @0 Celsius averaged value*/
#define Sigma_l80 0.06267               /* liquid water surface tension at 80 Celcius */
#define Sigma_l0 0.07564                /* liquid water surface tension at 0 Celcius */
#define theta 100.0          /* contact angle */
#define Diff_nil 1.0e-16
#define D_inf 1.0e10        /* an arbitraraly selected infinite large value */
#define Ds 0.001          /* liquid diffusivity in channel m2/s */
#define H0 2.0e7                        /* Henry's constant for oxygen, Pa m^3/kmol */
const double MW[] = { 2.0, 32.0, 18.0, 28.0 }; /* Molecular weight of four gas species */
#define c_h2_ref 40.0       /*mol/m3*/
#define c_o2_ref 40.0       /*mol/m3*/
static int MY_COUNTER = 1;
static float urf_s = 0.9;             /* urf for general source terms */
static float urf_T = 0.01;            /* urf for temperature source term */
static float urf_mw = 0.06;                  /* urf for nonfrozen membrane water */
static float urf_lq = 0.1;            /* urf for liquid water */
static float urf_ice = 0.1;                  /* urf for ice */
static float urf_fmw = 0.06;    /* urf for frozen membrane water */

/*
 *====================================================================
 *        Variable parameter functions
 *====================================================================
*/

double Get_Porosity(Thread *t) /* Intrinsic porosity */
{
    double por;
    int Zone_ID = THREAD_ID(t);
    if (Zone_ID == CL_a || Zone_ID == CL_c) por = 0.3;
    else if (Zone_ID == GDL_a || Zone_ID == GDL_c) por = 0.6;
    else por = 1.0;
```

```
    return por;
}

double Get_Diff_h2()        /* Hydrogen diffusivity */
{
    return 1.055e-4*pow((T0/333.15),1.5)*(1.0/P_a);
}

double Get_Diff_o2()        /* Oxygen diffusivity */
{
    return 0.2652e-4*pow((T0/333.15),1.5)*(1.0/P_c);
}

double Get_Diff_h2o_a()     /* Anode water diffusivity */
{
    return 1.055e-4*pow((T0/333.15),1.5)*(1.0/P_a);
}

double Get_Diff_h2o_c()     /* Cathode water diffusivity */
{
    return 0.2982e-4*pow((T0/333.15),1.5)*(1.0/P_c);
}

double Get_Diff_others()
{
    return 0.3e-4*pow((T0/333.15),1.5)*(1.0/P_c);
}

double Get_mu_h2()                  /* dynamic viscosity of hydrogen */
{
    return 3.205e-3*pow((T0/293.85),1.5)/(T0+72.0);
}

double Get_mu_o2()                  /* dynamic viscosity of oxygen */
{
    return 8.46e-3*pow((T0/292.25),1.5)/(T0+127.0);
}

double Get_mu_n2()                  /* dynamic viscosity of nitrogen */
{
    return 7.33e-3*pow((T0/300.55),1.5)/(T0+111.0);
}

double Get_mu_h2o()                 /* dynamic viscosity of water vapour */
{
    return 7.512e-3*pow((T0/291.15),1.5)/(T0+120.0);
}

double Get_mu_lq()                  /* dynamic viscosity of liquid water */
```

```
{
    return 2.414e-5*pow(10,(247.8/(MAX(273.15,T0)-140.0)));
}

double Get_P_sat(double T)            /* Saturation pressure vapour */
{
    double P_sat;
    double dT = T - 273.15;
    double exponent = -2.1794 + 0.02953*dT - 9.1837e-5*dT*dT + 1.4454e-7*dT*dT*dT;
    P_sat = pow(10.,exponent) * P0;
    return P_sat;
}

double Get_C_sat(double T)                          /* Saturation concentration of vapour, kmol/m3 */
{
    double P_sat = Get_P_sat(T);
    return P_sat/R_gas/T;
}


double Get_nflambda(double T)        /* Maxiumum allowed nofrozen water */
{
    double nflambda;
    if (T >= 273.15) nflambda = 30.0;
    else if (T < 273.15 && T > 223.15) nflambda = 1.0/(-0.00003594*T*T + 0.01479*T - 1.304);
    else nflambda = 4.83739;
    return MAX(0.0,nflambda);
}

double Get_eqlambda(cell_t c, Thread *t)        /* Equilibrium nofrozen membrane water */
{
   double act, P_sat, act_r;
    double c_h2o = 0.0;
    double lam = 0.0;
    P_sat = Get_P_sat(C_T(c,t));
    c_h2o = C_YI(c,t,i_h2o)*C_R(c,t)/MW[i_h2o];
    act = (c_h2o*R_gas*C_T(c,t))/P_sat;
   act_r = act + 2*MAX(MIN(1.0,C_UDSI(c,t,Lq)), 0.0);
    if (act_r < 0.0) act_r = 0.0;
    if (act_r > 3.0) act_r = 3.0;
       if (act_r <= 1.0)
          {
                lam = 0.04 + 17.81*act_r -39.85*act_r*act_r + 36.0*act_r*act_r*act_r;
          }
          if (act_r > 1.0)
          {
                lam = 14.0 + 1.4*(act_r-1);
          }
    return lam;
```

```
}

double Get_hfg()            /* condensation latent heat at different temperatures, J/kg */
{
    double hfg = -2438.479*MAX(273.15,T0)+3170748.0;
    return hfg;
}

double Get_Sigma_l()        /* surface tension of liquid water N/m */
{
    double Sigma_l = -0.000167591*MAX(273.15,T0) + 0.121836;
    return Sigma_l;
}

double RH_a()               /* Relative humidify, anode inlet */
{
    /*return MIN(1.0,MAX(0.0,(T0-273.15)/30.0));*/
    return 0.0;
}

double RH_c()               /* Relative humidify, cathode inlet */
{
    /*return MIN(1.0,MAX(0.0,(T0-273.15)/30.0));*/
    return 0.0;
}

double Mass_Fraction_Anode(int i)                       /* function to calculate the mass fraction of
    each speicies, anode */
{
    double C_total, C_h2o, C_h2;
    double  rho_total, rho_h2o, rho_h2;
    double y_h2o, y_h2;
    double Psat;
    Psat = Get_P_sat(Tin);
    C_total = P_a*P0/R_gas/Tin;
    C_h2o = RH_a()*Psat/R_gas/Tin;
    C_h2 = C_total-C_h2o;
    rho_h2o = C_h2o*MW[i_h2o];
    rho_h2 = C_h2*MW[i_h2];
    rho_total = C_h2o*MW[i_h2o]+C_h2*MW[i_h2];
    y_h2o = rho_h2o/rho_total;
    y_h2 = rho_h2/rho_total;
    if (i == 1) return y_h2o;
    else return y_h2;
}

double Mass_Fraction_Cathode(int i)                 /* function to calculate the mass fraction of each
    speicies, cathode */
{
```

```
    double C_total, C_h2o, C_o2, C_n2;
    double rho_h2o, rho_o2, rho_total;
    double y_h2o, y_o2;
    double Psat;
    Psat = Get_P_sat(Tin);
    C_total = P_c*P0/R_gas/Tin;
    C_h2o = RH_c()*Psat/R_gas/Tin;
    C_o2 = (C_total-C_h2o)*0.21;
    C_n2 = C_total-C_h2o-C_o2;
    rho_h2o = C_h2o*MW[i_h2o];
    rho_o2 = C_o2*MW[i_o2];
    rho_total = C_h2o*MW[i_h2o]+C_o2*MW[i_o2]+C_n2*MW[i_n2];
    y_h2o = rho_h2o/rho_total;
    y_o2 = rho_o2/rho_total;
    if (i == 1) return y_h2o;
    else return y_o2;
}

double Water_Activity (cell_t c, Thread *t)    /* water activity, only considering vapour */
{
    double act, P_sat;
    double c_h2o = 0.0;
    P_sat = Get_P_sat(C_T(c,t));
    c_h2o = C_YI(c,t,i_h2o)*C_R(c,t)/MW[i_h2o];
    act = (c_h2o*R_gas*C_T(c,t))/P_sat;
    return act;
}

double Water_Content(cell_t c, Thread *t)                    /* nofrozen water content */
{
    double lam;
    lam = C_UDSI(c,t,Mw);
    return lam;
}

double Water_Content_frozen(cell_t c, Thread *t)                    /* frozen water content */
{
    double flam;
    flam = C_UDSI(c,t,Fmw);
    return flam;
}

double Osmotic_Drag_Coefficient(double lam)
{
    double drag = 0.0;
    drag = 2.5/22.0 * lam;
    return drag;
}
```

```
double Membrane_Conductivity(double lam, double T)
{
    double Sigma;
    lam = MAX(1.0,lam);
    Sigma = (0.5139*lam-0.326)*exp(1268.0*(T-303.15)/(T*303.15));
    return Sigma;
}

double Water_Membrane_Diffusivity(double lam)
{
    double D_wm;
    if (lam < 0.0) lam = 0.0;
    if (lam > 17.0)  lam = 17.0;
    if (lam > 0 && lam <= 3.0) D_wm = Rho_m/EW*3.1e-7*lam*(exp(0.28*lam)-1.0)*exp(-
    2346.0/T0);
    else D_wm = Rho_m/EW*4.17e-8*lam*(1.0+161.0*exp(-lam))*exp(-2346.0/T0);
    return D_wm;
}

double Eta_total()          /* Total voltage loss, based on membrane water/liquid water product */
{
    double V_open;
    V_open = 1.229-0.846e-3*(T0-298.0)+R_gas*T0/(2.0*Farad)*(log(P_a-
    RH_a()*0.4669)+0.5*log((P_c-RH_c()*0.4669)*0.21));
    if (V_out <= 0.6 && MY_COUNTER < 20) return (V_open-0.65);
    else return (V_open - V_out);
}

double aj0_a_ref()                          /* Reference anode exchange current density, changes with
    temperature */
{
   return 1.0e9*exp(-1400*(1/T0 - 1/353.15));
}

double aj0_c_ref()                          /* Reference cathode exchange current density, changes with
    temperature */
{
    return 10000.0*exp(-7900*(1/T0 - 1/353.15));
}

double RR_a(cell_t c, Thread *t)                                    /* Butler_Volmer reaction rate,
    anode */
{
    double coeff, exp_1, exp_2, Ra;
    double c_h2 = 0.0;
    c_h2 = C_YI(c,t,i_h2)*C_R(c,t)/MW[i_h2];
    coeff = aj0_a_ref()*pow((c_h2/c_h2_ref),gamma_a);
    exp_1 = alpha_a*n_a*Farad/R_gas/C_T(c,t)*C_UDMI(c,t,eta);
    exp_2 = alpha_c*n_a*Farad/R_gas/C_T(c,t)*C_UDMI(c,t,eta);
```

```
    Ra = pow((1.0-MIN(MAX((C_UDSI(c,t,Lq) + C_UDSI(c,t,Ice)), 0.0),
    1.0)),2.5)*coeff*(exp(exp_1)-exp(-exp_2));
    return Ra;
}

double RR_c(cell_t c, Thread *t)                                    /* Butler_Volmer reaction rate,
    cathode */
{
    double coeff, exp_1, exp_2, Rc;
    double c_o2 = 0.0;
    c_o2 = C_YI(c,t,i_o2)*C_R(c,t)/MW[i_o2];
    coeff = -aj0_c_ref()*pow((c_o2/c_o2_ref),gamma_c);
   /*coeff = -aj0_c_ref()*pow((R_gas*C_T(c,t)/H0*c_o2/c_o2_ref),gamma_c);*/
    exp_1 = alpha_a*n_c*Farad/R_gas/C_T(c,t)*C_UDMI(c,t,eta);
    exp_2 = alpha_c*n_c*Farad/R_gas/C_T(c,t)*C_UDMI(c,t,eta);
    Rc = pow((1.0-MIN(MAX((C_UDSI(c,t,Lq) + C_UDSI(c,t,Ice)), 0.0),
    1.0)),2.5)*coeff*(exp(exp_1)-exp(-exp_2));
    return Rc;
}

double Get_K_GDL(cell_t c, Thread *t) /* real GDL permeability corrected by ice*/
{
    return K_GDL*pow((1.0-MAX(MIN(0.99,C_UDSI(c,t,Ice)), 0.0)),4.0);
}

double Get_K_CL(cell_t c, Thread *t)    /* real CL permeability corrected by ice*/
{
    return K_CL*pow((1.0-MAX(MIN(0.99,C_UDSI(c,t,Ice)), 0.0)),4.0);
}

double Get_Krl(cell_t c, Thread *t)                 /* liquid phase relative permeability */
{
    return pow(MAX(MIN(1.0,C_UDSI(c,t,Lq)), 0.0),4.0)*pow((1.0-
    MAX(MIN(0.99,C_UDSI(c,t,Ice)), 0.0)),4.0);
}

double Get_Krg(cell_t c, Thread *t)                 /* gas phase relative permeability */
{
    return pow((1.0-MAX(MIN(0.99,(C_UDSI(c,t,Lq)+C_UDSI(c,t,Ice))), 0.0)),4.0);
}

double Get_dJ_ds(cell_t c, Thread *t)      /* L J-function, derivative */
{
    if (theta >= 90.0) return 1.417-4.24*MAX(MIN(1.0,C_UDSI(c,t,Lq)),
    0.0)+3.789*MAX(MIN(1.0,C_UDSI(c,t,Lq)), 0.0)*MAX(MIN(1.0,C_UDSI(c,t,Lq)), 0.0);
    if (theta < 90.0) return 1.417-4.24*(1.0-MAX(MIN(1.0,C_UDSI(c,t,Lq)), 0.0))+3.789*(1.0-
    MAX(MIN(1.0,C_UDSI(c,t,Lq)), 0.0))*(1.0-MAX(MIN(1.0,C_UDSI(c,t,Lq)), 0.0));
}
```

```
double Get_J_s(cell_t c, Thread *t)                    /* L J-function */
{
    if (theta >= 90.0) return (1.417*MAX(MIN(1.0,C_UDSI(c,t,Lq)), 0.0)-
    2.12*pow(MAX(MIN(1.0,C_UDSI(c,t,Lq)),
    0.0),2.0)+1.263*pow(MAX(MIN(1.0,C_UDSI(c,t,Lq)), 0.0),3.0));
   if (theta < 90.0) return (1.417*(1.0-MAX(MIN(1.0,C_UDSI(c,t,Lq)), 0.0))-2.12*pow(1.0-
    MAX(MIN(1.0,C_UDSI(c,t,Lq)), 0.0),2.0)+1.263*pow(1.0-MAX(MIN(1.0,C_UDSI(c,t,Lq)),
    0.0),3.0));
}

double Get_lambda_l(cell_t c, Thread *t)   /*for uds Pl */
{
    double Krl = Get_Krl(c,t);
    double Krg = Get_Krg(c,t);
    return Krl/(Get_mu_lq()/Rho_l)/(Krl/(Get_mu_lq()/Rho_l)+Krg/(C_MU_L(c,t)/C_R(c,t)));
}

double Get_lambda_g(cell_t c, Thread *t)   /*for uds Pl */
{
    double lambda_l = Get_lambda_l(c,t);
    return (1.0-lambda_l);
}

double Get_niu(cell_t c, Thread *t)                    /* for uds Pl, kinematic viscosity */
{
    double Krl = Get_Krl(c,t);
    double Krg = Get_Krg(c,t);
    return 1.0/(Krl/(Get_mu_lq()/Rho_l)+Krg/(C_MU_L(c,t)/C_R(c,t)));
}

double Get_Pc_GDL(cell_t c, Thread *t)                    /* for uds Pl, Capillary pressure in GDL*/
{
    double J_s = Get_J_s(c,t);
    double Sigma_l = Get_Sigma_l();
    return Sigma_l*cos(theta*M_PI/180.0)*sqrt(Get_Porosity(t)/Get_K_GDL(c,t))*J_s;
}

double Get_Pc_CL(cell_t c, Thread *t)              /* for uds in Pl, Capillary pressure in CL */
{
    double J_s = Get_J_s(c,t);
    double Sigma_l = Get_Sigma_l();
    return Sigma_l*cos(theta*M_PI/180.0)*sqrt(Get_Porosity(t)/Get_K_CL(c,t))*J_s;
}

double Get_S_vl(cell_t c,Thread *t)                /* vapour - liquid phase change source term function
    (condensation/evaporation) */
{
    double Sw;
    double C_h2o, C_sat;
```

```
    double rho_h2o, rho_sat;
    double T = C_T(c,t);
    C_sat = Get_C_sat(T);
    C_h2o = C_YI(c,t,i_h2o)*C_R(c,t)/MW[i_h2o];
    rho_h2o = MW[i_h2o]*C_h2o;
    rho_sat = MW[i_h2o]*C_sat;
   if (T >= C_UDMI(c,t,Tfpd) + 273.15)
   {
    if (rho_h2o > rho_sat)  Sw = Get_Porosity(t)*Kvl*(rho_h2o-rho_sat)*(1.0-
    MAX(MIN(1.0,C_UDSI(c,t,Lq)+C_UDSI(c,t,Ice)), 0.0));
     else Sw = Get_Porosity(t)*Klv*(rho_h2o-rho_sat)*MAX(MIN(1.0,C_UDSI(c,t,Lq)), 0.0);
   }
   else
   {
    if (rho_h2o > rho_sat)  Sw = 0.0;
     else Sw = Get_Porosity(t)*Klv*(rho_h2o-rho_sat)*MAX(MIN(1.0,C_UDSI(c,t,Lq)), 0.0);
   }
   return Sw;
}

double Get_S_vi(cell_t c,Thread *t)                /* vapour - ice phase change source term function
    (desublimation/sublimation) */
{
    double Sw;
    double C_h2o, C_sat;
    double rho_h2o, rho_sat;
    double T = C_T(c,t);
    C_sat = Get_C_sat(T);
    C_h2o = C_YI(c,t,i_h2o)*C_R(c,t)/MW[i_h2o];
    rho_h2o = MW[i_h2o]*C_h2o;
    rho_sat = MW[i_h2o]*C_sat;
   if (T >= C_UDMI(c,t,Tfpd) + 273.15)
   {
    Sw = 0.0;
   }
   else
   {
    if (rho_h2o > rho_sat)  Sw = Get_Porosity(t)*Kvi*(rho_h2o-rho_sat)*(1.0-
    MAX(MIN(1.0,C_UDSI(c,t,Lq)+C_UDSI(c,t,Ice)), 0.0));
     else Sw = 0.0;
   }
   return Sw;
}

double Get_S_li(cell_t c,Thread *t)                /* liquid - ice phase change source term function
    (fusion/melting) */
{
   double Sw;
    double T = C_T(c,t);
```

```
   if (T < (C_UDMI(c,t,Tfpd) + 273.15))  Sw =
    Get_Porosity(t)*Kli*Rho_l*MAX(MIN(1.0,C_UDSI(c,t,Lq)), 0.0);
   else  Sw = -Get_Porosity(t)*Kil*Rho_i*MAX(MIN(1.0,C_UDSI(c,t,Ice)), 0.0);
   return Sw;
}

double Get_S_nv(cell_t c,Thread *t)                /* nonfrozen - vapour phase change source term
    function */
{
    double Sw;
    double C_h2o, C_sat;
    double nv, vn;
    int Zone_ID = THREAD_ID(t);
    double eqlam = C_UDMI(c,t,eqlambda);
    double lam = C_UDMI(c,t,lambda);
    double T = C_T(c,t);
    C_sat = Get_C_sat(T);
    C_h2o = C_YI(c,t,i_h2o)*C_R(c,t)/MW[i_h2o];
    nv = MIN(Knv*Rho_m/EW*(lam - eqlam),100.0*C_sat);
   vn = MAX(Kvn*Rho_m/EW*(lam - eqlam),-100.0*C_h2o);
    if (Zone_ID == CL_c || Zone_ID == CL_a)
    {
          if (lam > eqlam) Sw = nv*Get_Porosity(t)*(1.0-
    MAX(MIN(1.0,C_UDSI(c,t,Lq)+C_UDSI(c,t,Ice)), 0.0));
       else Sw = vn*Get_Porosity(t)*(1.0-MAX(MIN(1.0,C_UDSI(c,t,Lq)+C_UDSI(c,t,Ice)), 0.0));
    }
    else Sw = 0.0;
    return Sw;
}

double Get_S_ni(cell_t c,Thread *t)                /* nonfrozen - ice phase change source term function
    */
{
    double Sw;
    double T = C_T(c,t);
    double nflambda = MIN(14.0, C_UDMI(c,t,stlambda));
    double lam = C_UDMI(c,t,lambda);
   if (T < (C_UDMI(c,t,Tfpd) + 273.15))
    {
    if (lam > nflambda) Sw = Kni*Rho_m/EW*(lam - nflambda)*Get_Porosity(t)*(1.0-
    MAX(MIN(1.0,C_UDSI(c,t,Lq)+C_UDSI(c,t,Ice)), 0.0));
    else Sw = 0.0;
    }
   else Sw = 0.0;
   return Sw;
}

double Get_S_nl(cell_t c,Thread *t)                /* nonfrozen - liquid phase change source term
    function */
```

```
{
    double Sw;
    double T = C_T(c,t);
    double lam = C_UDMI(c,t,lambda);
    if (T >= (C_UDMI(c,t,Tfpd) + 273.15))
    {
    if (lam > 14.0) Sw = Knl*Rho_m/EW*(lam - 14.0)*Get_Porosity(t)*(1.0-
    MAX(MIN(1.0,C_UDSI(c,t,Lq)+C_UDSI(c,t,Ice)), 0.0));
    else Sw = 0.0;
    }
   else Sw = 0.0;
   return Sw;
}


double Get_S_nf(cell_t c,Thread *t)                /* nonfrozen - frozen phase change source term
    function */
{
    double Sw;
    double T = C_T(c,t);
    double nflambda = C_UDMI(c,t,stlambda);
    double lam = C_UDMI(c,t,lambda);
    if (lam > nflambda) Sw = Knf*Rho_m/EW*(lam - nflambda);
    else Sw = -Kfn*Rho_m/EW*C_UDSI(c,t,Fmw);
   return Sw;
}

/*
 *=========================================================================
 *        Define macros
 *=========================================================================
*/

DEFINE_PROPERTY(viscosity_hydrogen,c,t)
{
    return Get_mu_h2();
}

DEFINE_PROPERTY(viscosity_oxygen,c,t)
{
    return Get_mu_o2();
}

DEFINE_PROPERTY(viscosity_nitrogen,c,t)
{
    return Get_mu_n2();
}

DEFINE_PROPERTY(viscosity_vapour,c,t)
```

```
{
    return Get_mu_h2o();
}

DEFINE_PROFILE(porosity,t,i)
{
  cell_t c;
  begin_c_loop(c,t)
  {
    C_PROFILE(c,t,i) = Get_Porosity(t)*(1.0-MIN(MAX((C_UDMI(c,t,Lqq) + C_UDMI(c,t,Icee)),
    0.0), 0.99));
  }
  end_c_loop(c,t)
}

DEFINE_PROFILE(V_eta,t,i)              /* boundary condition, total over-potential on the anode
    surface */
{
    face_t f;

    begin_f_loop(f,t)
    {
        F_PROFILE(f,t,i) = Eta_total();
    }
    end_f_loop(f,t)
}

DEFINE_PROFILE(In_T_a,t,i) /* boundary condition, apply at the anode inlet and outlet, using T0
    */
{
    face_t f;
    begin_f_loop(f,t)
    {
        F_PROFILE(f,t,i) = T0;
    }
    end_f_loop(f,t)
}

DEFINE_PROFILE(In_T_c,t,i) /* boundary condition, apply at the cathode inlet and outlet, using T0
    */
{
    face_t f;
    begin_f_loop(f,t)
    {
        F_PROFILE(f,t,i) = T0;
    }
    end_f_loop(f,t)
}
```

```
DEFINE_PROFILE(RH_anode,t,i)        /* boundary condition, anode inlet relative humidity */
{
    face_t f;
    begin_f_loop(f,t)
    {
        F_PROFILE(f,t,i) = RH_a();
    }
    end_f_loop(f,t)
}

DEFINE_PROFILE(RH_cathode,t,i)      /* boundary condition, cathode inlet relative humidity */
{
    face_t f;
    begin_f_loop(f,t)
    {
        F_PROFILE(f,t,i) = RH_c();
    }
    end_f_loop(f,t)
}

DEFINE_PROFILE(Y_h2o_a,t,i)                 /* anode inlet boundary condition, water vapor */
{
    face_t f;
    double y_h2o;
    y_h2o = Mass_Fraction_Anode(1);
    begin_f_loop(f,t)
    {
        F_PROFILE(f,t,i) = y_h2o;
    }
    end_f_loop(f,t)
}

DEFINE_PROFILE(Y_h2_a,t,i)          /* anode inlet boundary condition, hydrogen */
{
    face_t f;
    double y_h2;
    y_h2 = Mass_Fraction_Anode(0);
    begin_f_loop(f,t)
    {
        F_PROFILE(f,t,i) = y_h2;
    }
    end_f_loop(f,t)
}

DEFINE_PROFILE(Y_h2o_c,t,i)                 /* cathode inlet boundary condition, water vapor */
{
    face_t f;
    double y_h2o;
    y_h2o = Mass_Fraction_Cathode(1);
```

```
    begin_f_loop(f,t)
    {
        F_PROFILE(f,t,i) = y_h2o;
    }
    end_f_loop(f,t)
}

DEFINE_PROFILE(Y_o2_c,t,i)          /* cathode inlet boundary condition, oxygen */
{
    face_t f;
    double y_o2;
    y_o2 = Mass_Fraction_Cathode(0);
    begin_f_loop(f,t)
    {
        F_PROFILE(f,t,i) = y_o2;
    }
    end_f_loop(f,t)
}

DEFINE_PROFILE(mf_a,t,i)            /* anode inlet boundary condition, mass flux */
{
    face_t f;
    double C_total, C_h2, C_h2o;
    double rho_total;
    double vel, mf;
    double Psat;
    Psat = Get_P_sat(Tin);
    C_total = P_a*P0/R_gas/Tin;
    C_h2o = RH_a()*Psat/R_gas/Tin;
    C_h2 = C_total-C_h2o;
    rho_total = C_h2o*MW[i_h2o]+C_h2*MW[i_h2];
    vel = ST_a*Ref_curr*Act_area/2.0/Farad/C_h2/Inlet_area;
    mf = rho_total*vel;
    begin_f_loop(f,t)
    {
        F_PROFILE(f,t,i) = mf;
    }
    end_f_loop(f,t)
}

DEFINE_PROFILE(mf_c,t,i)            /* cathode inlet boundary condition, mass flux */
{
    face_t f;
    double C_total, C_h2o, C_o2, C_n2;
    double rho_total;
    double Psat;
    double vel, mf;
    Psat = Get_P_sat(Tin);
    C_total = P_c*P0/R_gas/Tin;
```

```
    C_h2o = RH_c()*Psat/R_gas/Tin;
    C_o2 = (C_total-C_h2o)*0.21;
    C_n2 = C_total-C_h2o-C_o2;
    rho_total = C_h2o*MW[i_h2o]+C_o2*MW[i_o2]+C_n2*MW[i_n2];
    vel = ST_c*Ref_curr*Act_area/4.0/Farad/C_o2/Inlet_area;
    mf = rho_total*vel;
    begin_f_loop(f,t)
    {
        F_PROFILE(f,t,i) = mf;
    }
    end_f_loop(f,t)
}

DEFINE_PROFILE(permeability_GDL,t,i)                    /* GDL 1/permeability*/
{
  cell_t c;
  begin_c_loop(c,t)
  {
    C_PROFILE(c,t,i) = 1.0/K_GDL/pow((1.0-
    MAX(MIN(0.99,(C_UDMI(c,t,Lqq)+C_UDMI(c,t,Icee))), 0.0)),4.0);
  }
  end_c_loop(c,t)
}

DEFINE_PROFILE(permeability_CL,t,i)                     /* GDL 1/permeability*/
{
  cell_t c;
  begin_c_loop(c,t)
  {
    C_PROFILE(c,t,i) = 1.0/K_CL/pow((1.0-
    MAX(MIN(0.99,(C_UDMI(c,t,Lqq)+C_UDMI(c,t,Icee))), 0.0)),4.0);
  }
  end_c_loop(c,t)
}

DEFINE_ADJUST(PEM_adjust,d)
{
    Thread *t;
    cell_t c;

/* URF for governing equations */

   float uds_urf[6];
    float species_urf[3];

    uds_urf[0] = 0.01;
    uds_urf[1] = 0.01;
    uds_urf[2] = 0.999;
    uds_urf[3] = 0.01;
```

```
 uds_urf[4] = 0.999;
 uds_urf[5] = 0.999;
 species_urf[0] = 1.0;
species_urf[1] = 1.0;
 species_urf[2] = 1.0;

 if (MY_COUNTER <= 50)
   {
      uds_urf[0] = 0.01;
    uds_urf[1] = 0.01;
    uds_urf[2] = 0.00001;
    uds_urf[3] = 0.00001;
      uds_urf[4] = 0.00001;
    uds_urf[5] = 0.00001;
      species_urf[0] = 1.0;
      species_urf[1] = 1.0;
      species_urf[2] = 1.0;
      Domainvar_Set_Real(ROOT_DOMAIN_ID,"temperature/relax", 0.1);
   }
 else if (MY_COUNTER <= 100)
   {
      uds_urf[0] = 0.1;
    uds_urf[1] = 0.1;
    uds_urf[2] = 0.1;
    uds_urf[3] = 0.1;
      uds_urf[4] = 0.1;
    uds_urf[5] = 0.1;
      species_urf[0] = 1.0;
      species_urf[1] = 1.0;
      species_urf[2] = 1.0;
      Domainvar_Set_Real(ROOT_DOMAIN_ID,"temperature/relax", 0.1);
   }
 else if (MY_COUNTER <= 200)
   {
      uds_urf[0] = 0.9;
    uds_urf[1] = 0.3;
    uds_urf[2] = 0.9;
    uds_urf[3] = 0.9;
      uds_urf[4] = 0.9;
    uds_urf[5] = 0.9;
      species_urf[0] = 1.0;
      species_urf[1] = 1.0;
      species_urf[2] = 1.0;
      Domainvar_Set_Real(ROOT_DOMAIN_ID,"temperature/relax", 1.0);
   }
 else if (MY_COUNTER <= 300)
   {
      uds_urf[0] = 0.99;
    uds_urf[1] = 0.5;
```

```
      uds_urf[2] = 0.99;
      uds_urf[3] = 0.99;
         uds_urf[4] = 0.99;
      uds_urf[5] = 0.99;
         species_urf[0] = 1.0;
         species_urf[1] = 1.0;
         species_urf[2] = 1.0;
         Domainvar_Set_Real(ROOT_DOMAIN_ID,"temperature/relax", 1.0);
      }
    else if (MY_COUNTER <= 400)
      {
         uds_urf[0] = 0.999;
      uds_urf[1] = 0.6;
      uds_urf[2] = 0.999;
      uds_urf[3] = 0.999;
         uds_urf[4] = 0.999;
      uds_urf[5] = 0.999;
         species_urf[0] = 1.0;
         species_urf[1] = 1.0;
         species_urf[2] = 1.0;
         Domainvar_Set_Real(ROOT_DOMAIN_ID,"temperature/relax", 1.0);
      }
    else
      {
         uds_urf[0] = 0.999;
      uds_urf[1] = 0.9;
      uds_urf[2] = 0.999;
      uds_urf[3] = 0.999;
         uds_urf[4] = 0.999;
      uds_urf[5] = 0.999;
         species_urf[0] = 1.0;
         species_urf[1] = 1.0;
         species_urf[2] = 1.0;
         Domainvar_Set_Real(ROOT_DOMAIN_ID,"temperature/relax", 1.0);
      }

    Domainvar_Set_List_of_Float(ROOT_DOMAIN_ID, "uds/relax", uds_urf, 6);
    Domainvar_Set_List_of_Float(ROOT_DOMAIN_ID, "species/relax", species_urf, 3);

    if (urf_T < 1.0) urf_T += 0.005;
    else urf_T = 1.0;

    MY_COUNTER += 1;

/* Update values */

    thread_loop_c(t,d)
    {
         begin_c_loop_all(c,t)
```

```
{
        double lam,n_d,act;
        double T = C_T(c,t);
int Zone_ID = THREAD_ID(t);

        /* freezing the nitrogen mass fraction to zero at anode side */
        if (Zone_ID == Channel_a || Zone_ID == GDL_a || Zone_ID == CL_a)
 C_YI(c,t,i_n2) = 0.0;

        if (Zone_ID == CL_a || Zone_ID == CL_c)
        {
                C_UDMI(c,t,eta) += urf_s*((C_UDSI(c,t,Vs)-C_UDSI(c,t,Vm))-
C_UDMI(c,t,eta));
                C_UDMI(c,t,activity) += urf_s*(Water_Activity(c,t)-C_UDMI(c,t,activity));
                C_UDMI(c,t,lambda) += urf_s*(Water_Content(c,t)-C_UDMI(c,t,lambda));
                C_UDMI(c,t,eqlambda) += urf_s*(Get_eqlambda(c,t)-
C_UDMI(c,t,eqlambda));
                C_UDMI(c,t,stlambda) += urf_s*(Get_nflambda(C_T(c,t))-
C_UDMI(c,t,stlambda));
                C_UDMI(c,t,S_vl) += urf_lq*(Get_S_vl(c,t)-C_UDMI(c,t,S_vl));
                C_UDMI(c,t,S_vi) += urf_ice*(Get_S_vi(c,t)-C_UDMI(c,t,S_vi));
                C_UDMI(c,t,S_li) += urf_lq*(Get_S_li(c,t)-C_UDMI(c,t,S_li));
                C_UDMI(c,t,S_nv) += urf_mw*(Get_S_nv(c,t)-C_UDMI(c,t,S_nv));
                C_UDMI(c,t,S_ni) += urf_mw*(Get_S_ni(c,t)-C_UDMI(c,t,S_ni));
                C_UDMI(c,t,S_nl) += urf_mw*(Get_S_nl(c,t)-C_UDMI(c,t,S_nl));

                C_UDMI(c,t,Tfpd) =
Sigma_l0*273.15*cos(theta*M_PI/180.0)/Rho_i/hfl/rcl;
                C_UDSI(c,t,Ice) = MAX(MIN(C_UDSI(c,t,Ice),1.0), 0.0);
      C_UDSI(c,t,Lq) = MAX(MIN(C_UDSI(c,t,Lq),1.0-MAX(MIN(C_UDSI(c,t,Ice),1.0), 0.0)),
0.0);
                lam = C_UDMI(c,t,lambda);
                n_d = Osmotic_Drag_Coefficient(lam);

                if (Zone_ID == CL_a)
                {
                        C_UDMI(c,t,Ri) += urf_s*(RR_a(c,t)-C_UDMI(c,t,Ri));
                        C_UDMI(c,t,S_drag) += urf_mw*(-n_d*RR_a(c,t)/Farad-
C_UDMI(c,t,S_drag));
                }
                else
                {
                        C_UDMI(c,t,Ri) += urf_s*(RR_c(c,t)-C_UDMI(c,t,Ri));
                        C_UDMI(c,t,S_reac) += urf_mw*(RR_c(c,t)/Farad/2.0-
C_UDMI(c,t,S_reac));
                        C_UDMI(c,t,S_drag) += urf_mw*(n_d*RR_c(c,t)/Farad-
C_UDMI(c,t,S_drag));
                }
        }
```

```
                else if (Zone_ID == Membrane)
                {
                        C_UDMI(c,t,lambda) += urf_s*(Water_Content(c,t)-C_UDMI(c,t,lambda));
                        C_UDMI(c,t,flambda) += urf_s*(Water_Content_frozen(c,t)-
    C_UDMI(c,t,flambda));
        C_UDMI(c,t,S_nf) += urf_mw*(Get_S_nf(c,t)-C_UDMI(c,t,S_nf));
                        C_UDMI(c,t,stlambda) += urf_s*(Get_nflambda(C_T(c,t))-
    C_UDMI(c,t,stlambda));
                        C_UDSI(c,t,Mw) = MAX(C_UDSI(c,t,Mw), 0.0);
        C_UDSI(c,t,Fmw) = MAX(C_UDSI(c,t,Fmw), 0.0);
                }
                else if (Zone_ID == GDL_a || Zone_ID == GDL_c)
                {
        C_UDMI(c,t,activity) += urf_s*(Water_Activity(c,t)-C_UDMI(c,t,activity));
                        C_UDMI(c,t,S_vl) += urf_lq*(Get_S_vl(c,t)-C_UDMI(c,t,S_vl));
                        C_UDMI(c,t,S_vi) += urf_ice*(Get_S_vi(c,t)-C_UDMI(c,t,S_vi));
                        C_UDMI(c,t,S_li) += urf_lq*(Get_S_li(c,t)-C_UDMI(c,t,S_li));

                        C_UDMI(c,t,Tfpd) =
    Sigma_l0*273.15*cos(theta*M_PI/180.0)/Rho_i/hfl/rgdl;
                        C_UDSI(c,t,Ice) = MAX(MIN(C_UDSI(c,t,Ice),1.0), 0.0);
        C_UDSI(c,t,Lq) = MAX(MIN(C_UDSI(c,t,Lq),1.0-MAX(MIN(C_UDSI(c,t,Ice),1.0), 0.0)),
    0.0);
                }
                else if (Zone_ID == Channel_a || Zone_ID == Channel_c)
                {
                        C_UDMI(c,t,activity) += urf_s*(Water_Activity(c,t)-C_UDMI(c,t,activity));
                }
                else if (Zone_ID == Bp_a || Zone_ID == Bp_c)
                {
                }
                else
                {
                }
        }
        end_c_loop_all(c,t)
    }

    Message("\nMY_COUNTER = %d\n", MY_COUNTER);
    Message("\nurf_T = %g\n", urf_T);
    Message("\nT0 = %g\n", T0);
    Message("\nIref = %g\n", Ref_curr);
}

DEFINE_EXECUTE_AT_END(PEM_at_end)
{
    Domain *d;
    Thread *t;
    cell_t c;
```

```
 double temp = 0.0;
 double volume = 0.0;
 double curr_den=0.0;
 double volumegdl = 0.0;
double delta_S = delta_S_L;
double hfg = Get_hfg();
 d = Get_Domain(1);
 MY_COUNTER = 1;

 thread_loop_c(t,d)
 {
       int Zone_ID = THREAD_ID(t);
       begin_c_loop(c,t)
       {
       double Svl = C_UDMI(c,t,S_vl);
    double Svi = C_UDMI(c,t,S_vi);
   double Sli = C_UDMI(c,t,S_li);
       double Snv = C_UDMI(c,t,S_nv)*MW[i_h2o];
       double Sni = C_UDMI(c,t,S_ni)*MW[i_h2o];
    double Snf = C_UDMI(c,t,S_nf)*MW[i_h2o];
       double NV_VEC(Js), NV_VEC(Jm);
    ND_SET(Js[0], Js[1], Js[2], C_UDMI(c,t,Js_x), C_UDMI(c,t,Js_y), C_UDMI(c,t,Js_z));
    ND_SET(Jm[0], Jm[1], Jm[2], C_UDMI(c,t,Jm_x), C_UDMI(c,t,Jm_y), C_UDMI(c,t,Jm_z));
                if (unsteady_on)
      {
                        temp += (C_T(c,t)*C_VOLUME(c,t));
                   volume += C_VOLUME(c,t);
                }
                if (Zone_ID == Channel_a || Zone_ID == GDL_a || Zone_ID == CL_a)
       C_YI(c,t,i_n2) = 0.0;
                if (Zone_ID == CL_a || Zone_ID == CL_c)
                {
                        C_UDMI(c,t,Js_x) += urf_s*(-
 C_UDSI_G(c,t,Vs)[0]*C_UDSI_DIFF(c,t,Vs)-C_UDMI(c,t,Js_x));
                        C_UDMI(c,t,Js_y) += urf_s*(-
 C_UDSI_G(c,t,Vs)[1]*C_UDSI_DIFF(c,t,Vs)-C_UDMI(c,t,Js_y));
                        C_UDMI(c,t,Js_z) += urf_s*(-
 C_UDSI_G(c,t,Vs)[2]*C_UDSI_DIFF(c,t,Vs)-C_UDMI(c,t,Js_z));
                        C_UDMI(c,t,Jm_x) += urf_s*(-
 C_UDSI_G(c,t,Vm)[0]*C_UDSI_DIFF(c,t,Vm)-C_UDMI(c,t,Jm_x));
                        C_UDMI(c,t,Jm_y) += urf_s*(-
 C_UDSI_G(c,t,Vm)[1]*C_UDSI_DIFF(c,t,Vm)-C_UDMI(c,t,Jm_y));
                        C_UDMI(c,t,Jm_z) += urf_s*(-
 C_UDSI_G(c,t,Vm)[2]*C_UDSI_DIFF(c,t,Vm)-C_UDMI(c,t,Jm_z));
                        C_UDSI(c,t,Ice) = MAX(MIN(C_UDSI(c,t,Ice),1.0), 0.0);
          C_UDSI(c,t,Lq) = MAX(MIN(C_UDSI(c,t,Lq),1.0-MAX(MIN(C_UDSI(c,t,Ice),1.0), 0.0)),
 0.0);
                        C_UDMI(c,t,S_rev) = 0.0;
                        C_UDMI(c,t,S_act) = fabs(C_UDMI(c,t,eta))*C_UDMI(c,t,Ri);
```

```
                        C_UDMI(c,t,S_ohm) = NV_MAG2(Js)/C_UDSI_DIFF(c,t,Vs) +
NV_MAG2(Jm)/C_UDSI_DIFF(c,t,Vm);
                        C_UDMI(c,t,S_latent) = Svl*hfg + Svi*(hfg+hfl) + Sli*hfl - Snv*hfg +
Sni*hfl;
                        C_UDMI(c,t,Lqq) = C_UDSI(c,t,Lq);
                        C_UDMI(c,t,Icee) = C_UDSI(c,t,Ice);
                        if (Zone_ID == CL_c) C_UDMI(c,t,S_rev) =
delta_S/2.0/Farad*C_T(c,t)*C_UDMI(c,t,Ri);
                }
                else if (Zone_ID == Membrane)
                {
                        C_UDMI(c,t,Js_x) = 0.0;
                        C_UDMI(c,t,Js_y) = 0.0;
                        C_UDMI(c,t,Js_z) = 0.0;
                        C_UDMI(c,t,Jm_x) += urf_s*(-
C_UDSI_G(c,t,Vm)[0]*C_UDSI_DIFF(c,t,Vm)-C_UDMI(c,t,Jm_x));
                        C_UDMI(c,t,Jm_y) += urf_s*(-
C_UDSI_G(c,t,Vm)[1]*C_UDSI_DIFF(c,t,Vm)-C_UDMI(c,t,Jm_y));
                        C_UDMI(c,t,Jm_z) += urf_s*(-
C_UDSI_G(c,t,Vm)[2]*C_UDSI_DIFF(c,t,Vm)-C_UDMI(c,t,Jm_z));
                        C_UDMI(c,t,S_rev) = 0.0;
                        C_UDMI(c,t,S_act) = 0.0;
                        C_UDMI(c,t,S_ohm) = NV_MAG2(Jm)/C_UDSI_DIFF(c,t,Vm);
                        C_UDMI(c,t,S_latent) = Snf*hfl;
                }
                else if (Zone_ID == GDL_a || Zone_ID == GDL_c)
                {
                        C_UDMI(c,t,Js_x) += urf_s*(-
C_UDSI_G(c,t,Vs)[0]*C_UDSI_DIFF(c,t,Vs)-C_UDMI(c,t,Js_x));
                        C_UDMI(c,t,Js_y) += urf_s*(-
C_UDSI_G(c,t,Vs)[1]*C_UDSI_DIFF(c,t,Vs)-C_UDMI(c,t,Js_y));
                        C_UDMI(c,t,Js_z) += urf_s*(-
C_UDSI_G(c,t,Vs)[2]*C_UDSI_DIFF(c,t,Vs)-C_UDMI(c,t,Js_z));
                        C_UDMI(c,t,Jm_x) = 0.0;
                        C_UDMI(c,t,Jm_y) = 0.0;
                        C_UDMI(c,t,Jm_z) = 0.0;
                        C_UDSI(c,t,Ice) = MAX(MIN(C_UDSI(c,t,Ice),1.0), 0.0);
        C_UDSI(c,t,Lq) = MAX(MIN(C_UDSI(c,t,Lq),1.0-MAX(MIN(C_UDSI(c,t,Ice),1.0), 0.0)),
0.0);
                        C_UDMI(c,t,S_rev) = 0.0;
                        C_UDMI(c,t,S_act) = 0.0;
                        C_UDMI(c,t,S_ohm) = NV_MAG2(Js)/C_UDSI_DIFF(c,t,Vs);
                        C_UDMI(c,t,S_latent) = Svl*hfg+ Svi*(hfg+hfl) + Sli*hfl;
                        C_UDMI(c,t,Lqq) = C_UDSI(c,t,Lq);
                        C_UDMI(c,t,Icee) = C_UDSI(c,t,Ice);
                        curr_den += (C_UDMI(c,t,Js_y)*C_VOLUME(c,t));
                   volumegdl += C_VOLUME(c,t);
                }
                else if (Zone_ID == Bp_a || Zone_ID == Bp_c)
```

```
                {
                        C_UDMI(c,t,Js_x) += urf_s*(-
    C_UDSI_G(c,t,Vs)[0]*C_UDSI_DIFF(c,t,Vs)-C_UDMI(c,t,Js_x));
                        C_UDMI(c,t,Js_y) += urf_s*(-
    C_UDSI_G(c,t,Vs)[1]*C_UDSI_DIFF(c,t,Vs)-C_UDMI(c,t,Js_y));
                        C_UDMI(c,t,Js_z) += urf_s*(-
    C_UDSI_G(c,t,Vs)[2]*C_UDSI_DIFF(c,t,Vs)-C_UDMI(c,t,Js_z));
                        C_UDMI(c,t,Jm_x) = 0.0;
                        C_UDMI(c,t,Jm_y) = 0.0;
                        C_UDMI(c,t,Jm_z) = 0.0;
                        C_UDMI(c,t,S_rev) = 0.0;
                        C_UDMI(c,t,S_act) = 0.0;
                        C_UDMI(c,t,S_ohm) = NV_MAG2(Js)/C_UDSI_DIFF(c,t,Vs);
                        C_UDMI(c,t,S_latent) = 0.0;
                }
                else
                {
                        C_UDMI(c,t,Js_x) = 0.0;
                        C_UDMI(c,t,Js_y) = 0.0;
                        C_UDMI(c,t,Js_z) = 0.0;
                        C_UDMI(c,t,Jm_x) = 0.0;
                        C_UDMI(c,t,Jm_y) = 0.0;
                        C_UDMI(c,t,Jm_z) = 0.0;
                        C_UDMI(c,t,S_rev) = 0.0;
                        C_UDMI(c,t,S_act) = 0.0;
                        C_UDMI(c,t,S_ohm) = 0.0;
                        C_UDMI(c,t,S_latent) = 0.0;
                }
        }
        end_c_loop(c,t)
    }
  if (unsteady_on)
  {
    T0 = temp/volume;
    Ref_curr = (curr_den/volumegdl)/(-10000.0);
  }
}

DEFINE_INIT(PEM_initialization, d)
{
    Thread *t;
    cell_t c;
    int   Zone_ID;
    int i;

    Message(" \n\n Start initialization... \n\n");

    MY_COUNTER = 1;
```

```
thread_loop_c(t,d)
{
	Zone_ID = THREAD_ID(t);
	begin_c_loop(c,t)
	{
		C_T(c,t) = T0;
		for (i=0; i < NUM_UDM; i++) C_UDMI(c,t,i) = 0.0;
		if (Zone_ID == Channel_a || Zone_ID == GDL_a || Zone_ID == CL_a)
		{
			C_YI(c,t,i_h2) = Mass_Fraction_Anode(0);
			C_YI(c,t,i_o2) = 0.0;
			C_YI(c,t,i_h2o) = Mass_Fraction_Anode(1);
			C_UDMI(c,t,activity) = RH_a();
			if (Zone_ID == GDL_a)
			{
				C_UDSI(c,t,Vs) = 0.0;
				C_UDSI(c,t,Ice) = 0.0;
			}
			if (Zone_ID == CL_a)
			{
				C_UDMI(c,t,eta) = 0.0;
				C_UDSI(c,t,Vs) = 0.0;
				C_UDSI(c,t,Vm) = 0.0;
				C_UDSI(c,t,Ice) = 0.0;
				C_UDSI(c,t,Mw) = 5.0;
				C_UDMI(c,t,lambda) = 5.0;
			}
		}
		if (Zone_ID == Channel_c || Zone_ID == GDL_c || Zone_ID == CL_c)
		{
			C_YI(c,t,i_h2) = 0.0;
			C_YI(c,t,i_o2) = Mass_Fraction_Cathode(0);
			C_YI(c,t,i_h2o) = Mass_Fraction_Cathode(1);
			C_UDMI(c,t,activity) = RH_c();
			if (Zone_ID == GDL_c)
			{
				C_UDSI(c,t,Vs) = 0.0;
				C_UDSI(c,t,Ice) = 0.0;
			}
			if (Zone_ID == CL_c)
			{
				C_UDMI(c,t,eta) = 0.0;
				C_UDSI(c,t,Vs) = 0.0;
				C_UDSI(c,t,Vm) = 0.0;
				C_UDSI(c,t,Ice) = 0.0;
				C_UDSI(c,t,Mw) = 5.0;
				C_UDMI(c,t,lambda) = 5.0;
			}
		}
```

```
                if (Zone_ID == Membrane)
                {
                        C_UDSI(c,t,Mw) = 5.0;
                        C_UDMI(c,t,lambda) = 5.0;
                        C_UDSI(c,t,Fmw) = 0.0;
                        C_UDMI(c,t,flambda) = 0.0;
                }
                if (Zone_ID == Bp_a)    C_UDSI(c,t,Vs) = 0.0;
        if (Zone_ID == Bp_c)    C_UDSI(c,t,Vs) = 0.0;
         }
         end_c_loop(c,t)
    }
    Message(" Done. \n\n");
}

DEFINE_UDS_UNSTEADY(UDS_Unsteady,c,t,i,apu,su)          /* unsteady terms of Vs and Vm are
    negligible */
{
    double delta_t, w_old;
    int Zone_ID = THREAD_ID(t);
    delta_t = RP_Get_Real("physical-time-step");
    w_old = C_STORAGE_R(c,t,SV_UDSI_M1(i));

    if (i == Mw)
    {
         if (Zone_ID == CL_a || Zone_ID == CL_c)
         {
         *apu = -lm*Rho_m/EW*C_VOLUME(c,t)/delta_t;
         *su = lm*Rho_m/EW*C_VOLUME(c,t)*w_old/delta_t;
         }
         else
         {
         *apu = -Rho_m/EW*C_VOLUME(c,t)/delta_t;
         *su = Rho_m/EW*C_VOLUME(c,t)*w_old/delta_t;
         }
    }
    if (i == Lq)
    {
         *apu = -Get_Porosity(t)*Rho_l*C_VOLUME(c,t)/delta_t;
         *su = Get_Porosity(t)*Rho_l*C_VOLUME(c,t)*w_old/delta_t;
    }
   if (i == Fmw)
    {
         *apu = -Rho_m/EW*C_VOLUME(c,t)/delta_t;
         *su = Rho_m/EW*C_VOLUME(c,t)*w_old/delta_t;
    }
    if (i == Ice)
    {
         *apu = -Get_Porosity(t)*Rho_i*C_VOLUME(c,t)/delta_t;
```

```
        *su = Get_Porosity(t)*Rho_i*C_VOLUME(c,t)*w_old/delta_t;
    }
}

DEFINE_DIFFUSIVITY(diff_uds, c, t, uds_i)
{
    double diff = Diff_nil, lam;
    double T = C_T(c,t);
    int Zone_ID = THREAD_ID(t);
    if (uds_i == Vs)
    {
        if (Zone_ID == GDL_a || Zone_ID == GDL_c) diff = pow((1-
    Get_Porosity(t)),1.5)*Sigma_GDL;
        else if (Zone_ID == CL_a || Zone_ID == CL_c)  diff = pow((1-Get_Porosity(t)-
    lm),1.5)*Sigma_CL;
        else if (Zone_ID == Bp_a || Zone_ID == Bp_c) diff = Sigma_Bp;
        else diff = Diff_nil;
    }
    if (uds_i == Vm)
    {
        if (Zone_ID == Membrane || Zone_ID == CL_a || Zone_ID == CL_c)
        {
                lam = C_UDMI(c,t,lambda);
                if (Zone_ID == CL_a || Zone_ID == CL_c) diff = pow(lm,
    1.5)*Membrane_Conductivity(lam,T);
                else diff = Membrane_Conductivity(lam,T);
        }
        else diff = Diff_nil;
    }
    if (uds_i == Mw)
    {
                lam = C_UDMI(c,t,lambda);
                if (Zone_ID == CL_a || Zone_ID == CL_c) diff = pow(lm,
    1.5)*Water_Membrane_Diffusivity(lam);
                else diff = Water_Membrane_Diffusivity(lam);
    }
    if (uds_i == Lq)
    {
        double Krl = Get_Krl(c,t);
        double dJ_ds = Get_dJ_ds(c,t);
        double mu_lq = Get_mu_lq();
        double Sigma_l = Get_Sigma_l();
        if (Zone_ID == GDL_c || Zone_ID == GDL_a)
        {
                diff = -
    Rho_l/mu_lq*Sigma_l*cos(theta*M_PI/180.0)*sqrt(Get_Porosity(t)*K_GDL)*Krl*dJ_ds;
        }

        else if (Zone_ID == CL_c || Zone_ID == CL_a)
```

```
        {
                diff = -
    Rho_l/mu_lq*Sigma_l*cos(theta*M_PI/180.0)*sqrt(Get_Porosity(t)*K_CL)*Krl*dJ_ds;
        }

        else if (Zone_ID == Channel_c || Zone_ID == Channel_a) diff = Rho_l*Ds;
        else diff = Diff_nil;
    }
    if (uds_i == Ice)
    {
                diff = Diff_nil;
    }
    if (uds_i == Fmw)
    {
                diff = Diff_nil;
    }
    diff = MAX(Diff_nil, diff);
    return diff;
}

DEFINE_DIFFUSIVITY(diff_species, c, t, species_i)
{
    double diff = Diff_nil;
    int Zone_ID = THREAD_ID(t);
    double T = C_T(c,t);
    if (species_i == i_h2)
    {
        diff = Get_Diff_h2()*pow(Get_Porosity(t),1.5)*pow((1.0-
    MAX(MIN(0.9,C_UDSI(c,t,Lq)+C_UDSI(c,t,Ice)), 0.0)),1.5);
    }
    if (species_i == i_o2)
    {
        diff = Get_Diff_o2()*pow(Get_Porosity(t),1.5)*pow((1.0-
    MAX(MIN(0.9,C_UDSI(c,t,Lq)+C_UDSI(c,t,Ice)), 0.0)),1.5);
    }
    if (species_i == i_h2o)
    {
      if (Zone_ID == CL_a || Zone_ID == GDL_a || Zone_ID == Channel_a) diff =
    Get_Diff_h2o_a()*pow(Get_Porosity(t),1.5)*pow((1.0-
    MAX(MIN(0.9,C_UDSI(c,t,Lq)+C_UDSI(c,t,Ice)), 0.0)),1.5);
        else diff = Get_Diff_h2o_c()*pow(Get_Porosity(t),1.5)*pow((1.0-
    MAX(MIN(0.9,C_UDSI(c,t,Lq)+C_UDSI(c,t,Ice)), 0.0)),1.5);
    }
    diff = MAX(Diff_nil, diff);
    return diff;
}

DEFINE_SOURCE(source_Vs, c, t, dS, eqn)                    /* source of electronic phase
    potential */
```

```
{
    double S_Vs = 0.0;
    int Zone_ID = THREAD_ID(t);
    if (Zone_ID == CL_a)        S_Vs = -C_UDMI(c,t,Ri);
    if (Zone_ID == CL_c)        S_Vs = C_UDMI(c,t,Ri);
    dS[eqn] = 0.0;
    return S_Vs;
}

DEFINE_SOURCE(source_Vm, c, t, dS, eqn)                    /* source of electrolyte phase
    potential */
{
    double S_Vm = 0.0;
    int Zone_ID = THREAD_ID(t);
    if (Zone_ID == CL_a)        S_Vm = C_UDMI(c,t,Ri);
    if (Zone_ID == CL_c)        S_Vm = -C_UDMI(c,t,Ri);
    dS[eqn] = 0.0;
    return S_Vm;
}

DEFINE_SOURCE(source_h2, c, t, dS, eqn)                    /* source of hydrogen */
{
    double S_h2 = 0.0;
    S_h2 = -MW[i_h2]*C_UDMI(c,t,Ri)/2.0/Farad;
    dS[eqn] = 0.0;
    return S_h2;
}

DEFINE_SOURCE(source_o2, c, t, dS, eqn)                    /* source of oxygen */
{
    double S_o2 = 0.0;
    S_o2 = -MW[i_o2]*C_UDMI(c,t,Ri)/4.0/Farad;
    dS[eqn] = 0.0;
    return S_o2;
}

DEFINE_SOURCE(source_h2o, c, t, dS, eqn)            /* source of water vapor */

{
    double S_h2o = 0.0;
    int Zone_ID = THREAD_ID(t);
    if (Zone_ID == CL_c || Zone_ID == CL_a) S_h2o = - C_UDMI(c,t,S_vl) - C_UDMI(c,t,S_vi) +
    C_UDMI(c,t,S_nv)*MW[i_h2o];
    else if (Zone_ID == GDL_a || Zone_ID == GDL_c)    S_h2o = - C_UDMI(c,t,S_vl)-
    C_UDMI(c,t,S_vi);
    else if (Zone_ID == Channel_a || Zone_ID == Channel_c) S_h2o = 0.0;
    else S_h2o = 0.0;
    dS[eqn] = 0.0;
    return S_h2o;
```

```
}

DEFINE_SOURCE(source_Lq, c, t, dS, eqn)                 /* source of liquid water */
{
    double S_Lq;
    int Zone_ID = THREAD_ID(t);
    double S_convec;
    double mu_g = C_MU_L(c,t);
    double mu_lq = Get_mu_lq();
    double Krl = Get_Krl(c,t);
    double Krg = Get_Krg(c,t);
    S_convec = -Rho_l*mu_g*Krl/mu_lq/Krg*(C_DUDX(c,t)+C_DVDY(c,t)+C_DWDZ(c,t));
    if (Zone_ID == CL_c || Zone_ID == CL_a) S_Lq = C_UDMI(c,t,S_vl) - C_UDMI(c,t,S_li) +
    C_UDMI(c,t,S_nl)*MW[i_h2o];
    else if (Zone_ID == GDL_c || Zone_ID == GDL_a) S_Lq = C_UDMI(c,t,S_vl)-
    C_UDMI(c,t,S_li);
    else if (Zone_ID == Channel_a || Zone_ID == Channel_c)
    {
          S_Lq = 0.0;
          S_convec = 0.0;
    }
    else S_Lq = 0.0;
    dS[eqn] = 0.0;
    return (S_Lq + S_convec);
}

DEFINE_SOURCE(source_Ice, c, t, dS, eqn)                /* source of ice */
{
   double S_Ice;
   int Zone_ID = THREAD_ID(t);
    if (Zone_ID == CL_c || Zone_ID == CL_a) S_Ice = C_UDMI(c,t,S_vi) + C_UDMI(c,t,S_li) +
    C_UDMI(c,t,S_ni)*MW[i_h2o];
    else if (Zone_ID == GDL_c || Zone_ID == GDL_a) S_Ice = C_UDMI(c,t,S_vi) +
    C_UDMI(c,t,S_li);
    else S_Ice = 0.0;
    dS[eqn] = 0.0;
    return S_Ice;
}

DEFINE_SOURCE(source_Mw, c, t, dS, eqn)                 /* source of Mw */
{
   double S_Mw;
    int Zone_ID = THREAD_ID(t);
    double drag = C_UDMI(c,t,S_drag);
    double react = C_UDMI(c,t,S_reac);
    if (Zone_ID == Membrane) S_Mw = -C_UDMI(c,t,S_nf);
    else if (Zone_ID == CL_a) S_Mw = -C_UDMI(c,t,S_nv) - C_UDMI(c,t,S_ni) -
    C_UDMI(c,t,S_nl)+ drag;
```

```
    else if (Zone_ID == CL_c) S_Mw = -C_UDMI(c,t,S_nv) - C_UDMI(c,t,S_ni) -
    C_UDMI(c,t,S_nl)+ drag + react;
    else S_Mw = 0.0;
    dS[eqn] = 0.0;
    return S_Mw;
}

DEFINE_SOURCE(source_Fmw, c, t, dS, eqn)              /* source of Fmw */
{
   double S_Fmw;
    int Zone_ID = THREAD_ID(t);
    S_Fmw = C_UDMI(c,t,S_nf);
    dS[eqn] = 0.0;
    return S_Fmw;
}

DEFINE_SOURCE(source_mass, c, t, dS, eqn)             /* mass source */

{
    double S_mass = 0.0;
    int Zone_ID = THREAD_ID(t);
    if (Zone_ID == CL_a)
    {
          S_mass = - C_UDMI(c,t,S_vl) - C_UDMI(c,t,S_vi) + C_UDMI(c,t,S_nv)*MW[i_h2o];
          S_mass += -MW[i_h2]*C_UDMI(c,t,Ri)/2.0/Farad;
    }
    else if (Zone_ID == CL_c)
    {
          S_mass = - C_UDMI(c,t,S_vl) - C_UDMI(c,t,S_vi) + C_UDMI(c,t,S_nv)*MW[i_h2o];
          S_mass += -MW[i_o2]*C_UDMI(c,t,Ri)/4.0/Farad;
    }
    else if (Zone_ID == GDL_a || Zone_ID == GDL_c)    S_mass = - C_UDMI(c,t,S_vl) -
    C_UDMI(c,t,S_vi);
    else if (Zone_ID == Channel_a || Zone_ID == Channel_c) S_mass = 0.0;
    else S_mass = 0.0;
    dS[eqn] = 0.0;
    return S_mass;
}

DEFINE_SOURCE(source_energy, c, t, dS, eqn)                              /* energy source */
{
    double S_energy = 0.0;
    double heat_rev, heat_act, heat_ohm, heat_latent;
    double T = C_T(c,t);
    int Zone_ID = THREAD_ID(t);
    double delta_S = delta_S_L;
    double hfg = Get_hfg();
    double Svl = C_UDMI(c,t,S_vl);
    double Svi = C_UDMI(c,t,S_vi);
```

```
double Sli = C_UDMI(c,t,S_li);
double Snv = C_UDMI(c,t,S_nv)*MW[i_h2o];
 double Sni = C_UDMI(c,t,S_ni)*MW[i_h2o];
 double Snf = C_UDMI(c,t,S_nf)*MW[i_h2o];
 double NV_VEC(Js), NV_VEC(Jm);
 ND_SET(Js[0], Js[1], Js[2], C_UDMI(c,t,Js_x), C_UDMI(c,t,Js_y), C_UDMI(c,t,Js_z));
 ND_SET(Jm[0], Jm[1], Jm[2], C_UDMI(c,t,Jm_x), C_UDMI(c,t,Jm_y), C_UDMI(c,t,Jm_z));
 switch (Zone_ID)
 {
      case CL_c:
            heat_rev = delta_S/2.0/Farad*T*C_UDMI(c,t,Ri);
            heat_act = fabs(C_UDMI(c,t,eta))*C_UDMI(c,t,Ri);
            heat_ohm = NV_MAG2(Js)/C_UDSI_DIFF(c,t,Vs) +
 NV_MAG2(Jm)/C_UDSI_DIFF(c,t,Vm);
            heat_latent = Svl*hfg + Svi*(hfg+hfl) + Sli*hfl - Snv*hfg + Sni*hfl;
            break;
      case CL_a:
            heat_rev = 0.0;
            heat_act = fabs(C_UDMI(c,t,eta))*C_UDMI(c,t,Ri);
            heat_ohm = NV_MAG2(Js)/C_UDSI_DIFF(c,t,Vs) +
 NV_MAG2(Jm)/C_UDSI_DIFF(c,t,Vm);
            heat_latent = Svl*hfg + Svi*(hfg+hfl) + Sli*hfl - Snv*hfg + Sni*hfl;
            break;
      case Membrane:
            heat_rev = 0.0;
            heat_act = 0.0;
            heat_ohm = NV_MAG2(Jm)/C_UDSI_DIFF(c,t,Vm);
            heat_latent = Snf*hfl;
            break;
      case GDL_a:
            heat_rev = 0.0;
            heat_act = 0.0;
            heat_ohm = NV_MAG2(Js)/C_UDSI_DIFF(c,t,Vs);
            heat_latent = Svl*hfg+ Svi*(hfg+hfl) + Sli*hfl;
            break;
      case GDL_c:
            heat_rev = 0.0;
            heat_act = 0.0;
            heat_ohm = NV_MAG2(Js)/C_UDSI_DIFF(c,t,Vs);
            heat_latent = Svl*hfg+ Svi*(hfg+hfl) + Sli*hfl;
            break;
      case Channel_c:
            heat_rev = 0.0;
            heat_act = 0.0;
            heat_ohm = 0.0;
            heat_latent = 0.0;
            break;
      case Channel_a:
            heat_rev = 0.0;
```

```
                heat_act = 0.0;
                heat_ohm = 0.0;
                heat_latent = 0.0;
                break;
        case Bp_c:
                heat_rev = 0.0;
                heat_act = 0.0;
                heat_ohm = NV_MAG2(Js)/C_UDSI_DIFF(c,t,Vs);
                heat_latent = 0.0;
                break;
        case Bp_a:
                heat_rev = 0.0;
                heat_act = 0.0;
                heat_ohm = NV_MAG2(Js)/C_UDSI_DIFF(c,t,Vs);
                heat_latent = 0.0;
                break;
        default:
                heat_rev = 0.0;
                heat_act = 0.0;
                heat_ohm = 0.0;
                heat_latent = 0.0;
                break;
    }
    S_energy = heat_rev + heat_act + heat_ohm + heat_latent;
    dS[eqn] = 0.0;
    return urf_T*S_energy;
}

DEFINE_ON_DEMAND(Liquid_water)          /* calculating liquid phase pressure and velocity
    vecotr */
{
    Domain *d;
    Thread *t;
    cell_t c;
    face_t f;
    int Zone_ID;
    double lambda_l, lambda_g, niu;
    d = Get_Domain(1);

    thread_loop_f (t,d)
    {
        Zone_ID= THREAD_ID(t);

        if (NULL != THREAD_STORAGE(t,SV_UDS_I(Pl)) && NULL != T_STORAGE_R_NV(t-
    >t0,SV_UDSI_G(Pl)))
        {
                begin_f_loop (f,t)
                {
                        F_UDSI(f,t,Pl)=C_UDSI(F_C0(f,t),t->t0,Pl);
```

```
            }
        }
        end_f_loop(f,t)
}
thread_loop_c (t,d)
{
        Zone_ID= THREAD_ID(t);
        if (NULL != THREAD_STORAGE(t,SV_UDS_I(Pl)) && NULL !=
T_STORAGE_R_NV(t,SV_UDSI_G(Pl)))
        {
                begin_c_loop (c,t)
                {
                        if (Zone_ID == GDL_c || Zone_ID == GDL_a)
                        {
                        lambda_l = Get_lambda_l(c,t);
                        lambda_g = Get_lambda_g(c,t);
                        niu = Get_niu(c,t);
                        C_UDSI(c,t,Pl) = C_P(c,t)-Get_Pc_GDL(c,t);
                        C_UDMI(c,t,Jl_x) =
lambda_l*lambda_g/niu*K_GDL*C_UDSI_G(c,t,Pl)[0];
                        C_UDMI(c,t,Jl_y) =
lambda_l*lambda_g/niu*K_GDL*C_UDSI_G(c,t,Pl)[1];
                        C_UDMI(c,t,Jl_z) =
lambda_l*lambda_g/niu*K_GDL*C_UDSI_G(c,t,Pl)[2];
                        C_UDMI(c,t,Ul_x) = -
K_GDL*Get_Krl(c,t)/Get_mu_lq()*C_UDSI_G(c,t,Pl)[0];
                        C_UDMI(c,t,Ul_y) = -
K_GDL*Get_Krl(c,t)/Get_mu_lq()*C_UDSI_G(c,t,Pl)[1];
                        C_UDMI(c,t,Ul_z) = -
K_GDL*Get_Krl(c,t)/Get_mu_lq()*C_UDSI_G(c,t,Pl)[2];
                        }
                        if (Zone_ID == CL_c || Zone_ID == CL_a)
                        {
                        lambda_l = Get_lambda_l(c,t);
                        lambda_g = Get_lambda_g(c,t);
                        niu = Get_niu(c,t);
                        C_UDSI(c,t,Pl) = C_P(c,t)-Get_Pc_CL(c,t);
                        C_UDMI(c,t,Jl_x) = lambda_l*lambda_g/niu*K_CL*C_UDSI_G(c,t,Pl)[0];
                        C_UDMI(c,t,Jl_y) = lambda_l*lambda_g/niu*K_CL*C_UDSI_G(c,t,Pl)[1];
                        C_UDMI(c,t,Jl_z) = lambda_l*lambda_g/niu*K_CL*C_UDSI_G(c,t,Pl)[2];
                        C_UDMI(c,t,Ul_x) = -
K_CL*Get_Krl(c,t)/Get_mu_lq()*C_UDSI_G(c,t,Pl)[0];
                        C_UDMI(c,t,Ul_y) = -
K_CL*Get_Krl(c,t)/Get_mu_lq()*C_UDSI_G(c,t,Pl)[1];
                        C_UDMI(c,t,Ul_z) = -
K_CL*Get_Krl(c,t)/Get_mu_lq()*C_UDSI_G(c,t,Pl)[2];
                        }
                }
                end_c_loop (c,t)
```

```
            }
        }
    }
```